Cranfield University

J M Bridgeman

Investigating the Relationship Between Shear and Floc Fate using CFD

School of Applied Sciences

PhD THESIS

ProQuest Number: 10832219

All rights reserved

INFORMATION TO ALL USERS
The quality of this reproduction is dependent upon the quality of the copy submitted.

In the unlikely event that the author did not send a complete manuscript
and there are missing pages, these will be noted. Also, if material had to be removed,
a note will indicate the deletion.



ProQuest 10832219

Published by ProQuest LLC (2018). Copyright of the Dissertation is held by Cranfield University.

All rights reserved.
This work is protected against unauthorized copying under Title 17, United States Code
Microform Edition © ProQuest LLC.

ProQuest LLC.
789 East Eisenhower Parkway
P.O. Box 1346
Ann Arbor, MI 48106 – 1346

Cranfield University

School of Applied Sciences

PhD

2006

Jonathan Matthew Bridgeman

Investigating the relationship between shear and floc fate using CFD

Supervisors: Professor Simon A. Parsons and Dr Bruce Jefferson

November 2006

©Cranfield University, 2006. All rights reserved. No part of this publication may be reproduced without the written permission of the copyright holder.

This thesis is submitted in partial fulfilment of the requirements for the Degree of Doctor of Philosophy.

Abstract

The size, density and strength of flocs play a major role in the removal of contaminants from water in physico-chemical treatment processes. The efficiency of the main removal processes is a function of floc size, strength and density. Changes in these parameters affect floc removal and hence the removal of adsorbed organic matter. Coagulation and flocculation efficiency and floc strength are often assessed using a jar tester. Here, computational fluid dynamics (CFD) was used to model the flow field within standard jar test apparatus and, using a Lagrangian particle trajectory model, to study the effects of turbulence on individual flocs. The hydrodynamic environments were also investigated experimentally using laser Doppler anemometry (LDA) and particle image velocimetry (PIV) measurement techniques. Combining numerical and experimental data, velocity gradient values at which floc breakage occurs were postulated for three different floc suspensions. Although the threshold values are determined using jar test and CFD data in combination, they are based on the flocs' resistance to induced velocity gradients. This is a significant result, as previous breakage thresholds have been expressed only in terms of mixing speed and cannot be applied at full scale.

With this in mind, work was subsequently undertaken to use CFD to model numerically the hydrodynamic conditions within two full scale flocculation vessels; one mechanically mixed, the other hydraulically mixed. This section of work had two principal aims; firstly, to investigate the perceived benefits of using CFD to model the hydraulic performance of the flocculation process at two large surface water treatment works, and secondly, to investigate the practicality and effectiveness of using CFD and jar test results in combination to consider floc fate in the flocculation vessels (in terms of growth, breakage and residence time). This work drew upon the results and conclusions of the previous laboratory scale work and facilitated a greater insight into flocculation processes. Improved understanding of flocculator hydrodynamics can only serve to improve design procedures and standards for future installations.

Acknowledgements

The work reported in this thesis was sponsored by the American Water Works Association Research Foundation (AWWARF), Fort Collins Water (USA), Scottish Water, Severn Trent Water, Thames Water, United Utilities and Yorkshire Water, without whom this work would not have been possible.

Contrary to popular opinion, a PhD is not a one person affair; rather there are a lot of people without whom the project would have failed. Firstly, I must thank my supervisors, Professor Simon Parsons and Dr Bruce Jefferson, for their enthusiasm, advice and constructive criticism of the work. I would also like to thank Dr Peter Jarvis of Cranfield University for invaluable comments and advice.

I would like to thank Dr Waldemar Bujalski of the Department of Chemical Engineering at the University of Birmingham for allowing my unskilled hands access to his PIV instrumentation. Also at the University of Birmingham, I would like to thank Dr John West of the Department of Civil Engineering for his help, advice and insightful comments over the past year. Thanks must also go to Edward Throp at Fluent for his patience and advice.

On a personal level, thanks to my mum for having that sense of belief in me which only a mother can have, and thanks to my dad for being my, albeit unwitting, academic inspiration.

I thank Anna and James for their constant reminders that there is more to life than velocity gradients and computers.

But finally, above all, I must thank Kay who, despite not having the slightest interest in, nor understanding of, the subject matter in this thesis, remains the only person to understand me.

Table of Contents

ABSTRACT I

ACKNOWLEDGEMENTS II

TABLE OF CONTENTS III

LIST OF FIGURES IX

LIST OF TABLES XV

ABBREVIATIONS & NOTATION XVII

1 INTRODUCTION 1

1.1 Background 1

1.2 Motivation for the Work 2

1.3 Scope of Study 5

1.4 Thesis Plan 7

2 LITERATURE REVIEW 11

2.1 Fluid Flow 11
2.1.1 Introduction 11

2.2 Turbulence 13
2.2.1 Turbulent Flow 13

2.3 Mixing Processes 17
2.3.1 Mixing Scales 17
2.3.2 Flow Patterns 18
2.3.3 Velocity Gradient 19
2.3.4 Power Number 23
2.3.5 Residence Time Distribution 25

2.4 Flocculation **29**
2.4.1 Conceptual View of Flocculation 29
2.4.2 Flocculation Theory 30
2.4.3 The Jar Test 33
2.4.4 Laboratory Scale Investigations into Mixing Processes, Coagulation and Flocculation 34
2.4.5 Floc Strength 39
2.4.6 Floc Breakage 42
2.4.7 Floc Re-growth 45
2.4.8 Floc Size Measurement 46
2.4.9 Summary 48

2.5 Computational Fluid Dynamics **49**
2.5.1 General Description & History 49
2.5.2 Generic Methodology 51
2.5.3 Turbulence Modelling 53
2.5.4 Discretisation 66
2.5.5 Multiphase Modelling 68
2.5.6 Commercial CFD Software Packages 69
2.5.7 Use of CFD to Simulate Mixing Processes 70

2.6 Use of CFD in the Water Industry **73**
2.6.1 Sewerage 73
2.6.2 Sewage Treatment 76
2.6.3 Water Resources 81
2.6.4 Water Treatment 83

2.7 Summary **101**

3 OBJECTIVES **104**

4 EXPERIMENTAL METHODS AND RESULTS **105**

4.1 Experimental Methods **105**
4.1.1 Power Measurement 105
4.1.2 Laser Doppler Anemometry 107
4.1.3 Particle Image Velocimetry 109

4.2 Experimental Results **113**
4.2.1 Power Measurement 113
4.2.2 Laser Doppler Anemometry (LDA) Results – Cylindrical Vessel 115

4.2.3 Particle Image Velocimetry (PIV) Results – Hudson Vessel 120

4.3 Summary 125

5 CFD ANALYSES – METHODOLOGY AND VALIDATION 127

5.1 Methodology 127
5.1.1 Background 127
5.1.2 Modelling Rotating Flows 128
5.1.3 Boundary Conditions and Calculation Procedure 130
5.1.4 Grid Resolution 133
5.1.5 Turbulence Modelling 140

5.2 Model Validation 142
5.2.1 Introduction 142
5.2.2 Velocity Data 143
5.2.3 Turbulence Data 145

5.3 Turbulence Modelling and Rotating Mesh Discussion 147

5.4 Summary 153

6 JAR TEST CFD ANALYSES OF CYLINDRICAL AND HUDSON VESSELS: FLOW FIELD CHARACTERISTICS 154

6.1 Introduction 154

6.2 Velocity Magnitude 155

6.3 Axial and Tangential Velocities 160

6.4 Turbulence Dissipation Rate 164
6.4.1 Distribution of Turbulence Dissipation Rate 164
6.4.2 Magnitude of Turbulence Dissipation Rate 169

6.5 Summary 174

7 CYLINDRICAL JAR TEST APPARATUS - CFD PARTICLE TRAJECTORY ANALYSIS 176

7.1 Introduction 176

7.2 Modelling Particle Trajectories 178

7.3 Random Particle Analysis 180
7.3.1 Particle Trajectories and Fates 180
7.3.2 Local Velocity Gradient Variation Along Trajectory 181
7.3.3 Period of Exposure to Local Velocity Gradients 187

7.4 Summary 193

8 COMPARISON OF TRAJECTORY DATA WITH LABORATORY-DERIVED FLOC SIZE DATA 195

8.1 Previous Laboratory-Scale Work 195

8.2 CFD Results 198
8.2.1 Local Velocity Gradient Along Trajectory 198

8.3 Summary 215

9 FRANKLEY WTW FLOCCULATOR CFD ANALYSES 217

9.1 Introduction 217

9.2 Frankley WTW 218

9.3 Modelling Strategy 221

9.4 Results 224
9.4.1 Velocity Profiles 224
9.4.2 Particle Trajectory Analysis 225
9.4.3 Residence Time Distributions (RTD) 226
9.4.4 Average Velocity Gradient, Local Velocity Gradient and Turbulence Dissipation Rate 233

9.5 Summary 242

10 BAMFORD WTW FLOCCULATOR CFD ANALYSIS 244

10.1 Introduction 244

10.2 Bamford WTW 245

10.3 Modelling Strategy and Validation 247

10.3.1 Grid Density 247
10.3.2 Model Validation 250

10.4 Results 254
10.4.1 Velocity Profiles 254
10.4.2 Residence Time Distribution 256
10.4.3 Average and Local Velocity Gradients 259

10.5 Financial Implications 263

10.6 Summary 264

11 DISCUSSION 268

11.1 Introduction 268

11.2 Flow Visualisation 269

11.3 Jar Test CFD Modelling Strategy 271

11.4 Hydrodynamics of the Jar Test Apparatus 276

11.5 Effect of Jar Test Flow Regime on Flocs 278

11.6 Implications for Full Scale Flocculation 283
11.6.1 Frankley WTW 283
11.6.2 Bamford WTW 287

11.7 The Use of CFD in the Water Industry 288

12 CONCLUSIONS 291

12.1 Modelling Strategy and Methods 291

12.2 Hydrodynamics of the Jar Test Apparatus 291

12.3 Particle Trajectory Analysis in the Cylindrical Jar Tester 292

12.4 Floc Breakage Mechanisms and Criteria 293

12.5 Floc Growth Mechanisms and Criteria 294

12.6 Flocculator Assessment and Design Guidance 294

12.6.1 Frankley WTW Mechanical Flocculator 294
12.6.2 Bamford WTW Hydraulic Flocculator 295

12.7 The Use of CFD in the Water Industry 295

13 RECOMMENDATIONS FOR FURTHER WORK 296

REFERENCES 298

List of Figures

Figure 1-1: Raw water colour concentrations for Albert reservoir, Halifax, UK, January 1992 to May 2002. 3

Figure 2-1: Turbulent flow visualisations (from Bell, 2004). 15

Figure 2-2: Idealized visualisation of turbulent length scales (from Stanley & Smith, 1995). 16

Figure 2-3: Flow pattern associated with common radial flow impeller. 19

Figure 2-4: Power number vs. impeller Reynolds number for seven different impellers (from Bates *et al*, 1963). 24

Figure 2-5: Tracer curves from ideal reactors (a) plug flow reactor, (b) completely mixed flow reactor. 25

Figure 2-6: Example of a non-ideal tracer output from a stirred tank. 26

Figure 2-7: Exit age distribution as a function of normalised time – C Curve. 28

Figure 2-8: Exit age distribution as a function of normalised time – F Curve. 28

Figure 2-9: The relationship between the change in particle size and an increase in velocity gradient for 3 types of floc. Floc (a) is resistant to breakage, floc (b) is thought to break due to large scale fragmentation and floc (c) is thought to break by surface erosion (from Jarvis *et al*, 2005a). 41

Figure 2-10: Steady state floc size after exposure to increased levels of shear (from Jarvis *et al*, 2004). 44

Figure 2-11: Floc size profiles during coagulation and after exposure to increasing levels of RPM (from Jarvis *et al*, 2004). 45

Figure 2-12: Dynamic monitoring of kaolin suspensions, after dosing with alum and two PACl samples. Floc breakage (10s at 330 rpm) at 660s (from Gregory, 2004). 47

Figure 2-13: The "three dimensions" of fluid dynamics (from Anderson, 1995). 50

Figure 2-14: The CFD analysis process (from Shaw 1992). 53

Figure 2-15: Instantaneous flash mixer (from Byun *et al*, 2005). 84

Figure 2-16: Coagulant dispersion results (from Byun *et al*, 2005). 84

Figure 4-1: Modelled cylindrical and Hudson vessel configurations (not to scale, all dimensions in millimetres). 106

Figure 4-2: Torque transducer and chart recorder. 107

Figure 4-3: Principles of a backscatter LDA system (from Brown *et al*, 2004). 108

Figure 4-4: Principal operation of a PIV system (from Papadopoulos & Arik, 2004). 110

Figure 4-5: PIV system used. 111

Figure 4-6: Laser light sheet and axial profile measurement locations – plan view. 112

Figure 4-7: Power number versus impeller Reynolds number for flat, two blade impeller in cylindrical and Hudson vessels. 114

Figure 4-8: Comparison of vessel average velocity gradient values, $\overline{G}$ s^{-1} for different jar test configurations. 114
Figure 4-9: Mean axial velocities generated in cylindrical vessel at various mixing speeds. 117
Figure 4-10: Scaled mean axial velocities generated in cylindrical vessel at various mixing speeds. 117
Figure 4-11: Mean tangential velocities generated in cylindrical vessel at various mixing speeds. 118
Figure 4-12: Scaled mean tangential velocities generated in cylindrical vessel at various mixing speeds. 118
Figure 4-13: Phase resolved mean axial components at various vessel depths, N=100 rpm. 119
Figure 4-14: Phase resolved mean tangential components at various vessel depths, N=100 rpm. 119
Figure 4-15: Mean velocity fields for (a) 200 rpm, (b) 150 rpm & (c) 100 rpm. 121
Figure 4-16: Mean velocity fields for (a) 75 rpm, (b) 50 rpm & (c) 40 rpm. 122
Figure 4-17: Mean velocity profile with increasing distance from shaft (locations shown at Figure 4-6). 123
Figure 4-18: Instantaneous paddle positions for 200 rpm scenario. 124
Figure 4-19: Measured instantaneous velocities taken along velocity profile 0.82*r* through vessel centreline (H0) at various different paddle locations (Figure 4-6 and Figure 4-18 refer). N = 200 rpm. 125
Figure 5-1: Sliding mesh and multiple reference frames techniques. 130
Figure 5-2: Subdivisions of the near-wall region, (from Fluent 2005). 133
Figure 5-3: Grid Densities – cylindrical vessel. 135
Figure 5-4: Effect of grid density on axial velocity over tank depth at paddle face. (N = 200 rpm). 137
Figure 5-5: Detail on paddle and vessel walls – 98,517 grid mesh. 137
Figure 5-6: Sections through vertical mid-plane of Hudson vessel. Fine grid shown on left hand side, coarser grid on right hand side. 138
Figure 5-7: Effect of grid density on axial velocity over tank depth. Hudson vessel. 139
Figure 5-8: Hudson vessel grid (144,718 cells). 139
Figure 5-9: Simulated axial velocity profiles over tank depth for different turbulence models, N = 200 rpm. 141
Figure 5-10: Variation in turbulence dissipation rate at 200 rpm for different turbulence models. 141
Figure 5-11: Cumulative percentage of vessel volume containing G_L values less than the value shown, for RSM and standard k-ϵ turbulence models. N=200 rpm. 142

Figure 5-12: Simulated axial velocity profiles over tank depth for different turbulence models. (N = 100 rpm). 144
Figure 5-13: Absolute difference between axial velocity values calculated using various turbulence models and those measured using LDA. 145
Figure 5-14: Vessel average velocity gradient values calculated for various modelling approaches, compared to experimentally-derived value. N=100 rpm. 147
Figure 5-15: Experimental and CFD-derived power dissipation values, W, at stated mixing speeds for (a) cylindrical vessel and (b) Hudson vessel. 150
Figure 5-16: Experimental and CFD-derived *G* values, s^{-1}, at stated mixing speeds for (a) cylindrical vessel and (b) Hudson vessel. 151
Figure 6-1: Velocity vectors generated in cylindrical vessel, N=200 rpm. 155
Figure 6-2: Velocity vectors generated in Hudson vessel, N=200 rpm. 156
Figure 6-3: Velocity magnitude contours taken through midplane of cylindrical vessel. Mixing speed = 200 rpm. 157
Figure 6-4: Velocity magnitude contours taken through paddle centreline of cylindrical vessel. Mixing speed = 200 rpm. 157
Figure 6-5: Velocity magnitude contours taken through midplane of Hudson vessel. Mixing speed = 200 rpm. 158
Figure 6-6: Velocity magnitude contours taken through paddle centreline of Hudson vessel. Mixing speed = 200 rpm. 158
Figure 6-7: Velocity magnitude contours taken 2mm above base of cylindrical vessel. Mixing speed = 50 rpm. 159
Figure 6-8: Velocity magnitude contours taken 2mm above base of Hudson vessel. Mixing speed = 50 rpm. 159
Figure 6-9: Variation in axial velocity on an arc described by the impeller at N=100 and N=30 rpm for the cylindrical vessel. 160
Figure 6-10: Cylindrical vessel scaled mean radial velocities at various mixing speeds. 161
Figure 6-11: Hudson vessel scaled mean radial velocities at various mixing speeds. 162
Figure 6-12: Cylindrical vessel scaled mean axial velocities at various mixing speeds. 163
Figure 6-13: Hudson vessel scaled mean axial velocities at various mixing speeds. 163
Figure 6-14: Variation in turbulence dissipation rate across mid-plane at 200rpm for the cylindrical vessel. 165
Figure 6-15: Variation in turbulence dissipation rate across mid-plane at 200 rpm for the Hudson vessel. 165
Figure 6-16: Variation in local turbulence dissipation rate in cylindrical vessel at 200 rpm. 166
Figure 6-17: Kolmogorov length scale distributions in cylindrical and Hudson Vessels at 200 and 50 rpm. 168
Figure 6-18: Average turbulence dissipation rate, ϵ, in each of four zones, plotted against mixing speed for (a) cylindrical vessel and (b) Hudson vessel. 170

Figure 6-19: Comparison of average turbulence dissipation rate in paddle tip zone and vessel for the cylindrical and Hudson vessels. 172
Figure 6-20: Ratio of ϵ value in particular zone to vessel average ϵ value for cylindrical and Hudson vessels. 173
Figure 7-1: Particle trajectory: N=200rpm, ϕ=500μm, ρ=1,000 kg/m^3. Particle injected at mid-quadrant point at mid-depth. 181
Figure 7-2: Variation in local velocity gradient experienced by a 500μm neutrally buoyant particle subject to mixing speeds of 100 and 200 rpm. 182
Figure 7-3: Variation in local velocity gradient experienced by a 500μm neutrally buoyant particle subject to mixing speeds of 30, 40 and 50 rpm. 182
Figure 7-4: Percentage durations for which neutrally buoyant particles (ρ=1,000 kg/m^3) experienced local velocity gradients in excess of the vessel average velocity gradient. Particle residence time = 60s. 184
Figure 7-5: Percentage durations for which non-neutrally buoyant particles (ρ=1,250 kg/m^3) experienced local velocity gradients in excess of the vessel average velocity gradient. Particle residence time = 60s. 186
Figure 7-6: Variation in local velocity gradient with time for 250μm particles of different densities mixed at (a) 50 rpm and (b) 100 rpm. 187
Figure 7-7: Time spent by a particle experiencing ranges of local velocity gradient, N=200rpm, 500μm, 1,000 kg/m^3, 60s. 188
Figure 7-8: Cumulative percentage time spent by a neutrally buoyant, 500μm particle experiencing ranges of local velocity gradient at various mixing speeds, 60s particle residence time. 189
Figure 7-9: Maximum continuous and total times for which a 500μm particle experiences specific velocity gradient ranges, 60 s particle residence time. 191
Figure 7-10: Ratio of continuous time in bin to total time spent in bin plotted against velocity gradient. 192
Figure 8-1: Floc size profiles during coagulation and flocculation, and after exposure to increasing levels of RPM, from Jarvis *et al*, 2004. 197
Figure 8-2: Total time spent in bin, ϕ=960 µm, ρ=1,000 kg/m^3, N=200 rpm for representative sample. Error bars indicate 15% variation about mean, 660s analysis. 200
Figure 8-3: Variation in G_t for a ϕ=960µm, ρ=1,000 kg/m^3 particle, N=200 rpm, 60s analysis. 200
Figure 8-4: Floc size (d_{50}) and local velocity gradient profiles at mixing speeds of 30 and 200 rpm. 202
Figure 8-5: Total and cumulative time of exposure to different ranges of local velocity gradient, ϕ=960um, ρ=1,000 kg/m^3, N=200 for representative sample, 660s and 60s analyses. 203

Figure 8-6: Total and cumulative time of exposure to different ranges of local velocity gradient, ϕ=960um, ρ=1,000 kg/m^3, N=100 for representative sample, 660s and 60s analyses. 204
Figure 8-7: Total time of exposure to different ranges of local velocity gradient, ϕ=960um, ρ=1,000 kg/m^3, 30<N<200 rpm for representative sample, 660s analysis. 205
Figure 8-8: Maximum continuous time spent in bin, ϕ=960um, ρ=1,000 kg/m^3, N=various for representative sample, 660s analysis. 206
Figure 8-9: Degradation of ferric hydroxide floc, expressed in relation to cumulative $G_t t$. 210
Figure 8-10: Degradation of NOM floc, expressed in relation to cumulative $G_t t$. 210
Figure 8-11: Degradation of kaolin floc, expressed in relation to cumulative $G_t t$. 211
Figure 8-12: Ratio of final to initial floc size and turbulence dissipation rate vs. mixing speed. 212
Figure 8-13: Post breakage floc size (d_{50}) vs. vessel average turbulence dissipation rate. 213
Figure 8-14: Floc growth curves in relation to applied $G_t.t$. 215
Figure 9-1: Frankley and Bartley reservoir raw water characteristics – March to July 2006. 219
Figure 9-2: Schematic of treatment processes at Frankley WTW. 220
Figure 9-3: Empty flocculation vessel at Frankley WTW. 220
Figure 9-4: Plan and sectional views of meshed flocculation vessel. 223
Figure 9-5: Velocity vectors in horizontal plane (z=3.0m). N=2.4 rpm. 225
Figure 9-6: Velocity contours in horizontal plane (z=3.0m). N=2.4 rpm. 225
Figure 9-7: Trajectories of 50 particles injected into the flow. ϕ = 0.5mm, ρ= 1,200 kg/m^3. Flow rate = 21.1Ml/d. Mixing speed = 2.4 rpm. 226
Figure 9-8: Outlet measured tracer flow rate at 16 Ml/d. 229
Figure 9-9: Normalised residence time distribution curve at 16 Ml/d. 229
Figure 9-10: Outlet measured tracer flow rate at 21.1 Ml/d. 230
Figure 9-11: Normalised residence time distribution curve at 21.1 Ml/d. 230
Figure 9-12: Outlet measured tracer flow rate at 24.0 Ml/d. 231
Figure 9-13: Normalised residence time distribution curve at 24.0 Ml/d. 231
Figure 9-14: Contours of turbulence dissipation rate, ϵ greater than vessel average value taken through (a) z = 3.0m and (b) paddle section. N = 2.4 rpm, flow rate = 21.1 Ml/d. 235
Figure 9-15: Contours of local velocity gradient, G_L, greater than vessel average value taken through (a) z = 3.0m and (b) paddle section. N = 2.4 rpm, flow rate = 21.1 Ml/d. 236
Figure 9-16: Average and maximum local velocity gradient values at stated mixing speeds. 237
Figure 9-17: Local velocity gradient distribution. 238

Figure 9-18: Cumulative distribution of local velocity gradient at different mixing speeds. Flow rate = 21.1 Ml/d. 239
Figure 9-19: Camp numbers for each flow rate based on design parameters and CFD results. 241
Figure 10-1: Bamford WTW raw water characteristics – February to July 2006. 246
Figure 10-2: Bamford WTW Process Schematic. 247
Figure 10-3: Plan and isometric views of flocculator channel (shaded areas indicate planes used for model validation). 248
Figure 10-4: Cross-sections through two meshes (a) 395,328 cells, (b) 776,187 cells. 249
Figure 10-5: Comparison between measured and modelled velocity profile data. 252
Figure 10-6: Local velocity gradient distribution – comparison between two grids. 253
Figure 10-7: Velocity vectors along centreline of channel. 254
Figure 10-8: Contours of velocity magnitude. 255
Figure 10-9: Contours of turbulent kinetic energy. 255
Figure 10-10: Contours of local velocity gradient. 256
Figure 10-11: Bamford WTW CFD flow tracer study – Figure 10-12: Bamford WTW CFD flow tracer study - 257
Figure 10-13: Histogram of local velocity gradient distribution throughout flocculation channel and upstream mixing chamber. 261
Figure 10-14: Cumulative distribution of local velocity gradient for Bamford WTW and Frankley WTW at different mixing speeds. 261
Figure 11-1: Variations in velocity gradient, Camp number and retention time for jar tester, Frankley and Bamford WTW. (Shaded area indicates the recommended Camp No. optimum range for effective flocculation, from Crittenden *et al.*, 2005, Baruth, 2005). 286
Figure 11-2: Floc growth with time for various suspensions, showing Frankley and Bamford retention times. 288

List of Tables

Table 1-1: Brief Model Summaries. 6

Table 1-2: Thesis structure. 10

Table 2-1: RTD curve characterisation terms (from Crittenden *et al*, 2005). 29

Table 2-2: Proposed flocculator design parameters. 31

Table 2-3: Reported jar test experimental data. 35

Table 2-4: Turbulence model applications (from Morrison 1999). 62

Table 2-5: Comparison of available turbulence models (from Versteeg & Malalasekera, 1995, Marshall & Bakker, 2004, Fluent, 2005, & Menter, 2003). 63

Table 2-6: Interpolation Schemes for convective fluxes available in Fluent (from Fluent, 2005). 67

Table 2-7: Comparison of numerical and experimental results for a $1m^3$ axially-stirred flocculation vessel (from Essemiani & de Traversay, 2002a). 87

Table 4-1: PIV analyses undertaken on Hudson vessel. 112

Table 4-2: Maxima and minima mean axial and tangential velocities measured in the cylindrical vessel at different mixing speeds. 116

Table 4-3: Measured mean velocities in the Hudson vessel at stated mixing speeds. 120

Table 5-1: Vessel average velocity gradient values, G s^{-1}, for cylindrical vessel. N=100 rpm. 147

Table 6-1: Power curve coefficients of determination for turbulence dissipation rates and mixing speed from Figure 6-18 171

Table 7-1: Summary of particle size and density trajectories modelled (shading indicates analyses undertaken). 178

Table 7-2: Comparison of vessel average, trajectory average and trajectory maximum velocity gradients for various mixing speeds. 183

Table 8-1: Iron hydroxide precipitate floc size changes (d_{50}) after 1 minute and 11 minutes of increased mixing. 202

Table 8-2: Degree of floc breakage observed in the first minute of increased mixing for the iron hydroxide precipitate floc. 203

Table 8-3: Actual and percentage times particles spent in G_t bins at 30, 40 and 50 rpm. 209

Table 8-4: r^2 values for power curves obtained from d_{50} vs. cumulative $G_t t$ plots. 211

Table 8-5: Comparison of cumulative $G_t.t$, average G_t and observed floc behaviour. 213

Table 9-1 Frankley WTW average raw water characteristics – January 2003 to September 2005. 218

Table 9-2: Minimum and maximum velocities found in vessel at stated mixing speeds. Flow rate = 21.1 Ml/d. 224

Table 9-3: Frankley WTW Residence Time Distribution Results. 232

Table 9-4: Calculated average velocity gradient and $\overline{G}.t$ values. 233
Table 9-5: Comparison of Frankley design parameter values with those recommended by Crittenden *et al* (2005). 234
Table 9-6: Average turbulence dissipation rates and average and maximum values of local velocity gradient at stated mixing speeds. 238
Table 9-7: Percentage of vessel volume experiencing local velocity gradient values in excess of postulated breakage threshold. 240
Table 10-1: Raw Water Characteristics and Target Final Water Quality Standards for Bamford WTW. 246
Table 10-2: Bamford WTW Residence Time Distribution Results. 258
Table 10-3: Average turbulence dissipation rates and average and maximum values of local velocity gradient. 258
Table 10-4: Average velocity gradient. 259
Table 10-5: Impact on operating budget of varying flocculant aid dose. 263
Table 11-1: Comparison of modelling approaches for small scale, mechanically mixed scenarios. 275
Table 11-2: Threshold local velocity gradient values for various floc types. 282
Table 11-3: Mixing speed and corresponding velocity gradient increases. 284

Abbreviations & Notation

Abbreviations

1D	One dimensional
2D	Two dimensional
3D	Three dimensional
a.c.	Alternating current
ASM	Activated sludge model
ASP	Activated sludge plant
AWWARF	American Water Works Association Research Foundation
CAD	Computer aided design
CCD	Close coupled device
CFD	Computational fluid dynamics
DAF	Dissolved air flotation
DBP	Disinfection by-product
d.c.	Direct current
DLVO	Deryagin Landau Verwey Overbeek
DOC	Dissolved organic carbon
ECLAT	Experimental and Computational Laboratory for the Analysis of Turbulence at King's College, London.
FI	Flocculation index
HRT	Hydraulic retention time
ID	Internal diameter
LDA	Laser Doppler anemometry
MF	Micro-filtration
MFM	Multi-fluid microscale model
MIEX®	Magnetic Ion Exchange
Ml	Megalitre
MRF	Multiple reference frames
Nd:YAG	Neodymium-doped yttrium aluminium garnet ($Nd:Y_3Al_5O_{12}$)
NOM	Natural organic matter
NTU	Nephelometric turbidity units
PACl	Polyaluminium chloride
PIV	Particle image velocimetry
PBT	Pitched blade turbine
PC	Personal computer
PDA	Photometric dispersion analyser
PLV	Pulsed light velocimetry
polyDADMAC	Polydiallyldimethylammonium chloride
PSD	Particle size distribution
PVDF	Polyvinyldine fluoride
RANS	Reynolds averaged Navier Stokes
rpm	Revolutions per minute
Rk-ϵ	Realizable k-ϵ turbulence model
RNG	Renormalised group turbulence model
RSM	Reynolds stress model
SM	Sliding mesh

THM	Trihalomethane
UV_{254}	Ultraviolet absorbance at 254 nm
VOF	Volume of Fluid
WTW	Water treatment works
WWTW	Wastewater treatment works

Notation

A	Floc projected area
B_{VSR}	floc breakage in viscous sub-domain
B_{ISR}	floc breakage in inertial sub-domain
C	Concentration of tracer exiting vessel at time t
C_N	Normalised concentration
C	Floc strength coefficient
C'	Adapted floc strength coefficient
C_1, C_2	Coefficients used in k-ϵ model
C_μ	Constant used in defining μ
C_D	Drag coefficient
D	Floc diameter
D	Impeller diameter
D_ω	Cross-diffusion term
d_{10}	10 percentile equivalent diameter floc size
d_{50}	50 percentile equivalent diameter floc size
d_{90}	90 percentile equivalent diameter floc size
d_{95}	95 percentile equivalent diameter floc size
d_p	Particle diameter
D	Floc area
D_f	Floc fractal dimension
d_{max}	Maximum floc diameter
$E(\theta)$	Exit age distribution
F	Floc rupture force
F_D	Drag force
F_x	Force on particle arising from rotation of reference frame
G	Velocity gradient
G	Absolute velocity gradient / vessel average velocity gradient
G_k	Generation of k
G_L	Local velocity gradient
$\overline{G}$	Average local velocity gradient
G_{Lmax}	Maximum local velocity gradient
G_t	Local velocity gradient along a specific particle trajectory
G_ω	Generation of ω
J	Floc strength
k	Turbulent kinetic energy
L	Floc length
N	Impeller speed
P	Pressure
P	Power dissipated

P_0	Impeller power number
r	Vessel radius
R_{br}	Rate of particle breakage
R_{col}	Rate of particle collision
R_{floc}	Rate of floc growth
R_{part}	Radius of primary particle
Re	Reynolds number
S_{ij}	Mean rate of strain tensor
S_k, S_ϵ	User-defined source terms
t	Time
T	Vessel diameter
T_q	Applied torque
u_i, u_j	i^{th}, j^{th} component of mean velocity
u_i', u_j'	i^{th}, j^{th} component of instantaneous velocity
u_z	Axial velocity
u_θ	Tangential velocity
u_p	Particle velocity
$\overline{u_i u_j}$	Reynolds stresses
V	Volume
x_i, x_j	Cartesian co-ordinates
Y_k,	Dissipation of k due to turbulence
Y_ω	Dissipation of ω due to turbulence

α	Collision efficiency factor
α_ϵ	Turbulent Prandtl number for ϵ
α_k	Effective Prandtl number for k
α_n	Constant used in determination of C_D
γ	Floc size exponent
γ'	Floc size exponent
δ	Floc binding strength
δ_{ij}	Kronecker delta
Δt	Time step
E	Dissipation of turbulent kinetic energy per unit time
H	Kolmogorov's microscale of turbulence
θ	Normalised retention time
μ	Dynamic viscosity of water
μ_{eff}	Effective viscosity ($=\mu+\mu_t$)
μ_t	Turbulent or eddy viscosity
ν	Kinematic viscosity of water
ρ_f	Density of floc
ρ_l	Density of liquid
ρ_s	Density of solid in floc
σ	Floc strength
σ_ϵ	Inverse turbulent Prandtl number for ϵ
σ_k	Inverse turbulent Prandtl number for k
τ	Theoretical retention time

ϕ	Particle diameter
ω	Rate at which turbulent kinetic energy is dissipated

1 Introduction

1.1 Background

"All processes used in water treatment are interrelated. A change in any one of these processes may require or enable a change in the design or management of one or more of the others. For example, an improvement in mixing and flocculation may make possible reduction in chemical dosages simultaneously with the allowance of higher settling basin loading and filter rates and improved filtered water quality." (Hudson, 1981).

Throughout both water and waste water treatment, mixing plays a fundamental role in unit process performance and its role should not be underestimated. Mixing processes are to be found at most unit process stages in water and waste water treatment. For example, mixing is required for chemical dosing (pH control, coagulation, disinfection, phosphate control, and chemical nutrient removal), mass transfer (aeration), solids restratification (multimedia filtration) and blending (service reservoirs). If designed and operated correctly, mixing processes can yield significant benefits to the performance of a water or waste water treatment works. However, poorly designed or operated mixing plant will result in sub-optimal performance, with a consequential deleterious impact on either or both final product (potable water or sewage effluent) quality and increasing operational costs. In a period of intense regulatory scrutiny, water companies must operate to extremely tight performance standards laid down by the quality regulators (*i.e.* the Drinking Water Inspectorate and the Environment Agency), yet must also generate financial efficiencies in order to satisfy the expectations of key stakeholders, such as shareholders and city analysts, whilst also satisfying the economic regulatory requirements of OFWAT. Consequently, mixing has a key role to play in both the operational and financial performance of water companies. However, even the most cursory analysis of many water treatment or waste water treatment works or service reservoirs will show that mixing processes have either been designed poorly, or are

being operated at a sub-optimal level. In the author's experience of plant design and operation in the UK, it is not uncommon to find makeshift, rudimentary amendments to flow distribution facilities. It is clear that historically the role and importance of mixing has been overlooked to some extent by plant designers and operatives alike.

1.2 Motivation for the Work

Effective coagulation and flocculation processes are fundamental to the efficient operation of surface water treatment works. Coagulation brings about a change in the nature of small particles, rendering them unstable, whilst flocculation encourages particle agglomeration via gentle mixing and the formation of irregularly-shaped, loosely connected aggregates, known as flocs. Ineffective coagulation and flocculation results in poorer quality feed water to clarifiers and filters, potentially jeopardising treated water quality and increasing operational costs. Several interrelated criteria govern the efficiency and effectiveness of the coagulation and flocculation stages; *viz.* coagulant dosage (including coagulant type), pH and mixing arrangements.

The strength of flocs is of great importance for particle removal efficiency. Boller and Blaser (1998) showed that particle removal efficiency decreases with decreasing particle size. Therefore, flocs must be able to withstand shear energy applied to them in various different unit processes. When the degree of shear exceeds a threshold value, floc breakage will occur. This breakage has, for certain flocs, been shown to be irreversible (Yukselen and Gregory, 2004) and measurement of the shear energy required for breakage is of major operational significance. However, quantification of the energy requirements for floc breakage is not straightforward, and despite much work in this field, no standard strength test exists.

It is known that water treatment works which are served from moorland sources receive raw water which is highly coloured, rich in organics and exhibiting low alkalinity and low turbidity, and that the flocs developed from such water are fragile in comparison to other flocs (Bache *et al.*, 1997). Raw water characteristics vary with season with

concomitant variations in coagulant dose (Figure 1-1 refers). It is also believed that floc structure deteriorates with season, with weak, fragile flocs being inadequately removed at the clarification stage, giving rise to high solids loading on downstream filters, shortened run times and increased backwash frequency.

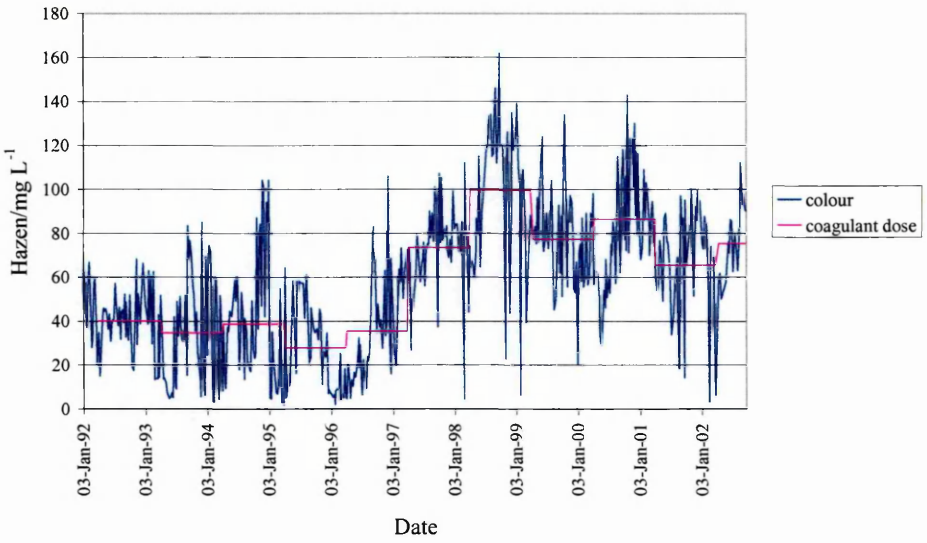


Figure 1-1: Raw water colour concentrations for Albert reservoir, Halifax, UK, January 1992 to May 2002.

The work presented in this thesis forms part of a wider American Water Works Association Research Foundation (AWWARF) tailored collaborative project on the 'Treatment of elevated organic content waters'. The main objectives of the overall project were to:

(1) Investigate the use of conventional and alternative coagulants for organic removal from low alkalinity waters specifically at high organic loads.

(2) Evaluate treatment strategies at pilot scale.

(3) Investigate the effect of organic content, coagulant and coagulation conditions on floc size, structure, strength, growth and break up.

The focus of the work reported in this thesis concentrated on points (2) and (3) through the development and analysis of computational models of mixing scenarios and combining the resulting data with laboratory data generated as part of the same wide project to increase understanding of floc formation and breakage mechanisms.

Previous work (Jarvis *et al.*, 2004) provided a quantitative analysis of NOM flocs. The work reported in this thesis complements that previous work, providing important understanding of the hydrodynamic environments to which flocs are exposed, whilst also providing potential guidance for flocculator design and operation.

Chapter 2 of this thesis shows that the literature contains examples of practical investigations into floc strength using the standard jar test apparatus and procedure (*e.g.* Gregory & Rossi, 2001, Jarvis *et al.*, 2004, Jefferson *et al.*, 2004). However, there is little reported research which has attempted to model the process using computational fluid dynamics (CFD). The research which has been published (Korpijarvi *et al.*, 1999, 2000, Essemiani & de Traversay, 2002a, b) is limited in scope. These papers considered the flow field generated by a jar tester, and recognised the limitations of the average velocity gradient as a design parameter. However, none of the papers considered, other than qualitatively, how this would impinge on flocculation performance. Korpijarvi *et al.* (1999) recognised the value of the approach and identified the need to consider, *inter alia*, the modelling of flocs and the calculation of floc densities. Despite having been written some seven years ago, there is no evidence from the literature that this has yet been achieved. This knowledge gap is addressed as part of the work recorded in this thesis. The literature shows many examples of floc breakage characteristics obtained from the jar test (*e.g.* Jarvis *et al.*, 2005a, Gregory, 2004). However, breakage and the shear forces imparted to yield breakage are usually expressed in terms of the impeller mixing speed. Clearly, this is of limited value if one wishes to understand the impact of the induced hydrodynamic environment on flocs in a full scale flocculator. The clear differences in mixing scenarios mean that it is not possible to transfer results from one scale to another. The work reported here seeks to overcome this difficulty and to contribute to our knowledge of flocculation processes by investigating the practicalities and effectiveness of using CFD to assess flocculator characteristics, to align the measured hydrodynamic environment with known floc behaviour (growth / breakage) patterns, from which parameters for effective flocculation design and operation can be developed. Key parameters governing effective flocculation are elucidated and quantified, enabling process scientists and engineers to develop effective design criteria and operational strategies.

1.3 Scope of Study

The work reported in this thesis is focussed on physical and numerical analyses of laboratory and full scale flocculators. The laboratory scale work examined two different jar test configurations, whilst the full-scale studies considered the operation of the flocculators at Severn Trent Water's Frankley WTW in Birmingham, UK and Bamford WTW in Derbyshire, UK. The work reported here used computational fluid dynamics (CFD) to investigate the nature of mixing at each of the two scales and possible links between hydraulic characteristics of the flow (such as velocity gradient and turbulence dissipation rate) and floc formation and breakage. A number of CFD techniques have been adopted depending on the process configuration being modelled:

- Steady and unsteady flow
- Conventional single-phase hydraulic modelling
- Two-phase modelling where a dispersed second phase is mixed with the bulk phase
- Residence time distributions.

A selection of the detailed modelling aspects are summarised at Table 1-1.

Table 1-1: Brief Model Summaries.

Process	Volume, litres	Mesh Size (No. of cells)	Turbulence Model	Paddle Rotation Treatment	Scalars solved (in addition to *u, v, w, p, k & ϵ*)	Flow Rate, Ml/d
Cylindrical Section Jar Test Vessel	1	87, 777 98, 517 283, 470 337,944	Standard *k-ϵ* Realizable *k-ϵ* RNG *k-ϵ* *k-ω* SST *k-ω* Reynolds Stress Model	Multiple Reference Frames Sliding Mesh	Discrete phase model	-
Square Section Jar Test Vessel	2	144, 718 281, 785	Reynolds Stress Model	Multiple Reference Frames	Discrete phase model	-
Frankley WTW Mechanically Mixed Flocculator	212, 800	338, 213	Standard *k-ϵ* Realizable *k-ϵ*	Multiple Reference Frames Sliding Mesh	Discrete phase model Tracer concentration	16.0 Ml/d 21.1 Ml/d 24.0 Ml/d
Bamford WTW Hydraulic Flocculator	743, 822	395, 328 776, 187	Standard *k-ϵ*	N/A	Tracer concentration	160 Ml/d

1.4 Thesis Plan

An outline of each Chapter objective and the parameters reviewed or measured to meet each objective is shown at Table 1-2. Initially a review of the literature was undertaken to evaluate the role of mixing in water treatment, and the extent to which CFD can be used to model mixing processes (Chapter 2). The review also gave consideration to good modelling practice. The review demonstrated that whilst CFD is an emerging tool in the design and operation of water and waste water treatment systems, the industry is still lagging behind other engineering and process industries with regard to its implementation. An abridged version of the review of CFD in the water industry has been submitted to *Water Research* for publication.

Laboratory and CFD studies were carried out on two standard laboratory flocculation (*i.e.* jar test) vessels. Specifically, an analysis of the turbulent flows generated in a cylindrical vessel and a square section (on plan) vessel were studied. Two different flow measurement techniques were employed (*viz.* particle image velocimetry and laser Doppler anemometry) to determine flow patterns and characteristics within the different vessels and also to verify results obtained from the CFD models (Chapter 4). Significant time and effort was spent developing a robust technique for modelling the swirling flow found in a jar test vessel (Chapter 5). Both sliding mesh and multiple reference frames techniques were used to model the rotational motion of the paddles, and six different turbulence models were used and their results compared. The unsuitability of the standard k-ϵ turbulence model to this modelling scenario was confirmed.

The information obtained from both the physical and numerical flow measurement exercises was most useful in determining the flow characteristics of the two vessels and, in particular, the differences between the scenarios. This is important since workers in this field have generally adopted more than one standard test configuration, but nonetheless have compared results arising from both. This work identified those parameters of most interest to the flocculation stage (floc strength and turbulence

dissipation rate) and compared the velocity and turbulence characteristics of the different configurations. The results then led to a critical evaluation of the validity of inter-vessel comparisons particularly with regard to floc breakage mechanisms (Chapter 6).

Gregory (1989) argued that floc transport and attachment should be viewed as two distinct processes. The work reported in this thesis considered floc transport within the jar test vessel and also considered how the turbulent effects experienced might be related, in a conceptual manner, to breakage, via the turbulence dissipation rate and the local velocity gradient.

Having studied and characterised the turbulent flow patterns of two distinct jar test configurations, an analysis was undertaken of the impact of the flat impeller used in both scenarios on floc size and, in particular, growth and breakage mechanisms. Further CFD studies were carried out on the cylindrical jar test configuration, and the results of laboratory based floc growth and breakage experiments were compared with the CFD results. A Lagrangian approach was adopted to single particle trajectory analysis, from which the magnitude and extent of shear stresses to which flocs might be exposed were elucidated (Chapters 7 and 8). Velocity gradients generated locally to the floc were compared with the average vessel velocity gradient. Good overall mixing of the vessel was observed; the consequential result being that the average local velocity gradient experienced by a particle was approximately equal to the vessel average velocity gradient. However, very high local velocity gradient values were experienced by the particle and this work enabled conclusions to be drawn with regard to the breakage mechanisms of flocs in the jar tester. An abstract outlining this work has been accepted for presentation at the forthcoming International Water Association Conference on Particle Separation, to be held in Toulouse, France in July 2007.

A CFD model was constructed of a flocculation vessel at Frankley Water Treatment Works in Birmingham, UK (Chapter 9). Frankley WTW is a 440Ml/d works, supplying the majority of the conurbation of Birmingham. The works is run with two streams operating 24 hours a day. Consequently, the Works Manager is unable to stand down a

flocculator to test its performance in any event other than an emergency. The CFD model was used to determine the hydraulic performance of the flocculator by considering residence time distributions at different flow rates and mixing speeds. The model was also used to develop an understanding of the hydrodynamic environment within the flocculator. The distribution of shear stresses within the vessel was determined and compared to those found in a jar test vessel. The perceived impacts of this shear distribution on flocculation were discussed. It was found that the local velocity gradient values found in the full scale flocculator are of the same order of magnitude of those found in the jar test vessel at the lowest mixing speeds. Although some short-circuiting was observed in the residence time distribution results, it was concluded that the hydrodynamic environment generated by the flocculators at Frankley was conducive to floc growth.

A further model was constructed of an hydraulic flocculator at Bamford Water Treatment Works in Derbyshire, UK (Chapter 10). This works treats an upland raw water which is similar in nature to that treated at Frankley WTW and is almost identical to that used by Jarvis *et al.* (2004) in their laboratory work. As a result, it was possible to compare and contrast the impact of jar tests, mechanical mixing and hydraulic mixing on similar waters. It was found that the Bamford flocculator is volumetrically undersized, with inadequate mixing provided for the coagulation stage. The work on full scale flocculation has been submitted to *J. Water Supply: Research & Technology – AQUA* for publication.

The combined findings of the research are summarised in Chapter 11 and conclusions from the work are drawn in Chapter 12. Suggestions for further work arising from this study are made in Chapter 13.

Table 1-2: Thesis structure.

Chapter	2(a)	2(b)	4	5	6	7	8	9	10
Principal objective of chapter	Review of literature – mixing & flocculation	Review of literature – use of CFD in water industry	Experimental methods for assessing jar test flow field characteristics	CFD jar test modelling strategy development	Jar test CFD analyses	Initial trajectory analyses	Comparison of lab data with numerical data	Full-scale flocculation – mechanically mixed	Full-scale flocculation – hydraulically mixed
				Parameters investigated					
Turbulence modelling		✓		✓	✓	✓	✓	✓	✓
Power / PIV / LDA	✓	✓	✓	✓					
Velocity gradient & turbulence dissipation rate	✓	✓	✓	✓	✓	✓	✓	✓	✓
Floc size and density	✓	✓				✓	✓		
Floc strength/breakage	✓					✓	✓	✓	✓
Residence Time Distribution	✓							✓	✓

2 Literature Review

2.1 Fluid Flow

2.1.1 Introduction

The study of fluid flow has been of great interest to scientists and engineers alike for many centuries. The topic has a long history and remains one of the most challenging areas of study of the natural environment.

The physical flow of a fluid around and within an object is determined to some extent by the interaction of several different, perhaps competing, phenomena, such as dissipation, diffusion, convection, boundary layers, slip surfaces, and turbulence. The flow of most fluids may be analysed mathematically by the use of two sets of equations. The first, the Continuity Equation, requires that the mass of fluid entering a fixed control volume either leaves that volume or accumulates within it. It is thus a mass balance requirement posed in mathematical form, and is a scalar equation.

For the conservation of mass over a small fluid element, using Cartesian tensor notation, and assuming a constant viscosity, isothermal incompressible fluid, the continuity equation may be represented as:

$$\frac{\partial \hat{u}_i}{\partial x_i} = 0 \qquad \textbf{Equation 2-1}$$

where $\hat{u}_i$ denotes a component of the instantaneous velocity of fluid and x_i denotes any of the three Cartesian coordinate directions according to the summation convention, *i.e.* wherever the same subscript is repeated within one term of an equation, summation over all possible values of that subscript is implied such that

$$\frac{\partial \hat{u}_i}{\partial x_i} = \frac{\partial \hat{u}_1}{\partial x_1} + \frac{\partial \hat{u}_2}{\partial x_2} + \frac{\partial \hat{u}_3}{\partial x_3} = 0 .$$

The second set of governing equations is the Momentum Equation, or Navier-Stokes Equations. The equations were derived independently in the early to mid nineteenth century by two European scientists (Claude-Louis Navier and George Gabriel Stokes). They are a series of equations which relate the local pressures and velocities within a body of moving fluid. These equations comprise the conservation of mass, momentum and energy. The Navier-Stokes equations are second order, non-homogenous, non-linear partial differential equations that require at least two boundary conditions for solution, and they represent the foundation on which advanced fluid dynamics analysis is based. The Navier-Stokes equations are vector equations; hence there is a separate equation for each of the three coordinate directions.

For the conservation of momentum in the x, y and z directions, the following equation applies:

$$\frac{\partial u_i}{\partial t} + u_j \frac{\partial u_i}{\partial x_j} = -\frac{1}{\rho}\frac{\partial p}{\partial x_i} + \frac{1}{\rho}\frac{\partial}{\partial x_j}\left(\mu \frac{\partial u_i}{\partial x_j}\right) \qquad \textbf{Equation 2-2}$$

Equations 2-1 and 2-2 are derived from mass and momentum balances over small control volumes within the flow field (Anderson, 1995).

The mathematical complexity of the Navier Stokes equations meant that they remained obscure and poorly understood for many years, and only a few solutions to simplified flows were understood. It was almost a century later before these equations in their complete form provided any useful insight into the analysis and design of fluid devices.

2.2 Turbulence

2.2.1 Turbulent Flow

2.2.1.1 General Description of Turbulence

Fluid motion can be characterised by the Reynolds number, calculated as the ratio of a flow's inertial forces to its viscous forces, and expressed in algebraic terms as

$$\mathrm{Re} = \frac{uL}{\nu} \qquad \textbf{Equation 2-3}$$

where:

Re	=	Reynolds number
u	=	velocity of flow
L	=	characteristic length
ν	=	kinematic viscosity

For a mixing vessel, the Reynolds number may be expressed in algebraic terms as

$$\mathrm{Re} = \frac{\rho_l D^2 N}{\nu} \qquad \textbf{Equation 2-4}$$

where:

ρ_l	=	liquid density
D	=	impeller diameter
N	=	mixing speed

Turbulence is the chaotic state which arises once the velocity of a fluid exceeds that threshold below which viscous forces dominate. From the above, it is clear that if inertial forces are high in comparison to the viscous ones, the Reynolds number is high and the flow tends towards turbulence. Considering flow in a pipe (from which the original concept of the Reynolds number is derived), and taking pipe diameter as the characteristic length, laminar flow is observed at a Reynolds number of below 2,000 (Chow, 1986). Chadwick and Morfett (1998) state that at Reynolds number of 4,000,

flow in a pipeline can be considered turbulent, with flows between 2,000 and 4,000 being in a transitional flow regime. However, these values should be taken only as a guide. For a mixing vessel, the interface between laminar and transitional flow is much lower, at a Reynolds number of approximately 10. Most flows of engineering significance are turbulent. Indeed, Moin and Kim (1997) stated "... turbulence is the rule, not the exception, in fluid dynamics."

Rodi (1984) described turbulence as "... an eddying motion which, at high Reynolds numbers usually prevailing, has a wide spectrum of eddy sizes and a corresponding spectrum of fluctuating frequencies; its motion is always rotational and can be thought of as a tangle of vortex elements whose vorticity vectors can be aligned in all directions and are highly unsteady." This is demonstrated in Figure 2-1 below.

Turbulence is a dominant feature of flow in mixing vessels and is not a feature of the fluid but of the fluid flow. The velocity field is a function of time and position. In turbulent flow, velocity can be assumed to be composed of a mean velocity and non periodic velocity fluctuations that can be considered to be stable, since huge variations from the mean value do not exist, Pope (2000). At high Reynolds numbers, there is a separation of turbulence scale. The large-scale motion is influenced by the geometry of flow represented by the boundary conditions, while the small-scale motion is determined by viscosity and rate of energy dissipation from the large-scale to the small-scale. In turbulent flow, the fluctuation is irregular in space and time and is the result of the presence of numerous eddies of various sizes. However, turbulent flow poses enormous challenges to scientists and engineers, to the extent that Tritton (1988) expressed the view that no short definition exists for turbulent flow, and Frost and Moulden (1977) preferred not to define turbulent motion but only to discuss its characteristics. However, Piquet (2001) proffered a definition of turbulent flow as "short lived, non propagating, highly localized modes of disturbances known as eddies". Eddies can have large or small sizes but the region occupied by large eddies can also contain small eddies. The Reynolds number of large eddies is high and, as a result, the direct effects of viscosity are small and can be assumed to be negligible. Due to the fact that large eddies are not stable, they break up into smaller eddies accompanied by

energy transfer from the large scale to the smaller one. These smaller eddies undergo similar break up into even smaller eddies where the energy is transformed from the smaller to the smallest eddies. This phenomenon continues until the Reynolds number is small, the eddy is stable and the viscous forces dissipate the energy. Richardson (1922), cited by Moin and Kim (1997) summarized the process as "big whorls have little whorls, which feed on their velocity; and little whorls have lesser whorls, and so on to viscosity", and the process is shown schematically at Figure 2-2.

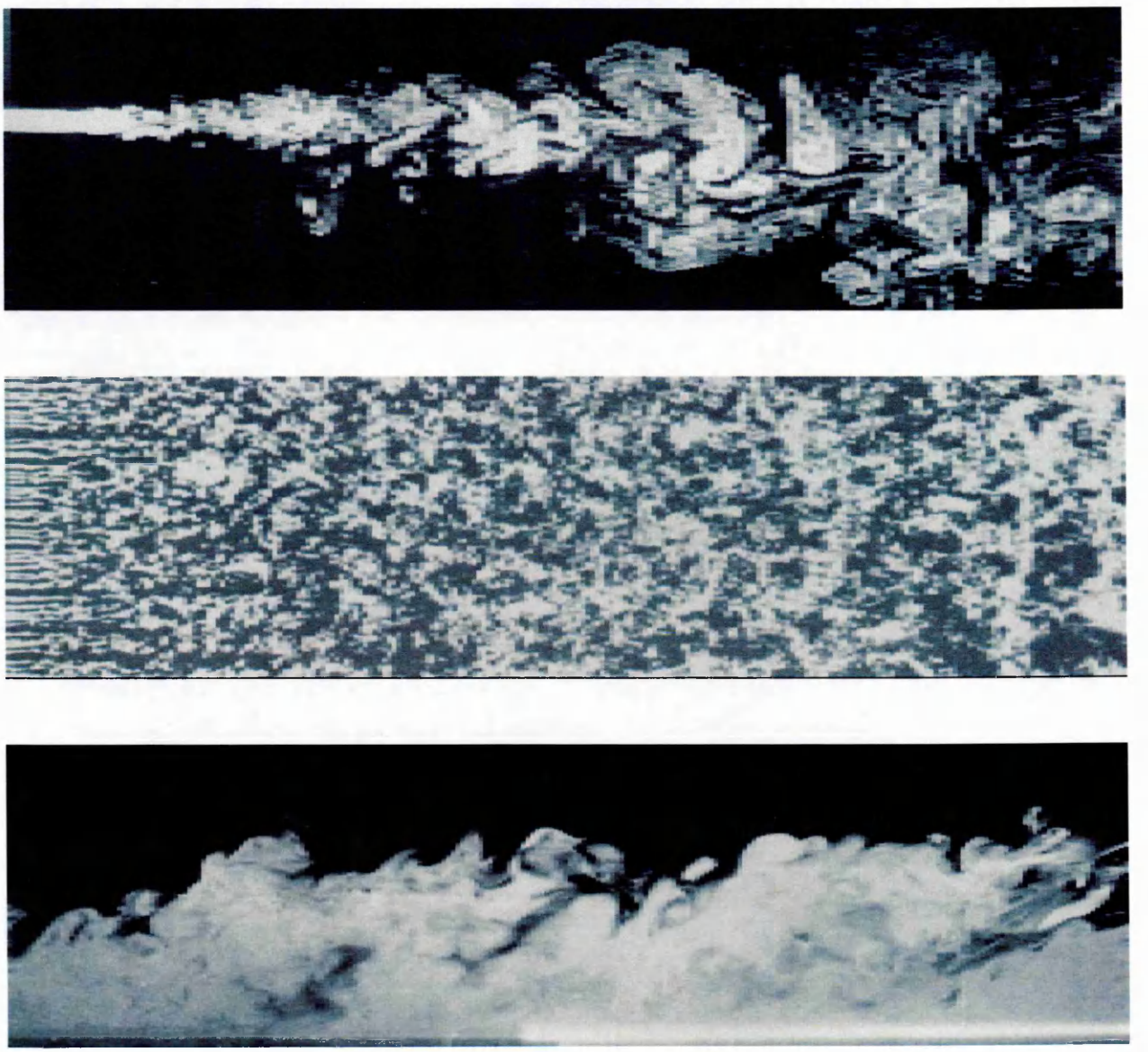


Figure 2-1: Turbulent flow visualisations (from Bell, 2004).

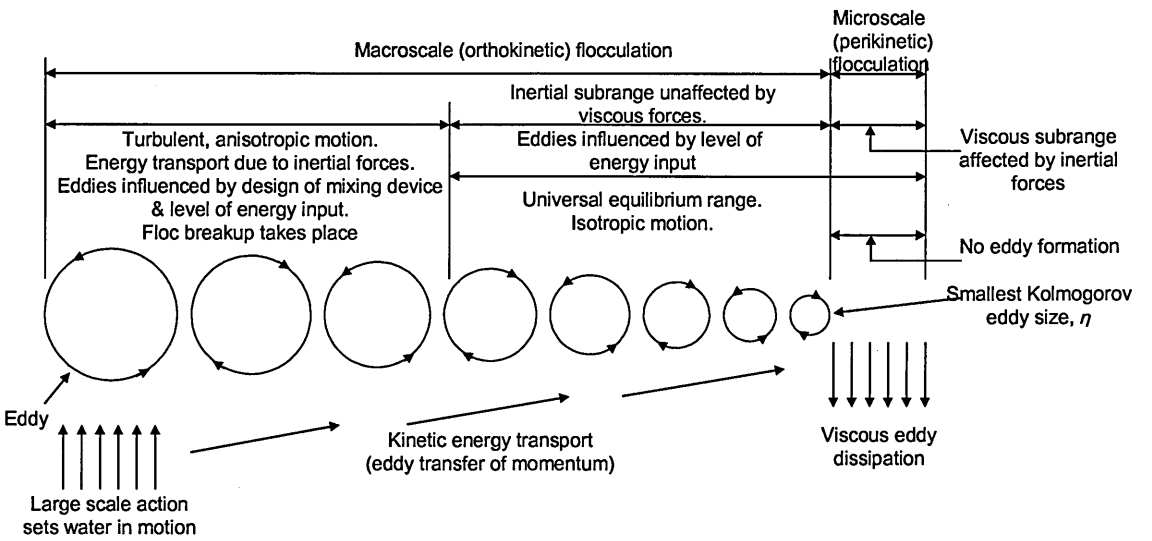


Figure 2-2: Idealized visualisation of turbulent length scales (from Stanley & Smith, 1995).

In turbulent flow, the instantaneous velocity in any direction is given by the sum of a mean velocity and the velocity fluctuation with respect to the mean. These velocity fluctuations result in a momentum exchange generated by shear stresses known as Reynolds shear stresses. Reynolds stresses, or turbulent stresses, arise solely from the presence of turbulence in the flow and so do not exist in laminar flow. They are the result of turbulent random motion induced by velocity fluctuations. In turbulent flow, the total shear stress is the sum of the viscous stress and the Reynolds stress. As one moves in a direction perpendicular to a boundary, the viscous stress become negligibly small compared with the Reynolds stress. As the Reynolds number increases, the fraction of the vessel occupied by the viscous region decreases. Reynolds stresses play a crucial role in the equations used to determine the mean velocity field and they arise from the momentum transfer by fluctuations in the velocity field. Consequently, assuming that the instantaneous velocity component, $\hat{u}_i$, can be decomposed into mean and fluctuating elements,

$$i.e. \quad \hat{u}_i = \hat{U}_i + u'_i \qquad \textbf{Equation 2-5}$$

where $\hat{U}_i$ represents the mean velocity in the i direction,

u'_i represents the fluctuating velocity in the i direction

and the average of u' is zero, but the product of two fluctuating values $(u'^2, v'^2, w'^2, u'v', u'w', v'w')$ is not necessarily zero, then it follows that the averaged continuity equation may be rewritten as:

$$\frac{\partial U_i}{\partial x_i} = 0 \qquad \textbf{Equation 2-6}$$

and the time-averaged momentum equation may be rewritten as:

$$\frac{\partial U_i}{\partial t} + U_j \frac{\partial U_i}{\partial x_j} = -\frac{1}{\rho}\frac{\partial p}{\partial x_i} + \frac{\partial}{\partial x_j}\frac{1}{\rho}\left(\mu \frac{\partial U_i}{\partial x_j} - \overline{u_i u_j}\right) \qquad \textbf{Equation 2-7}$$

With the exception of the final term ($\frac{\partial \overline{u_i u_j}}{\partial x_j}$), these equations form a closed set. However, the additional final term, which represents the product of two fluctuating components of velocity at the same point, causes the equations to be unclosed. This term is one of the Reynolds stresses and is a measure of the additional momentum transfer which occurs in turbulent flows but is absent in laminar ones. Solution techniques for these equations are discussed in Section 2.5.3 below, and it is within this turbulent environment that many mixing processes in water treatment take place.

2.3 Mixing Processes

2.3.1 Mixing Scales

Mixing processes in a stirred vessel occur at three levels of homogenisation over a range of scales; specifically, macromixing, mesomixing and micromixing. These are characterised by the timescale over which mixing occurs, from the largest (macro) to the smallest (meso). Macromixing is driven by the largest scales of motion in the fluid and is the homogenisation of the minor phase within the bulk flow, arising as a result of large scale convection and impeller movement. Consequently, macromixing is a function of the flow pattern generated within the mixing vessel. Mesomixing occurs at

scales between those of micro and micromixing and manifests itself via two mechanisms: turbulent diffusion and eddy disintegration to a size at which micromixing occurs. Micromixing is mixing on the smallest scales of motion (the Kolmogorov scale) and at the final scales of molecular diffusivity (the Batchelor scale). The Kolmogorov lengthscale, η, relates the smallest eddies present in the flow to the turbulent energy dissipation rate, ϵ, (*i.e.* the dissipation of turbulent kinetic energy being caused by work done by the smallest eddies against viscous stresses) and kinematic viscosity, ν, via:

$$\eta = \left(\frac{\nu^3}{\varepsilon}\right)^{1/4} \qquad \textbf{Equation 2-8}$$

The Kolmogorov lengthscale divides the equilibrium range into two distinct sub-ranges; *i.e.* the inertial sub-range where $l > \eta$, and the viscous sub-range where $l < \eta$. When eddies are larger than the particle, the eddies entrain the particles, causing little surface stress, with laminar shear dominating. When eddies are smaller than the particles, the eddies induce particle shear, surface drag and pressure forces. Consequently, the relationship between η and particle size, d, is important. Thus, micromixing controls the rate at which mixing occurs at a molecular scale where diffusion has a significant effect. Vortices are formed within the flow via two mechanisms: laminar stretching and turbulent erosion. A full account of the mixing scales may be found at Amirtarajah *et al.* (1991) and Patterson *et al.* (2004).

2.3.2 Flow Patterns

Observed flow patterns in mixing vessels are complex and are a function of vessel geometry, impeller type and location, operating conditions and fluid properties. The flow patterns play an important role in the efficiency of a mixing system as they affect particulate suspension, the formation of dead zones and so the overall homogeneity of the mixture. The jar test (which forms a substantial part of the work recorded in this thesis) uses a flat impeller which acts as a radial flow device, producing a flow pattern as shown at Figure 2-3 below. Two circulating loops are generated; one above and one below the impeller. Mixing is found to occur between the two loops and also within the

loops themselves. It is interesting to note that other impellers (such as the pitched blade turbine (PBT) or the Rushton turbine) have been the subject of detailed analyses within the engineering and mixing communities; whereas the flat impeller (or paddle) has been studied to a much lesser degree (*e.g.* Hemrajani & Tatterson, 2004).

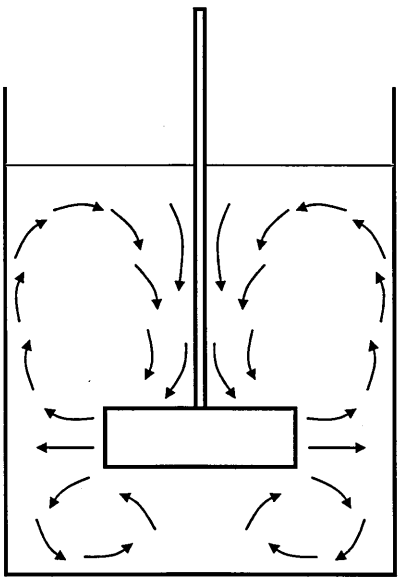


Figure 2-3: Flow pattern associated with common radial flow impeller.

2.3.3 Velocity Gradient

The concept of the average velocity gradient, G (s^{-1}) was developed by Camp and Stein (1943) to characterize mixing in flocculation basins, and the G value is now used worldwide to characterize mixing in a wide range of environmental engineering applications (Crittenden *et al.*, 2005, Metcalf & Eddy, 2003, Droste, 1997). From the consideration of the angular distortion of an elemental volume of water arising from the application of tangential surface forces, G was defined as the root mean square velocity gradient in a mixing vessel and was expressed algebraically by Camp and Stein as

$$G = \left\{ \left(\frac{\partial u}{\partial y} + \frac{\partial v}{\partial x} \right)^2 + \left(\frac{\partial u}{\partial z} + \frac{\partial w}{\partial x} \right)^2 + \left(\frac{\partial v}{\partial z} + \frac{\partial w}{\partial y} \right)^2 \right\}^{0.5} \qquad \textbf{Equation 2-9}$$

where u, v and w are the velocity components in the x, y and z directions of a Cartesian coordinate system.

Camp and Stein termed this the absolute velocity gradient and related this to work done per unit volume per unit time via:

$$\Phi = \mu G^2 \qquad \textbf{Equation 2-10}$$

From which:

$$G = \sqrt{\frac{P/V}{\mu}} = \sqrt{\frac{\varepsilon}{\nu}} \qquad \textbf{Equation 2-11}$$

where Φ work of shear per unit volume per unit time at a point,

P is power dissipated,

V is tank volume

μ is the dynamic viscosity of the water,

ϵ is the energy dissipation rate per unit mass

ν is the kinematic viscosity of the water

In theory, the absolute velocity gradient can be calculated at any point within a mixing vessel, provided that the power dissipated is known at that point. In practice, however, the flow characteristics vary within the mixing vessel from point to point, and so too does the energy dissipation. Consequently the velocity gradient is a function of both time and position. Given the difficulties associated with calculation of G, workers have traditionally replaced the absolute velocity gradient with an approximation of the exact value; that is its average value throughout the vessel, $\overline{G}$:

$$\overline{G} = \sqrt{\frac{P_{ave}}{V\mu}} \qquad \textbf{Equation 2-12}$$

where the average power consumption, P_{ave}, is readily obtained via

$$P_{ave} = P_o \rho N^3 D^5 \qquad \textbf{Equation 2-13}$$

Where P_o is the impeller power number

ρ is the fluid density

N is the rotational speed of the impeller

D is the impeller diameter

Since its introduction in the 1940s, the average velocity gradient value, $\overline{G}$ has been used as a cornerstone in the design of mixing processes, including flocculators. The

concept is taught globally and is to be found in most standard texts (*e.g.* Crittenden *et al.*, 2005, Metcalf & Eddy, 2003, Droste, 1997). The concept has been developed further to consider the dimensionless product of $\overline{G}$ and retention time, t, (the Camp number) to design and classify coagulation and flocculation vessels. However, since its introduction, authors have argued that the concept of the $\overline{G}$ value is flawed, as it attempts to represent a complex flow field within a single number (Cleasby, 1984, Clark, 1985, Graber, 1994, Luo, 1997, Jones, 1999). Clark (1985) and Graber (1994) demonstrated that the original derivation of the $\overline{G}$ value was flawed for three dimensional flows, and consequently it cannot be universally applied to different types or sizes of mixer. Furthermore, the distribution of velocity gradients within a stirred tank is clearly not uniform, and local power consumption at a point of high turbulence within a vessel (*e.g.* adjacent to the impeller) can be several orders of magnitude in excess of the rest of the vessel (Luo, 1997).

Different impellers will also produce different performance levels at the same average velocity gradient, and thus the parameter can only be used to scale up flocculation results from stirred tanks with extreme care (Lai *et al.*, 1975, Ducoste & Clark, 1998a & b). In a somewhat damming condemnation, Amirtarajah (1978) described $\overline{G}$ as "simplistic and totally inadequate". Consequently, despite its widespread use, it is believed that this well-established parameter does not describe adequately the fluctuations in local velocity gradient experienced at a specific point within the flow field (Boller and Blaser, 1998, Essemiani & de Traversay, 2002a & b). This is unfortunate as it is precisely the magnitude and fluctuations in local shear to which a floc is subjected, and not the average value, which determine the likelihood of floc agglomeration, breakage and re-growth (as studied by Jarvis *et al.*, 2004 and Gregory & Dupont, 2001).

Essemiani and de Traversay (2002a & b) also questioned the validity of this average (or, global) $\overline{G}$ approach, as it yields only an average value, giving no detail regarding local shear rate distribution within the tank. Essemiani and de Traversay (2002a & b) argued that as the rate of floc formation is directly proportional to the local shear rate distribution within the tank, different mixing rates will yield different levels of

performance. Furthermore, the authors argued that different impellers will also produce different performance levels at the same average velocity gradient, $\overline{G}$.

In order to quantify and understand the local impact of mean flow and turbulence on floc formation and break-up, the concept of the local velocity gradient, G_L, as developed by Luo, 1997, has been successfully adopted by several authors in recent years (Jones, 1999, Essemiani & de Traversay 2002a, Korpijarvi *et al.*, 2000). G_L is a function of the local turbulence energy, such that:

$$G_L = \sqrt{\frac{\varepsilon}{\nu}} \qquad \textbf{Equation 2-14}$$

Luo, 1997, expanded this such that:

$$G_L = \frac{\mu_{eff}}{\mu}\left\{2\left[\left(\frac{\partial u}{\partial x}\right)^2+\left(\frac{\partial v}{\partial y}\right)^2+\left(\frac{\partial w}{\partial z}\right)^2\right]+\left(\frac{\partial u}{\partial y}+\frac{\partial v}{\partial x}\right)^2+\left(\frac{\partial v}{\partial z}+\frac{\partial w}{\partial y}\right)^2+\left(\frac{\partial u}{\partial z}+\frac{\partial w}{\partial x}\right)^2\right\}^{0.5}$$

Equation 2-15

where,

$$\mu_{eff} = \mu + \rho C_\mu \frac{k^2}{\varepsilon} = \mu + \mu_t \qquad \textbf{Equation 2-16}$$

and k = turbulence kinetic energy

ϵ = rate of dissipation of turbulence kinetic energy

C_μ = a constant taken from experimental data = 0.09

μ_t = turbulent viscosity

Luo (1997) claimed that the two approaches produced similar results and that either could be used. However, close inspection of Luo's work shows that he plotted contours of the two parameters on a log scale, and the results appear to be consistent only to within an order of magnitude. It is assumed that these discrepancies arose as a result of the numerical calculation process, possibly indicating a lack of convergence of solution.

Essemiani and de Traversay (2002a & b) argued that the distribution of this G_L value is significant as it controls particle suspension, distribution, coalescence and break-up efficiency. Thus Essemiani and de Traversay suggested that the local approach facilitated the definition of optimum conditions for minimizing shear and maximizing

flow for each unit of energy imparted to the fluid. The authors did not, however, attempt to quantify the effects of local shear on floc characteristics; a gap which the work reported in this thesis attempts to fill.

2.3.4 Power Number

In order to describe energy requirements within a mixing vessel at given operating conditions, workers have traditionally made use of the Power number, P_o, and the Reynolds number, Re, relationships. For impeller mixing, the Reynolds number is defined at Equation 2-1 whilst the Power number is defined at Equation 2-17 below:

$$P_o = \frac{P}{\rho N^3 D^5} \qquad \textbf{Equation 2-17}$$

where: P = power mixer input
N = mixing speed
D = impeller diameter
ρ = liquid density

Thus, the power number is a dimensionless parameter that provides a measure of the power requirements for the operation of an impeller and in order to characterise the impeller, one must have knowledge of the operating environment; specifically, fluid, vessel and impeller properties. (Such properties include blade width, number of blades, blade angle, ratio of blade diameter to vessel diameter and impeller elevation). Power numbers vary to a wide degree according to impeller and mixing vessel design (generally $0.1<P_o<10$ in the turbulent region), and much published data is available for impellers and systems commonly used in the chemical engineering industries. (Hemrajani & Tatterson, 2004). The relationship between power number and Reynolds number for a selection of impeller types is shown at Figure 2-4.

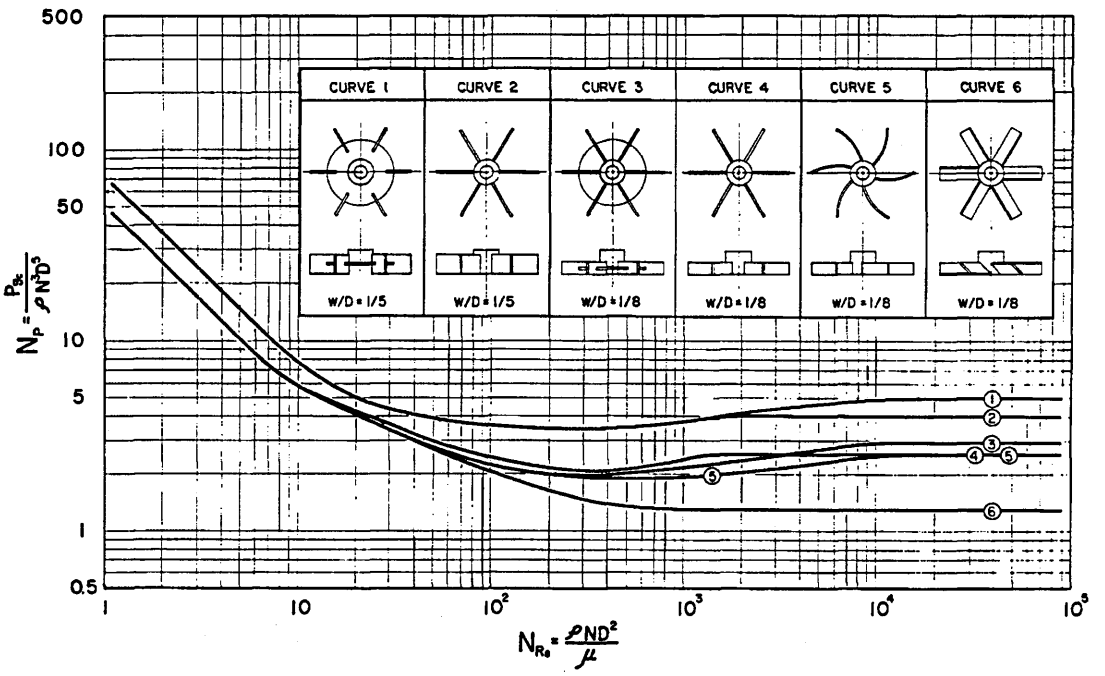


Figure 2-4: **Power number vs. impeller Reynolds number for seven different impellers (from Bates *et al*, 1963).**

Three separate zones can be identified:

1.	Laminar zone	$Re < 10$	$P_o \alpha Re^{-1}$
2.	Transitional zone	$10 < P_o < 10^4$	$P_o \alpha Re^{-a}$, $0 < a < 1$
3.	Turbulent zone	$Re > 10^4$	P_o = constant

The relationship between P_o and Re is useful in that it enables one to determine suitable operating conditions for a specific mixing scenario. In the laminar region, the Power number is inversely proportional to the Reynolds number. In the fully turbulent region, the Power number is independent of the Reynolds number and can be seen to be constant. In the transitional region between the laminar and turbulent regions, no simple relationships between the two parameters have been found, although a number of system-specific functions have been published. In the case of the jar tester, one is considering a low viscosity fluid (water) and so one would wish to achieve turbulent conditions for most effective mixing.

2.3.5 Residence Time Distribution

In many industrial applications (including the water industry) mixing tanks are designed on the basis that flow through the tank is "ideal". Two different ideal flow situations exist for steady state flow systems; *viz.* plug flow and completely mixed flow. The flow in a plug flow reactor is such that all fluid particles have the same residence time. As a result, the minimum retention time is equal to the theoretical retention time and is calculated as:

$$\tau = \frac{V}{Q} \qquad \textbf{Equation 2-18}$$

where V is the volume of the vessel and Q is the flow rate through it.

Ideal flow within a completely mixed reactor implies perfect mixing such that concentrations throughout the vessel are uniform, are equal to the concentration within the exit stream and are represented by:

$$C = C_0 e^{-\theta} \qquad \textbf{Equation 2-19}$$

where C_0 is the concentration at time t_0 and θ is the ratio of retention time to theoretical retention time (*i.e.* $\theta = t/\tau$). Tracer curves for ideal reactors are shown below at Figure 2-5.

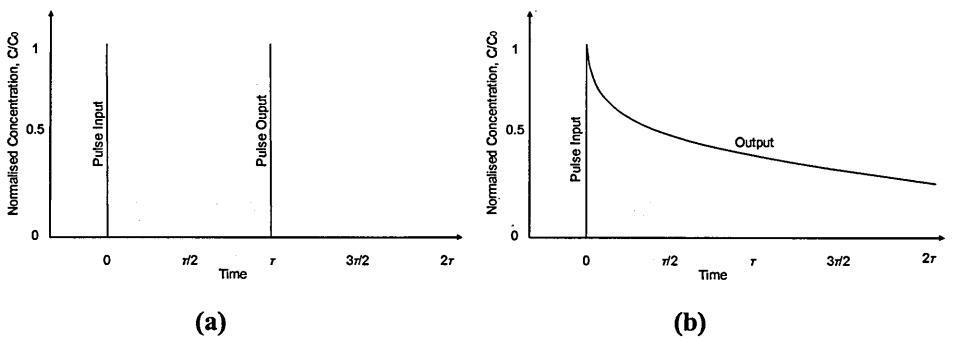


Figure 2-5: **Tracer curves from ideal reactors (a) plug flow reactor, (b) completely mixed flow reactor.**

However, although the ideal flow assumption often yields an adequate design, deviations caused by short-circuiting, recirculation or the creation of dead zones can be significant. For ideal plug flow, $\theta = 1$; however, in reality such performance is not achievable because of the effects of variation in velocity profile, axial dispersion and

flow separation. Crow *et al.* (1997), cited in O'Neil (2001) considered that these effects would limit plug flow efficiency such that θ would never exceed 0.7. Such non-idealities are to be avoided in view of their detrimental impact on process performance.

Fluid elements taking different paths through a vessel will take different lengths of time to pass through the vessel. The distribution of these times for the exit stream is termed the residence time distribution (RTD) or Exit Age Distribution of the fluid, where the term "age" refers to the time spent by an element in the vessel, yielding a distribution of residence times. Thus, the RTD function is a measurement of ideal or non-ideal flow associated with the bulk flow patterns (*i.e.* macromixing) in a mixing vessel, and is used to measure the residence time of fluid elements within a vessel and to identify areas of poor or no mixing. Much information is available on the theory of RTD analyses. However, the fundamental approaches were laid down by Levenspiel (1967) cited in Brown *et* al (2004) and Danckwerts (1953), cited in Nauman (2004). Excellent summaries of the RTD analysis are to be found at Crittenden *et al.* (2005) and Nauman (2004).

An RTD curve can be developed by introducing a conservative tracer to the flow at the vessel inlet and measuring the concentration of tracer at the outlet with time. A non-ideal tracer output from a stirred tank is shown at Figure 2-6.

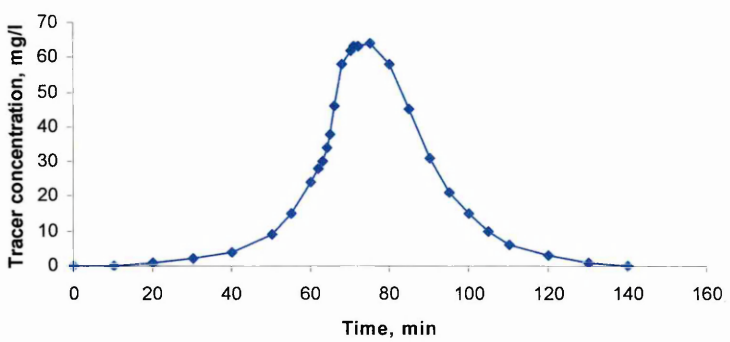


Figure 2-6: Example of a non-ideal tracer output from a stirred tank.

It is common practice to standardise RTD analyses via normalisation of time and output concentration. Time is normalised on the basis of the mean residence time, $\bar{t}$, where

$$\bar{t} = \frac{\int_0^\infty Ct\ dt}{\int_0^\infty C\ dt}$$ **Equation 2-20**

C = concentration at outlet at time t,

t = time since addition of tracer.

The normalised time, θ, is then defined as

$$\theta = \frac{t}{\bar{t}}$$ **Equation 2-21**

The normalised concentration is calculated as C/C_N, where

$$C_N = \int_0^\infty C\ d\theta$$ **Equation 2-22**

The RTD function, referred to as the exit age distribution, $E(t)$, is defined such that

$$\int_0^\infty E(t)dt = 1$$ **Equation 2-23**

The proportion of the fluid that is older than time t_1 is expressed via

$$\int_{t_1}^\infty E(t)dt = 1 - \int_0^{t_1} E(t)dt$$ **Equation 2-24**

For a completely mixed reactor, the exit age distribution is defined as:

$$E(\theta) = \frac{C}{C_N} = \frac{C_0 e^{-\theta}}{\int_0^\infty C_0 e^{-\theta}\ d\theta} = e^{-\theta}$$ **Equation 2-25**

There are two common tracer tests; *viz.* pulse input and step change. The pulse input method requires the injection of tracer over a short period of time. The concentration of the tracer is measured at the outlet until it reaches zero. The normalised response yields the C curve, as shown at Figure 2-7 below.

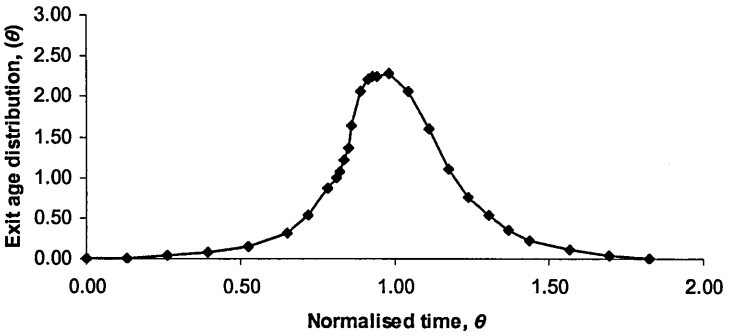


Figure 2-7: Exit age distribution as a function of normalised time – C Curve.

The step change method requires the introduction and maintained input of a concentration of tracer, C_0. The output concentration is measured until its value reaches C_0. The normalised response yields the F curve, as shown at Figure 2-8 below.

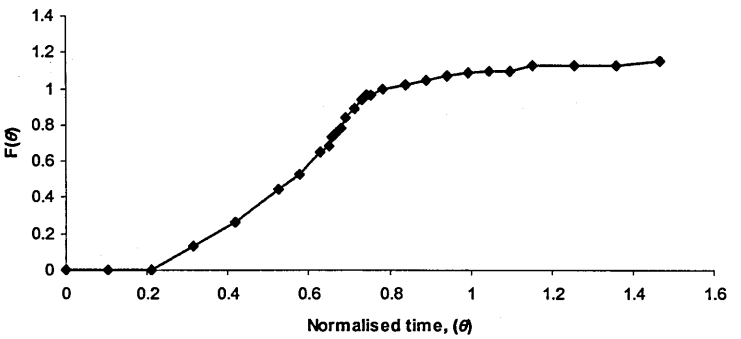


Figure 2-8: Exit age distribution as a function of normalised time – F Curve.

Crittenden *et al.* (2005) presented the key terms used to characterise RTD curves and these are presented below at Table 2-1 below.

Table 2-1: RTD curve characterisation terms (from Crittenden *et al*, 2005).

Term	Definition
t	Theoretical hydraulic retention time, = V/Q
t_i	Time at which tracer first appears
θ	Normalised retention time = t/t
t_p	Time at which peak concentration of tracer is observed
$\bar{t}$	Mean residence time = centroid of $E(\theta)$ curve
t_{10}, t_{50}, t_{90}	Time at which 10, 50 and 90% of tracer has passed through reactor.
t_{50}/t_{90}	Morrill dispersion index
t_i/τ	Index of short-circuiting. Ideal plug flow reactor = 1. Tends to 0 with increased short-circuiting
t_{50}/τ	Index of mean retention time. Measure of skew of $E(\theta)$ curve

2.4 Flocculation

2.4.1 Conceptual View of Flocculation

Flocculation is the transformation of smaller destabilised particles into larger aggregates or flocs, with the rate of growth governed by the rate of inter-particle collisions. Floc densities tend to be similar to the density of water (Gregory, 1997, Jarvis *et al.*, 2005b), and so the flocs follow the paths of the flow itself. As a result, particle collisions, and hence flocculation, are directly related to the local velocity gradient, G_L, as defined at Equation 2-9 above. However, flocs are mass fractal objects whose density is found to decrease as size increases. Consequently, as the flocs grow in size, induced shear forces may give rise to floc breakage. Jarvis *et al.* (2005a) suggest that the rate of floc growth may be expressed conceptually as

$$R_{floc} = \alpha R_{col} - R_{br} \qquad \textbf{Equation 2-26}$$

Where R_{floc} = overall rate of floc growth

α = collision efficiency factor ($0 < \alpha < 1$)

R_{col} = rate of particle collision

R_{br} = rate of floc breakage

More accurately, the αR_{col} term should be broken down further into its constituent parts as follows:

$$\alpha_{ij} R_{col_{ij}} = {}^{BM}\alpha_{ij}\,{}^{BM}R_{col_{ij}} + {}^{Sh}\alpha_{ij}\,{}^{Sh}R_{col_{ij}} + {}^{DS}\alpha_{ij}\,{}^{DS}R_{col_{ij}} \qquad \textbf{Equation 2-27}$$

Where i and j refer to discrete particles, and BM, Sh and DS refer to the collision mechanisms of Brownian Motion, shear and differential settlement respectively.

For all flocs in their initial growth phase, and for those which exhibit regrowth capabilities, the floc formation process is understood to be a balance between the rate of aggregation and the rate of breakage for given shear conditions (Biggs & Lant, 2000). As a result, flocs do not continue to grow throughout the flocculation stage, but rather, attain a limiting size beyond which breakage prevents further overall growth. This limiting size is governed, not by the characteristics of the floc, but by the shear conditions within the containing vessel. Consequently, it is the vessel hydrodynamics which control the different phenomena in flocculation.

2.4.2 Flocculation Theory

2.4.2.1 Particle Agglomeration (Floc Growth)

The original description of flocculation lies with Schmoluchowski (1917) who defined a population balance model to describe the change in concentration of particles of any size as follows (Lawler & Nason, 2004).

Rate of change with time of the number concentration of particles of size k	=	Rate of increase in the number concentration of particles of size k by flocculation of smaller particles (the sum of whose volumes is size k)	=	Rate of decrease in the number concentration of particles of size k by flocculation of size k particles with any size particles

Traditionally workers have ignored the so-called short-range forces on collision frequency (and therefore assumed that just one value of α_{ij} exists for all three mechanisms as shown in Equation 2-26).

Smoluchowski proposed that the particle collisions involved in flocculation, might be described such that

$$^{Sh}\beta(d_i,d_j)=\frac{\partial U}{\partial Z}\frac{(d_i+d_j)^3}{6} \qquad \textbf{Equation 2-28}$$

Camp and Stein (1945) subsequently generalised this equation for use in turbulent conditions via the use of the velocity gradient (as described above) such that

$$^{Sh}\beta(d_i,d_j)=G\frac{(d_i+d_j)^3}{6} \qquad \textbf{Equation 2-29}$$

Camp (1955) proposed that flocculator design be based on a dimensionless parameter (known as the Camp number) expressed as the product of the average velocity gradient and retention time, t. Camp proposed that flocculators be designed with a $\overline{G}.t$ value of between 23,000 and 210,000. Ives (1968) refined this approach by recognizing the fact that acceptable flocculation performance might be achieved with $\overline{G}.t$ values significantly lower than those recommended by Camp. Ives proposed flocculator design based on a constant value of $\varphi.\overline{G}.t$, where φ is the volume of particles per unit volume of suspension, expressed as $\varphi=\frac{1}{6}\pi.d^3n_0$. Subsequently, O'Melia (1972) proposed that flocculator design be based on a constant value of $\alpha_{emp}.\varphi.\overline{G}.t$, where α_{emp} is an empirical dimensionless correction factor, used to align experimental and model data. Lawler and Nason (2004) presented new guidelines for flocculator design in which the design is based on the calculation of a characteristic reaction time for the loss of 1μm particles using a reaction rate which incorporates all collision mechanisms (as shown in Equation 2-27. Currently, however, this work is of an academic nature only and no full scale applications of it are known.

Table 2-2: Proposed flocculator design parameters.

Reference	Flocculator Design Parameter
Camp, 1955	$\overline{G}.t$
Ives, 1968	$\varphi.\overline{G}.t$, $\varphi=\frac{1}{6}\pi.d^3n_0$
O'Melia, 1972	$\alpha_{emp}.\varphi.\overline{G}.t$, α_{emp} = empirical dimensionless correction factor
Lawler & Nason, 2004	$\frac{1}{t_{char}}=\frac{1}{t_{char,Br}}+\frac{1}{t_{char,Sh}}+\frac{1}{t_{char,DS}}$

2.4.2.2 Floc Breakage

Whilst Jarvis *et al.* (2005a) used Equation 2-26 to describe the rate of floc growth in conceptual terms, floc size may be considered to be a balance between the hydrodynamic forces exerted on a floc and the strength of the floc. Where the floc strength is resistant to the hydrodynamic forces, one would expect floc size either to remain constant or for growth to occur. Where the hydrodynamic forces exceed floc strength, floc breakage will occur. Consequently, the conceptual growth breakage mechanism may be expressed as follows (Coufort *et al.*, 2005):

$$B = \frac{\text{Hydrodynamic Forces}}{\text{Floc Strength}} = \frac{F}{J} \qquad \textbf{Equation 2-30}$$

where F represents the hydrodynamic forces exerted by the flow, and J represents the strength of the floc. It is clear from above that breakage will occur when $B>1$, and floc size will be maintained or increased when $B<1$. Floc strength, J, is a function of the physico-chemical conditions (raw water type, coagulant type and dose) and the floc structure, and is discussed in detail by Jarvis (2005).

Yeung and Pelton (1996) suggested that the hydrodynamic force required to pull apart a floc in tensile mode may be expressed as:

$$F \approx \frac{\pi}{4}.\sigma.d^2 \qquad \textbf{Equation 2-31}$$

where σ represents the hydrodynamic stress exerted on the floc, and d is the area of the floc. In the viscous subrange (*i.e.* $l<\eta$), $\sigma = \mu.G$ and $G = \sqrt{\varepsilon/\nu}$

Substituting into Equation 2-30 shows that the breakage mechanism in the viscous sub-range, B_{VSR}, may be expressed as:

$$B_{VSR} = \frac{C_1 \mu \sqrt{\varepsilon/\nu}.d^2}{J} \qquad \textbf{Equation 2-32}$$

where C_1 is a constant.

Thomas (1964) suggested that in the inertial sub-range

$$\sigma = \bar{\rho}.\overline{u'}^2 \qquad \textbf{Equation 2-33}$$

and

$$\overline{u'}^2 = C_2(\varepsilon.d)^{2/3} \qquad \textbf{Equation 2-34}$$

Substituting into Equation 2-30 shows that the breakage mechanism in the inertial sub-range, B_{ISR}, may be expressed as:

$$B_{ISR} = \frac{C_2 \rho \varepsilon^{2/3}.d^{8/3}}{J} \qquad \textbf{Equation 2-35}$$

where C_2 is a constant.

Consequently, it is deduced from Equations 2-32 and 2-35 that floc size is dependent on the turbulence energy dissipation rate and floc strength, irrespective of subrange. This is clearly of great significance when one attempts to gain an understanding of floc breakage mechanisms and limiting floc size as it directs workers to focus their efforts towards ϵ and J.

2.4.3 The Jar Test

Effective coagulation and flocculation are fundamental to the successful operation of many water treatment works, and so it is imperative that these unit processes are designed and operated in the most efficient manner for the raw water being treated. This optimisation is generally considered at the laboratory scale, using the common jar test apparatus and procedure. The history of the jar test dates back to Langelier (1921) (cited by Crittenden *et al.*, 2005), and consequently it is one of the most well-established process optimisation techniques available within the water industry, allowing a rapid assessment of key variables such as coagulant dose, pH, mixing speed and flocculation time. The test apparatus typically comprises four or six glass vessels, each with a powered paddle to stir the contents of the vessel and each containing the same volume of raw water. The paddles are set to rotate at high speed for a short period, during which time different quantities of coagulant (and acid or alkali for pH adjustment as necessary) are added to each vessel and mixed. After a short period of intense mixing (typically one minute) to simulate the coagulation process, the paddle speed is reduced to a produce more gentle mixing to simulate the flocculation process.

After 20 minutes of flocculation, mixing is terminated, the paddles removed and the suspensions allowed to settle. The flocs in each vessel may then be analysed for size and strength, turbidity removal and organics removal, allowing conclusions to be drawn regarding optimum coagulant dose and pH. These conclusions may then be applied to the operation of the main treatment plant. However, no absolute standard apparatus or procedure exists for the jar test. Various different jar test configurations are in use today and the potential implications of this are discussed further below. Traditionally most, but not all, workers have used a flat impeller within either an unbaffled cylindrical vessel or an unbaffled square section (on plan) vessel (Table 2-3). More recently, some workers have adopted the Kemira Kemwater mini flocculator (Korpijarvi *et al.*, 1999 & 2000, Duan & Gregory, 1998, Yukselen & Gregory, 2002 & 2004, Gregory, 2004).

2.4.4 Laboratory Scale Investigations into Mixing Processes, Coagulation and Flocculation

The literature contains many examples of practical investigations into flocculation and floc strength using the jar test apparatus and procedure. Jarvis *et al.* (2005a) have published a comprehensive review of floc strength. Therefore, only those elements of floc strength which are directly related to the research reported in this thesis are considered here. Close inspection of the literature shows that, whilst the procedure for the jar test is generally applied in a common fashion, the apparatus used varies from worker to worker. Table 2-3 shows the different experimental approaches used by several workers in recent years.

Table 2-3: Reported jar test experimental data.

Reference	Vessel Volume	Vessel Shape	Vessel Dimensions, mm	Impeller Type & Size, mm	Impeller Clearance, mm	Impeller Mixing Speed, rpm	Vessel Average Velocity Gradient, G, s^{-1}	Flow Measurement / Model Validation Technique
Armenante *et al.*, 1997	2L	Cylindrical	293 ϕ, 293 deep	6-blade, 45 ° pitched-blade turbine, 98 ϕ	73	450 700		Laser Doppler Anemometry
Bache & Rasool, 2001	2L	Square	115 x 115 x 150 (assumed)	2 blade, 76 x 25			10-400	
Biggs & Lant, 2000	1.2L	Cylindrical, baffled	115 ϕ, 150 deep	6 blade, flat, 30 ϕ		100 - 700	19.4 - 444	
Bouyer *et al.*, 2001		Cylindrical	100 ϕ	75 (approx) x 20	15	30 45 60 90 150	9 12 15 21 33	Particle Image Velocimetry
Bouyer *et al.*, 2005 a & b	1L	Cylindrical	94	74 x 20	50	30 45 60 150 300	13 23 34 133 350	Particle Image Velocimetry
Ciofalo *et al.*, 1996	170L	Cylindrical	600ϕ, 600 deep	Rushton turbine & 8 blade flat impeller	300	72		
Coufort *et al.*, 2005	1L	Cylindrical	94 ϕ, 145 deep	2 blade, 74 x 20	50	30 45 60 150 300	13 23 33 125 323	Particle Image Velocimetry
Duan & Gregory, 1996	250 ml	Cylindrical (assumed)		N/A – magnetic stirrer				

Reference	Vessel Volume	Vessel Shape	Vessel Dimensions, mm	Impeller Type & Size, mm	Impeller Clearance, mm	Impeller Mixing Speed, rpm	Vessel Average Velocity Gradient, G, s^{-1}	Flow Measurement / Model Validation Technique
Duan & Gregory, 1998	800 ml	Cylindrical (assumed)		Flocculator 90, Kemira Kemwater, 2 blade, 70 x 25	45	350, 50		
Ducoste & Clark, 1998 (I & II), 1999	5L	Square		Rushton turbine			40	
				A310 foil			40	
	28L	Square		Rushton turbine			40	
				A310 foil			40	
	560L	Square		Rushton turbine			40	
				A310 foil			40	
Fitzpatrick *et al.*, 2003	800 ml					50	23	
						400	520	
Francois, 1987	4L						21-1018	
Gregory & Dupont, 2001	800 ml			Flocculator 90, Kemira Kemwater, 2 blade, 70 x 25	45	30-300		
Gregory & Rossi, 2001	500ml	Square		2 x cross-shaped paddles, each 20 x 20		40		
						60		
						80		
						100		
						140		
						200		
Haque *et al.*, 2006	5.4L	Cylindrical	190ϕ, 190 deep	6 blade Rushton turbine, 95ϕ	63	139		
						194		
						240		
	157L	Cylindrical	585ϕ, 585 deep	8 blade flat impeller, 243ϕ	243	72		

Reference	Vessel Volume	Vessel Shape	Vessel Dimensions, mm	Impeller Type & Size, mm	Impeller Clearance, mm	Impeller Mixing Speed, rpm	Vessel Average Velocity Gradient, G, s^{-1}	Flow Measurement / Model Validation Technique
Hudson & Wagner, 1981	2L	Square	115 x 115 x 150	Not stated (assumed 2 blade, 75 x 25)				
Jarvis *et al.*, 2004	1 L	Cylindrical	100 ϕ	2 blade, 76 x 25		30 40 50 75 100 150 200	Not recorded	
Lai *et al.*, 1975	2L	Cylindrical, baffled and unbaffled		2 blade paddle, 76 x 25, 3 blade propeller, 50 ϕ, 2 blade PBT, 50 ϕ x 7, 2 blade paddle, 72 x 41 2 blade paddle, 72 x 32	41 60 57.1 69.2 87.6	50 - 800	2 - 400	
Leentvaar & Rebhun, 1983	2L			Turbine			160-500	
Luo, 1997		Cylindrical, unbaffled, covered	293 ϕ, 293 deep	6 blade, 45 deg PBT. $\phi = 98$	73	450 700		
		Rectangular, baffled (10mm width)	300 x 300 x 450	2 blade paddle, 66 x 35	130	350		

Reference	Vessel Volume	Vessel Shape	Vessel Dimensions, mm	Impeller Type & Size, mm	Impeller Clearance, mm	Impeller Mixing Speed, rpm	Vessel Average Velocity Gradient, G, s^{-1}	Flow Measurement / Model Validation Technique
		Cylindrical, baffled (6.25mm width), uncovered	293 ϕ, 293 deep	6 blade, 45 deg PBT. ϕ = 101.6 & 76.2	73	159		Laser Doppler Anemometry
						256		
Rossini *et al.*, 1999	2L	Square, baffled (13mm width),	130 x 130 x 130	6 blade (Rushton) turbine, 43 ϕ	43	30-200	40-400	
Spicer & Pratsinis, 1996, Spicer *et al.*, 1998	2.8 L	Square, baffled	150 x 150 x 150	Rushton Lightnin R100 impeller	Z/3 to centre	100	50 (growth)	
						156	100,	
						248	200	
						325	300,	
						460	500 (breakage)	
Stanley & Smith, 1995	2 L	Square	115 x 115 x 150	1 blade, 75 x 25		20	10	Laser Doppler Anemometry
						40		
						60		
						80		
						100	125	
Wu *et al.*, 2003	Couette						10-400	
Yukselen & Gregory, 2002 & 2004, Gregory, 2004	800 ml			Flocculator 90, Kemira Kemwater		300	340 (breakage)	
							11 (growth)	
						30	518	
						400	23	
						50		

It is clear from Table 2-3 that the reported literature contains results of jar test experiments in which the shape of the containing vessel, the shape and location of the impeller, the volume of water, and the mixing speed have all differed. It is also clear that not all workers have reported the jar test configurations they have used to develop their results and conclusions. Within the literature, data from previous work is often compared with current work, and workers have compared and contrasted the chemical characteristics of flocs and coagulants in detail. However, Mhassalker *et al.* (1991) concluded that it is physical parameters such as mixing intensity and retention time which bring a greater bearing on coagulation and flocculation efficiency than chemical parameters such as pH and alkalinity of the raw water. It is interesting to note that there is usually no allowance made for the different conditions under which the experiments have invariably taken place. One of the key elements of the work reported in this thesis is to examine how, if at all, changes to the configuration of the jar test experiments might affect the results. It is also interesting to note the lack of physical flow measurement undertaken to verify CFD models.

2.4.5 Floc Strength

Jarvis *et al.* (2005a) published a comprehensive review of floc strength, and the interested reader is directed towards that publication for a full review. However, the key research relating to work covered in this thesis is discussed briefly below.

The strength of flocs formed is of fundamental importance to the successful and efficient removal of particulate matter from water and is a function of inter-particulate bonding between the structural components of the aggregate. Zhang *et al.* (1999) suggested that floc strength may be described as the energy required to cause floc breakage in tension, compression or shear. It is clear that, having expended time and energy in developing flocs, operating conditions must not subsequently cause their break up. As a result, floc strength, growth and breakage have been the subject of detailed research in recent years (*e.g.* Leentvaar & Rebhun, 1983, Bache *et al.*, 1999, Gregory & Dupont, 2001, Gregory, 2004, Yukselen, & Gregory, 2004, Jarvis *et al.*, 2004).

Despite the attention focused on floc strength and breakage, Jarvis *at al* (2005a) found no established floc strength test in their review of the literature, but identified a number of techniques which have been used and which may be categorized as "macroscopic" (a measure of the energy required to cause floc breakage) and "microscopic" (measurement of the inter-particle forces within individual flocs). By exposing flocs to an increased degree of shear within a simple mixing vessel, Francois (1987) and Fitzpatrick *et al.* (2003) considered floc strength to be defined as the ratio of floc size pre and post breakage, via the expression:

$$\text{Strength Factor} = \frac{d_2}{d_1} \times 100 \qquad \textbf{Equation 2-36}$$

where d_1 is the average floc size (having attained steady state conditions) before breakage, and d_2 is the corresponding figure following floc breakage. The strength factor is dependent on the degree of applied shear, and so, thus far, can only be used to consider the responses of different flocs to the same mixing conditions. One of the purposes of the research reported in this thesis is to quantify the degree of applied shear (by measuring the locally applied velocity gradients) to enable comparisons of flocs grown and broken in different mixing systems.

Again using a simple mixing vessel, but this time considering several levels of increased shear and the associated energy input, researchers (Bache, 2004, Bache *et al.*, 1999, Francois, 1987, Parker *et al.*, 1972) have also observed and considered the following empirical relationship between floc strength and applied shear in turbulent conditions:

$$\log d_{\max} = \log C - \gamma \log \overline{G} \qquad \textbf{Equation 2-37}$$

where d_{max} is the maximum floc diameter, C is a strength coefficient, γ is a floc strength constant with a value between 0 and 2, and $\overline{G}$ is the average velocity gradient (as defined at Equation 2-12 above). This relationship has been used to provide an indication of floc strength in two ways; firstly, for a given $\overline{G}$, the greater the magnitude of C, the stronger the floc. Secondly, assuming a constant C for a given floc, strength is implicit in the relationship between d_{max} and $\overline{G}$, with the former decreasing as the latter increases.

From Equation 2-37, it follows that

$$\log d_{\max} = \log C - \gamma \log \sqrt{\varepsilon / \nu} \qquad \textbf{Equation 2-38}$$

Whilst the value of γ has been shown to vary little, irrespective of the choice of characteristic value of d (*i.e.* d_{max}, d_{95}, d_{50}), (Leentvaar & Rebhun, 1983), the value of log C is dependent on both d and the method of particle size measurement. Consequently, it is permissible to use log C only as a general comparison of floc strength within a single system, and comparison between studies where the vessel geometry and impeller type vary is not appropriate. Other macroscopic floc strength tests include the application of an ultrasonic field to a floc suspension and observation of floc breakage / erosion (Chu *et al.*, 2001), and the exposure of flocs to hydrodynamic stress from an oscillatory mixer (Bache *et al.*, 1999).

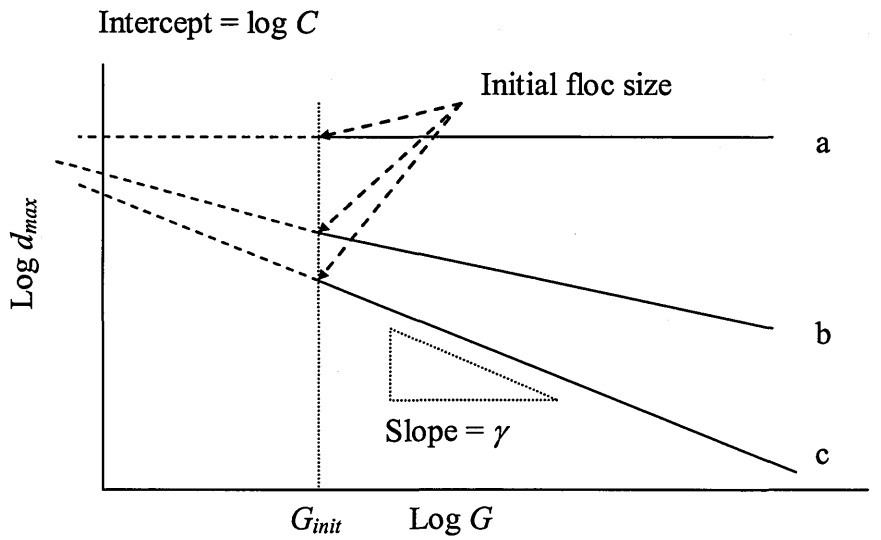


Figure 2-9: The relationship between the change in particle size and an increase in velocity gradient for 3 types of floc. Floc (a) is resistant to breakage, floc (b) is thought to break due to large scale fragmentation and floc (c) is thought to break by surface erosion (from Jarvis *et al*, 2005a).

2.4.6 Floc Breakage

Gregory (2004) has shown that the development and nature of floc suspensions are governed by the prevailing shear conditions and will reach a steady state. Increasing the shear beyond a critical threshold will induce breakage within the suspension until a new steady state is reached. Breakage is believed to be brought about via either surface erosion or large scale fragmentation. Jarvis *et al.* (2005a) describe surface erosion as "the removal of small particles from the floc surface, resulting in an increase in the small particle size ranges" and large scale fragmentation as "the cleavage of flocs into pieces of a similar size without an increase in primary particle concentration". Erosion is believed to arise as a result of shear stresses acting tangentially to the floc surface, whilst fragmentation is thought to be the result of tensile stresses in the normal direction across the floc. Due to the largely irreversible nature of floc breakage, as identified by Yukselen, & Gregory (2004), most flocs are unable to regrow if broken in a higher shear level, although the addition of flocculant aids has been shown to improve regrowth potential. As a result, gaining a sound appreciation of the shear energy required to break individual flocs or a floc suspension is key to the efficient operation of the flocculation process on a water treatment works. One objective of this study was to replicate laboratory scale flocculation using CFD models and to reconcile the numerical data with floc breakage characteristics identified within the laboratory with a view to developing an enhanced appreciation of the causes and mechanisms of floc breakage.

Fitzpatrick *et al.*, 2004, used a series of jar test experiments to study the effect of temperature on flocculation and found that size, strength and ability to reform were all affected by temperature, with warmer temperatures producing bigger flocs which both broke and reformed less well at lower temperatures. The authors also found that aluminium-based coagulants produced flocs which exhibited a greater degree of size and strength variation than ferric sulphate flocs.

Jarvis *et al.* (2004) undertook laboratory experiments using a jar tester to compare the strength, breakage and regrowth characteristics of three different types of floc suspensions; specifically, coagulant precipitate flocs (iron hydroxide precipitate formed

by adding coagulant to de-ionised water containing a small amount of alkalinity in the form of $NaHCO_3$ (20 mg/L)), turbidity flocs (kaolin suspended in tap water at a concentration of 80 mg/L at pH 7.5) and organic matter flocs (upland raw water with high colour and DOC (10mg/l as carbon), low turbidity (2.4 NTU) and low alkalinity (<10 mg/l as $CaCO_3$) at pH 6.0). A dynamic laser diffraction instrument (Malvern Mastersizer 2000, Malvern, UK) was used to measure floc size as the coagulation and flocculation processes proceeded. The suspension was developed in a cylindrical jar test device using a typical two-blade flat impeller and the suspension was monitored by drawing water through the optical unit of the Mastersizer and thence returned to the jar via a peristaltic pump on the return tube. The authors placed inflow and outflow tubes opposite to each other at a depth just above the impeller in the holding ports. The authors found that the initial floc size (expressed as the median volumetric equivalent diameter, d_{50}) observed the hierarchy iron hydroxide > raw water > kaolin flocs. Increasing the mixing speed was found to decrease d_{50} in all cases until a steady state was reached some 30 minutes following the increase. The rate of degradation increased with the increase in mixing speed (*i.e.* a mixing speed of 200 rpm caused a faster rate of d_{50} decrease than a mixing speed of 50 rpm).

The steady state floc sizes after exposure to increased levels of shear reported by Jarvis *et al.* (2004) are shown in Figure 2-10, from which it can be seen that, on exposure to increased mixing speeds (and so increased shear) the kaolin and raw water flocs demonstrated a constant rate of degradation. However, the behaviour of the coagulant precipitate was somewhat different; at mixing speeds of 50 rpm and below, d_{50} was found not to change greatly, indicating resistance to the shear levels induced at these mixing speeds. However, at mixing speeds of 75 rpm and above, the rate of degradation increased and flocs were observed to reduce in size from 900 μm to 250μm. Jarvis *et al.* found that the organic flocs demonstrated the greatest proportional size change across the range of shears applied, whilst kaolin had the smallest proportional size change across the same range. For all three suspensions, only small scale changes to floc size were observed at mixing speeds of 50 rpm and below; whereas once the mixing speed was increased to 75 rpm and greater, larger scale reductions in floc size were observed.

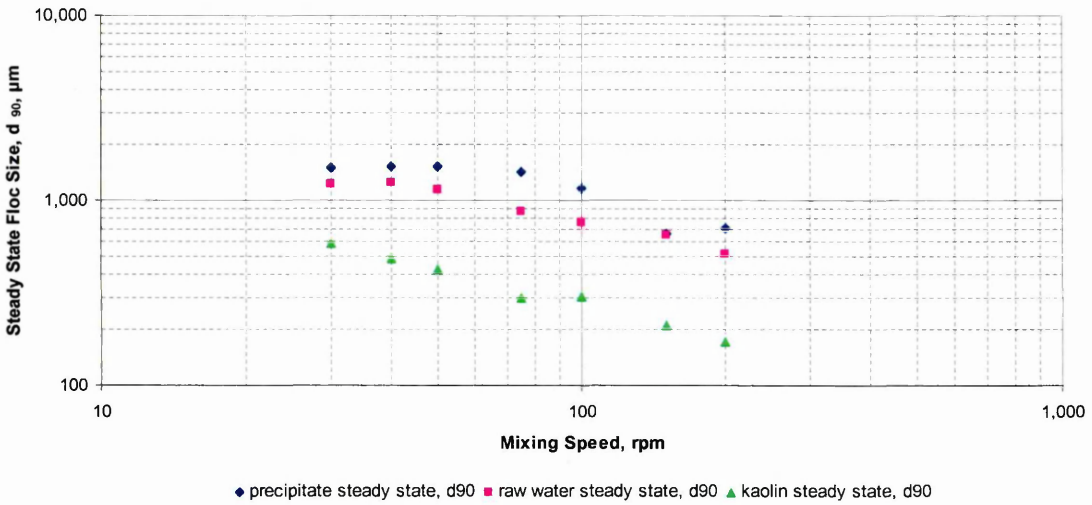


Figure 2-10: **Steady state floc size after exposure to increased levels of shear (from Jarvis *et al*, 2004).**

Whilst Figure 2-10 shows the steady state d_{50} values for the three suspensions, Figure 2-11 shows the development of the steady state values for the ferric hydroxide suspension. It is clear that one minute after increasing the mixing speed from 30 rpm to a speed equal to or in excess of 100 rpm, significant floc breakage occurred. This is an interesting observation on two levels. Firstly, the results demonstrate that the precipitate flocs are resistant to the shear levels induced by mixing at speeds of up to 50 rpm (there is some reduction in d_{50} with time at 75 rpm). Secondly, it appears that a significant proportion of floc breakage seen at speeds of 100 rpm and above is due to the increase in shear generated via an instantaneous increase in mixing speed. As time progresses, the rate of degradation is seen to decrease, despite the fact that the high mixing speed is maintained. Part of the modelling work included within this thesis examined the floc break-up characteristics of different particles and attempted to mimic them using CFD.

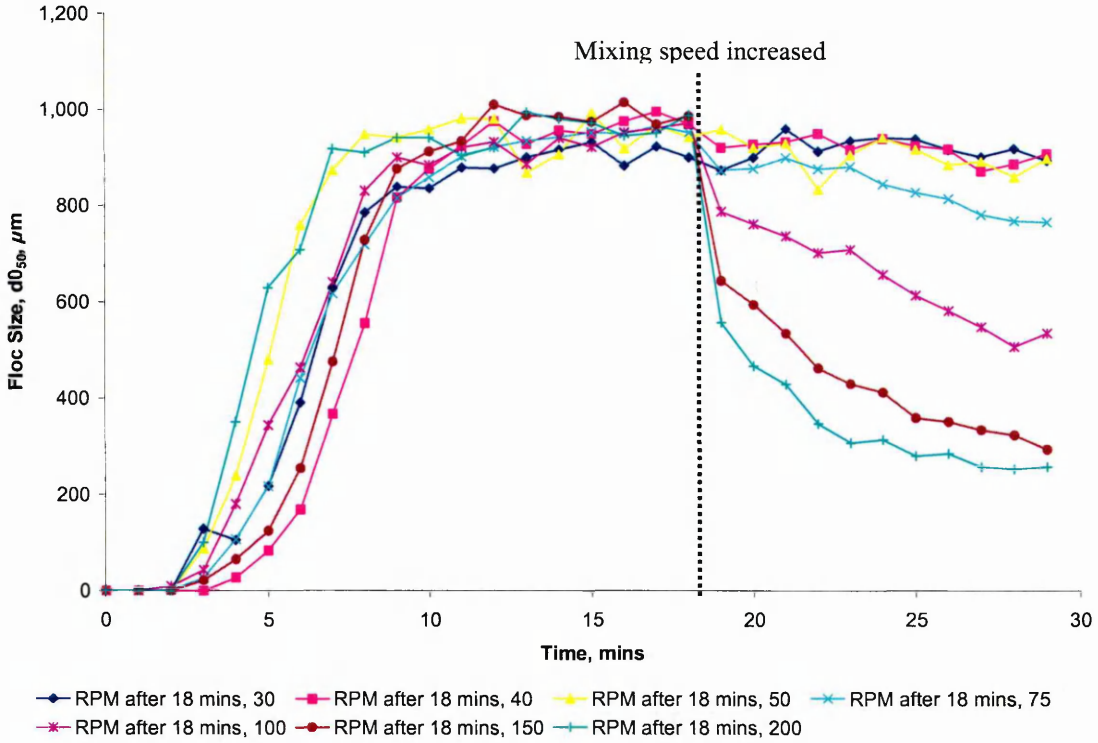


Figure 2-11: Floc size profiles during coagulation and after exposure to increasing levels of RPM (from Jarvis *et al*, 2004).

2.4.7 Floc Re-growth

Should a floc be broken within a flocculator by entering an area of shear beyond its threshold strength, it is important to know whether or not that floc might re-grow to all or part of its original size if it spends sufficient additional time within the flocculator. Therefore, whilst several researchers have studied the propensity of flocs to break under certain prevailing shear conditions, as demonstrated above, the study of floc re-growth following breakage is equally important and has also warranted close inspection. Gregory and Dupont (2001) used a Kemira Kemwater jar test device to compare the floc formation and breakage characteristics of aluminium sulphate and three commercial polyaluminium chloride (PACl) coagulants on model clay suspensions. The authors found the commercial products produced flocs which were larger and stronger than those produced using alum. Floc breakage for all coagulants was found to be essentially irreversible and the response of flocs to increased shear (or, more precisely, mixing

speed) was seen to depend not on the conditions during floc formation, but rather on the imposed shear rate.

Yukselen and Gregory (2002, 2004) confirmed the irreversibility of PACl and alum flocs under sweep flocculation conditions, but found that flocs formed using a cationic polyelectrolyte acting predominantly by charge neutralisation exhibited almost full reversibility of floc formation after breakage. The authors conceded that the underlying mechanisms of irreversible floc breakage remained unclear, but suggested that the effect was specific to sweep flocculation and was a result of the breakage of chemical bonds during floc disruption, as when particle interaction is physical (*e.g.* van der Waal's forces or electrostatic attraction), there is no clear reason as to why flocs should not reform after breakage. Chaignon *et al.* (2002) also found full reversibility in flocs formed by charge neutralisation. Jarvis *et al.* (2005c & d) demonstrated that, like hydrolyzing coagulants, flocs formed with NOM rich water and iron precipitate flocs did not regrow following breakage. The authors ascribed this phenomenon to the fact that NOM and iron precipitate flocs are held together by chemical rather than physical bonds but, like Yukselen and Gregory, were unable to account for the irreversibility of hydrolyzing coagulant flocs.

2.4.8 Floc Size Measurement

Flocs are mass aggregate fractal particles, the density of which decreases as size increases. Consequently, the measurement of floc characteristics poses specific challenges. Jarvis *et al.* (2005b) reported that there exists a range of techniques for measuring floc size, shape and fractal dimension. Of the sizing techniques, microscopy requires significant amounts of time in respect of sample preparation and analysis time. Alternatives to microscopy and photography include on-line light scattering techniques. Jarvis *et al.* (2005b) concluded that light scattering performs well on small, open flocs of low refractive index whilst larger flocs of low porosity and of high colour contrast are more suited to settling and 2D image analysis using microscopy. Thus, microscopy and photography remain the only reliable methods of accurately confirming floc shape characteristics.

Gregory and Nelson (1986) developed an approach to floc size monitoring using a photometric dispersion analyser (PDA). The intensity of light transmitted through a flowing suspension is monitored by a photodiode. The output of this photodiode is a large direct current (d.c.) component, and a smaller, fluctuating, alternating current (a.c.) component. Gregory and Nelson (1986) showed that the ratio of the root mean square value of the amplified a.c. signal to the d.c. signal is a function of particle aggregation and, hence, floc size. Gregory and Nelson defined this ratio as the Flocculation Index (FI). Gregory has since used the FI approach extensively (*e.g.* Gregory, 2004). An example of the output developed from a PDA / FI-type analysis is given below at Figure 2-12

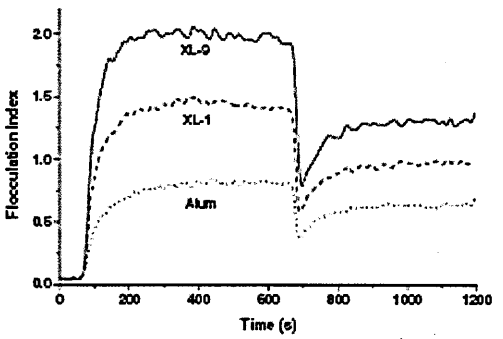


Figure 2-12: Dynamic monitoring of kaolin suspensions, after dosing with alum and two PACl samples. Floc breakage (10s at 330 rpm) at 660s (from Gregory, 2004).

Whilst the PDA / FI approach has now been used extensively for 20 years, it has, in this author's opinion, two distinct limitations. In the first instance, the flocs are removed from the jar tester and pumped to the PDA. Because of the fragile, fractal nature of floc structure, there can be no certainty that flocs will not be damaged in the pumping transfer process. Secondly, whilst the FI approach can be used to demonstrate the degree of floc breakage, by comparing flocculation indices prior to and after breakage, the method cannot yield information on the absolute degree of breakage, measured in terms of actual floc size.

It should also be noted that, like the PDA approach of Gregory and Nelson (1986) the work of Jarvis *et al.* (2004) relies on (a) appropriate selection of a floc extraction point, and (b) transfer of flocs by pumping. The same concerns regarding potential floc breakage arising from pumping transfer as applied to Gregory and Nelson are applicable

to the method of Jarvis *et al.* also. In addition, it is possible that the floc sizes measured by the Mastersizer are also a function of the point of extraction. Laser Doppler anemometry, particle image velocimetry and computational fluid dynamics techniques are all used in the research reported in this thesis to determine the impact of sample point location on median floc size.

2.4.9 Summary

A review of the literature has shown the great range and depth of work which has been undertaken, particularly in recent years, studying the flocculation process. Understanding and modelling of the flocculation process has improved, from when Schmoluchowski developed his original description of the process in 1917, and includes such significant work as that of Camp and Stein (1945) on the development of the velocity gradient, Camp's development of the concept of the *G.t* value (Camp number) and Ives's consideration and refinement of it (1968). Subsequent years have seen further workers involved in further refinement of our understanding of flocculation (*e.g.* O'Melia, 1972), with the latest model being offered by Lawler and Nason (2004).

In parallel with the above work, several workers have spent considerable time investigating the strength of specific floc suspensions, grown and broken in particular circumstances. Considering the issue from a theoretical perspective, workers have expressed floc strength in terms of the hydrodynamic force required to break a floc and have related that to the turbulence dissipation rate (Yeung and Pelton, 1996). However, the situation remains that there exists no established floc strength test, although many different tests have been adopted by workers at both the macroscopic and microscopic levels (*e.g.* Francois, 1987, Fitzpatrick *et al.*, 2003, Leentvaar & Rebhun, 1983, Bache *et al.*, 1999, Yeung and Pelton, 1996, Zhang *et al.*, 1999). Using one of several forms of jar tester, many workers have chosen to consider the relationship between the maximum or mean floc size developed under certain shear conditions (where shear is measured simply in terms of mixing speed), with the vessel average velocity gradient for that mixing speed. Whilst the results may be of interest, they will be only applicable to that specific scenario and it would be unwise to extend the results of one floc growth

/ breakage simulation to another as power draw will vary depending on impeller, mixing speed and vessel used. Consequently, in the absence of a specific floc strength test, carried out under prescribed conditions, there will remain an issue associated with the interpretation of results and, in particular, comparison of one set data set with another.

2.5 Computational Fluid Dynamics

2.5.1 General Description & History

It is from the Navier Stokes equations (discussed in Section 2.1.1 above) that the velocity and pressure distribution of fluid flow around the object are derived. The pressure at any one specific point is a function of the flow at many other points, and consequently solutions of the Navier Stokes equations must be obtained at many points simultaneously. Computational Fluid Dynamics (CFD) involves the solution of these equations for any point in space adjacent to an object.

Consequently CFD may be described as the computer-based simulation of systems involving fluid flow and heat transfer, solving the fundamental, non-linear equations of fluid flow (*i.e.* the Navier-Stokes equations coupled with appropriate turbulence transport equations). This powerful technique has found applications within many different industries, including aerodynamics, hydrodynamics, chemical process engineering, meteorology, biomedical engineering and the internal and external environments of buildings.

CFD codes are based around numerical algorithms which solve the equations describing the flow, and commercially available packages are able to simulate steady-state, time-dependent, laminar or turbulent flows, multiple phases (e.g. solid, liquid and gas), as well as concurrent transport processes such as heat transfer, mass transfer or chemical reaction which interact with the flow. The strategy underpinning the CFD process is the replacement of the continuous problem domain with a discrete domain using a grid. In the continuous domain, each flow variable is defined at every point in the domain.

However, in the discrete domain, each flow variable is defined only at the grid points. Consequently, unlike a theoretical solution which is valid at every point in the flow field, in a CFD solution the relevant flow variables are solved only at the grid points. Values at other locations are determined via interpolation.

Anderson (1995) presented the concept that CFD represents the combination of the two traditional approaches to the solution of fluid flow problems; *i.e.* theory and experimentation. The initial approach of researchers interested in the motion of fluids focussed on experimentation alone. The study of theoretical fluid dynamics followed as an understanding of the basic concepts increased. To this end, Anderson argued that whilst forty years ago, one would have adopted a two-phase strategy in pursuit of a solution, thanks to the recent advances in computing power, these two previously independent approaches may now be combined into a single mode of analysis. Anderson presented this concept graphically as shown in Figure 2-13 below.

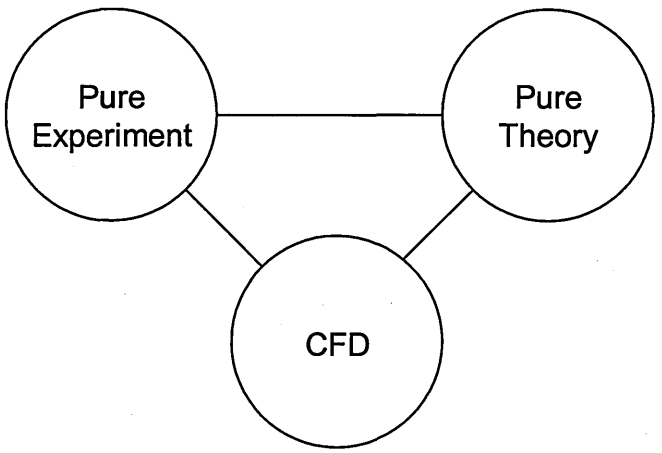


Figure 2-13: The "three dimensions" of fluid dynamics (from Anderson, 1995).

Understanding the hydraulic behaviour of unit processes is a frequent need of the process scientist and engineer. Whilst early applications of CFD focused almost exclusively on simple flow problems within the field of aeronautics, today CFD is routinely used to simulate three dimensional laminar and turbulent flows around complex geometries in almost all engineering applications involving fluid dynamics. In the context of the international water industry, CFD is a tool which, if applied correctly, is capable of facilitating improvements in both hydraulic and process performance for new and existing assets, be they raw water reservoirs, water treatment works,

distribution systems (including treated water storage), collection systems, or sewage treatment works.

CFD can offer the scientist and engineer the information necessary to design, optimise or even retrofit various treatment processes. Consequently, the development of dynamic simulation software for potable water treatment processes which has taken place over the last thirty years, in parallel with significant improvements in computing power, has allowed operators and engineers to benefit from greater insight into the day-to-day operation and potential flexibility of treatment works. Hamill (1998) cited the principal reasons for utilisation of CFD within the water industry and other industries as reduced dependence on expensive model tests and reduced risk in investigating novel designs and technologies. Further advantages include reduced lead-in times and costs for new designs, the ability to examine the behaviour of systems at the limit or beyond design capacity (*i.e.* safety studies), and the ability to study large systems where controlled experiments at full-scale would be difficult, if not impossible, to perform. Andoh (2006) claimed that a CFD model (in this instance simulating stormwater separation) could be built and evaluated within one week, at less than 20% of the cost of a physical prototype model; a cost saving that enabled an optimised design to be offered to the industry at an economical price. Yeung (2001) concluded that CFD offers distinct advantages over physical modelling, not least because CFD removes subjectivities in the interpretation of results.

2.5.2 Generic Methodology

Jones (1999) presented the critical prerequisites for the construction of a CFD model as follows:

- The mathematical equations that describe the flow field are known.
- Discrete approximations of these equations can be formulated that faithfully represent the underlying physical properties.
- A computational grid discretizing the geometrical domain of interest with sufficient spatial resolution can be constructed.

- Iterative numerical methods for solving the discrete equations on this computational mesh can be developed and implemented.

In general terms, the solution of a problem using CFD involves a number of distinct key processes, *viz*;

- Determination of flow field boundaries.
- Mesh construction.
- Application of boundary conditions.
- Resolution of the equations of conservation of mass, momentum and energy in three directions for each cell within the mesh.
- Post processing and analysis of results.

Shaw (1992) presented the flow chart shown at Figure 2-14 to represent the process of conceiving, developing and solving a fluid dynamic problem via the use of CFD techniques. However, this is clearly a gross simplification of the modelling process (*e.g.* it does not consider boundary conditions or turbulence model selection). Successful flow simulation and results derivation involve a wide range of issues including, *inter alia*, grid generation, selection of boundary conditions and governing equations, gridding strategy and numerical methods, turbulence modelling, and interpretation of results (Anderson, 1995, Versteeg & Malalasekera, 1995).

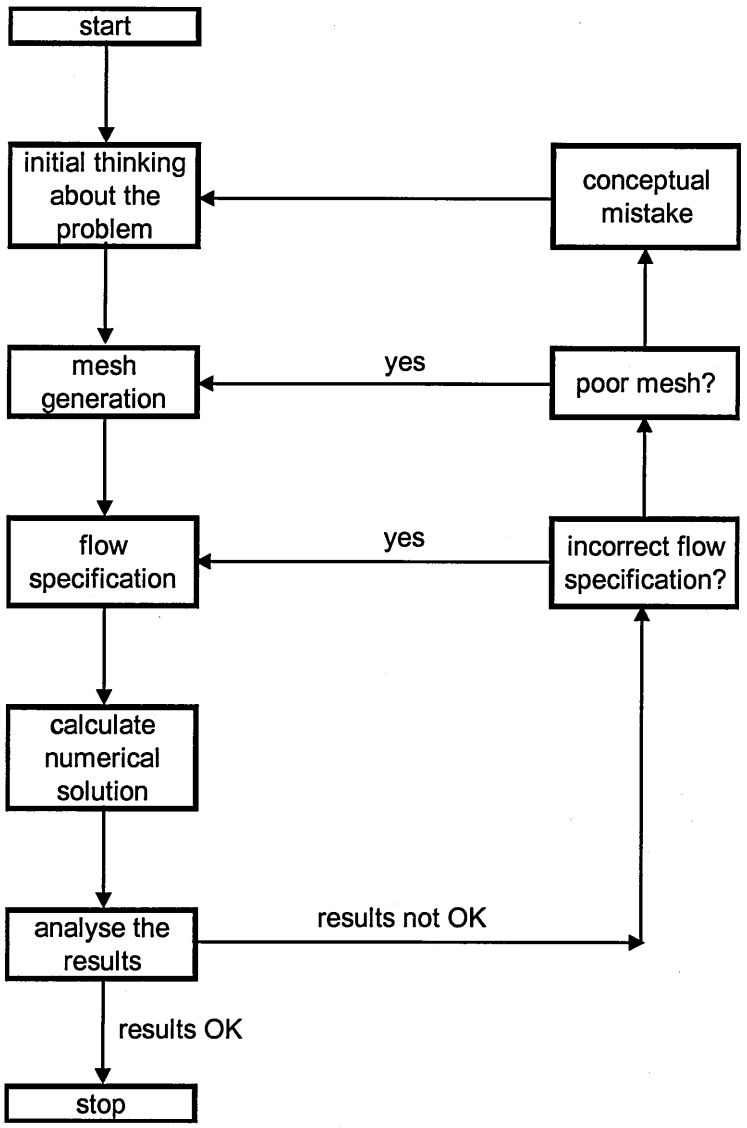


Figure 2-14: **The CFD analysis process (from Shaw 1992).**

2.5.3 Turbulence Modelling

Notwithstanding the major developments which have occurred in computing power over the past quarter of a century, the accurate prediction of complex, three-dimensional turbulent flows still represents a significant challenge to CFD. High Reynolds number flows around complex geometries are all impacted to some degree by increased pressure gradients, three-dimensional separation and vortex formation, large scale unsteady flow, and surface roughness. Analysis is further complicated by the simultaneous occurrence of such phenomena over a wide range of scales from metres (large scale coherent structures) to microns (the smallest, Kolmogorov scales where molecular viscosity acts).

Turbulent flow comprises vortices of varying sizes which form and break down into smaller vortices within the flow. There is a minimum size of a vortex, below which it dissipates viscously into heat. Moin and Kim (1997) suggested that the ratio of the smallest to largest vortex size is calculated by raising the Reynolds number to the power 0.75. The cube of this ratio is then used to provide an indication of the number of grid points required for a numerical simulation of a problem.

It is clear that for many engineering applications, the Reynolds number (*i.e.* the ratio of viscous to inertial forces) will be greater than 2,000, and consequently the flow is classified as either being turbulent, or in the transitional range between laminar and turbulent.

Recalling the unclosed set of equations at Equations 2-7, there are six Reynolds stresses which are introduced by the averaging process. Consequently, there are four equations (*i.e.* continuity and three momentum equations) and ten unknowns (three velocities, six Reynolds stresses and pressure). These stresses need to be expressed in terms of the other variables (mean quantities or derivatives) in order to obtain a closed system of equations, and they are derived via use of a turbulence-closure model. Closure is determined by the identification of solutions to the Reynolds stresses such that the average flow properties are obtained.

2.5.3.1 Two Equation Models

The most straightforward complete turbulence models are the two-equation models where the turbulent velocity and length scales are determined via solution of two separate transport equations; one for turbulent kinetic energy, k, and one for the turbulence length scale or some equivalent parameter, (ϵ, the dissipation of turbulence kinetic energy per unit time, or ω, the rate at which turbulent energy is dissipated). These equations account for the production, diffusion and destruction of turbulence within the flow field. The principal assumptions for these models are that the flow

does not depart far from local equilibrium, and that the Reynolds number is high enough to ensure that local isotropy is satisfied.

There are four principal turbulence models which are generally packaged with commercially available CFD packages. Specifically, these are the standard k-ϵ model, the low Reynolds number k-ϵ model (LRN k-ϵ), the renormalized group k-ϵ model (RNG k-ϵ), and the Reynolds stress model (RSM). (In addition, the Fluent code, which is used in the CFD work reported in this thesis, provides the Spalart-Allmaras model, the realizable k-ϵ model, the standard k-ω model, the shear-stress transport (SST) k-ω model, and the Large Eddy Simulation model). This most common class of models (*i.e.* the two-equation turbulence models) is based on the eddy viscosity concept of Boussinesq

2.5.3.1.1 The Boussinesq Hypothesis

The Boussinesq hypothesis is founded on the assumption that the Reynolds stresses are linearly dependent on the mean velocity gradient, with the constant of proportionality being the turbulent or eddy viscosity (*i.e.* the turbulent viscosity is an isotropic scalar). (Rodi, 1993).

Closure models that employ the Boussinesq assumption (known as isotropic eddy-viscosity models) are widely used in complex engineering calculations due to their relative simplicity and computational expedience. This eddy-viscosity model states that the Reynolds stresses are related to the local shear via eddy viscosity, ν_t, in the following manner (Rodi, 1993):

$$-\overline{u_i u_j} = \nu_t \left(\frac{\partial U_i}{\partial x_j} + \frac{\partial U_j}{\partial x_i} \right) - \frac{2}{3} k \delta_{ij} = 2\nu_t s_{ij} - \frac{2}{3} k \delta_{ij} \qquad \textbf{Equation 2-39}$$

The turbulent eddy viscosity, ν_t, is defined in terms of the turbulent kinetic energy, k, and the rate of dissipation of turbulent energy per unit mass, ϵ, according to:

$$k\text{-}\epsilon \text{ model:} \qquad \nu_t = C_\mu \frac{k^2}{\varepsilon} \qquad \textbf{Equation 2-40}$$

$$k\text{-}\omega \text{ model} \qquad \nu_t = C_\mu \frac{k}{\omega} \qquad \textbf{Equation 2-41}$$

$$k = \frac{u_i u_j}{2} \text{ and } \varepsilon = \nu \frac{\partial U_i}{\partial x_j}\left(\frac{\partial U_i}{\partial x_j} + \frac{\partial U_j}{\partial x_i}\right) \qquad \textbf{Equation 2-42}$$

δ_{ij} represents the Kronecker delta and is defined as:

$$\delta_{ij} = \begin{cases} 1 & i = j \\ 0 & i \neq j \end{cases}$$

A detailed discussion of the terms in the k-ϵ models can be found in Launder and Spalding (1974). The different forms of two equation models are discussed below.

2.5.3.1.2 Standard k-ϵ Model

The standard k-ϵ model is a robust, computationally stable model which has found applications in a wide variety of scenarios. This model was developed by Launder and Spalding (1974) and it is clear from the literature that, historically, this has been the model of choice for the majority of workers in this field.

Equations for k and ϵ are given below.

$$\frac{\partial}{\partial t}(\rho k) + \frac{\partial}{\partial x_i}(\rho k u_i) = \frac{\partial}{\partial x_j}\left[\left(\mu + \frac{\mu_t}{\sigma_k}\right)\frac{\partial k}{\partial x_j}\right] + G_k - \rho\varepsilon \qquad \textbf{Equation 2-43}$$

$$\frac{\partial}{\partial t}(\rho \varepsilon) + \frac{\partial}{\partial x_i}(\rho \varepsilon u_i) = \frac{\partial}{\partial x_j}\left[\left(\mu + \frac{\mu_t}{\sigma_\varepsilon}\right)\frac{\partial \varepsilon}{\partial x_j}\right] + C_1 \frac{\varepsilon}{k} G_k - C_2 \rho \frac{\varepsilon^2}{k} \qquad \textbf{Equation 2-44}$$

The turbulent viscosity, μ_t, is calculated according to

$$\mu_t = \rho C_\mu \frac{k^2}{\varepsilon} \qquad \textbf{Equation 2-45}$$

and the generation of turbulence kinetic energy due to mean velocity gradients, G_k, is calculated according to

$$G_k = \mu_t \left(\frac{\partial u_i}{\partial x_j} + \frac{\partial u_j}{\partial x_i}\right)\frac{\partial u_j}{\partial x_i} \qquad \textbf{Equation 2-46}$$

The empirical model constant values are generally accepted as $C_\mu = 0.09$, $C_1 = 1.44$, $C_2 = 1.92$, $\sigma_k = 1.0$ and $\sigma_\epsilon = 1.3$.

The solution process for k-ϵ models is summarised by Marshall and Bakker (2004) as:

i. Transport equations are solved for turbulence energy (k) and turbulence dissipation rate (ϵ).

ii. Solutions for k and ϵ are used to compute the turbulent viscosity, μ_t.

iii. Reynolds stresses are computed using μ_t and k, and are substituted into the momentum equations.

The derivations of the above equations are predicated on the assumption that the flow is turbulent. Hence, the standard k-ϵ model should only be used for fully turbulent flows. Whilst it is clear that the standard k-ϵ model has been extremely popular over the years, it is interesting to note that Marshall and Bakker (2004) and Fluent (2005) do not recommend its use in highly swirling flows. The standard k-ϵ model is also an inappropriate choice for flows which exhibit rapid changes in strain rate or significant streamline curvature.

2.5.3.1.3 Renormalized Group (RNG) k-ϵ Model

The RNG k-ϵ model develops a more general model of turbulence, applying statistical methods used in renormalization group theory to resolve the smallest eddies in the inertial range. Having resolved these small-scale eddies, a band of the smallest eddies is eliminated by representing them in terms of the next smallest eddies. Bands of the smallest eddies are successively removed until a modified set of the momentum equations is obtained, which is then solved using a relatively coarse grid.

$$\frac{\partial}{\partial t}(\rho k) + \frac{\partial}{\partial x_i}(\rho k u_i) = \frac{\partial}{\partial x_j}\left[(\alpha_k \mu_{eff})\frac{\partial k}{\partial x_j}\right] + G_k - \rho\varepsilon \qquad \textbf{Equation 2-47}$$

$$\frac{\partial}{\partial t}(\rho \varepsilon) + \frac{\partial}{\partial x_i}(\rho \varepsilon u_i) = \frac{\partial}{\partial x_j}\left[(\alpha_\varepsilon \mu_{eff})\frac{\partial \varepsilon}{\partial x_j}\right] + C_{1\varepsilon}\frac{\varepsilon}{k}G_k - C_2\rho\frac{\varepsilon^2}{k} - R_\varepsilon \qquad \textbf{Equation 2-48}$$

α_k and α_ε are the inverse effective Prandtl numbers for k and ϵ, respectively.

Marshall and Bakker (2004) report that the RNG k-ϵ model has greater success that the standard k-ϵ model at modelling swirling flows and flow separation. However, the RNG k-ϵ model is not well suited to round jets and is less stable than the standard k-ϵ version.

2.5.3.1.4 Realizable k-ϵ Model

The Realizable k-ϵ model is a further, more recent variation on the standard k-ϵ model. This model, developed by Shih (1995) recognises the fact that in highly strained flows, some of the normal Reynolds stresses (*i.e.* u_i^2) can become negative, which is clearly unphysical (or unrealizable). To overcome this effect, the realizable k-ϵ model calculates the turbulent viscosity according to Equation 2-45, but employs a varying value for C_μ. C_μ is calculated as a function of the local strain rate and the rotation of the fluid. Full details are to be found in Fluent (2005). The realizable k-ϵ model also employs alternative source and sink terms for eddy dissipation, causing this model to yield more accurate results for flows generated by a rotating impeller blade. Unlike the RNG k-ϵ model, the realizable k-ϵ model is suited to round jets, as well as swirling flows and flows where separation occurs.

$$\frac{\partial}{\partial t}(\rho k) + \frac{\partial}{\partial x_j}(\rho k u_j) = \frac{\partial}{\partial x_j}\left[\left(\mu + \frac{\mu_t}{\sigma_k}\right)\frac{\partial k}{\partial x_j}\right] + G_k - \rho\varepsilon + S_k \quad \textbf{Equation 2-49}$$

$$\frac{\partial}{\partial t}(\rho \varepsilon) + \frac{\partial}{\partial x_j}(\rho \varepsilon u_j) = \frac{\partial}{\partial x_j}\left[\left(\mu + \frac{\mu_t}{\sigma_\varepsilon}\right)\frac{\partial \varepsilon}{\partial x_j}\right] + \rho C_1 S_\varepsilon - \rho C_2 \frac{\varepsilon^2}{k + \sqrt{\nu\varepsilon}} + C_{1\varepsilon}\frac{\varepsilon}{k} C_3 G_b + S_\varepsilon$$

Equation 2-50

C_2 is a constant. σ_k and σ_ϵ are the turbulent Prandtl numbers for k and ϵ, respectively. S_k and S_ϵ are user-defined source terms. The empirical model constant values are generally accepted as $C_{1\epsilon} = 1.44$, $C_1 = \max\left[0.43, \frac{\eta}{\eta+5}\right]$, $C_2 = 1.9$, $\sigma_k = 1.0$ and $\sigma_\epsilon = 1.2$.

2.5.3.1.5 *k*-ω Model

The standard *k*-ω model is an empirical model based on model transport equations for the turbulence kinetic energy (*k*) and the specific dissipation rate (ω), where $\omega = \frac{\varepsilon}{k}$.

Whilst the *k*-ϵ model solves for the dissipation of turbulent kinetic energy, the *k*-ω model solves for the rate at which the dissipation occurs. An alternative interpretation is the inverse of the time scale on which dissipation takes place, which is set by the largest eddies.

The *k*-ω model resolves the details of the near-wall flow without reliance on the wall-function approach utilised in most commercial CFD packages. Whilst the *k*-ϵ models are valid for turbulent flows away from the walls, the *k*-ω model is designed to be applied throughout the boundary layer, subject to sufficiently fine grid resolution.
Equations for *k* and ω are given below.

$$\frac{\partial}{\partial t}(\rho k) + \frac{\partial}{\partial x_i}(\rho k u_i) = \frac{\partial}{\partial x_j}\left[\Gamma_k \frac{\partial k}{\partial x_j}\right] + G_k - Y_k + S_k \qquad \textbf{Equation 2-51}$$

$$\frac{\partial}{\partial t}(\rho \omega) + \frac{\partial}{\partial x_i}(\rho \omega u_i) = \frac{\partial}{\partial x_j}\left[\Gamma_\omega \frac{\partial \omega}{\partial x_j}\right] + G_\omega - Y_\omega + S_\omega \qquad \textbf{Equation 2-52}$$

Γ_k and Γ_ω represent the effective diffusivity of *k* and ω respectively and

$$\Gamma_k = \mu + \frac{\mu_t}{\sigma_k} \qquad \textbf{Equation 2-53}$$

and

$$\Gamma_\omega = \mu + \frac{\mu_t}{\sigma_\omega} \qquad \textbf{Equation 2-54}$$

G_k represents the generation of turbulence kinetic energy due to mean velocity gradients. G_ω represents the generation of ω. Y_k and Y_ω represent the dissipation of *k* and ω due to turbulence. S_k *and* S_ϵ are user-defined source terms.

2.5.3.1.6 SST k-ω Model

A variation on the standard *k*-ω model is the shear-stress transport (SST) *k*-ω model. Here, the definition of the turbulent viscosity is modified to account for the transport of the principal turbulent shear stress, so offering advantages over both the standard *k*-ω model and the standard *k*-ϵ model. Other modifications include the addition of a cross-diffusion term in the ω equation and a blending function to ensure that the model equations behave appropriately in both the near-wall and far-field zones.
Equations for *k* and ω are given below.

$$\frac{\partial}{\partial t}(\rho k)+\frac{\partial}{\partial x_i}(\rho k u_i)=\frac{\partial}{\partial x_j}\left[\Gamma_k \frac{\partial k}{\partial x_j}\right]+G_k-Y_k+S_k \qquad \textbf{Equation 2-55}$$

$$\frac{\partial}{\partial t}(\rho \omega)+\frac{\partial}{\partial x_i}(\rho \omega u_i)=\frac{\partial}{\partial x_j}\left[\Gamma_\varpi \frac{\partial \omega}{\partial x_j}\right]+G_\omega-Y_\omega+D_\omega+S_\omega \qquad \textbf{Equation 2-56}$$

The equations are the same as for the standard *k*-ω model, with the exception of the additional term, D_ω, in the equation for ω (D_ω represents the cross-diffusion term) and the different treatment of turbulent viscosity, μ_t.

2.5.3.2 Reynolds Stress Model

Whilst the two-equation eddy viscosity models are based on the assumption of isotropic turbulent viscosity and, in the case of the standard *k*-ϵ model, assign just one value to this parameter, the Reynolds Stress model avoids the isotropic eddy assumption and computes each of the individual stresses, $\overline{u_i\, u_j}$, individually using differential transport equations. The Reynolds stresses are then used to obtain closure of the Reynolds averaged momentum equations. Thus, this more robust solution process is better able to account for the effects of streamline curvature and highly swirling flows (and the body forces so induced), such as might be found in an unbaffled stirred tank. In physical terms this is the most comprehensive model as there is an exact transport equation for each Reynolds stress. Consequently, there are an additional six transport equations to

be solved (plus an equation for the dissipation rate) with a consequential increase in computational effort and time.

Considering an incompressible flow without body forces and ignoring transport due to rotation, the exact equation for the transport of the Reynolds stresses ($=\rho\overline{u_i\,u_j}$) is (Versteeg & Malalasekera, 1995, Fluent, 2005)

$$\frac{\partial}{\partial t}(\rho\overline{u_i'u_j'}) + \frac{\partial}{\partial x_k}(\rho u_k\overline{u_i'u_j'}) = -\frac{\partial}{\partial x_k}\left[\rho\overline{u_i'u_j'u_k'} + \overline{p(\delta_{kj}u_i' + \delta_{ik}u_j')}\right] + \frac{\partial}{\partial x_k}\left[\mu\frac{\partial}{\partial x_k}(\overline{u_i'u_j'})\right]$$

local time derivative ***convection*** ***turbulent diffusion*** ***molecular diffusion***

$$-\left(\rho\overline{u_i'u_k'}\frac{\partial u_j}{\partial x_k} + \rho\overline{u_j'u_k'}\frac{\partial u_i}{\partial x_k}\right) + \overline{p\left(\frac{\partial u_i'}{\partial x_j} + \frac{\partial u_j'}{\partial x_i}\right)} - 2\mu\left(\frac{\partial u_i'}{\partial x_k}\frac{\partial u_j'}{\partial x_k}\right)$$

stress production ***pressure strain*** ***dissipation***

The close coupling of the equations generates less stability in the convergence process and therefore convergence is generally harder to obtain than with the standard k-ϵ model. It is estimated that the computational effort required to obtain a solution using this model is between 50 and 60% greater than that required by the standard k-ϵ model. However, this additional effort may be offset against the greater accuracy of solution obtained.

2.5.3.3 Turbulence Model Selection

Each of the available closure models offers advantages and disadvantages over the others in certain applications, and it is a fact that no single turbulence model can be judged to be the optimum model in all circumstances. Consequently, it is necessary to evaluate each circumstance individually and form a view as to which model would provide the best fit for the flow under examination. Factors to consider in this analysis include, *inter alia*, the physics encompassed in the flow, the established practice for a specific class of problem, the level of accuracy required, the available computational resources, and the amount of time available for the simulation.

Morrison (1999), citing Hope (1996), gave the general purpose applications of these models as shown in Table 2-4 below.

Table 2-4: Turbulence model applications (from Morrison 1999).

Model Classification	Application
Standard k-ϵ model	Flows just above transition
Low Reynolds number k-ϵ model	Relatively shallow recirculating flows
Renormalized group k-ϵ model	Flows with high Reynolds number
Reynolds stress model	Anisotropic turbulence problems

Table 2-5 below summarises the key features of each classification of model.

Table 2-5: Comparison of available turbulence models (from Versteeg & Malalasekera, 1995, Marshall & Bakker, 2004, Fluent, 2005, & Menter, 2003).

Model	Advantages	Disadvantages
Standard k-ϵ	• Simplest model. • Excellent performance for many flows. • Well established.	• Poor performance in some scenarios (*i.e.* rotating flows, flow separation, adverse pressure gradients). • Assumes isotropy in turbulence. • Poor prediction of lateral expansion in 3-d wall jets.
RNG k-ϵ	• Improved performance for swirling flow compared to the standard *k-ϵ* model.	• Less stable than the standard *k-ϵ* model.
Realizable k-ϵ	• Suited to round jets, as well as swirling flows and flows where separation occurs.	• Not recommended for use with multiple reference frames.
Standard k-ω	• Valid throughout the boundary layer, subject to sufficiently fine grid resolution.	• Separation is typically predicted to be excessive and early.
SST k-ω	• Suitable for adverse pressure gradients and pressure-induced separation. • Accounts for the transport of the principal turbulent shear stress.	• Less suitable for free shear flows.
Reynolds Stress Model	• The most general of all models. • Accurate calculation of mean flow properties and all Reynolds stresses. • Yields superior results to *k-ϵ* models for flows with stagnation points.	• Computationally expensive. • Not always more accurate than two-equation models. • Harder to obtain converged result.

2.5.3.4 Applications of Turbulence Models to Mixing Scenarios

Armenante *et al.* (1997) examined the velocity and turbulent kinetic energy profiles generated by a six blade pitched blade turbine in a closed, unbaffled stirred tank reactor. The mean and fluctuating velocities were measured using Laser Doppler Velocimetry (LDV) at 100 separate locations and were then compared with numerical data produced via a Fluent simulation. The authors used the standard k-ϵ and Reynolds Stress models to simulate turbulence (Reynolds numbers of 7.1×10^4 and 11.1×10^4 were simulated). The authors reported that numerical predictions were generally in substantial agreement with the experimental data, but that the RSM always yielded superior results than the k-ϵ model for both velocity and turbulent kinetic energy. Armenante *et al.* (1997) attributed these differences to the isotropy assumption inherent in the standard k-ϵ model.

Jaworski and Zakrzewska (2002) used the Fluent software to investigate the impacts of different turbulence models on the modelled flow characteristics of a baffled, cylindrical stirred tank with the contents mixed with a pitched blade turbine. Using standard wall functions, the authors assessed the standard, LRN, RNG and Reynolds Stress models and compared the results with Laser Doppler Anemometry (LDA) experimental data. Somewhat surprisingly, Jaworski and Zakrzewska concluded that, for the tank configuration and pitched blade turbine impeller considered, the closest agreement between modelling predictions and experiments for the axial mean velocity was obtained using the standard k-ϵ model. The authors also found that the widest discrepancy was obtained using the realizable k-ϵ model, and their overall conclusion was that the standard k-ϵ model led to high accuracy predictions, and the other models, with the exception of the realizable model, generated a "fair" degree of accuracy. It is unfortunate that Jaworski and Zakrzewska did not state what their definition of "fair" was; however, analysing the data within the paper, it can be inferred that the difference between the two sets of results was approximately 100% of the lower (more accurate) results. It is interesting to note that Jaworski and Zakrzewska found little difference between modelled and experimental results for the tangential velocity for all turbulence models. Finally, the authors demonstrated that turbulent kinetic energy was under-

predicted by all four models, although, once more the standard k-ϵ model yielded the most accurate results. These are most interesting results as they would appear to contradict directly conclusions and recommendations of other authors (Marshall and Bakker, 2004, Fluent, 2005) who suggest that the standard k-ϵ model is not recommended for highly swirling flows such as might be found in a stirred tank reactor.

It is clear from the foregoing that the selection of turbulence model is not a straightforward one. The modeller must take into account, *inter alia*, the flow field which is likely to be generated, the Reynolds number and computational expense. Menter (2003) correctly suggested that one should resist the temptation to claim that one model is superior to another, as the robustness of a turbulence model is undoubtedly a function of the code being used and the scenario being modelled.

2.5.3.5 Direct Numerical Simulation / Large Eddy (Vortex) Simulation

Two additional numerical procedures which involve the use of the time dependent Navier-Stokes equations to facilitate the resolution of turbulent flow data information are the Direct Numerical Simulation (DNS) and the Large Eddy Simulation (LES) methods.

2.5.3.5.1 Direct Numerical Simulation (DNS)

Offering numerically accurate solutions, the DNS method is, in principal, the mathematically correct solution to a turbulent flow problem. The Navier-Stokes equations are numerically integrated, resolving all spatial and temporal fluctuations without the need for modelling. However, in application, the method necessitates grid construction in proportion with the Reynolds number and hence the smallest eddy length scale of the flow. The Kolmogorov turbulence length scale can yield a ratio of 1:10,000 between the smallest grid cell in the computational domain and the boundary layer thickness. This issue is further compounded by the need to select a time step such that the smallest time scale of the eddies might be resolved. Consequently, the DNS

method requires a computationally intensive (and hence timely and expensive) approach. To place this into context, Kaneda *et al.* (2003) published the largest DNS to date, using a $4{,}096^3$ grid. This approach demanded approximately 0.5 terabytes of memory per variable. As such, the DNS approach currently finds applications only in low Reynolds number flows around simple geometries and is not appropriate for the work undertaken here.

2.5.3.5.2 Large Eddy Simulation (LES)

The LES method balances mathematical accuracy with computational effort and so is a more practical alternative to the simulation of turbulent flows. This method provides a solution for just the largest length scale of the eddies. The remaining, sub-grid scale eddies are modelled in such a way as to have no consequential impact on the final results. The clear advantage of the LES method over the DNS is the reduction in resolution of the computational domain required to obtain a sufficiently accurate solution.

However, both the DNS and LES approach place enormous additional computational requirements on a process which is already computationally intensive (and expensive). Because of this, the most common form of dealing with turbulent flow predictions is to solve the RANS equations using the turbulence models discussed earlier. Wilcox (1998) and Marshall and Bakker (2004) provide commentaries on turbulence modelling for the interested reader.

2.5.4 Discretisation

The differential equations described above are all intractable except for very simplified flows (*e.g.* flow between parallel plates and flow in a circular pipe). Consequently, numerical methods are required to calculate particular solutions for a specific set of boundary conditions. The equations are "discretised", such that they are expressed in algebraic, rather than differential, terms. Using the computational grid (or mesh),

discrete equations are formed by integrating the governing equations over the surface area and volume of each cell, so generating discrete equations which conserve quantity on a control-volume basis.

Field variables, which are stored at cell centres, must be interpolated to the faces of the control volumes, and a number of interpolation schemes are available within commercially-available CFD packages.

For diffusion terms, linear interpolation between cell centres (*i.e.* central differencing) is used to obtain boundary values. However, use of central differencing for convection terms yields instability due to its inherently one-way effect (*i.e.* in a convection-dominated flow, values at a specific point are dependent on corresponding upstream, not downstream values). Central differencing places an unphysical dependence on downstream effects, giving rise to instability. Fluent (the CFD package used in this research) offers four alternatives for calculating convective fluxes, as shown in Table 2-6 below.

Table 2-6: Interpolation Schemes for convective fluxes available in Fluent (from Fluent, 2005).

Interpolation Scheme	Comments
First-Order Upwind	• Easiest to converge. • Only first-order accurate. • Can lead to numerical diffusion where flow not aligned with grid (can flatten velocity profiles and reduce turbulence generation).
Power Law	• More accurate than first order for low Reynolds number flows.
Second-Order Upwind	• Uses larger stencil for second-order accuracy. • Essential with triangular / tetrahedral mesh. • Essential when flow not aligned with grid. • Slower to converge than above.
Quadratic Upwind Interpolation (QUICK)	• Applies to quad / hex mesh. • Useful for rotating / swirling flows. • Third-order accurate on uniform mesh. • Increased computational cost.

2.5.5 Multiphase Modelling

Multiple phase systems comprising liquid and solid phases are very common in both the process and water industries. Current CFD applications are free surface and two phase (water / air, water / solid) calculations. The free surface application is used for instances of hydraulic jump (standing wave) or flow over a weir. Water / solid calculations may be undertaken to model particulate motion, including sedimentation and particle deposition. Other examples include mixing tanks where the desired result is to generate a fluid flow pattern that produces a state of complete solids suspension, where all of the solid particles are in motion. The fluid flow pattern in a mixing tank is a function of the design of impellers used in the tank, together with baffle arrangement and tank size and configuration. Finally, water / air calculations can be used to study dissolved air flotation (DAF) and aeration.

With the addition of fluid and solid phases, there is a requirement for additional models to describe phase interactions, momentum transfer (via drag), heat exchange, mass transfer and chemical reaction between the phases. In general there are two modelling approaches for multiphase flows; *viz.* the Eulerian multiphase model and the Lagrangian particle model.

In the Eulerian multiphase model, the fluid phases are treated as continuous fluids coexisting in the flow. The fluid is represented by the primary phase, and all secondary phases are solids. The equations of conservation of mass, momentum and energy are solved for each fluid phase together with the inter-phase transfer models. From the computation, one can derive a spatial distribution of the phases, velocities and temperatures.

Whilst the Eulerian multiphase model considers a whole collection of particles (or bubbles) as a dispersed phase and treating it as a continuous fluid, the Lagrangian particle model considers each particle individually. The equations of motion are solved for each particle to obtain its trajectory in space and time. Equations for temperature and species concentration can be added to model heat and mass transfers between the

particles and the surrounding fluid. The Lagrangian particle model therefore provides very detailed information regarding the particles, their position (in both space and time), trajectories, temperature and species concentration. This detailed information is ideal for modelling, *inter alia*, bubble paths within DAF plants and particle trajectories in sedimentation tanks.

To exemplify the differences between the two modelling approaches, Rogers (1978) rather prosaically, but effectively, stated "In the Eulerian system we can think of ourselves as standing on the bank of a river and watching it flow past; in the Lagrangian system we are in a boat drifting with the river."

2.5.6 Commercial CFD Software Packages

Over the past 30 years, many commercial CFD packages have been launched into the market place, attracting interest from universities, research establishments and, more recently, industrial organisations for use as a design tool. Published comparisons of the more commonly available packages are few; indeed just two have been found (Freitas, 1995, and Iaccarino, 2000). Freitas examined a series of five benchmark tests using different codes, of which three involved laminar flow, the other two being turbulent in nature. Freitas (1995) found several anomalies and uncertainties, specifically relating to the development of the initial computational grid, the definition and treatment of boundary conditions, convergence, and the numerical simulation of the scheme chosen. This led Freitas to conclude that it was not possible to draw specific conclusions from the comparison and that further research into more advanced turbulence models for use in commercial CFD codes is required.

Iaccarino (2000) compared the use and performance of CFX, Fluent and Star-CD when applied to the problem of a turbulent separated flow. In doing so, Iaccarino (2000) attempted to address and, where possible, eliminate, the issues raised by Freitas (1995). Iaccarino (2000) undertook a two-dimensional flow field analysis in a diffuser which exhibited flow separation. Iaccarino elected to use a low Reynolds number (LRN) version of the standard k-ϵ turbulence model (available as a standard option in all codes)

as well as the less well-known v^2–f model of Durbin (1995) (implemented via the use of user-defined subroutines in each of the codes). The author did not state the Reynolds number of the scenario modelled. The same grid and spatial discretization were used for all simulations. Iaccarino (2000) reported that all codes converged to steady state in the same number of iterations, irrespective of turbulence model. The v^2–f model produced accurate results (compared to experimentally-derived data). However, the LRN k-ϵ model did not represent the experimental data well. The flow developed by the LRN k-ϵ model was not separated, leading to severe under-prediction of the maximum velocity in the diffuser. The results of the v^2–f model were consistent, irrespective of the code used. The differences between the LRN k-ϵ model were more significant and could not be reproduced across codes. As the v^2–f model had been specifically defined for this analysis whereas the standard LRN k-ϵ models found in the codes had been used, Iaccarino concluded that these discrepancies were less due to the codes' numerical procedures, but rather the definition of the turbulence model itself. Iaccarino concluded that the basic numerical techniques used in the three codes are reliable and deliver the expected accuracy and convergence characteristics. However, Iaccarino was also able to conclude that turbulence model selection is crucial for simulation success.

2.5.7 Use of CFD to Simulate Mixing Processes

Ducoste and Clark (1999) used the commercially-available code, FIDAP, to study the flow fields generated within five litre and 28 litre reactors by two different impellers (a Ruston turbine and an A310 fluid foil impeller). The analysis utilised the standard k-ϵ turbulence model using results from experimental studies to establish the impeller boundary conditions. Others (*e.g.* Korpijarvi *et al.*, 1999 & 2000 and Essemiani and de Traversay, 2002 a & b) avoided this via the use of the multiple rotating frames and sliding mesh techniques, discussed in Chapter 5 below. Ducoste and Clark concentrated their analysis on the turbulence energy dissipation, ϵ. FIDAP was unable to predict accurately ϵ produced by the Rushton turbine, and the authors suggested that this might be due to the existence of vortices trailing the impeller blades, and that the experimental data might have lacked the necessary accuracy. Despite these issues, Ducoste and Clark

concluded that maintaining constant unit mass energy dissipation does not necessarily ensure the same turbulence characteristics in different scale systems or in the same scale systems with different geometries.

Jaworski and Pianko-Oprych (2002) modelled laminar two-phase (liquid-liquid) flows through a static mixer, using both the Eulerian and Lagrangian approaches. The authors concluded that the two techniques yielded different information regarding the mixer, all of which was relevant to future design and development needs. However, the authors also found that mesh density was far more important for the Lagrangian analysis than for the Eulerian analysis, although they accepted that the density was relatively coarse and so this was to be expected. Limitations on the grid density meant that the authors could develop only qualitative conclusions regarding particle tracks and residence times from the Lagrangian analysis. This is disappointing since, as the authors state themselves, "knowledge of these distributions is essential in optimizing the process conditions of static mixers". The authors concluded that further work on grid refinement was necessary. Whilst these results are interesting, it must be borne in mind that the simulations were of laminar flows, and so flows which are not generally found in water treatment applications.

Ng *et al.* (1999) used the STAR-CD software to model the flow field generated by a Rushton turbine in a small (100 mm diameter) cylindrical baffled vessel. Using the standard k-ϵ turbulence model, logarithmic wall functions and the sliding mesh solution technique (discussed in Chapter 5), the stirred reactor was modelled at an impeller speed of 2,165 rpm (corresponding to a Reynolds number of 40,000). In their analysis, Ng *et al.* paid specific attention to the distribution of the rate of dissipation of turbulence energy, ϵ, throughout the vessel. The authors calculated volume-weighted averages of ϵ for various different regions within the vessel, and compared these with published data which had been measured (either directly or indirectly) or simulated numerically. Interestingly, the CFD and direct measurement data showed a substantial amount of energy being dissipated within the bulk of the flow and near the walls and baffles (50% close to the vessel wall and 31% in the impeller stream). This is an important conclusion for all mixing processes, as it implies that despite high turbulence dissipation

rate values occurring near the impeller, a substantial proportion of the energy input is not dissipated near the impeller and so may not be utilised most effectively for mixing. The authors did, however, recognise that use of the k-ϵ model in all regions of the flow might not be appropriate due to the presence of strong streamline curvature and the acknowledged limitations of this turbulence model in such regions. The authors also questioned the validity of the wall functions used. It is, therefore, unfortunate that the authors did not test the sensitivity of either different turbulence models or wall functions. The authors did test the sensitivity of mesh refinement, concluding that little improvement was to be gained in the results for turbulent kinetic energy from improving the mesh from 46,000 to 240,000 cells.

Daskopoulos and Harris (1996) presented a useful review of modelling techniques and software available to simulate turbulent flow in baffled stirred tank reactors. The authors considered two separate scenarios (a Rushton turbine and a pitched blade impeller) and solved the flow fields using three different techniques; *viz.* using impeller boundary conditions, the multiple reference frames, and the sliding mesh method. (These techniques are discussed in Chapter 5). Daskopoulos and Harris found that CFD predicted the qualitative features the flow and demonstrated moderate success in qualitative prediction of the mean flow. However, the CFD models were found to under-predict turbulence properties of the flow by up to one order of magnitude, particularly at locations distant from the impeller. Daskopoulos and Harris also considered the computational expense of the sliding mesh and MRF models. At between twenty and fifty hours, the Fluent sliding mesh method was the most computationally demanding by a factor of four. (These times were incurred solving meshes of sizes from 20 x 20 x 23 (9,200 cells) to 38 x 38 x 44 (63,536 cells)). Daskopoulos and Harris commented that it is only with the advent of parallel computing methods that large models of several million cells can realistically be solved.

2.6 Use of CFD in the Water Industry

The use of CFD, whilst traditionally strong and widespread in the chemical, mechanical and manufacturing industries, has only recently begun to be exploited within the water industry. However, interest and experience in this field are both growing apace, and CFD has now been successfully used in water and sewage treatment and sewerage applications, both in the UK and abroad. Examples of such are described and discussed below, with emphasis placed on water treatment applications.

2.6.1 Sewerage

The principal area of application of CFD within the sewerage arena has been the study of flows upstream of, and within, combined sewer overflows and storage chambers. Stovin has published a series of publications which describe the use of the Fluent CFD code to model sedimentation and hence chamber efficiency via two methods (i) an assessment of the critical shear stress and (ii) particle tracking (Stovin & Saul, 1996, Stovin & Saul, 1998, Stovin *et al.*, 1999, Stovin *et al.*, 2002). Within these papers, the authors developed a 31,488 cell grid of a chamber and employed the standard k-ϵ turbulence closure model. Comparison between experimental and numerical longitudinal and transverse velocity components at a specified depth showed good agreement between the two sets of data, demonstrating that CFD could be used to describe accurately the flow field within a storage chamber. Particle tracking was undertaken using the built-in Discrete Phase Model (DPM) which is discussed in detail in Chapter 6 of this thesis. In summary, the DPM is a Lagrangian technique which allows the trajectories of single or groups of particles to be modelled within a flow field. The user is able to set various parameters, including particle density, diameter, number and boundary conditions. Stovin and Saul (1996 & 1998) selected 68 particles of fixed size and density (47μm and 2,500kg/m^3 respectively) and considered their trajectories (and, in particular, their fates) under various different inlet location and velocity scenarios. The authors were able to predict sediment deposition (quantity and location), and to examine the model's sensitivity against selected parameters including sediment

type, injection location and boundary conditions. From the results, Stovin and Saul were able to conclude that deposition was extremely sensitive to injection location.

Stovin *et al.* (1999) compared CFD flow patterns and predicted sedimentation performance generated for a storage chamber with field measurements of a full size version of the same chamber. Again, the models were developed using Fluent. The authors observed differences between observed and modelled flow patterns, and also between observed and modelled efficiency. They ascribed the former to an over-simplification of the boundary conditions and the latter to limitations of the DPM. Stovin *et al.* also found that particle density and settling velocity were key parameters in determining sedimentation rates, whereas particle size was not.

Finally, whereas Stovin's previous work had considered steady state flow conditions, Stovin *et al.* (2002) reported preliminary results from an investigation into the modelling of a storage chamber under storm conditions, during which the flow and pollutant load might both be considered to be variable. The unsteady volume of fluid multiphase model available in Fluent software was applied to a simple two-dimensional model of a stilling pond CSO chamber and was used to simulate time-dependency and the hydraulic conditions arising in the chamber in response to an inflow hydrograph. The results demonstrated that sedimentation efficiency is enhanced during the emptying stage, rather than during filling of the chamber.

UKWIR (1997) reported the results of an investigation into the flow patterns within, and particle retention efficiency of, a stilling pond combined sewer overflow chamber. Using the Fluent software, the authors examined firstly the effect of the location of an anti-blockage device on efficiency, and secondly the effects of size variation of the chamber assuming a fixed anti-blockage device. By employing CFD, the authors were able to demonstrate in a simple and straightforward manner the benefits to be gained from inclusion of an anti-blockage device and its optimum location.

Also considering suspended solids concentration and deposition in sewerage systems, Pollert and Stransky (2003) ran a 1-D hydrodynamic simulation model of a sewer /

surface water system and used the results to provide an inflow hydrograph as input to a 3-D Fluent model of a CSO structure. The authors used the RNG k-ϵ model, although their reasons for this are unclear. The CFD model was then used to estimate CSO separation efficiency for a range of particles ($1{,}300<\rho<2{,}600$ kg/m^3, and $0.01<d<$ 1mm), although few details are provided. The authors claimed that combining two models, even though they have different dimensions, enabled an increased degree of understanding of system hydrodynamics to be obtained. Once more, however, the basis of this conclusion is unclear.

Tyack and Fenner (1999) and Faram and Harwood (2003) used CFD to consider the interception of sediments in sewer systems, and the subsequent retention of those sediments within the sewer system. Tyack and Fenner (1999) focussed on the performance of hydrodynamic separators and constructed a three-dimensional CFD model of a 1600mm diameter prototype using the FIDAP code. Although the authors began their work using the standard k-ϵ turbulence model, in view of the highly swirling flow generated in the vortex separator, the authors subsequently switched to the RNG k-ϵ turbulence model. Although the authors recognised the unsuitability of the standard k-ϵ model in this scenario, it is somewhat surprising that they do not appear to have considered the use of the RSM which would have been better suited to the anisotropic conditions found in the separator. Nevertheless, the authors observed a reasonable correlation between numerical and measured velocity data in the separator, concluding that CFD was an appropriate means of obtaining data in situations where it is difficult to measure experimental data.

Faram and Harwood (2003) used CFD to model the hydrodynamics of sediment interceptors of various types within sewerage systems. Using the Fluent software code, the authors developed models of a number of interceptors of different configurations (gravity sedimentation device, a gully pot, a simple vortex separator and an advanced vortex separator) and applied the RSM to solve the flow field. Subsequently, the authors used the Fluent DPM to simulate particle trajectories and fates from which they concluded that it is the more sophisticated interceptors (such as vortex separators) which offer the best performance characteristics.

Andoh (2006) reported the results of an exercise undertaken to develop several design concepts for sediment removal from storm water using Fluent. No modelling details were provided, but Andoh claimed that the exercise had been successful as CFD enabled several concepts to be eliminated prior to the construction of a prototype, thereby saving time and money in the development process.

2.6.2 Sewage Treatment

2.6.2.1 Waste stabilization Ponds

Applications of CFD to sewage treatment have, thus far, been limited with most work having been focused on waste stabilization ponds. For example, Wood *et al.* (1995 and 1998) attempted to develop accurate two-dimensional models of the performance of three waste stabilization ponds using FIDAP, with a view to then using the models to predict performance. The authors had limited success, with just one of the three models exhibiting flow characteristics similar to those found via experimentation. Wood *et al.* cited the principal reasons for the discrepancies between numerical and experimental data as being the representation of a three-dimensional inlet structure within a two-dimensional model, and the sensitivity of the model results to the assumptions used to model the inlet. It is interesting to note that the authors claimed that the models were unaffected by changes in parameters which are difficult to predict, such as the turbulent inlet. However, it is difficult to understand the justification of this statement as the authors concede that the models did not correlate at all with experimental data and so there would appear to be little basis on which to draw conclusions from the models' results.

Salter *et al.* (2000) used CFD to model the hydraulic behaviour of facultative lagoons used to treat industrial waste water in Thailand. Turbulence was modelled using the standard k-ϵ model. The authors also assumed stratification of the lagoons and so assigned different temperatures to different layers across the lagoons' depth. A computational residence time distribution analysis was undertaken, as described in section 2.3.5 above. However, the authors did not model the effects of winds on the

flow patterns in the lagoons, although they accepted within the paper that a prevailing wind directed towards the inlet would increase short-circuiting. Despite this apparent limitation, the authors obtained good correlation between modelled surface flow characteristics and measured surface velocity data. From the results, the authors were able to identify areas of stagnation within the lagoons and short-circuiting of flow, and concluded that this short-circuiting could be minimised via the introduction of baffles in the central region of the lagoons.

Shilton *et al.* (2000) also reported results from a CFD study of ponds. Shilton *et al.* used the PHOENICS code and applied the standard k-ϵ turbulence model to solve the flow in a small community waste stabilisation pond. Similar to Salter *et al.* (2000), Shilton *et al.* examined flow field characteristics with and without a baffle and used this to demonstrate that treatment efficiency could be readily predicted using CFD. Vega *et al.* (2003) undertook a similar configuration optimisation exercise using the 2D depth-integrated MIKE21 code to study an anaerobic pond in south west Colombia. The authors found optimum flow conditions were achieved with a diagonally opposed inlet and outlet, a length : breadth ratio of 2:1 and cross baffles at one third and two thirds along the pond. Unfortunately, almost no modelling details were published.

2.6.2.2 Sedimentation Processes

Matko *et al.* (1996) carried out an extensive review of numerical modelling in waste water treatment. Although not presenting any data of their own, the authors concluded that CFD models can predict the flow patterns in sedimentation tanks with a greater degree of accuracy than the traditional mass flux and lumped flow models. Matko *et al.* also identified particle density and size, suspended solids settling velocity distribution, water velocity distribution, turbulent mass diffusion of suspended solids and solids suspension as the most critical factors for CFD modelling. (This is in contradiction to Stovin *et al.*, 1999, who did not find particle size to be of great significance). The authors also noted the lack of work undertaken using CFD to study sedimentation tank performance by analysing *inter alia* baffle design, wind effects, inlet / outlet geometry, side wall depth, floor slope, hopper design and peripheral weir design. It is interesting

to note, therefore, that in the ten years since this review was published, little work addressing these issues appears to have been undertaken.

2.6.2.3 Activated Sludge Processes

Karama *et al.* (1999) used the commercially available PHOENICS code to construct a CFD model of the anaerobic zone of an activated sludge reactor. However, no modelling details were provided by the authors. The numerical results were compared with two experimental results of residence time distribution and oxidation reduction potential and were found to exhibit similar characteristics, to the extent that the authors concluded that the model could be used to predict and improve hydraulic flow within an anaerobic zone of the activated sludge reactor. The authors subsequently used the model to predict an area of very low velocity, indicating a dead zone within the anaerobic zone.

Alex *et al.* (2002) used the little-known CHAMPION3D CFD model to develop a process to analyse and optimise activated sludge plant (ASP) design and operation. Using the standard k-ϵ turbulence model, solutions for the air and water phases were obtained for a range of hydraulic loads and air requirements for a site in Germany. The authors developed profiles of particle age, velocity and dissolved oxygen and nitrate concentration plots. The authors used their model to justify an argument that CFD can be used to remove a degree of empiricism from ASP design, and to suggest that future designs could be based on an integrated engineering tool applying simulation models and techniques to draft CAD drawings. Although a laudable aspiration, this author believes that the industry is still some way from achieving such a goal.

Recognising the potential benefits of CFD, Gujer (2006) stated his expectation "to see the first reliable combinations of CFD and biokinetics based on models as complex as ASM3 [the IWA proposed Activated Sludge Model 3] in the near future, first in 2D and quite soon also in 3D". Indeed the results of such 3D models were published by Oda *et al.* and Glover *et al.* in 2006. Oda *et al.* (2006) combined CFD with ASMs to develop a model to consider microbial reactions and sludge flow in the activated sludge process.

This ambitious work combined an activated sludge model to simulate microbial reactions, a sludge settling model, and oxygen transfer models for coarse and fine bubbles into a traditional CFD solver. Turbulent flow was solved using the RNG k-ϵ turbulence model. After calibration with measured data, the combined model was used to optimise air demand in the activated sludge reactors. Using the model, the authors were able to specify optimum values for aeration cycle time (five minutes on, 85 minutes off), air flow rate (0.15 $m^3/h/m^3$ tank) and blower spacing (250 mm). At the same time, Glover *et al.* (2006) published work in which they combined ASMs with the Fluent code to study a pilot plant oxidation ditch (a closed loop reactor operated as a sequencing batch reactor), an aerated batch reactor (perfectly mixed) and a full scale oxidation ditch (closed loop reactor). Terming their combined approach as "CFD-bio modelling", the authors found that, in general, the addition of CFD to traditional ASMs was beneficial. However, the authors concluded that CFD was unnecessary in the case of a simple closed loop reactor with well-functioning hydraulics, as this can be modelled successfully by a simple perfectly mixed unit. The comprehensive models of Oda *et al.* and Glover *et al.* represent the current state of the art for sewage treatment modelling using CFD.

2.6.2.4 Disinfection

Janex *et al.* (1998) utilised CFD to develop an accurate simulation of dose distribution within a pilot-sized UV disinfection system for application within sewage treatment. The CFD model enabled the authors to understand further the flow mixing mechanisms within the reactor, leading them to suggest that the tool be used in future for evaluation of alternative designs and configurations to facilitate an increase in disinfection efficiency. Details of the modelling software and technique are limited, other than the use of the standard k-ϵ turbulence model, even to the extent that the proprietary software is not named.

2.6.2.5 Sewage Sludge

Craig *et al.* (2002) used Fluent to optimise the hydraulic behaviour of sludge settlement tanks. The CFD model was used to predict the increase in hydraulic surface flow rate arising from a storm event within the catchment, and also to predict and analyse the effect of this increase on the height of the sludge zone within the tank and the total suspended solids profiles. At dry weather flow, the difference between modelled and measured heights was just 2%. There was a four-fold increase in flows for the two scenarios (238 – 1,000 m^3/hr) and the difference rose to 17% for storm flows. However, the authors would appear to have been satisfied with this result. The validated model then enabled the researchers to optimise the design and performance of the sludge settling tanks for a range of flow rates and various inlet and outlet dimensions.

The modelling of sludge flow is a complex operation. Sludge is a non-Newtonian fluid which introduces additional modelling complexities, yet these complexities have been overlooked by Craig *et al.* This is a justifiable decision as Craig *et al.* were predominantly interested in the flow and settlement of waste water, rather than the resultant sludge formation and flow.

A limited amount of work has been undertaken to model the flow of sewage treatment sludge in pipes in both laminar (Bechtel, 2003) and turbulent flow regimes (Bechtel, 2005); the non-Newtonian nature of sludge making its hydraulic modelling a complex task. Bechtel (2005) applied a specific rheological model to account for this non-Newtonian feature which described the sludge's shear stress / shear rate relationship. Using a bespoke CFD code, Bechtel studied turbulent sludge flow for a range of solids content (3% - 10% by weight) in horizontal pipes of four diameters (150 – 360 mm). Bechtel developed head losses through the pipes and found good correlation with experimental datasets, and concluded that the technique offered an accurate and efficient means of performing head loss calculations, with applications to more complex geometries such as pipe fittings and valves. However, Bechtel (2005) also recognised the need for further work on turbulence modelling in this area.

2.6.3 Water Resources

Ta and Brignal (1998) examined flow within a large UK storage reservoir using the CFX code. CFD analysis demonstrated that flow through the reservoir exhibits horizontal flow patterns which gives rise to short-circuiting and stagnation zones. The authors concluded that this horizontal flow circulation originated from feed current momentum and depended crucially on reservoir geometry. Using CFD, Ta and Brignal analysed various options for modifying the inlet and outlet arrangements, including central outlet, submerged baffle and manifold inlet. Ta and Brignal concluded that flow circulation could be minimised by careful inlet design, and that of the three proposed modifications, the submerged baffle was the favoured option as it offered low installation cost together with a reasonable balance between the degree of mixing and residence time.

Bayley *et al.* (2001) also used CFD to study flow circulation in raw water, open reservoirs. This approach simulated the flow in a reservoir using its geometry (dimensions, inlet/outlet arrangements) for specified boundary conditions (wind, temperature) and operational conditions (reservoir throughput). It is interesting to note that for large reservoirs, Bayley *et al.* found it necessary to account for the Coriolis effect, using a rotating frame of reference technique. Unfortunately, the authors did not provide a definition of "large". The decision to account for the Coriolis is an interesting and complex point. Rotation is known to occur naturally with any large body of water. However, the effect is only significant on large bodies of fluid with little engineering to affect them, and for reservoirs this rotation is generally influenced by the inlet and outlet configurations to a greater extent than the different rotation speed of the earth dependent on the latitude. Indeed, it is to this that Ta and Brignal referred when they stated that horizontal flow circulation characteristics were a function of geometry and feed current momentum. In order to take the effect into account, it is necessary to include the reservoir in a rotating frame of reference (*i.e.* the earth) which adds significant numerical complexity and computational expense to the analysis. The authors did not provide justification for their decision to take the Coriolis effect into account which is unfortunate. It would have been of great interest to see a comparison

between model results which accounted for the effect and those which did not, particularly since there appears to be a lack of agreement amongst workers in this field.

Building on the work of Ta and Brignal (1998), Bayley *et al.* (2001) considered aquatic and sediment transportation, natural and artificial mixing, and water age and short-circuiting within the reservoirs. Transportation was modelled using the disperse phase Lagrangian technique where the release and subsequent motion of a polydisperse sample of particles was simulated within the steady flow field. Wind-induced mixing was simulated using the Volume of Fluid technique which assumes conservation of momentum across the air / water interface. Artificial mixing was modelled using a disperse phase Lagrangian model technique and an Eulerian-Eulerian technique, although the authors reaffirmed a point made by Ta and Brignal (1998), that achieving convergence in multiphase models is difficult and time-consuming (and, hence, expensive). However, it must be appreciated that in the five years since publication (and so likely six years since the work was undertaken) computing power and techniques have improved significantly. Finally, Bayley *et al.* (2001) considered water age and the potential for short-circuiting in the reservoirs by simulating tracer tests. A slug of species was introduced at the inlet and its propagation through the reservoir modelled using an exponential decay rate model. By considering each of the above factors, Bayley *et al.* were able to use CFD successfully to substantially increase retention and subsequent improvements to water quality.

In a rather superficial paper, Lee *et al.* (2006) reported the CFD modelling of a $6x10^6$ m^3 impounding reservoir undertaken to assess retention time which the user required to be a minimum of seven days to reduce any *Cryptosporidium* oocyst challenge at the downstream water treatment works. It is noteworthy that the authors assumed the reservoir extraction rate to be equal to inflow. This assumption was made to reduce computational complexity by removing the need for modelling depth variations with time. However, no modelling details were provided regarding turbulence or RTD treatment. No reference was made to the potential impact of wind-induced effects, nor the Coriolis effect. Thus, it is difficult for the interested modeller to glean much useful

information from the paper, other than the authors' reported success at modelling large bodies of water.

2.6.4 Water Treatment

Recent years have seen an increase in the use and application of CFD techniques to issues within several water treatment unit processes, some of which are considered below.

2.6.4.1 Coagulation

Byun *et al.* (2005) used CFD to consider the performance of a new pilot scale instantaneous flash mixer for coagulation which comprised an injector nozzle and deflector plate inserted within a bespoke short section of pipeline (Figure 2-15 refers). The CFD analysis, undertaken using Fluent, considered the physical configuration of the flash mixer (*e.g.* distance from nozzle to deflector plate), the ratio of the injected coagulant to bulk flow, and the ratio of the main pipe diameter to inlet pipe diameter. The standard k-ϵ model was used to solve the turbulent flow, and it should be noted that this is in contradiction to Jones (1999) who suggested that the k-ω model was a more appropriate choice in a similar scenario. No reference is made by Byun *et al.* (2005) regarding model verification, and so it is not clear if the standard k-ϵ model was appropriate in this instance. Byun *et al.* (2005) found that the absolute velocity of the bulk and coagulant flows did not affect coagulant dispersion, whereas the ratio of the two was critical, with a value of greater than 10 achieving complete dispersion of the coagulant in one second. The dispersion characteristics of the coagulant were represented by plotting the mass diffusivity of the coagulant along the pipe length, as shown at Figure 2-16.

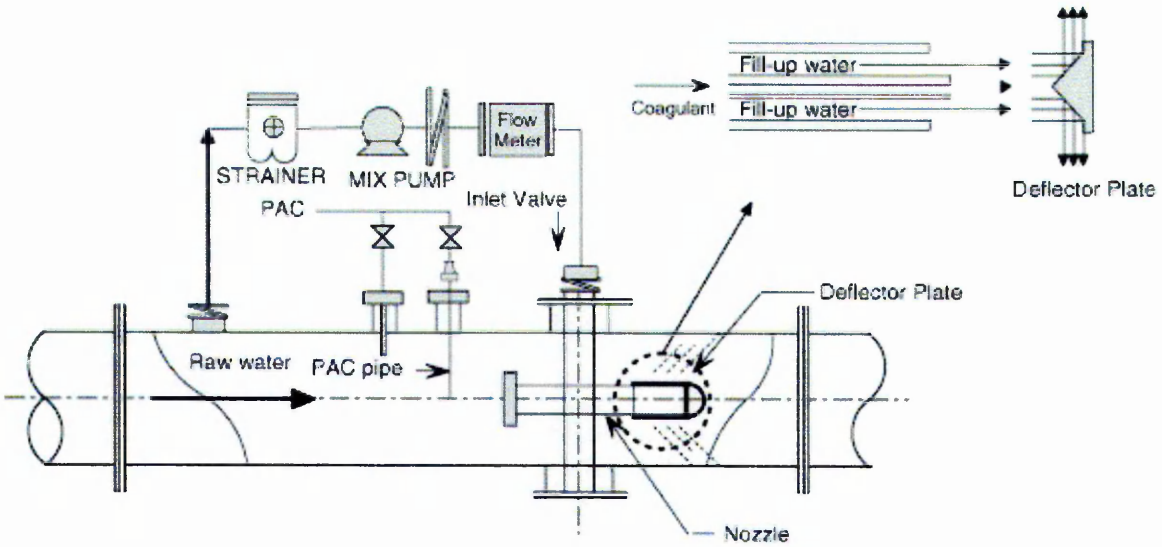
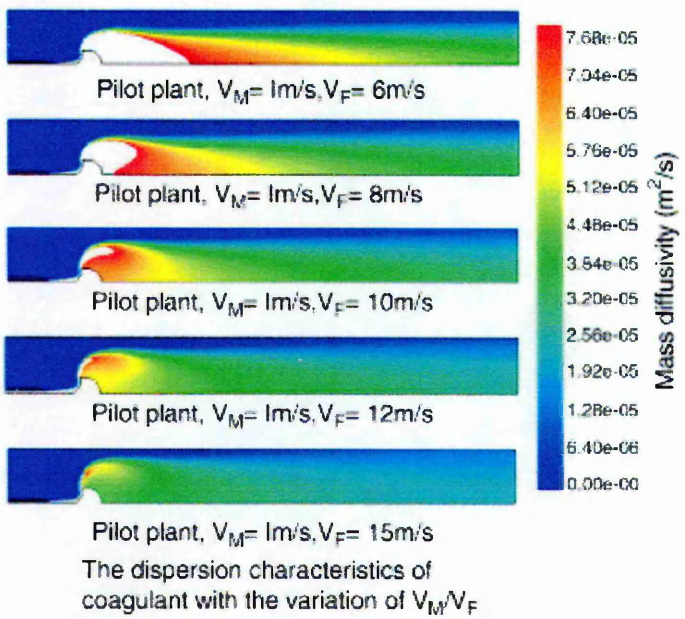


Figure 2-15: **Instantaneous flash mixer (from Byun *et al*, 2005).**



The dispersion characteristics of coagulant with the variation of V_M/V_F

Figure 2-16: **Coagulant dispersion results (from Byun *et al*, 2005).**

2.6.4.2 Flocculation

CFD has been used by researchers in the evaluation of the effects of hydraulic parameters on the flocculation process, using the results of their analyses to optimise flocculator configurations and operational regimes. Much of this work has, however,

taken place at laboratory and pilot scales and has not considered the effects of turbulence and shear on individual flocs.

Ducoste & Clark (1998a & b) demonstrated that for a constant average turbulence energy dissipation rate, ϵ, in a flocculation vessel, the equilibrium floc size distribution is reduced with increasing vessel size. The same authors subsequently measured turbulence characteristics in laboratory scale flocculation vessels and compared the results with those from a FIDAP CFD model of the same configuration (Ducoste & Clark, 1999). The authors demonstrated satisfactory agreement between the numerical and practically-obtained data, with both demonstrating that maintaining a constant value of ϵ does not ensure that the same turbulence characteristics are maintained in vessels of different scale, or same scale with different impellers.

Korpijarvi *et al.* (1999) used CFX v4.2 to model the flow patterns found within a Kimera Kemwater mini-flocculator, a variant on the standard jar test device. The mini-flocculator comprises a supported paddle mixer and one litre beaker with mixer rotation speed being adjusted from an accompanying console. Korpijarvi *et al.* (1999) tested the sensitivity of the flow patterns within two grids of different coarseness to four different turbulence models; *viz.* standard k-ϵ, RNG k-ϵ, LRN k-ϵ and the Reynolds stress models. The authors developed grids of 30,000 and 67,000 cells to represent the one litre vessel and found that velocities within the mini-flocculator were insensitive to changes in turbulence model or grid density. Korpijarvi *et al.* demonstrated that the total dissipated power in the fine grid mesh was more than twice that found in the coarser mesh. The difference observed by the authors when comparing total dissipated power associated with LRN k-ϵ and RSM models using the coarse grid rose to in excess of ten-fold. Korpijarvi *et al.* recommended that additional work be undertaken to verify their work and also to extend understanding of the magnitude of the turbulence quantities. The work reported in this thesis addresses some of these issues, albeit using a different flocculator arrangement.

Subsequently, Korpijarvi *et al.* (2000) presented a useful summary of the Navier Stokes and the standard k-ϵ turbulence model. Again studying the hydrodynamics of the

Kimera Kemwater mini-flocculator, Korpijarvi *et al.* (2000) demonstrated the very large variability of the local velocity gradient value (G_L), as described by Luo (1997) within this vessel, thus questioning the validity of the use of the $\overline{G}$ value. Unsurprisingly, the largest G_L values were to be found near the paddles and particularly in the turbulent area behind the panel, stretching in a radial direction towards the wall.

In the same paper, Korpijarvi *et al.* also examined average ($\overline{G}$) and local (G_L) velocity gradient values for a large scale rapid mixer and a dissolved air flotation tank inlet section and were again able to identify the points of greatest G_L value. Korpijarvi *et al.* concluded that CFD was a useful tool to evaluate the impact of various mixer and flocculator designs, and to determine the extent of mixing required. The authors also suggested that the flow simulation techniques available via CFD could also be used for design to avoid floc breakage; and this topic forms a key element of the work reported in this thesis. However, having clearly undertaken a significant volume of work in assessing several configurations, it is unfortunate that the authors did not extend their analysis to make recommendations regarding design parameters. It is likely that they were prevented from doing so by not considering likely turbulence and shear effects on flocs.

In a similar vein, Essemiani and de Traversay (2002a) used CFD to examine flocculation performance at pilot scale. Using a $1m^3$ rectangular flocculation stirred vessel, Essemiani and de Traversay used Fluent software to investigate fluid flows induced by an axial impeller, and also to evaluate the mixing efficiency needed for flocculation. Whilst maintaining water quality, impeller type, coagulant and flocculant aid type and dose constant, the authors examined the effects of varying inlet flow rate (from 2 to 6 m^3/hr) and impeller rotational speed (36 and 73 rpm), although unfortunately the authors chose to publish only the results relating to $2m^3/hr$ inflow and 73 rpm rotational speed. The impact of varying inlet flow rate on velocity gradients for a full scale flocculator is considered in this thesis at Chapter 9.

Essemiani and de Traversay (2002a) took numerical results relating to the pumping number, power number and residence time distribution for fixed operating conditions,

compared them to experimental measurements and recorded good correlation between the two datasets. Table 2-7 below presents the results of the comparison. The table shows good correlation between numerical and experimental data, with the exception of the pumping number which shows a 24% discrepancy. Essemiani and de Traversay suggest that this error is a function of the use of central inlet tube in the numerical model which modified the pumping behaviour of the impeller; a factor which is not taken into account in the batch reactor used as correlation. Model results enabled the authors to determine areas of highest shear stress (where floc break-up is to be anticipated) and also areas of the lowest values where, subject to a *de minimus*, one would expect coalescence (*i.e.* floc growth) to occur. Similar to Korpijarvi *et al.* (1999 & 2000), the authors found that the distribution of local velocity gradients, as defined by Luo (1997), indicated high G_L intensity adjacent to the impeller, decreasing with distance from it.

Table 2-7: Comparison of numerical and experimental results for a 1m^3 axially-stirred flocculation vessel (from Essemiani & de Traversay, 2002a).

	Batch reactor	CFD	Discrepancy, %
Power Number	1.0	0.9	10
Pumping Number	0.56	0.74	24
Power Dissipated (W)	30	27	10
$\overline{G}$ (s^{-1})	174	163	6

When calculated using the traditional approach of Camp and Stein (1943), Essemiani and de Traversay found that for the system considered, $\overline{G}$ and the average G_L values exhibited reasonably close correlation, although there was a great range of G_L values. Essemiani and de Traversay concluded that $\overline{G}$ does not account for variables such as impeller position, geometry, operating mode and residence time. However, these parameters do affect the velocity gradient distribution, and therefore, spatial floc size distribution. As a result, Essemiani and de Traversay suggested that for the same $\overline{G}$ value, changing mixing rates and impeller type will affect performance. This conclusion corroborates that of Ducoste and Clarke (1998).

Essemiani and de Traversay (2002b) extended their work and furthered the argument that the comparison of different mixer configurations should not be made on the basis of

the global mixing intensity. Essemiani and de Traversay (2002b) argued that additional competitive parameters need to be considered also. The authors developed a new methodology for comparing coagulation and flocculation designs, based on the ratios of hydraulic residence time to mean residence time and mixing time to mean residence time. The methodology also incorporated mean velocity and mean local gradient. The authors presented additional data in this second paper showing results from different flow rates and rotational speeds.

The results indicated that there was no short-circuiting or recirculation within the vessel and that there was a high degree of mixing. The results for the mean local velocity gradient are very interesting. Increasing the speed of rotation by a factor of 2 (from 37 to 73 rpm), yielded a corresponding increase in G_L of between 4.3 and 4.9. However, in such circumstances, the $\overline{G}$ value was found to increase by a factor of just 2.8. As a result, Essemiani and de Traversay were able to conclude that the G_L takes into account local turbulence effects which are not included with the $\overline{G}$ calculation. Essemiani and de Traversay concluded that the local turbulence effects in this instance arose as a result of a non-standard inlet arrangement where the flow was introduced via a vertical, central tube immediately below the impeller.

Craig *et al.* (2002) developed a model using Fluent to simulate the operation and performance of a simple flocculation tank equipped with an axial impeller generating turbulent flow conditions. Unfortunately, no details of modelling technique or turbulence model used are provided in the paper. Craig *et al.* used the model to demonstrate variations in the G_L value, and to identify maximum and minimum G_L values associated with different operational scenarios. The authors identified that use of G_L values in this manner enabled the identification within the flocculation tank of those areas where both coalescence and floc break-up would occur. Similar to Essemiani and de Traversay (2002) above, this led the authors to question the validity of the use of the $\overline{G}$ value as a design parameter.

Haarhoff and van der Walt (2001) used the lesser-used Flo++ code to study flow in an around-the-end hydraulic flocculator. Building on previous work (van der Walt, 1998),

Haarhoff and van der Walt used CFD to develop qualitative guidelines for three fundamental geometric ratios (slot width ratio, overlap ratio and depth ratio). No details of modelling strategy were provided in the paper.

Haarhoff and van der Walt also studied the variation of the $\overline{G}$ value in hydraulic flocculators. It is known that hydraulic flocculators incur zones of high turbulence at the baffle edges which can cause floc break up. The authors showed variations in G_L in the flocculator in both absolute terms and normalized by dividing by the $\overline{G}$ value. They then introduced the concept of a 95th percentile of the normalized G value distribution in the flocculator as an arbitrary (but, in their opinion, realistic) performance indicator for flocculator optimisation (*i.e.* a G value which is exceeded only in 5% of the total flocculator volume). The authors argued that use of this G_{95} figure enables the designer to compare absolute and normalized G values on a more representative basis than by simply using the average. Using this approach, Haarhoff and van der Walt were able to conclude that the slot width ratio is the single most important geometric ratio for design purposes. The effect of the overlap ratio was found to have a less pronounced impact on the G values, whilst the effect of the depth ratio was inconsequential if the channel velocity was maintained. Although the results are undoubtedly of interest, it remains that the selection of a G_{95} value on which to base analysis and design criteria was an arbitrary choice based on the authors' preferences rather than an analysis of the underlying fundamental science.

2.6.4.3 Clarification

Brouckaert and Buckley (1999) used CFD modelling techniques to assess the performance of both wastewater and potable water treatment unit processes. For two sites, the principal aim of the exercise was to develop low cost enhancements to clarification processes, rather than incur significant capital expenditure in major works improvements. The work, undertaken using PHOENICS software, demonstrated that even when significant simplifications and assumptions are made regarding flow characteristics, CFD can still be employed to good effect. In this instance, the CFD

models reaffirmed the need to minimize secondary circulation in clarifiers to achieve a greater solids separation efficiency. For each process, the authors were able to recommend the installation of a small, inexpensive baffle to enhance the flow distribution characteristics. The authors subsequently analysed the performance of the wastewater clarifier and reported successful operation.

Brouckaert and Buckley (1999) demonstrated that there is a balance to be struck between the need for accurate and precise modelling and the benefits to be gained from such an approach. The authors elected to make a number of significant assumptions and simplifications in the development of their CFD models and conceded that "the model would not be expected to be a completely accurate representation of all details of the actual clarifier behaviour". In particular, no account was taken of the presence and size of desludging equipment, despite recognition of the fact that such equipment would have an effect on flow conditions within the clarifiers. However, in spite of these assumptions, the authors were still able to use their models to develop theoretical solutions to the problem of clarifier under-performance. From a purist's perspective, it is unfortunate that Brouckaert and Buckley (1999) elected to employ simplifying techniques in their models. However, their outputs were successful and they undoubtedly made savings in time and computing capacity by reducing the complexity of their problem, and so were justified in this pragmatic approach to problem-solving.

Lainé *et al.* (1999) used Fluent CFD software to develop a CFD model to analyse an observed temperature-related periodic under-performance of a circular flocculator-settling tank. Whilst operational performance of the tank was satisfactory when the influent and settling water were constant, it was noted that during periods of warming, when the influent was approximately 1.5°C higher than the water in the settling zone, solids carry-over from the settling zone into the effluent channel occurred. Consequently, the quality of the final water was impaired. The authors used Fluent software to construct a two-dimensional model of the structure and subsequently to examine flow patterns under both steady and temperature-varying conditions. Taking advantage of the tank's symmetry, the authors were able to construct a two-dimensional model from the centre out in one direction only. The RNG k-ϵ turbulence model was

used, although unfortunately no reason for this choice was given. It would have been interesting to compare these results with results gained from using other models; in particular the standard k-ϵ and Reynolds Stress models. The model demonstrated that the tank developed and maintained satisfactory flow characteristics under constant temperature conditions. However, once the ambient temperature and the temperature of the influent were increased, the flow characteristics were observed to change. Warmer, lower density water, introduced into the base of the settling zone from the coagulation and flocculation zones, was observed to rise through the settling zone quicker than water of a lower temperature and density. This bubble of warm air rising through the settling zone was observed to drag some of the lighter flocs within it up to the surface of the structure which were subsequently transported to the outlet trough. Thus, the mechanism causing the reduced performance of the flocculator was established. This research raises an interesting point with regard to the selection of turbulence closure model. The reasons for the selection of the RNG k- ϵ model are not immediately clear and the choice is not justified by the authors at the outset. However, the fact remains that use of this turbulence model would appear to have produced satisfactory results in this instance. This is a further demonstration of the fact that no single turbulence model can or should be judged solely appropriate for a particular application. Nevertheless, from an academic perspective, it would be potentially enlightening to consider these results alongside those produced using an alternative turbulence model and to judge the individual merits of each turbulence model.

2.6.4.4 Dissolved Air Flotation

One of the earliest published applications of CFD to Dissolved Air Flotation (DAF) was the work of Eades and Brignal (1995) as part of the development of the now-established counter-current dissolved air flotation / filtration process (COCO-DAFF). The authors used the Phoenics code to confirm that the pilot scale inlet could be scaled-up successfully. However, the reported work focuses on the development of the new process, and few details are provided relating to the modelling process.

Ta and Brignal (1997) used Fluent v4.4 to construct a single phase model of a DAF tank to study water flow patterns only (*i.e.* no air bubble movement was modelled) and the results were used to infer DAF tank performance. Ta and Brignal defended the use of a single phase model (rather than a two phase model) working on the assumption that air bubble movement is dominated by water flow. In the absence of verified data, this would appear to be a realistic assumption; however, Fawcett (1997) demonstrated at the same time, the invalidity of this assumption using a dual phase model. (Fawcett, 1997, is discussed further below). Ta and Brignal (1997) used a two dimensional 76 x 30 grid to fit the geometry of a pilot-scale model of the DAF plant and assumed steady state conditions. The model used the standard k-ϵ turbulence model. Dye tests were simulated using the time dependent chemical species transport model. Taking advantage of the unit's symmetry, only a strip across the width of the DAF tank was modelled.

Ta and Brignal (1997) compared their numerically-derived results with dye test results from a 1:5 scale model of the DAF tank for verification purposes, and the authors concluded that, by inspection, there was satisfactory agreement between the two sets of data. Having satisfied themselves of the validity of their model, the authors then used it to optimize design parameters for the DAF tank. In particular, Ta and Brignal analysed the sensitivity of the DAF tank to changes in the aspect ratio (length to height ratio), baffle arrangements, outlet configurations and flow rates. Aspect ratios of 1.0, 1.4, 1.6, 2.0, 3.0 and 4.0 were modelled. Unfortunately, the authors did not report the flow rate values used in the study. Ta and Brignal's CFD-derived results indicated that performance was impaired by strongly recirculating flows at aspect ratios of 2.5 and below. However, the authors found that performance increased with increased aspect ratios, thus leading them to conclude that this is an important design parameter. Interestingly, Ta and Brignal found no significant performance enhancement arising from changes to baffle, floor or outlet arrangements. Although an interesting exercise, the failure to acknowledge the impact of the air bubbles on the water flow make this a largely academic exercise and it is both interesting and instructive to compare this analysis with that of Fawcett (1997), published at the same time.

Fawcett (1997) used CFX v4.4 to develop a two-dimensional multiphase model of a DAF tank which solved equations for both the air and water phases. Although an advancement on the single phase model of Ta and Brignal, Fawcett acknowledged that this two-dimensional model was also limited as no analysis of nozzle spacing was undertaken, nor were the effects of significant velocity profiles (*e.g.* tank inlet) on air distribution considered. Fawcett cited the need for computational speed as the principal driver behind the choice of a two-dimensional model. Fawcett concurred with Ta (1999) by recognising that even a simple two-dimensional multiphase model can take several hours to reach a point of convergence. Furthermore, Fawcett was unable to model the dynamics of solid / bubble agglomerates. Consequently, Fawcett used numerically-derived velocities and air concentrations alone to infer process performance. Indeed, this has remained a difficulty until very recently, with Fluent releasing an additional generic population balance model in 2005. No further model details were presented.

Accepting these limitations of the CFD model, Fawcett (1997) was able to draw some significant conclusions. Specifically, Fawcett demonstrated that the effect of modelling entrained air within the flow had a significant effect on tank hydrodynamics. Indeed, rather than having a negligible affect (as assumed by Ta and Brignal, 1997), Fawcett's two phase model demonstrated that bubble buoyancy dominated flow within the reaction zone, giving rise to a more uniform velocity distribution than had been found for single phase flow. Fawcett agreed with Ta and Brignal that the aspect ratio was an important design parameter, but Fawcett also concluded that the principal design parameter for effective DAF tank performance was, in fact, the ratio of air recycle to main flow momentum. Fawcett also used his model analysis to demonstrate that the surface loading rate governs the concentration of air leaving the tank via the clarified water outlet, and that a loading rate below bubble rise velocity would ensure no bubble (and hence, flow) carry-over into the downstream processes.

Recognising the limitations of earlier DAF tank CFD models, Ta *et al.* (2001) developed an Eulerian-Eulerian multiphase model to analyse air / water flow, allowing the introduction of floc particles as additional phases. The authors initially used the

standard k-ϵ model for water phase and laminar flow model for the air phase. However, whilst developing the model, the authors found it unnecessary to use two separate models and used the standard k-ϵ model for both phases. Unfortunately, Ta *et al.* did not state specific reasons for adopting this approach, other than the k-ϵ model apparently converged more readily than the laminar model. Floc transport was simulated as Lagrangian particle movement, coalescing with air bubbles as they moved within the tank. The assumption was made that floc particle movement created minor drag only and so was not coupled to the main flow.

The authors recognised the need for experimental measurements to verify the model because of the use of a multiphase model and the limited understanding of flow behaviour in these circumstances. The authors compared the numerical results with flow measurement data arising from an acoustic sensor mounted within the actual DAF tank modelled. The results compared favourably in the dominant flow region near the water surface. However, reverse flow immediately below the water surface was identified by the acoustic sensor, but was not predicted by the CFD model at the same location. The authors also used an underwater camera to locate the bubble layer within the tank. On a qualitative basis, the observed layer agreed with the CFD results, but the camera also identified unsteady flow features, including lateral dispersion of the bubble cloud. This was later confirmed by Hague *et al.* (2001) using an LDA technique. This result demonstrates a further limitation of this model, as it assumed steady state conditions only.

2.6.4.5 Filtration

A study of the literature shows that the published application of CFD to filtration mechanisms in either water or wastewater treatment is somewhat limited. Tung *et al.* (2004) used the Fluent software to simulate flow fields through deep bed filters, but modelling details were not provided. The authors employed various types of granular packing structures (simple cubic packing, bodycentered packing and face-centered packing) to analyse the tracks of particles ranging in size from 0.05μm to 3μm through the beds. The authors found good correlation between experimental and numerical results for the body-centred packed granular beds and the random packed granular bed.

However, the simulation of a simple cubic packing granular bed structure underestimated capture efficiencies due to the simplicity of the cubic packing structure where a free vertical downward flowing path gives rise to a higher packing porosity.

Hillis *et al.* (1998) used the CFX code to develop three dimensional models of membrane microfiltration (MF) processes. The purpose of the modelling work was to provide an initial screen for options, thus reducing the number of pilot scale options required. The models were used to track particle trajectories, to study fouling processes and the removal of fouling material during backwash. Unfortunately, the authors provided no model details, nor diagrammatic representation of their results. Rahimi *et al.* (2005) undertook further work applying CFD to MF by considering permeate flux through a membrane. The authors employed their own code with the RNG k-ϵ turbulence model to simulate flow through a Millipore polyvinyldine fluoride (PVDF) membrane (average pore diameter 0.22μm) and results were compared with experimental data. The authors concluded that they were able to model effectively the permeate flux through the membrane and to produce results which were more accurate than simple calculations using the generalised Darcy equation for permeate flux. The authors were also able to identify a feed mass flow rate dependency on the results using CFD.

2.6.4.6 Ozonation

It is interesting to note that while some traditional physical processes, such as sedimentation and filtration have not yet been studied extensively using CFD, other more modern processes have received far more attention. One such example is ozone treatment.

Do-Quang *et al.* (2000) used a combination of CFD modelling and full-scale experimentation to examine the efficacy of ozone treatment when used for disinfection within water treatment processes. Employing the ASTRID CFD code (developed by Electicité de France), the authors combined batch kinetics and ozone decay with the Navier-Stokes equations into a global hydraulic model which allowed them to study the

hydrodynamics and ozone mass transfer within an industrial ozonation tower, and to estimate micro-organism removal in a full scale reactor. The results were compared with experimental data to validate the model. Do-Quang *et al.* studied reactor operation assuming continuous, steady-state flow. Ozone residual differences between the model and experimental results were 0.05 mg/l which, the authors asserted, was satisfactory to assume that model ozone profiles were accurate representations of a full scale reactor. (Ozone concentration in gas was 18mg/l). The authors used the CFD model to develop a design for a new ozone reactor predicting ozone residual concentration, and taking into account instantaneous ozone demand and ozone decay kinetics. Do-Quang *et al.* concluded that ozone contactor performance was heavily dependent on the hydrodynamics of the vessel which, in turn, was governed by geometry and operational regime. The authors further concluded that, rather like other unit processes, CFD could be used for the design and operation of disinfection reactors.

Huang *et al.* (2002 and 2004) developed a single-phase CFD model of an ozone reactor, based on a full scale installation in Durban, South Africa. Having successfully validated the model with experimental data, the model was used to determine the reactor's hydraulic retention time as a function of inflow rate, and to optimize disinfection efficiency by selecting the optimum location for residual ozone monitoring, and achieving the most efficient use of the dosed ozone. The model was constructed using the Fluent 5.5 software, incorporating the standard k-ϵ turbulence model. It is unfortunate that there is no discussion regarding the selection of turbulence model (other than to state that this is the most widely used), nor is there any reference to the Reynolds number. It is also noted that, due to difficulties associated with measuring turbulent intensity at the inlet, the authors forced the verification of the model, with the turbulent intensity adjusted to give the best fit with experimental data. Despite this, the authors were satisfied that the results obtained were adequate for the purpose, so demonstrating that a relatively straightforward single phase model can be sufficient for some purposes, without the need to develop a more complex and computationally expensive multiphase model. However, from an academic perspective, forced verification is to be avoided and so the results of this research must be viewed with a degree of caution.

Craig *et al.* (2002) employed Fluent to assess the hydraulic efficiency and hydraulic retention times of three ozone contactors of different sizes and configurations. The model demonstrated that those contactors with larger water height to compartment length ratios exhibited better, more efficient performance than those with lower ratios. The models also showed that performance was enhanced further in those contactors with central, rather than lateral, inlets. Craig *et al.* then used the model to optimise the design of the poorest performing contactor, via the addition of baffles to increase the ratio of water height to compartment length. Unfortunately, no modelling details were provided by the authors. However, Ta and Hague (2004) also used CFD for the design and optimisation of a laboratory scale ozone reactor by studying flow distributions, but did not consider aspect ratio in any depth. Considering a single column ozone reactor, the authors adopted an Eulerian-Eulerian multiphase approach to model the high gas concentration in conjunction with the standard k-ϵ model, and demonstrated a strong link between both flow distribution and gas concentration and gas inlet velocity and entry angle. Model data were validated using LDA and PIV measurements. The authors also considered a multi-compartment reactor and found that the counter-current flow gave rise to mixing (which was enhanced with increased flow), whereas co-current flow yielded plug flow conditions. The authors also produced RTD curves using a chemical species transport equation from which they were able to deduce that ozone reactors can produce different levels of performance (measured in terms of gas distribution), yet still produce similar RTD curves.

Lee *et al.* (2006) presented results from the modelling of three ozone reactors of varying complexity in which the authors examined velocity profiles within reactors and demonstrated a lack of short-circuiting and good diffusion of ozone. The authors also identified that the presence of internal pipework within the reactor had little impact on flow patterns. It is disappointing to note that Lee *et al.* (2006) provided no details of turbulence model selection, software used or verification of results.

2.6.4.7 Disinfection

Wang and Falconer (1998) examined the impact of various turbulence models and numerical schemes on solute transport processes in a chlorine contact tank. The authors considered the effects of four hydrodynamic / turbulence models and two solute transport models in various scenarios. The standard k-ϵ model was found to under-estimate cross-sectional average velocity, and hence the cross-sectional solute transport flux, producing longer times to peak concentration. The results also showed that bulk flow characteristics, such as depth of flow and average velocity, have a significant impact on solute transport processes. Wang and Falconer suggested that errors can be overcome via the use of higher order numerical discretisation schemes for advection, such as the QUICK and third order upwind difference schemes. However, Wang and Falconer concluded overall that there was a need for a more sophisticated turbulence model to represent the spatial distribution of turbulent diffusion in contact tanks. This is an interesting observation as other published work in this field has all used the standard k-ϵ model.

Chataigner *et al.* (1999) used Fluent to analyse the size and configuration of efficient chlorination tank design and concluded that the installation of longitudinal baffles within chlorination tanks is an effective means of securing the necessary retention time. Details of the actual analysis are, unfortunately, sparse; however, the authors were able to make some specific comments regarding the use of CFD for this application. Of particular interest are the authors' comments regarding mesh structure and resolution. The authors recognised the critical nature of these parameters in achieving an accurate simulation of the hydrodynamics within the chlorination tank. However, they concluded that in the case of their study, additional cells had little overall influence on the results and did not change the flow pattern significantly. Unfortunately, Chataigner *et al.* gave no details concerning the numbers of cells used in their study, and so it is not possible to develop this argument further without additional data. It is, however, probable, that the initial number of cells chosen was sufficient to provide an adequately resolved solution for the parameters of interest to the authors, and that further addition

of cells represented a computationally-expensive and unnecessary additional burden on the calculation procedure.

Greene *et al.* (2002 and 2004) further investigated the effect of different inlet configurations on disinfection capability using CFD techniques which they subsequently corroborated with experimental data. Using CFX 4, Greene *et al.* constructed a three dimensional model to simulate flow, tracer transport and chlorine decay in a continuous flow pilot scale reactor. The model was subsequently used to examine the efficiency of various different inlet configurations. Interestingly, the authors examined low Reynolds number flows (Re=400) only, based on what they perceived to be a reasonable assessment of normal operating procedure. Consequently, the modelled flow regime was towards the laminar end of the transitional flow regime. In view of this low Reynolds number, Greene *et al.* employed the low Reynolds number k-ϵ model to account for localized turbulence at the inlet and internal baffles. CFD results indicated that inlet configurations can impact the flow field within the reactor significantly, even at a Reynolds number as low as 400.

More recently, Liu and Ducoste (2006) developed a PHOENICS CFD simulation of three jet diffusers to analyse ammonia injection methods in chlorinated water. In particular, the authors considered the impacts of mixing on the downstream formation of chloramines. For a cone diffuser, a three bar diffuser and a T-bar diffuser, the authors firstly obtained a converged solution for the RANS equations and RNG k-ϵ equations for the flow domain. Chemical transport and reactions were then solved using both a single fluid modelling and approach and a multi-fluid microscale (MFM) approach to consider the impact of micromixing on species concentration. The simulations were also conducted experimentally. The cone diffuser was found to exhibit the least effective chloramine production, and comparison of the results with the numerical data showed a significant over-prediction of chloramine formation by the single flow model. The MFM approach produced improved free chlorine residual production for the cone and three bar diffusers, but over-predicted mixing and chemical reaction rates for the T-bar diffuser. This led the authors to question the turbulence

model selection and to recommend further work using the RSM instead of the RNG k-ϵ equations.

2.6.4.8 Treated Water Distribution and Storage

Hannoun and Boulos (1997) presented a rigorous three-dimensional hydrodynamic model of chemical mixing and flow behaviour within service reservoirs. Starting from the Navier Stokes and continuity equations, the authors presented a logical and thorough approach to the problem, including an analysis of the modelling of a variable water elevation using the volume of fluid approach. Hannoun and Boulos used their model to analyse flow patterns within a serpentine clearwell (76.2m x 38.1m) using the standard k-ϵ turbulence model. The authors discretized the clearwell with 29,394 computational cells. The authors stated that "the chosen resolution was deemed adequate to accurately describe the clearwell geometry while maintaining acceptable execution time". Unfortunately, no justification is presented for this statement, and there is no sensitivity analysis given. However, Hannoun and Boulos did state that computational results relating to short-circuiting agreed well with model scale test results for a rectangular tank of similar aspect ratio. Hannoun and Boulos presented some useful and informative results, demonstrating the flow enhancements to be derived via the installation of a perforated screen within the flow immediately downstream of each bend. The authors concluded that their model could be used effectively to study flow patterns within service reservoirs of different configurations and for different seasonal characteristics.

Morrison (1999) used the commercial software CFX v4.1 to model service reservoir performance across a range of sizes and configurations, and employed a scalar transport equation to determine average water age within each. Morrison took a numerical output and compared it to the results of a physical model simulation. Whilst this exercise revealed significant differences in the residence time distribution curves produced, both simulations identified strong peripheral circulation with dead spots within the central area. Morrison then evaluated and presented flow visualization plots, residence time distribution plots and water age plots for rectangular service reservoirs with different

inlet configurations; *viz.* annular inlet above top water level, circular inlet above top water level, and a circular inlet at base level.

Yeung (2001), like Morrison (1999), used CFX v4.1 to analyse the performance of rectangular service reservoirs with aspect ratios (*i.e.* L:W) of 1.1, 1.5 and 2.0. Yeung used CFD to study flow fields and water age within the reservoir arising from steady flows and concluded that reservoirs with side wall inlets have better mixing characteristics than those with top water level inlets. Yeung developed a multi-channel recirculating reactor to assess flows within service reservoirs which he suggested could then employed for feed forward control of chlorine residual at reservoir outlets. However, Yeung recognized that this analysis was limited as flows in service reservoirs are not steady and consequently advised that additional work was required in this area.

2.7 Summary

This literature review has demonstrated the expanding use and application of CFD within the water industry. Examples of the technique's application have been drawn from across the spectrum of the international water industry, from the storage of raw water, through detailed and technical water treatment processes, sewerage, to sewage treatment. Because the greater part of this thesis is devoted to the numerical representation of the coagulation and flocculation processes, this review has focused to a greater extent on the application of CFD to water, rather than waste water applications.

In reviewing the literature, it has become apparent that although several water and waste water unit processes have been examined, along with analyses of linear systems such as sewers, there is a paucity of published CFD material relating to water industry applications which examines and discusses modelling strategies and philosophy in detail. With the exception of the work of Stovin & Saul (1996), Morrison (1999) and O'Neil (2001), almost all other published work which has been examined as part of this review omits some fundamental element of the modelling procedure. For example,

several authors do not disclose the nature of the turbulence model employed. Of those that do, few discuss the rationale behind the choice of model, and even fewer report the results of sensitivity analyses on either turbulence model or grid resolution. Away from the water industry specifically, other workers do present turbulence model and grid resolution discussions, but coverage of these issues is still not extensive. In addition, a great deal of published work does not provide details of any validation exercises using flow measurement techniques such as PIV, LDA or RTD.

The work reported in later chapters of this thesis has drawn on the work of previous researchers undertaken to date. In view of the apparent lack of rigour shown towards turbulence model selection, significant time has been spent determining the optimum modelling strategy for the scenarios considered.
However, where the necessary details are presented are in the literature, this review has demonstrated that, subject to careful, well-planned use, CFD can act as a valuable tool in the design of new assets and the optimization of existing ones. Chataigner *et al.* (1999) stated that "numerical analysis software represents a valuable decision-aid tool to professionals working in the fluid mechanics sector." However, the same authors qualified this statement somewhat by stating that tools such as Fluent provide "a representation of hydraulic phenomena on condition that appropriate meshing works have been carried out", thus emphasizing the need for careful use of the software.

This has been reaffirmed by several authors (*e.g.* Freitas, 1995 and Iccarino, 2000) who urged caution in the unilateral promotion of one code, turbulence model, convergence criteria or discretisation technique at the expense of all others. Specific factors relating to the scenario being analysed must always be accounted for. In particular, Iaccarino (2000) concluded that turbulence model selection is crucial for simulation success. Van der Walt (2002) summarised the situation succinctly when he wrote "CFD is, and will always remain, a modelling tool subject to the limitations of models. Some of these limitations can be improved through verification and validation, but the CFD model will always remain an approximation of reality."

Nevertheless, in the context of the international water industry, the potential uses for CFD are undoubted. CFD is a tool which, if applied correctly, is capable of facilitating improvements in both hydraulic and process performance for new and existing assets, be they raw water reservoirs, water treatment works, distribution systems (including treated water storage), collection systems (*i.e.* sewerage), or sewage treatment works.

3 Objectives

This thesis aims to contribute to the field of mixing in flocculation processes. In particular, the work reported in this thesis aimed to develop a means by which flocculation and flocculator performance might be characterised using a combination of shear and floc breakage mechanisms as a design parameter for full-scale flocculators. This aim was achieved by addressing the following objectives:

- to examine and develop pragmatic methods of modelling complex swirling flow in laboratory and full scale flocculators.

- to examine data from the above to elucidate previously unknown data regarding the vessels' hydrodynamic environments, with particular emphasis on velocity components, velocity magnitude, turbulence dissipation rate, velocity gradients and particle trajectories.

- to develop a conceptual understanding of floc breakage mechanisms by comparison of numerical data with laboratory data.

- to develop floc growth and breakage criteria which are transferable from one flocculation scenario and scale to another.

- to formulate guidance with regard to the effectiveness of the use of CFD as a tool to design, analyse and modify flocculators by construction and analysis of CFD models of full-scale mechanical and hydraulic flocculators.

4 Experimental Methods and Results

4.1 Experimental Methods

4.1.1 Power Measurement

Knowledge of the power draw of a system is a fundamental requirement to inform the user. Chapter 2, Equation 2-13 defined impeller power draw as:

$$P_{ave} = P_o \rho N^3 D^5 .$$

However, power may also be defined as:

$$P_{ave} = 2\pi N T_q \qquad \textbf{Equation 4-1}$$

where T_q is the applied torque. Therefore, the power input to a system can be determined if the mixing speed and applied torque are known.

In this work, two standard jar test configurations were selected for the CFD simulations. The first comprised an unbaffled 100 mm diameter Perspex stirred vessel, liquid depth 127 mm (thus containing 1 litre of water), and hereafter known as the "cylindrical vessel". The second vessel comprised a 115 mm square section Perspex vessel, liquid depth 150 mm (thus containing 2 litres of water), hereafter known as the "Hudson Vessel". The contents of both vessels were mixed with a 76 mm diameter, 25 mm deep paddle impeller, mounted on a 6 mm diameter shaft. For the cylindrical vessel, the paddle offset from the base of the vessel was 35 mm, whereas the corresponding distance for the Hudson vessel was 53 mm. The two configurations are shown below at Figure 4-1.

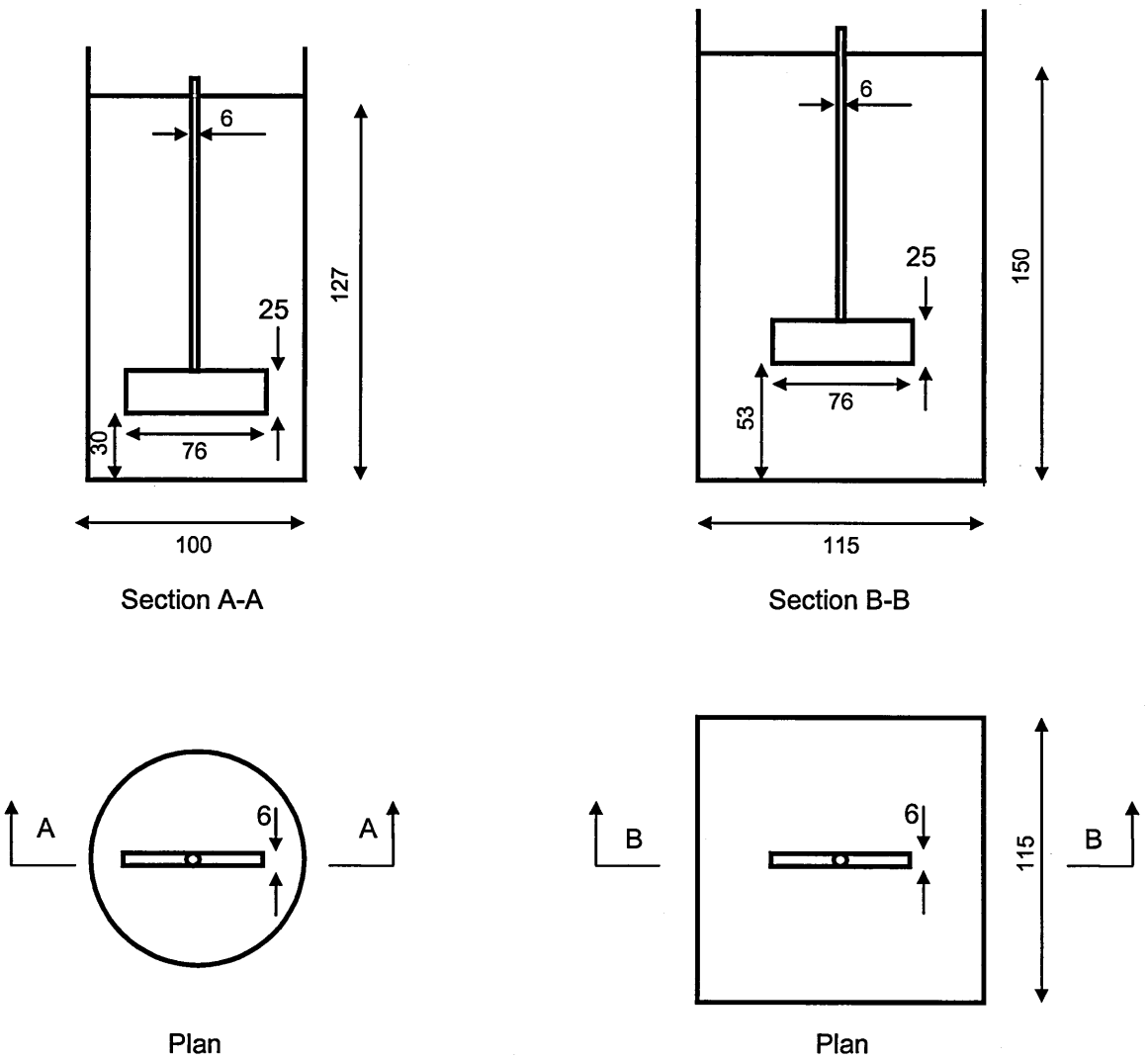


Figure 4-1: **Modelled cylindrical and Hudson vessel configurations (not to scale, all dimensions in millimetres).**

Torque measurements were taken for the standard jar test two blade impeller when rotating in water in both the cylindrical and Hudson vessels using a Coesefeld D4600 torque transducer unit as shown at Figure 4-2. The torque transducer was used in combination with a Goerz Servogor chart recorder. The torque measurements were subsequently converted to units of power via a calibration factor and Equation 4-1 to determine the power number, P_o. Frictional errors were compensated for by first measuring the induced torque when running the impeller in air. The results gained from this were subtracted from the results gained when running the impeller in each of the two full vessels. The torque transducer and chart recorder were calibrated before each set of experimental procedures and the calibration checked immediately afterwards.

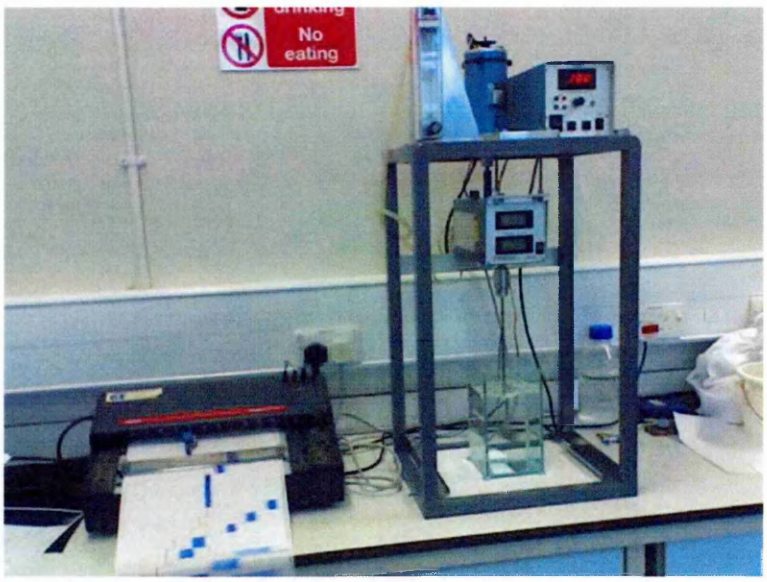


Figure 4-2: **Torque transducer and chart recorder.**

4.1.2 Laser Doppler Anemometry

Laser Doppler anemometry (LDA) is an optical, non-intrusive, highly accurate method of determining velocity measurements in gas or liquid flows. LDA uses the principle of the Doppler effect where the wavelength of light is shifted as an object (*i.e.* flow tracer) moves across a light beam, interfering with a second light source and so creating greater intensity peaks.

The LDA technique is founded on the concept of introducing tracer (or seeding) particles into the flow. The size, shape and density of these particles are such that they can be considered as perfect flow tracers, the presence of which has no bearing on the flow patterns. Ideally, the particles must demonstrate good flow tracing characteristics, be of a sufficient size to scatter sufficient light for imaging purposes but not interact with each other (Westerweel, 1993).

The flow measurements are performed at the intersection of two laser beams where there exists an interference fringe pattern of light and dark planes. The seeded particles scatter light in all directions; however, the intensity of the scattered light is a function of the position of detection. Scattered light is captured by a receiving optical set-up, and a photomultiplier converts the light intensity fluctuations to electrical signals which are subsequently converted to velocities using system-specific software. Thus, the LDA

technique derives ensemble averages for a given point in the flow, yielding rapid and accurate determinations of mean values as well as the fluctuating velocity component at a given point.

LDA techniques can operate in either forward or backscatter mode. The early LDA techniques adopted the forward scattering approach. However, this has now largely been superseded by the back scatter mode of analysis, as shown at Figure 4-3. This has the advantage of combining the transmission and receiving optics in one unit, avoiding the need to align two separate units. A useful summary of LDA analysis techniques may be found at Brown *et al.* (2004), which draws from the classical text on the subject of Durst *et al.* (1976).

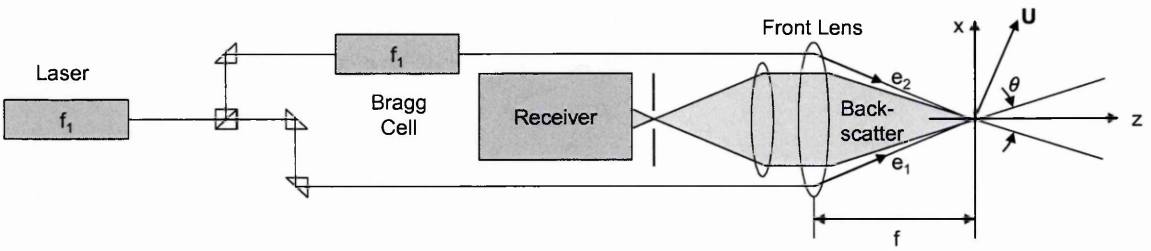


Figure 4-3: Principles of a backscatter LDA system (from Brown *et al*, 2004).

In this work, two-channel LDA measurements were undertaken on the cylindrical jar test vessel by the Experimental and Computational Laboratory for the Analysis of Turbulence (ECLAT) at King's College London, UK. The experimental apparatus consisted of a laser Doppler anemometer operating in dual beam mode. A 3 Watt argon-ion laser was used. The system included a beamsplitter and Bragg cell for frequency shifting. The signal was fed to a correlation-type signal processor and the amplified Doppler signal was monitored on a digital oscilloscope. Signal processing was performed on a personal computer. The axial and tangential components were measured simultaneously along an axial profile at r=0.5T (*i.e.* midway between shaft and wall). 23 measurements were taken along the profile at 5mm intervals and at seven different mixing speeds; *viz.* 30, 40, 50, 75, 100, 150 and 200 rpm. Unfortunately, the turbulence data from these experiments were not made available and so it was not possible to compare directly experimental and numerical turbulence data. However, it

was possible to validate the model on the basis of power dissipation. This was calculated for the CFD models via the use of the turbulence dissipation rate volume integral, as described in Section 5.2.3 below, thus providing validation of the turbulence data arising from the models.

4.1.3 Particle Image Velocimetry

Particle image velocimetry (PIV) is a two-dimensional optical technique used to infer details of a flow field simultaneously at many points and can be used to develop instantaneous two-dimensional velocity vectors over the full flow field. This is achieved by exploiting the optical characteristics of light when interacting with an inhomogeneous medium which is added to the flow as an indicator or marker. PIV is a subset of a broader group of optical techniques known as pulsed light velocimetry (PLV), and its principles have been considered several times in the literature (Lourenco *et al.*, 1989, Adrian, 1991, and Raffel *et al.*, 1998).

Similar to LDA measurements, seeded particles are assumed to be good flow tracers and so their velocities are taken as being representative of the local velocities within the flow field. A cross-section of the vessel is illuminated by a pulsing laser light sheet and the locations of particles are recorded at successive time intervals using a high resolution (2,000 pixels by 2,000 pixels) CCD camera positioned at right angles to the light sheet. The local fluid velocity is then calculated as the particle displacement divided by the time between two successive exposures. In order for accurate velocity measurements to be obtained, the time between exposures should be small compared to the timescales in the flow. The principal of operation of a PIV system, as presented by Papadopoulos & Arik (2004), is reproduced below at Figure 4-4

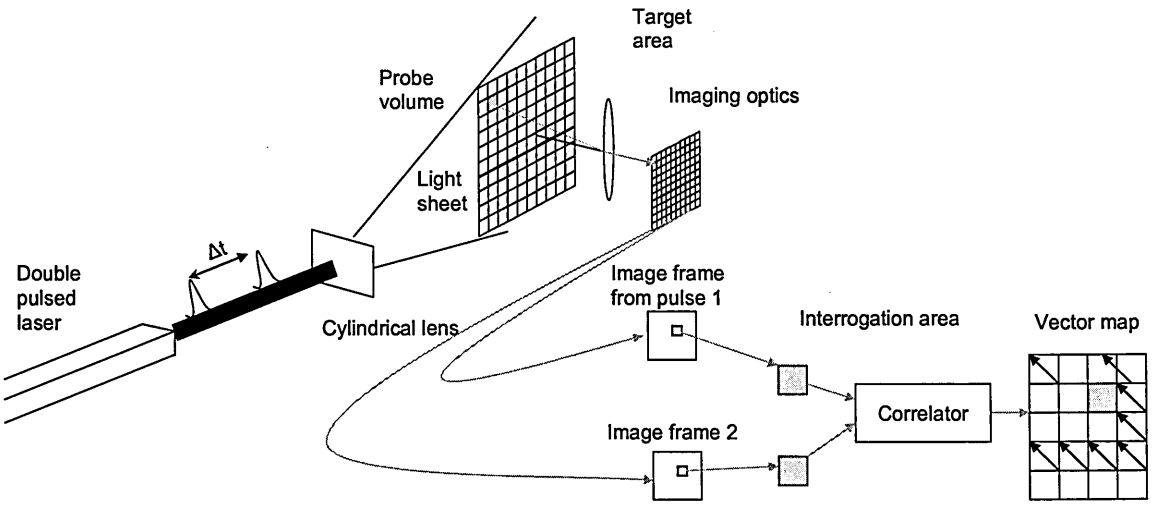


Figure 4-4: Principal operation of a PIV system (from Papadopoulos & Arik, 2004).

The light sheet is produced by a laser and associated sheet-generation optics. Image acquisition is undertaken using short light pulses to avoid streaking, and so either pulsed lasers (*e.g.* Nd:YAG) are used, or alternatively argon lasers with a shuttering facility to produce pulses are employed. The laser sheet so produced is typically just a few millimetres thick and illuminates the plane of study. The recorded images are divided into small adjacent or overlapping "interrogation areas", and the local fluid velocity is inferred from the displacement of the tracer particles over a finite time, Δt. If the particles are not ideal (*i.e.* they do not follow the flow field exactly), errors will be introduced into the velocity determination, and so careful selection of seeding particles is imperative for the successful application of the PIV technique. Melling (1997) reviewed the type and application of tracer materials that workers have employed in both liquid and gas PIV experimentation. In summary, particles should be non-toxic, non-corrosive and chemically inert, with specific examples being silver-coated hollow glass spheres, polystyrene, polymers, titanium dioxide, aluminium oxide and hydrogen bubbles. Furthermore, as local velocities can only be inferred from locations where particles are present, care must be taken to ensure that the density of seeding particles is appropriate for the volume of fluid considered. If the seeding concentration is low, only limited flow information will be obtained. However, as the density increases, it becomes increasingly difficult to discern particle pairs across two successive images.

Interrogation areas range in size from 16 x 16 pixels to 32 x 32 pixels. Although it is possible to capture multiple images on a single frame and determine displacements by an auto-correlation technique, this method is not without its limitations, and so the currently preferred method in PIV is to capture two successive images on separate frames and use cross-correlation techniques to determine displacements. Detailed descriptions of these techniques are to be found at Westerweel (1993) and Keane and Adrian (1992). Raw PIV data obtained from cross-correlation of two images are validated and smoothed before statistical valuations are calculated. Once the data have been validated, the mean velocity components and standard deviation of the mean may be calculated.

In this work, PIV measurements were undertaken on the Hudson vessel. The PIV system used is shown at Figure 4-5 and comprised a New Wave Solo III laser, a PIVCAM 10-30 Camera and a LaserPulse Synchroniser (TSI Inc.). Seeding material used was spherical glass hollow silver particles, $10\mu m<d<30\mu m$ in size. Data processing was undertaken using the Insight-NT PIV software, mounted on a personal computer.

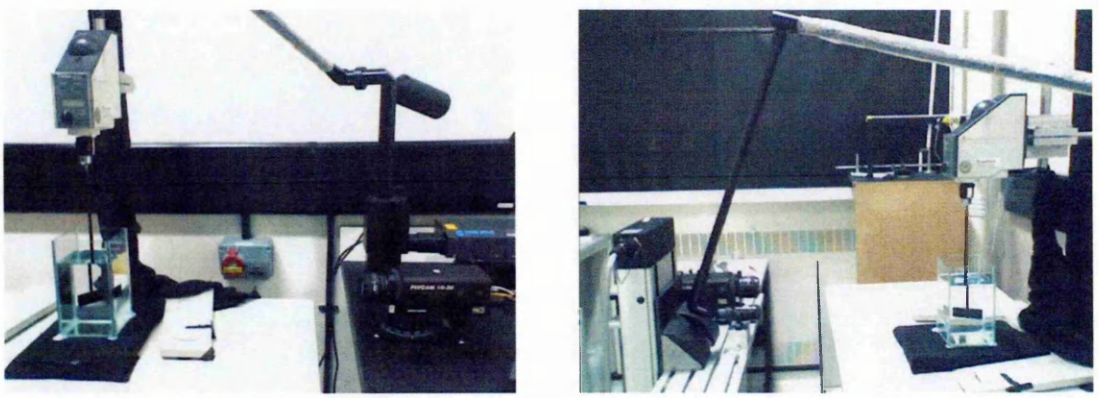


Figure 4-5: PIV system used.

Laser light sheets were generated at six distances from the centre-line of the vessel for six different mixing speeds. Table 4-1 below shows the locations of the laser light sheet and the mixing speeds analysed. The laser light sheet and axial profile measurement locations are shown at Figure 4-6. 200 pairs of images ($\Delta t = 300\mu s$) were recorded for each scenario, and in total 7,200 pairs of images were recorded, generating in excess of

15GB of data. The image files were analysed using a bespoke software cross-correlation function to generate instantaneous vector fields. The data output arising from the PIV software provided the magnitude and direction of each vector in the frame. The software also generated an overall mean flow for each mixing speed and displacement.

Table 4-1: **PIV analyses undertaken on Hudson vessel.**

Mixing speed, rpm	Displacement from centreline of vessel, mm					
	0	10	20	30	40	50
40	✓	✓	✓	✓	✓	✓
50	✓	✓	✓	✓	✓	✓
75	✓	✓	✓	✓	✓	✓
100	✓	✓	✓	✓	✓	✓
150	✓	✓	✓	✓	✓	✓
200	✓	✓	✓	✓	✓	✓

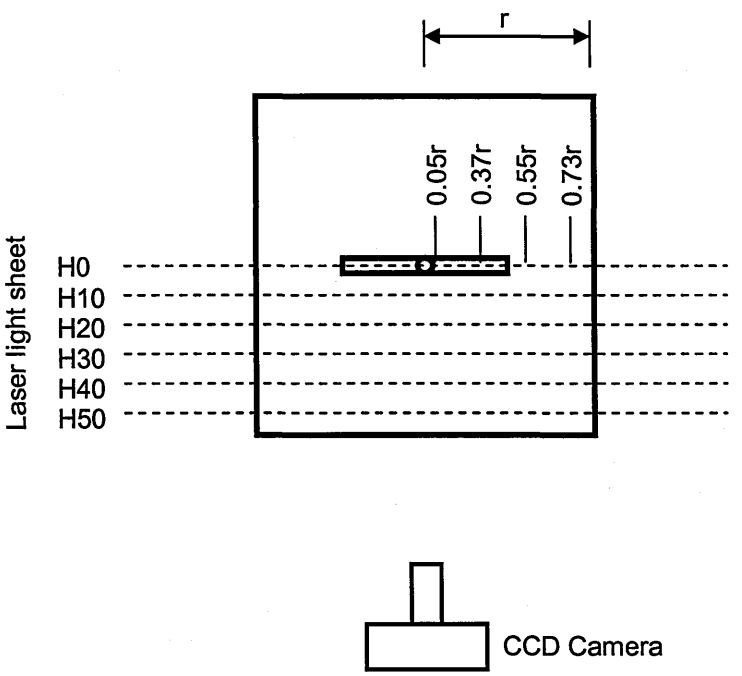


Figure 4-6: **Laser light sheet and axial profile measurement locations – plan view.**

4.2 Experimental Results

4.2.1 Power Measurement

Power number experiments were undertaken as described in section 4.1.1 above. The resulting relationships between Power number and Reynolds number for the two vessels are shown below at Figure 4-7. (Reynolds number has been calculated according to Equation 2-4, *i.e.* $R_e = \frac{\rho_l D^2 N}{\nu}$). In the turbulent flow regime, the plots are largely similar and typical. As has been shown elsewhere (*e.g.* Amirtharajah *et al.*, 1991), within the transitional flow range, no simple relationship or generalised value can be ascribed to the Power number. However, as the Reynolds number increases, the value of the Power number attains a constant value. At lower Reynolds numbers (*i.e.* <7,000), it was found that the value of the frictional losses were greater than 25% of the losses in water. It is believed that where the frictional losses are so high relative to the losses in water, the torque measurement technique is not applicable (Bujalski, 2006). Certainly, the results from the cylindrical vessel at Reynolds numbers below 9,500 appear anomalous and unreliable.

However, irrespective of the influence of frictional losses, the difference between the Power numbers for the two systems at the same Reynolds number (and so, mixing speed) is apparent. It is clear that the degree of power input is significantly larger for the square vessel as opposed to the circular one. In the turbulent zone, the average Power number for the Hudson vessel is 2.31, whereas the corresponding value for the cylindrical vessel is 0.46. It is concluded that this is due to the additional volume of water motivated and the action of the square walls acting as surrogate baffles within the vessel, whereas the energy input required to motivate the flow within an unbaffled circular vessel is less. Applying Equation 2-12, the vessel average velocity gradients have been calculated for each vessel and each mixing speed and are plotted at Figure 4-8 below. It is apparent that, as mixing speed increases, the vessel average velocity

gradients are greater for the Hudson vessel than the cylindrical vessel, with the degree of divergence at a maximum at a mixing speed of 200 rpm.

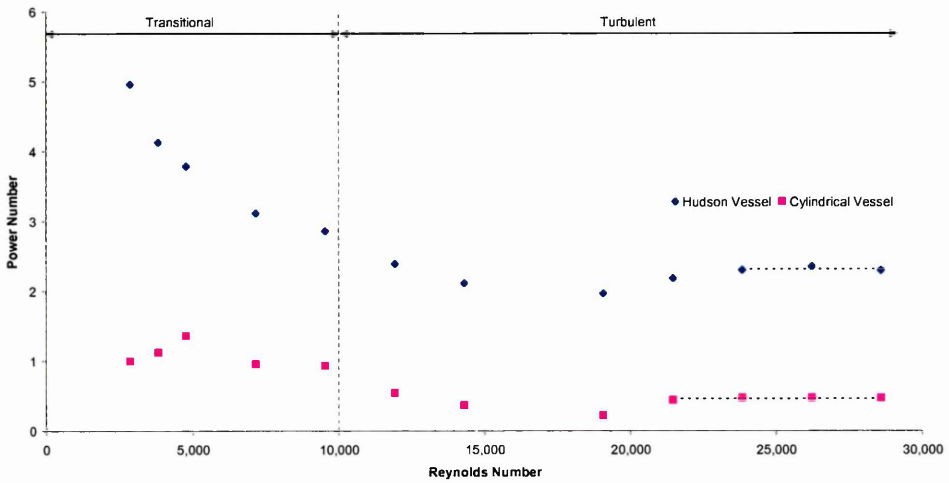


Figure 4-7: **Power number versus impeller Reynolds number for flat, two blade impeller in cylindrical and Hudson vessels.**

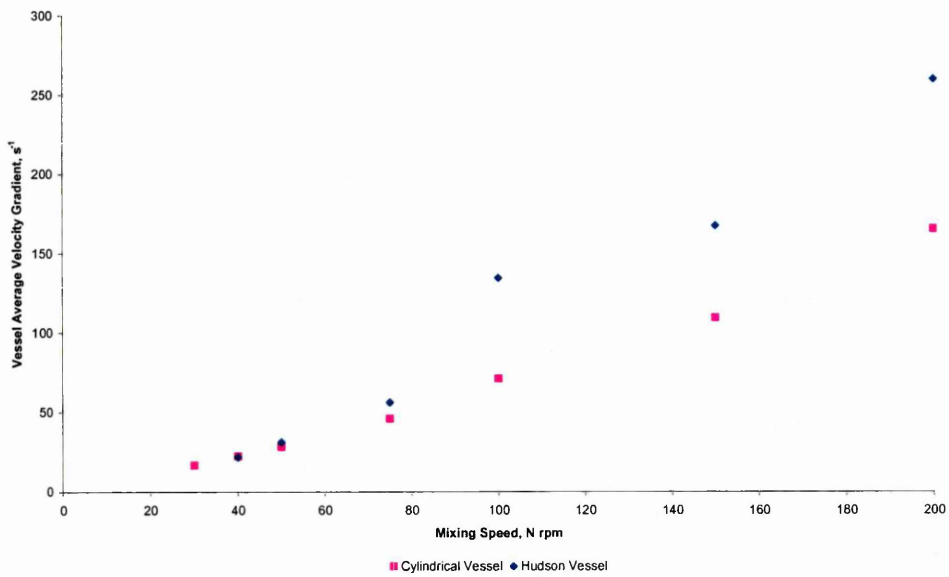


Figure 4-8: **Comparison of vessel average velocity gradient values, $\overline{G}$ s^{-1} for different jar test configurations.**

The relationships between Power number and Reynolds number for seven different impellers are plotted at Figure 2-4. It is clear from this Figure that different impeller

configurations have significantly different Power numbers. Furthermore, Table 2-3 shows that, whilst there is some uniformity in selection of impeller (*i.e.* two blade flat paddle) for jar test experiments, this choice is not universal.

The foregoing are important observations with regard to floc formation and breakage. Greater power input will have a consequential impact on the hydrodynamics of the vessel and, in particular, turbulence energy dissipation. Chapter 2 demonstrated and discussed the link between floc breakage and turbulence energy dissipation. Chapter 2 also showed the many different configurations of jar tester which workers have used to analyse floc growth and breakage, often comparing results from one scenario to another. In many instances, workers have used their results from one jar test scenario as a comparator with the results of another worker who had used a different raw water or coagulant. Conclusions have been drawn on the basis of the chemical reaction differences between the two scenarios. However, the result presented here shows that the different hydrodynamic environments encountered within the two different vessels will also have an influence on floc growth and, in particular, breakage. As a result, comparisons made between different jar test configurations must be treated with a degree of caution. Oldshue (1983) postulated that for low viscosity mixing the presence of baffles increases the Power number (and therefore the power drawn by the impeller) but reduces the overall general motion of fluid in the mixing vessel. The conclusion to be drawn from this is that one might expect higher absolute values of turbulence energy dissipation in the paddle region of a Hudson vessel, but that the turbulence energy dissipation values will be less well-distributed overall in the Hudson vessel compared to a cylindrical vessel. This observation is considered further at Chapter 6 below.

4.2.2 Laser Doppler Anemometry (LDA) Results – Cylindrical Vessel

A series of LDA experiments was undertaken on the cylindrical vessel as described in Section 4.1.2 above. The absolute ensemble average of the axial and tangential velocities were measured and these are shown at Figure 4-9 and Figure 4-11 below. If the flow is fully turbulent, workers have shown that the flow field can be made dimensionless using a characteristic length scale and velocity scale (Stanley & Smith

1995, Nouri *et al.*, 1987). For a stirred tank, dimensionless velocities scale with the characteristic velocity, *i.e.* $N\pi D$. Nouri *et al.* (1987) calculated radial velocity profiles in the discharge stream of a Rushton turbine for three different mixing speeds and three different fluids. The authors showed that by scaling the velocities with the tip speed, all profiles were reduced to a single line. Scaling variables work only in situations where both fully turbulent flow and exact geometric similarity are maintained (Kresta & Brodkey, 2004), the latter point meaning that it is not possible to extrapolate the LDA results obtained for the cylindrical vessel to the Hudson vessel. Here, the LDA axial and tangential velocity data obtained for the cylindrical vessel have been scaled on impeller tip speed ($=\pi ND$) for each mixing speed and are presented at Figure 4-10, and Figure 4-12. The maximum and minimum mean axial and tangential velocities for each mixing speed are tabulated below.

Table 4-2: Maxima and minima mean axial and tangential velocities measured in the cylindrical vessel at different mixing speeds.

Mixing Speed, rpm	Mean Axial Velocity, ms^{-1}		Mean Tangential Velocity, ms^{-1}	
	Maximum	Minimum	Maximum	Minimum
30	0.01094	-0.00507	0.06571	0.00538
40	0.01867	-0.00638	0.08908	0.07512
50	0.01653	-0.00786	0.1111	0.09646
75	0.02198	-0.01132	0.17323	0.1512
100	0.02691	-0.01516	0.2383	0.20908
150	0.03277	-0.02059	0.36759	0.32693
200	0.03668	-0.02393	0.4987	0.44531

For all mixing speeds, the flow fields are similar, with components highest for axial positions close to the impeller. Axial velocity vectors take opposite signs above and below the impeller as a result of the vessel walls deflecting the fluid in an upward and downward direction above and below the impeller respectively. It is noted that the tangential velocity shows a linear increase with increasing height. It is concluded that this phenomenon is a direct result of the strong centrifugal forces applied to the water by the impeller. It is also noted that, in contrast to Nouri *et al.* (1987), the velocities do not appear to scale exactly. It is concluded that this is because for the lower mixing speeds (100 rpm and below), the flow is not fully turbulent, but rather it is in the transitional range as indicated at Figure 4-7.

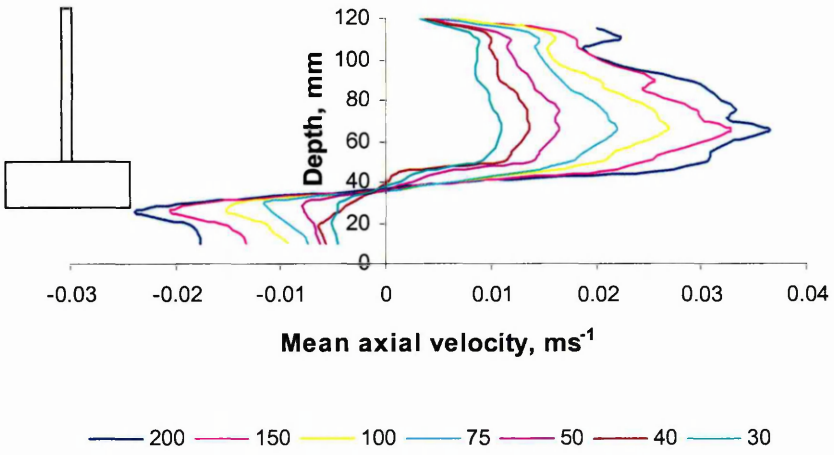


Figure 4-9: **Mean axial velocities generated in cylindrical vessel at various mixing speeds.**

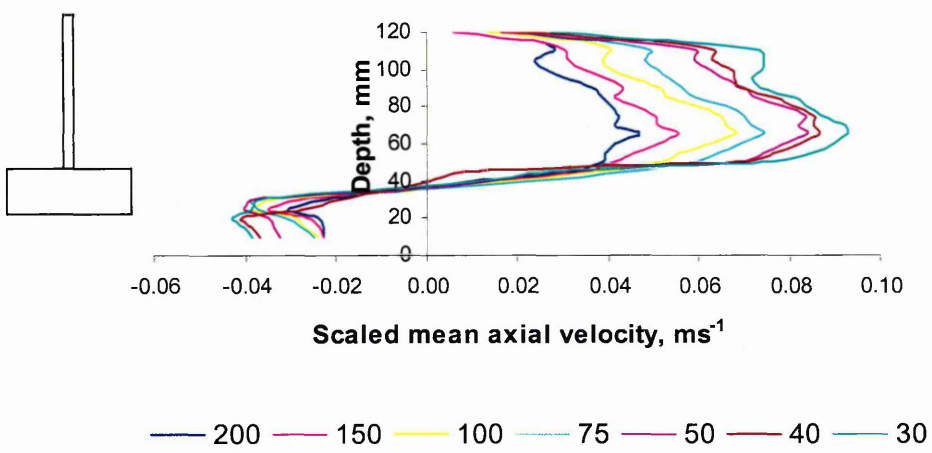


Figure 4-10: **Scaled mean axial velocities generated in cylindrical vessel at various mixing speeds.**

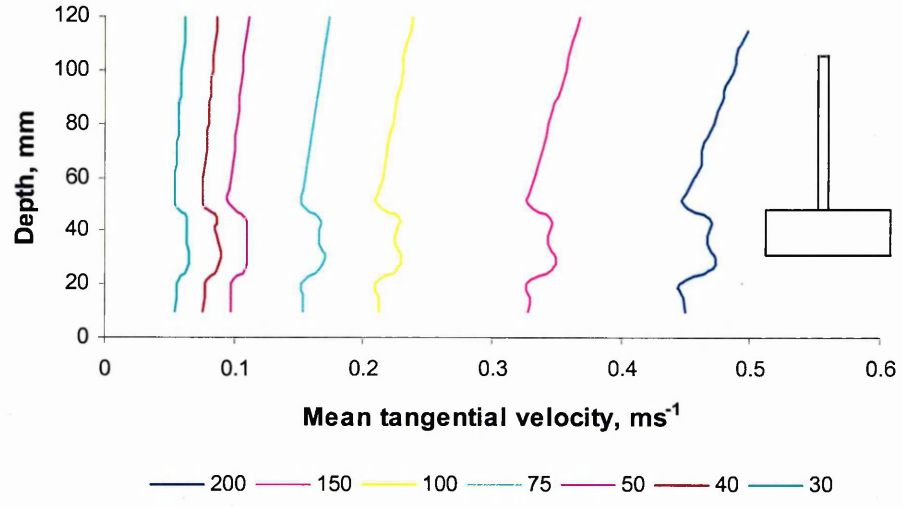


Figure 4-11: **Mean tangential velocities generated in cylindrical vessel at various mixing speeds.**

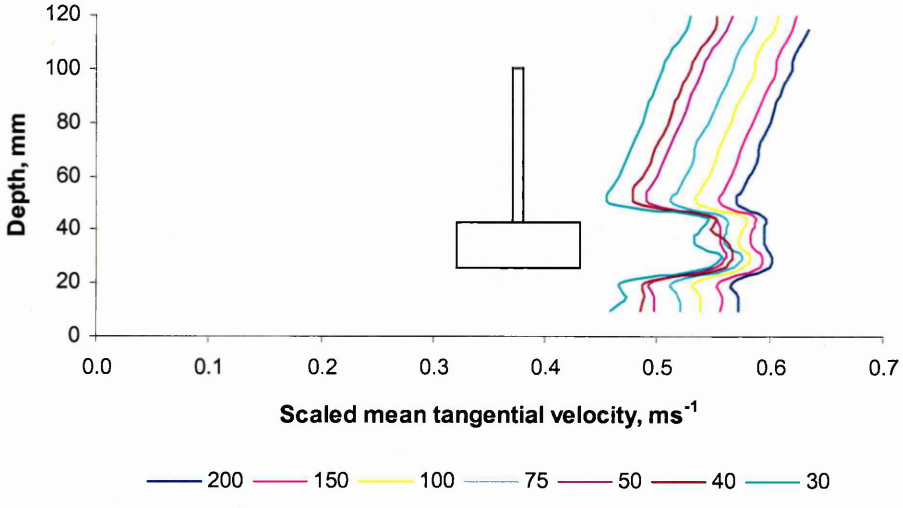


Figure 4-12: **Scaled mean tangential velocities generated in cylindrical vessel at various mixing speeds.**

Phase resolved mean axial and tangential velocity components for a mixing speed of 100 rpm at four depths within the vessel are shown below at Figure 4-13 and Figure 4-14. It is clear that the velocity components vary significantly in the vicinity of the paddle (z = 35mm and z = 60mm), whereas the velocities in the upper and lower reaches are more stable. However, there is still some evidence of the impeller influence on the tangential velocity component at z = 120mm, indicating a degree of fluid agitation (*i.e.* mixing) throughout the vessel, not just confined to the paddle region.

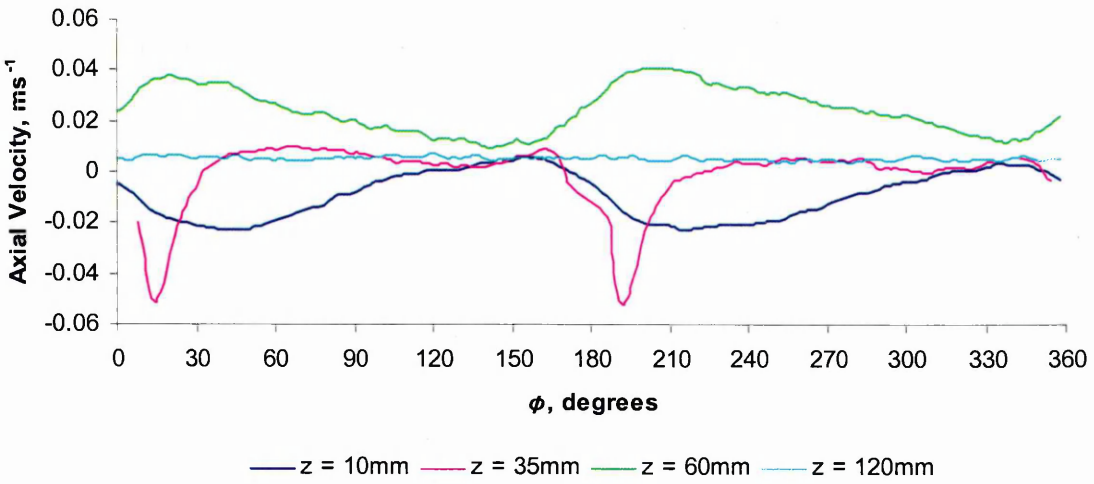


Figure 4-13: **Phase resolved mean axial components at various vessel depths, N=100 rpm.**

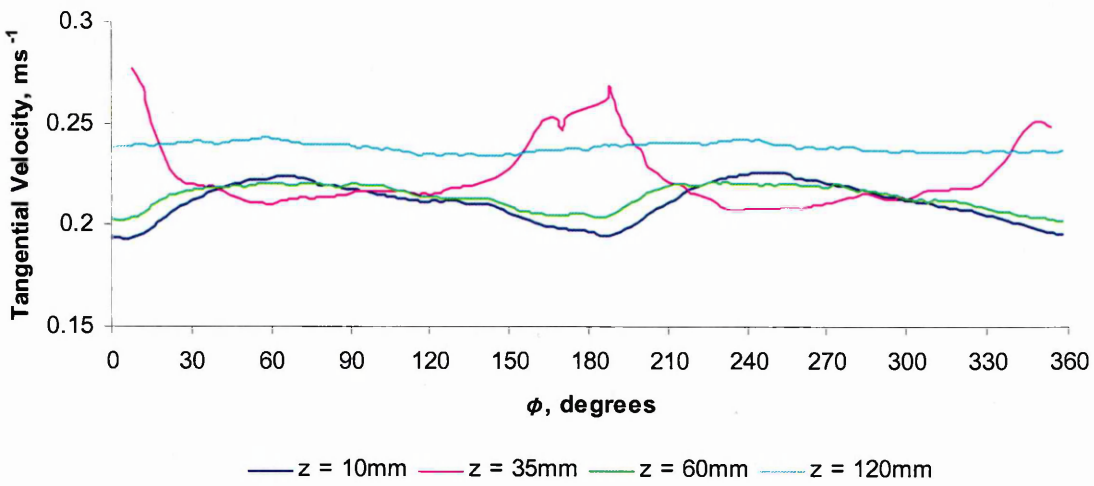


Figure 4-14: **Phase resolved mean tangential components at various vessel depths, N=100 rpm.**

4.2.3 Particle Image Velocimetry (PIV) Results – Hudson Vessel

Using the techniques outlined in Section 4.1.3 above, mean velocity fields were obtained for the Hudson vessel for each mixing speed after statistical averaging over 200 instantaneous velocity fields. The mean velocity fields for one half of the flow field, taken through the centreline of the vessel (line H0, Figure 4-6 refers), for the 200, 150, 75 and 40 rpm mixing speeds are shown at Figure 4-15 and Figure 4-16. It can be seen that the structure of the mean flow is similar in each case, with the recirculation loops above and below the impeller region clearly displayed in each case. It is also clear that the mean velocities increase with increasing mixing speed. The mean and maximum velocities found in each flow field are shown at Table 4-3 below.

Table 4-3: Measured mean velocities in the Hudson vessel at stated mixing speeds.

Mixing Speed, rpm	Velocity Magnitude Mean, ms^{-1}	Velocity Magnitude Maximum, ms^{-1}
40	0.015138	0.182515
50	0.020092	0.153939
75	0.022102	0.133202
100	0.026952	0.099003
150	0.036539	0.118915
200	0.047620	0.166482

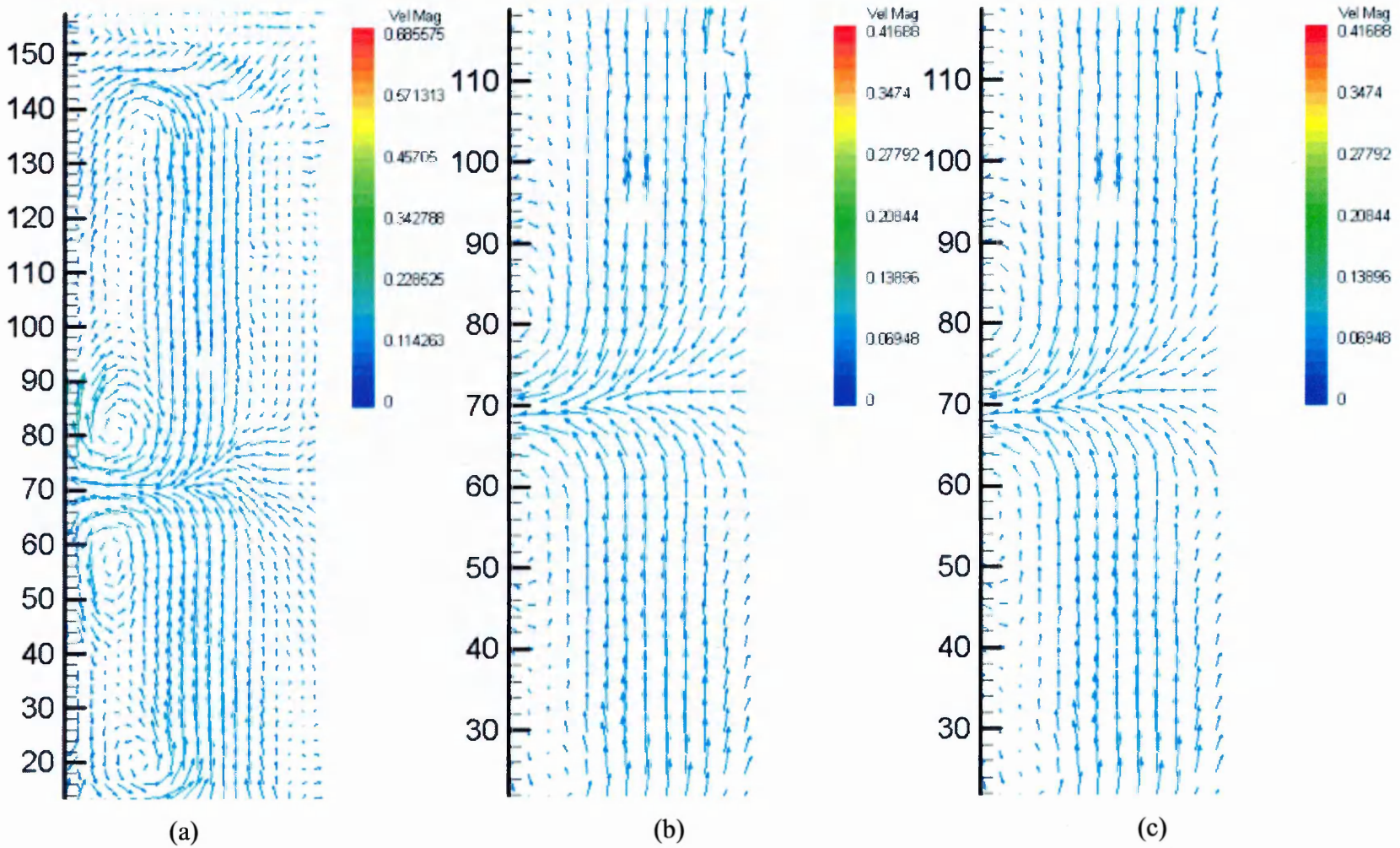


Figure 4-15: **Mean velocity fields for (a) 200 rpm, (b) 150 rpm & (c) 100 rpm.**

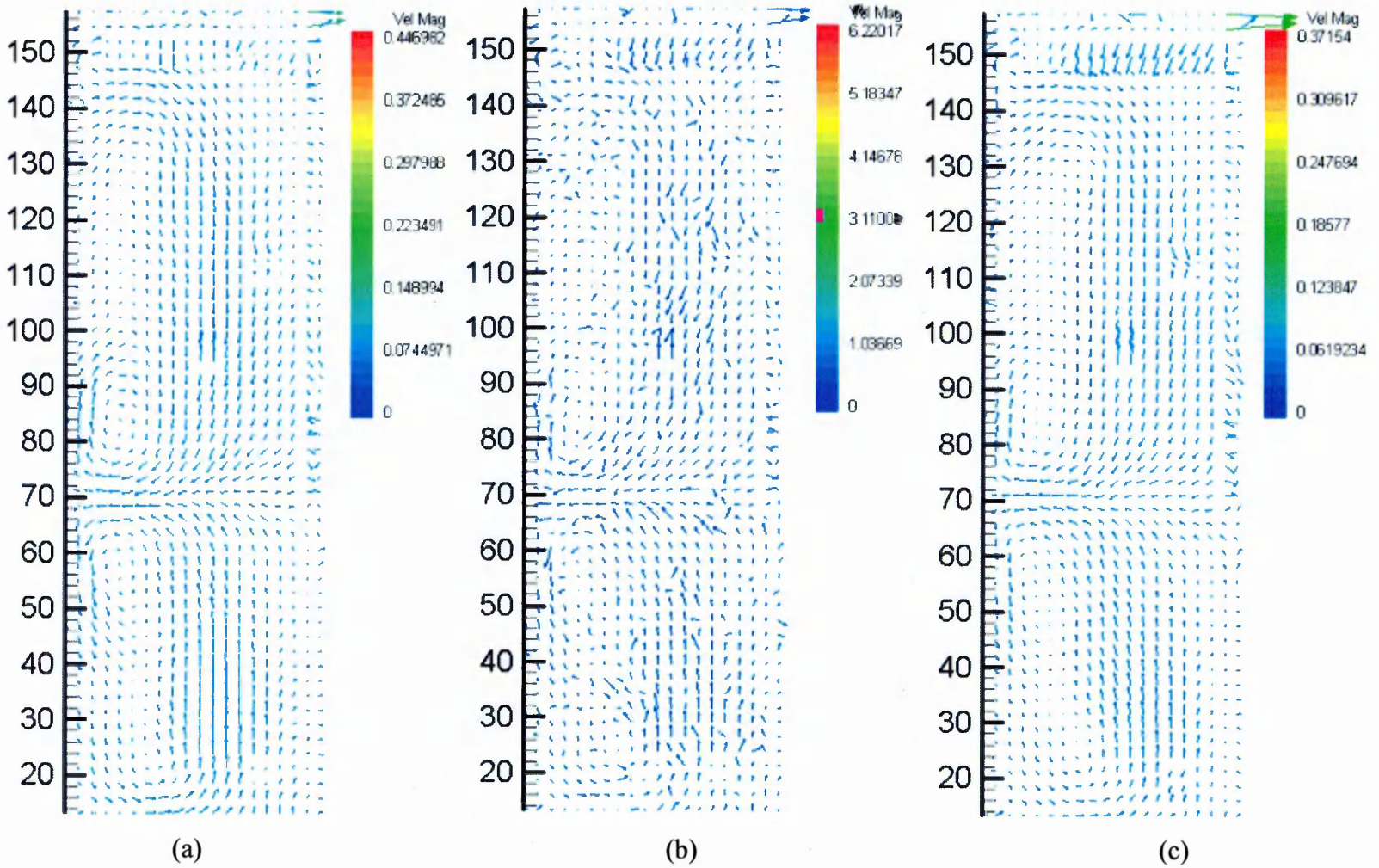


Figure 4-16: **Mean velocity fields for (a) 75 rpm, (b) 50 rpm & (c) 40 rpm.**

Mean velocities along depth profiles with increasing distance from the shaft are plotted at Figure 4-17. All profiles show an increase in mean velocity in the paddle region, and the effect of distance from the shaft (*i.e.* increased proximity to the paddle tip) is apparent.

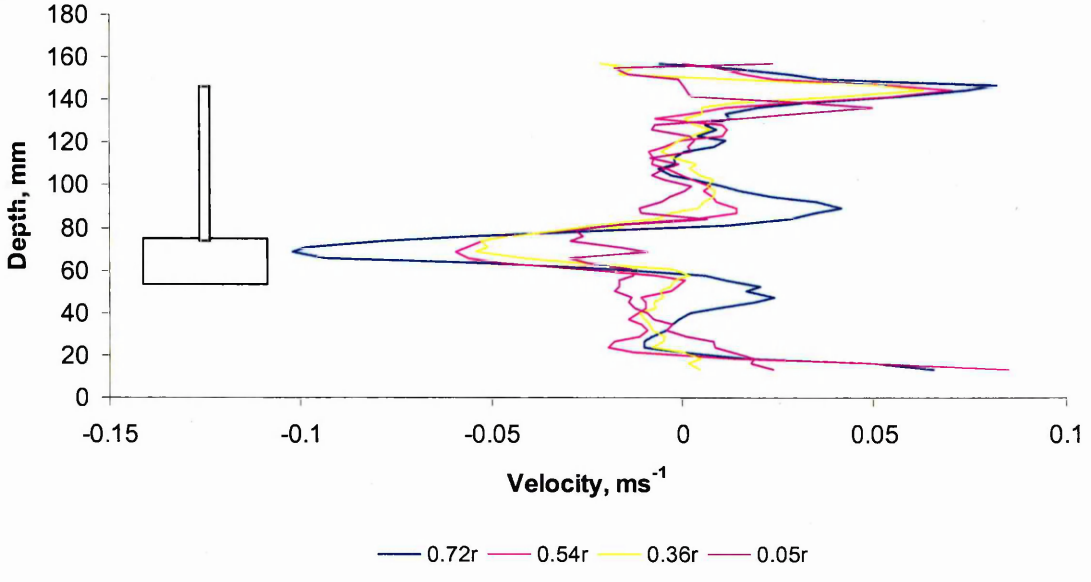


Figure 4-17: Mean velocity profile with increasing distance from shaft (locations shown at Figure 4-6).

However, useful as the mean flow field plots are as an indication of the velocities generated within the vessel, they are meaningful only in terms of statistical averages. In order to understand better the local and instantaneous phenomena which control floc size, it is important to consider the instantaneous velocity fields. Plots of four instantaneous paddle positions for the 200 rpm scenarios are given below at Figure 4-18. Instantaneous velocity profiles along an axial line just beyond the paddle tip (0.82*r*) for each of the paddle positions are shown at Figure 4-19. Significant differences between velocity components at the same position are apparent.

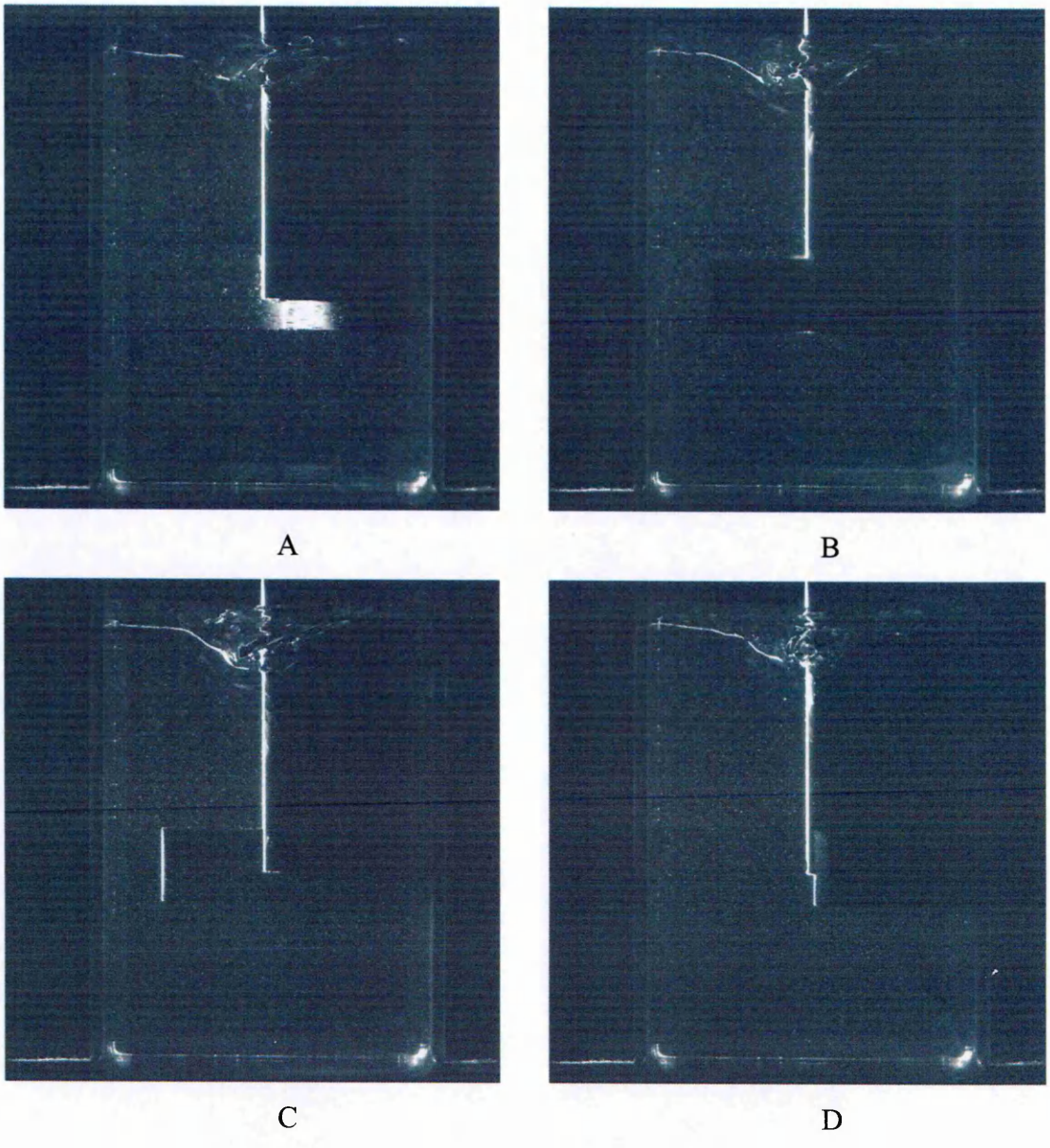


Figure 4-18: **Instantaneous paddle positions for 200 rpm scenario.**

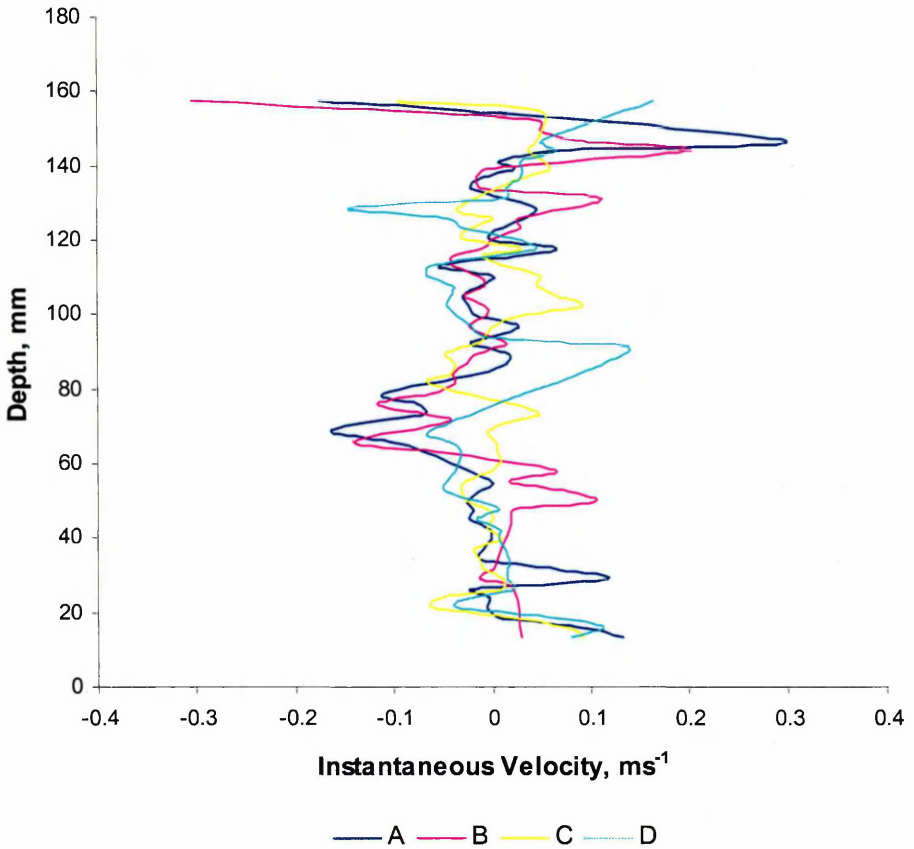


Figure 4-19: **Measured instantaneous velocities taken along velocity profile 0.82*r* through vessel centreline (H0) at various different paddle locations (Figure 4-6 and Figure 4-18 refer). N = 200 rpm.**

4.3 Summary

The experimental determinations of the impeller Power number, developed using the torque transducer, have demonstrated significant differences between the cylindrical and Hudson vessels. Using these data, it has been possible to determine vessel average velocity gradients for each of the two vessels. Significant variations in the vessel average velocity gradients were observed, thus demonstrating the different hydrodynamic environments generated within them arising as a result of the geometrical differences alone. Consequently, comparisons of floc growth and breakage data made between different jar test configurations must be treated with caution.

Comparisons of the measured Power number values with previously published data for other paddles show further significant variations. Again, this gives rise to a variation in the velocity gradients generated (both local and vessel average). Chapter 2 showed that there has been no absolute uniformity of choice of jar test paddle amongst workers in the past and so this result renders the validity of comparison of breakage mechanisms across different configurations open to question.

As anticipated, PIV and LDA data demonstrated that the highest velocity components were to be found in the impeller region for both vessels. PIV data demonstrated the consistency of the average flow structure across the range of mixing speeds. However, the variations in instantaneous velocity at constant mixing speed were also demonstrated.

LDA data measured on the cylindrical vessel showed reasonable scaling of axial velocity components at different mixing speeds when scaled on paddle tip speed ($N\pi D$). Scaling was not exact, and this is concluded to be a result of flow regimes being in the transitional, as opposed to fully turbulent, zones.

Although maximum velocities are found in the impeller regions for both vessels, for the cylindrical vessel, the LDA data shows evidence of impeller influence on the tangential velocity component very close to the water surface at z = 120mm.

5 CFD Analyses – Methodology and Validation

5.1 Methodology

5.1.1 Background

As discussed in Chapter 2, the flow of most fluids may be analyzed mathematically by the use of two sets of equations; the Continuity Equation and the Navier-Stokes equations. Computational fluid dynamics (CFD) involves the solution of these equations for any point in space adjacent to an object.

During the development and use of any CFD model, several project-specific criteria must be taken into account, including the choice of turbulence model, grid density, and the selection of appropriate boundary conditions. The case of the simple jar test, where there is highly swirling flow within a constricted volume, presents some specific and interesting challenges for the modeller. The aims of the research reported in this chapter of the thesis were to consider the challenges of numerical simulation of the flow field generated in a jar tester, to assess the options available to address these and to develop a robust strategy for doing so.

The literature contains examples of practical investigations into floc strength using a standard jar test apparatus and procedure (*e.g.* Gregory & Rossi, 2001, Bouyer *et al.*, 2001, Jarvis *et al.*, 2004, Jefferson *et al.*, 2004, Fitzpatrick *et al.*, 2004). However, there is little reported research which has attempted to model the process using CFD. The research which has been published (Korpijarvi *et al.*, 1999, 2000, Essemiani & de Traversay, 2002a & b) is limited in scope. These papers considered the flow fields generated by a jar tester and a pilot scale flocculator and recognised the limitations of the average velocity gradient, G_{ave}, as a design parameter. However, none of the papers considered, other than qualitatively, how these results would impinge on flocculation performance.

In this work, the commercially-available CFD code, Fluent v6 (Fluent, Sheffield, UK) was used to model the flow field within the two sets of jar test apparatus described in Chapter 4. The MixSim v2.0 code (Fluent) was used to define and pre-process the grid geometry for the cylindrical vessel. The Gambit code (Fluent) was used to define and pre-process the Hudson grid geometry.

5.1.2 Modelling Rotating Flows

The modelling of the rotating paddle and its relationship with the fluid contained within the beaker is clearly of great importance in a simulation such as this and a number of approaches are available to the modeller to represent this scenario.

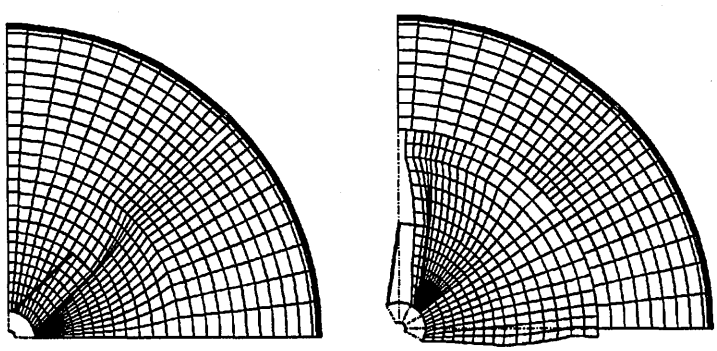
The traditional approach to modelling the paddle mixers (or impellers) was to apply experimentally-obtained velocity data in the outflow of the impeller (*e.g.* Ducoste & Clark, 1999). However, such methods have now largely been superseded by explicit calculation of the flow pattern in the vicinity of the blades without recourse to experimental data. This is to be favoured above the application of experimental data, since it may be necessary to extrapolate any such experimental data in order to apply it to situations for which no experiments have been, or can be, performed.

One method of explicitly calculating the flow field in this scenario is the sliding mesh method. With the sliding mesh method, the tank is divided into two regions that are treated separately: 1) the impeller region and 2) the tank region which includes the bulk of the liquid, the tank wall, the tank bottom and the baffles. The grid in the impeller region rotates with the impeller, whilst the grid in the tank remains stationary. The two grids slide past each other at a cylindrical interface (Figure 5-1a). The sliding grid model explicitly calculates the mixer region, and then rotates this section of the grid relative to the rest of the domain. The sliding mesh model assumes that the flow field is unsteady, and models the actual interactions as they occur. Consequently, the sliding mesh model is the preferred option in instances where interaction between rotor and baffle is strong and a more accurate simulation of the system is desired. It is accepted

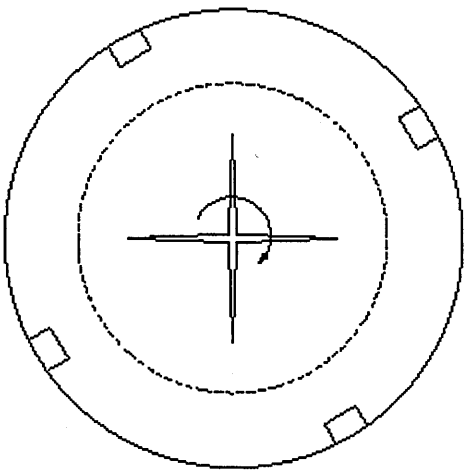
that the sliding mesh model is the most accurate method for simulating flows in multiple moving reference frames, but also the most computationally demanding. (An alternative approach is discussed below). Using the sliding mesh model to analyse laminar flows in a stirred reactor, Bakker *et al.* (2000) used a time step of 0.01s and 1000 time steps to study the flow created by a pitched blade turbine in a tank. With an impeller rotational speed of 3.75 s^{-1}, 37.5 revolutions were simulated. Bakker *et al.* reported that the calculation time was approximately 15 minutes per impeller revolution on a Cray C-90 computer, giving a total CPU usage time of 9.75 hours.

An alternative means of modelling the mixing process is to use the Multiple Reference Frames (MRF) approach (Luo *et al.*, 1994). This approach adopts two reference frames; one stationary frame related to the vessel walls; the other related to the rotating shaft and impeller (Figure 5-1b). The fluid zone is divided into two separate regions, one of which is related to the stationary zone, whilst the other, close to the rotating impeller, is related to the moving zone. The momentum equations and closure models are resolved in the separate zones and a steady-state approximation is made at the zone interface. The mesh does not move in this technique.

The MRF is computationally far more expedient than the sliding mesh method and for steady state applications has been used successfully to model mixing systems of various types. However, if an unsteady solution is required, the sliding mesh approach is the method of choice. For the research reported here, in the first instance, the mixing process was modelled initially using both approaches in order to assess the accuracy of each.



(a) Sliding mesh in two orientations, shown in 2D (from Marshall & Bakker, 2004).



(b) Cylindrical mixing tank with an MRF boundary surrounding the impeller (from Fluent, 2005).

Figure 5-1: Sliding mesh and multiple reference frames techniques.

5.1.3 Boundary Conditions and Calculation Procedure

For the purposes of the CFD simulations, the liquid free surface was considered as a symmetry plane and, therefore, flat and frictionless. It is accepted that in reality, some vortexing is experienced at the surface and consequently the models are, to some degree, limited by this. Using CFD it is possible to track the shape of the liquid surface during mixing using the Volume of Fluid (VOF) Model. In this approach, the computational domain is extended beyond the surface to span the air / water interface, and the volume fraction of each phase is determined throughout the flow field by solving the continuity equation for one of the phases. For a homogeneous multiphase system consisting of air and water, the equation is solved for the volume fraction of the liquid phase. In a given computational cell, the volume fraction of unity represents pure water and zero represents pure air. Thus, the volume fraction of the air is obtained as the difference between the liquid phase volume fraction and unity. The air / water interface is determined by identifying the cells where the volume fraction is between zero and unity. (Further details are available at Fluent, 2005). Haque *et al.* (2006) adopted the VOF approach to simulate the flow field in unbaffled vessels using a paddle impeller and a Rushton turbine (Table 2-3 refers). Using the MRF approach to

modelling rotating flow and the Reynolds Stress Transport model to model turbulence, Haque *et* al (2006) reported a typical run time of 70 hours to achieve convergence. Thus, it can be seen that the computational expense of considering the vortex is significant. Whilst the authors reported reasonable correlation between observed and numerically-obtained vortex shapes, they found discrepancies between the predicted and measured values in the vicinity of the shaft. Haque *et al.* (2006) also compared axial velocities at various locations, but did not consider turbulence quantities.

Despite the reasonable results obtained by Haque *et al.*, it is noteworthy that Marshall and Bakker (2004) recommended that this approach should not be adopted for the prediction of vortex shape. Marshall and Bakker recognized that the VOF model has application in the monitoring of liquid surface shape, but suggested that the model is ill-equipped to deal with the bubble formation arising from the breaking of the air / water interface when air passes through grid cells where large momentum sources exist. As a result, Marshall and Bakker (2003) concluded that it is appropriate to use the VOF model to indicate whether or not vortexing will occur, but that it should not be used to predict the flow condition afterwards.

In this work, the extent of the vortexing is very small compared to the overall volume (vortex depth in the cylindrical vessel at 200 rpm was measured as 10mm). Haque *et al.* (2006) reported that the additional numerical complexity and computational expense of adopting the VOF model to simulate the free surface is significant, extending MRF run times to just under three days. This unfortunate aspect is further compounded by the conclusion of Marshall and Bakker (2004) that this approach is an inappropriate choice for modelling vortex development. As a result of the above, the decision was taken that for this work, the vortex would not be modelled. The validity of this decision is discussed further in Section 5.3.

The nature of the governing equations requires that the boundary conditions be specified for all dependent variables at the walls. Free slip conditions were specified at the water surface and no slip conditions were specified at the walls. In the region of flow adjacent to a no slip wall, the velocity profile will vary from zero at the wall surface to the free

stream velocity beyond the boundary layer. The boundary layer (or, near-wall region) comprises three layers: a viscous sub-layer where the flow can be considered to be approximately laminar, an outer, fully-turbulent layer, and a buffer zone in between. These zones are shown below at Figure 5-2, taken from Fluent (2005). A common approach to modelling the near-wall region (and the one adopted in this work) is via the use of semi-empirical formulae, termed wall functions, which link the solution variables at the near-wall with the wall itself. This is achieved via a standard wall function:

$$U^+ = \frac{1}{\kappa}\ln(E.y^+) \qquad \textbf{Equation 5-1}$$

where, κ represents the von Karman constant, and E is an empirical constant. Fluent (2005) provides the following definitions for U^+ *and* y^+:

$$U^+ \equiv \frac{U_P C_\mu^{1/4} k_P^{1/2}}{\tau_w / \rho} \qquad \textbf{Equation 5-2}$$

$$y^+ \equiv \frac{\rho C_\mu^{1/4} k_P^{1/2} y_P}{\mu} \qquad \textbf{Equation 5-3}$$

Where U_P = mean fluid velocity at point P,

k_P = turbulence kinetic energy at point P,

y_P = distance from point P to the wall,

μ = dynamic viscosity of the fluid.

The standard wall function in Fluent adopts Equation 5-1 where $y^+ \geq 1.225$. Where $y^+ < 11.225$, Fluent sets $u^+ = y^+$.

For the work reported here, wall function constants were set at κ=0.4187, E=9.793 and y^+=11.225. Prior to commencement of iteration, all velocities were set to zero, whilst k and ϵ were each set to 0.001 m^2s^{-2} and 0.01 m^2s^{-3} respectively.

In line with current best practice, a partially-converged solution was obtained using a first order discretisation scheme. A higher order scheme was then adopted in order to obtain the final converged solution. For all simulations, the monitored residuals (continuity, x, y and z velocities, turbulent kinetic energy, turbulence dissipation rate,

specific dissipation rate, and Reynolds stresses, as appropriate) were set to $1x10^{-5}$ which is in line with guidance on convergence criteria provided by Fluent (2005).

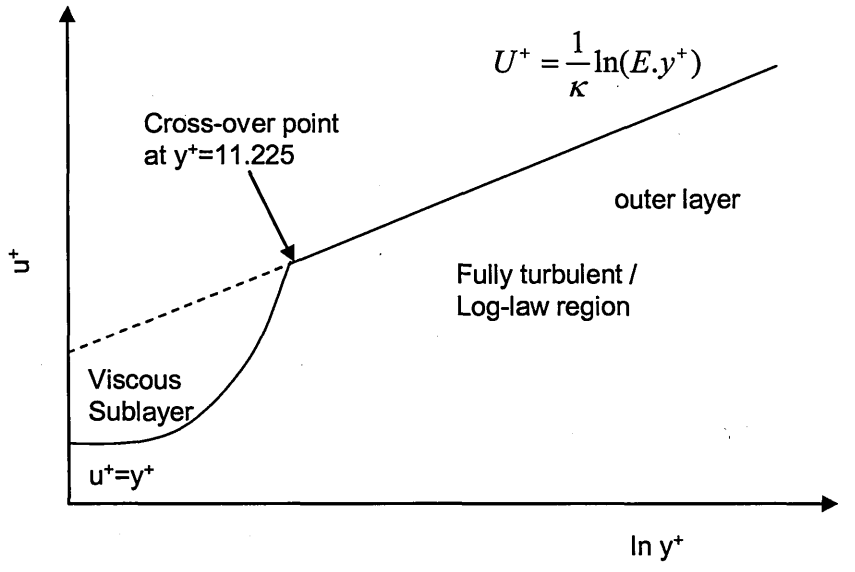


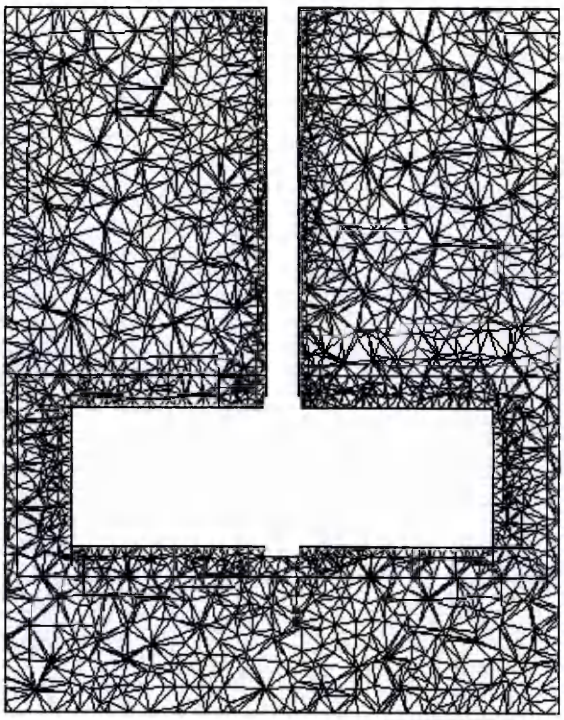
Figure 5-2: Subdivisions of the near-wall region, (from Fluent 2005).

5.1.4 Grid Resolution

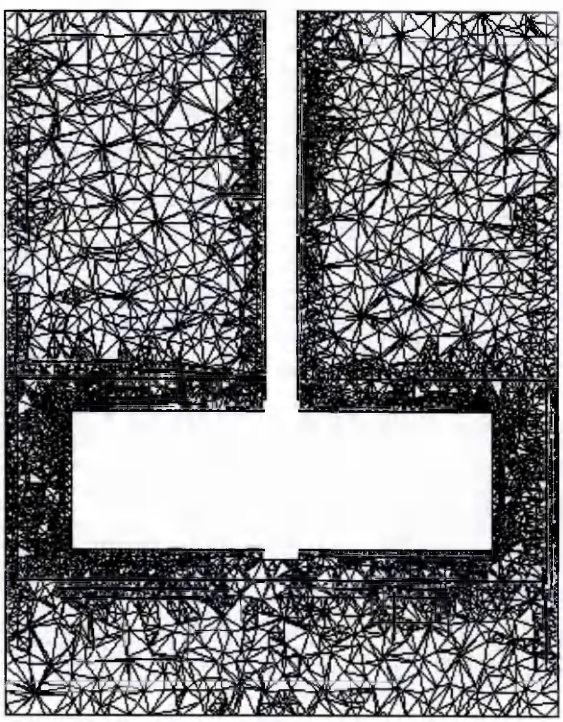
Adequate grid resolution is a key requirement of any CFD analysis. Poor or insufficient resolution will yield errors in the simulation results, whether or not all other key modelling requirements have been satisfied. If the grid is too coarse, solution detail will be lost as a result of interpolation between nodes. However, increasing grid density serves to increase time and computational expense. Consequently, it is imperative that the grid used is of sufficient quality and density.

In the cylindrical vessel analysis, four different grids were constructed and analysed to determine the effect of grid resolution on the simulated results. An initial coarse grid was produced using the default settings found in MixSim which set the initial grid size to 5mm and applied a mesh growth factor of 1.4. The mesh growth factor determines the steepness of mesh coarsening from the impeller into the volume. Fluent (2003) advises that a factor of 1.0 generates an equally fine mesh all over the volume; a factor of 1.2 generates a high-quality 'fine' mesh; and a factor of 1.4 achieves low cell counts while trying to maintain acceptable mesh quality. Applying a mesh grid factor of 1.4

yielded a grid of 87,777 tetrahedral cells, whereas a mesh growth factor of 1.2 yielded a grid of 98,517 cells in total. The second grid was refined further using the standard gradient adaptation technique and two further grids were developed by adapting the gradients of turbulent kinetic energy and turbulent energy dissipation. This process yielded grids of 283,470 and 337,944 cells, the latter being produced by setting adaption values of 0.5×10^{-3} m^2s^{-2} and 5.0×10^{-6} m^2s^{-3} for k and ϵ respectively. Slices through the mid-plane of the coarsest and finest grids are shown in Figure 5-3. The increased grid density along the impeller edges and vessel walls in the finer grid is clear.



(a) 87,777 cells



(b) 337,944 cells

Figure 5-3: **Grid Densities – cylindrical vessel.**

The effect of grid resolution on axial velocity is shown below in Figure 5-4. Mesh rotation was solved using the MRF approach and the RSM was used to solve the turbulence equations. For each grid density, axial data were extracted for a line x=0.025m, y=0.025m, $0<z<0.127$m. For depths of less than 0.025m, the four grids all show similar results. 0.025m corresponds to approximately 20% of overall tank depth, and it is interesting to note that Bhattacharya and Kresta (2002) reported a similar result when modelling a baffled stirred tank reactor of similar size.

It is clear from Figure 5-4 that the coarsest grid yields results which are significantly different to the three finer grids in the upper levels of the tank. Such is the discrepancy between the coarse grid and the other three that the results obtained might be deemed unsatisfactory for anything other than comparative exercises between different model parameters.

At peak and minimum axial velocities, the 98,517 cell grid yields results which are noticeably below the two finer grids at the scale shown. However, the difference is actually only 6.2×10^{-3} ms^{-1}. Whilst the finest grid yields the greatest range of values, there is little discernible difference between the results obtained from this grid and the 283,470 cell grid.

A key element of this research was an examination of the issues associated with the numerical simulation of a small stirred tank. One such issue is computing time and expense. There is a three-fold increase in grid density between grids (b) and (c), and in this instance, using a 1.4 GHz, 256 MB RAM laptop computer, this led to an increase in computing time from 16 hours to 24 hours. It was concluded that the increased computational effort was not reflected in a corresponding increase in accuracy of results and so the 98,517 cell grid was selected for use in this study. A grid paddle detail is shown at Figure 5-5. Validation of the model results using laser Doppler anemometry is discussed in Section 5.2 below. It is interesting to note that Korpijarvi *et al.* (1999) used two grid densities (30,470 cells and 67,584 cells) for modelling a similar size (1.1 litre) vessel. The grid density used for the cylindrical vessel in this research is some

46% finer than that used by Korpijarvi *et al.* (1999) and this observation is discussed below.

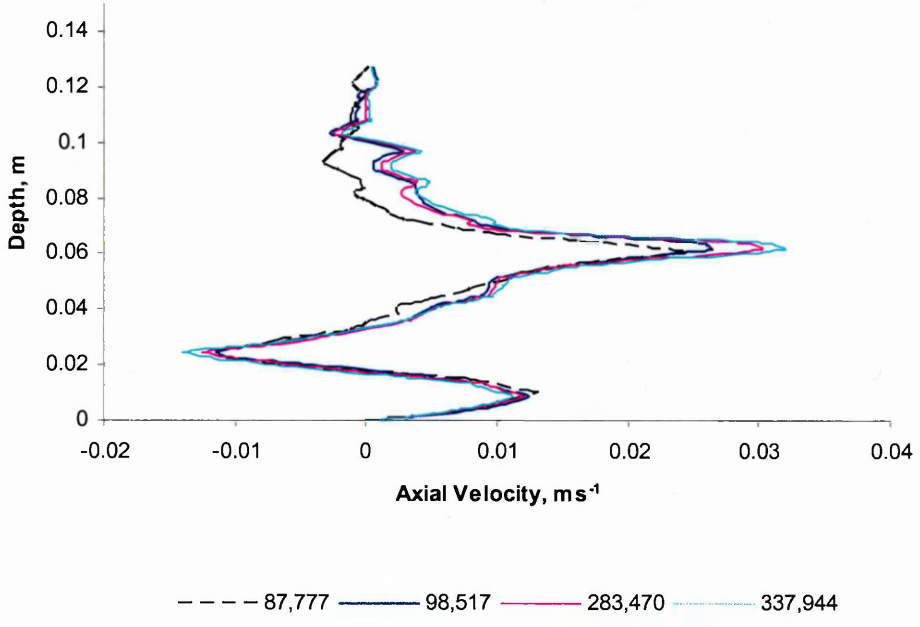


Figure 5-4: **Effect of grid density on axial velocity over tank depth at paddle face. (N = 200 rpm).**

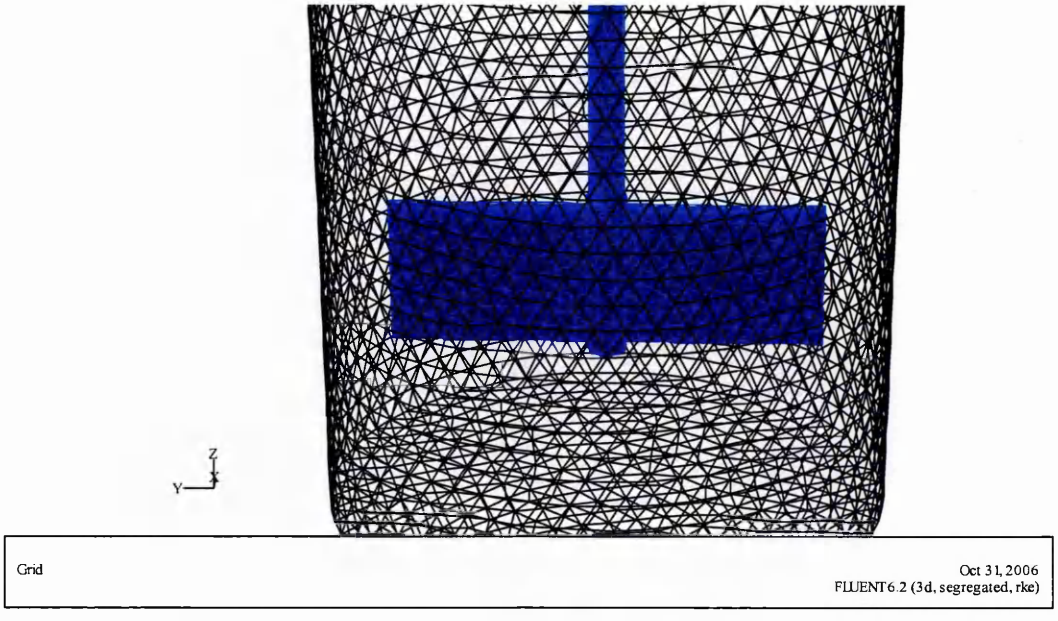


Figure 5-5: **Detail on paddle and vessel walls – 98,517 grid mesh.**

A similar grid resolution exercise was also undertaken for the Hudson vessel. Two separate grids were developed, one with 144,718 cells and the other with almost twice as many cells (281,785). Grid densities, taken through one half of the vertical mid-plane for the two vessels are at Figure 5-6. The left hand side shows the finer mesh, while the mesh on the right hand side is the coarser one. Additional mesh detail is apparent in the finer mesh around the paddle and also along the wall in the vicinity of the paddle. Axial velocity data were extracted for the two models along the same line, just beyond the paddle tip and they are plotted at Figure 5-7. Excellent agreement is observed between the two sets of data. However, the increase in computing time when undertaken on a laptop was significant. Convergence for the coarser of the two grids was achieved in 17 hours, whereas the finer grid took 30 hours to converge. In view of the good agreement between the two datasets, and taking account of the increased computing time associated with the finer grid, it was decided to use the model grid density of 144,718 cells for all future work, as shown at Figure 5-8.

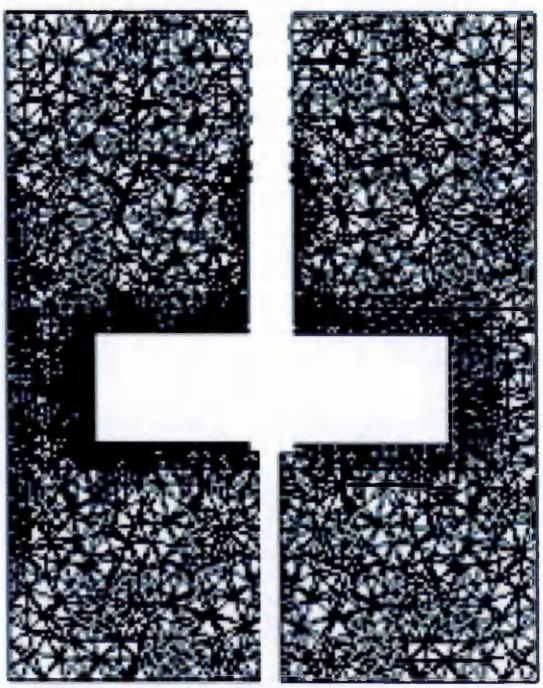


Figure 5-6: Sections through vertical mid-plane of Hudson vessel. Fine grid shown on left hand side, coarser grid on right hand side.

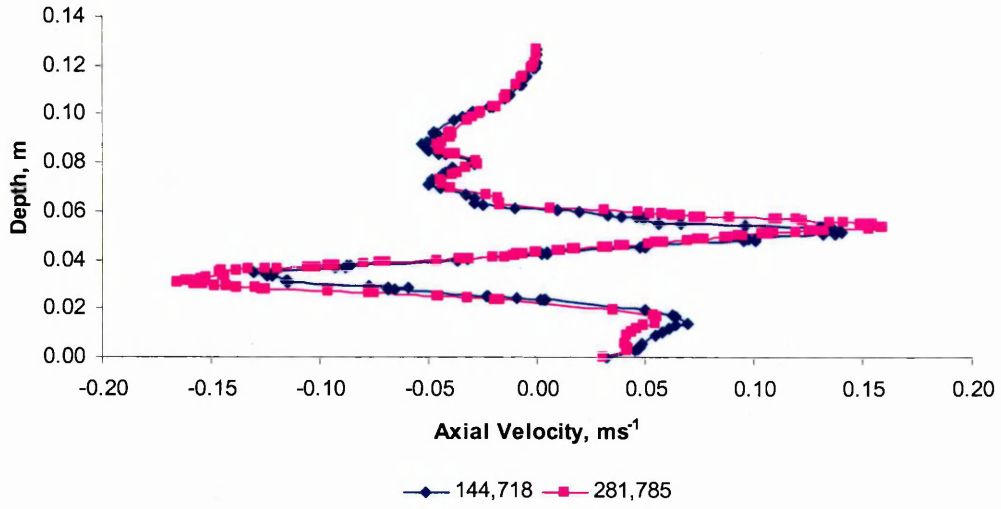


Figure 5-7: **Effect of grid density on axial velocity over tank depth. Hudson vessel.**

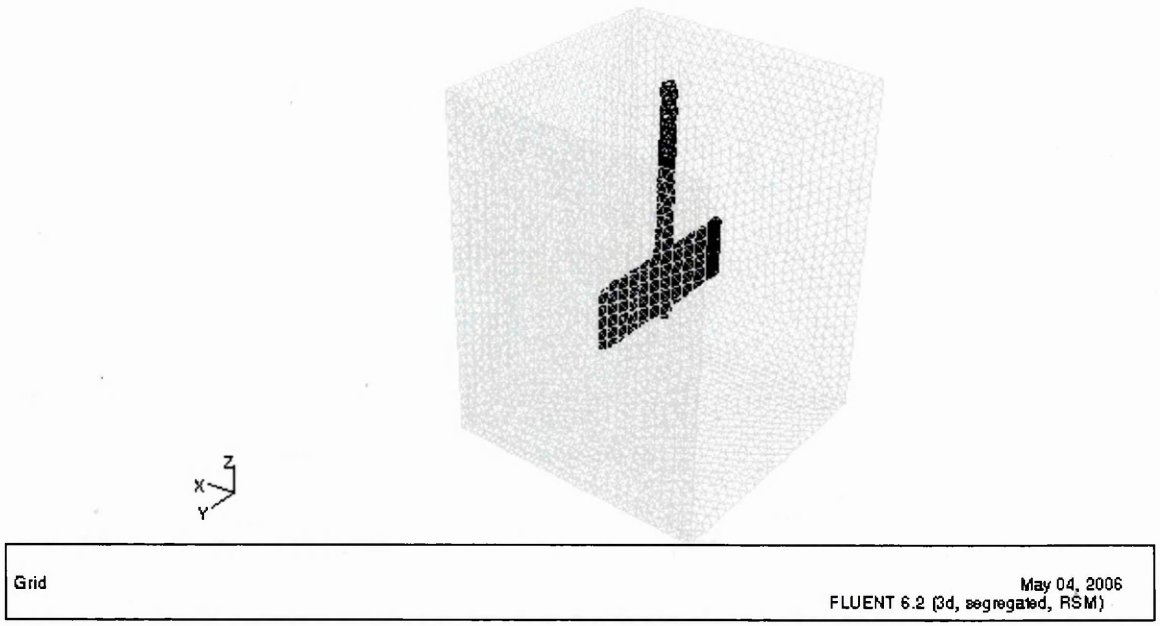


Figure 5-8: **Hudson vessel grid (144,718 cells).**

5.1.5 Turbulence Modelling

Fluent (2005) suggests that for modelling turbulent flows with a significant amount of swirl (such as that found in an unbaffled jar tester), consideration should be given to using one of the advanced turbulence models. A series of sensitivity analyses was undertaken on the CFD model of the cylindrical vessel. Using the computationally expedient MRF approach, five turbulence models were initially selected for comparison; the standard k-ϵ, realizable k-ϵ, k-ω, SST k-ω and Reynolds Stress models. (The RNG k-ϵ model was also assessed at a later stage.) For the two-equation models, using a 1.4GHz, 250MB RAM laptop computer, a steady-state solution for shaft and paddle rotation of 200 rpm was developed in approximately 12 hours. (Later work used the high performance computing facility at Cranfield University to reduce computing time). A converged solution for the RSM was obtained in 16 hours. Mean velocity profiles in the axial direction using different turbulence models and a rotational speed of 200 rpm are shown below in Figure 5-9. The profiles were obtained for a vertical line through the tank depth, 0.019m from tank centre (*i.e.* mid paddle). Visual inspection of the data suggests that there is good correlation between the results of all five models. This conclusion is in line with a similar piece of work reported by Korpijarvi *et al.* (1999).

A key focus of the research reported in this thesis is the velocity gradient, which is, of course, implicitly linked to turbulence dissipation rate, ϵ, via Equation 2-11. Consequently, it is instructive to examine variations in local turbulence dissipation rate, calculated using different turbulence models (Figure 5-10). All values have been calculated along a line extending from top water level to the bottom of the vessel, midway between the centre and the vessel wall. (The location of the paddle in relation to the results is shown for information).

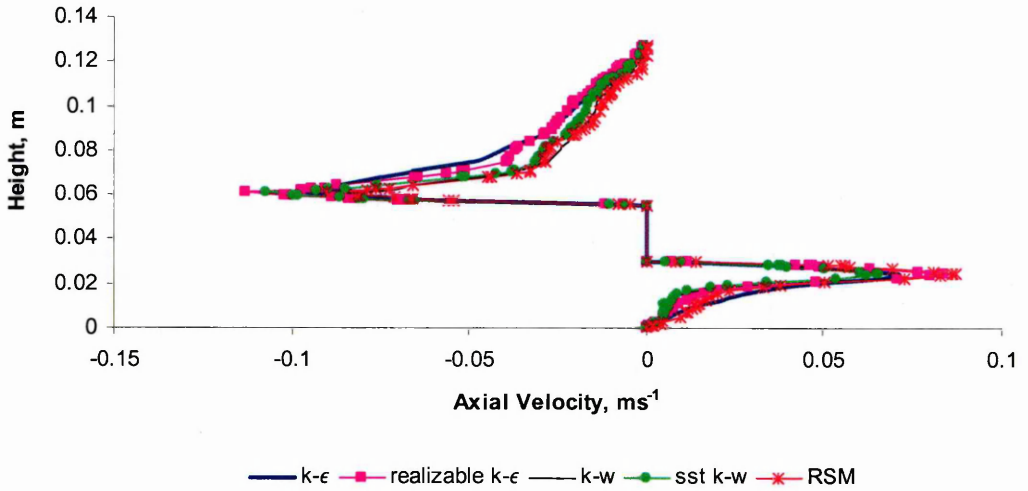


Figure 5-9: **Simulated axial velocity profiles over tank depth for different turbulence models, N = 200 rpm.**

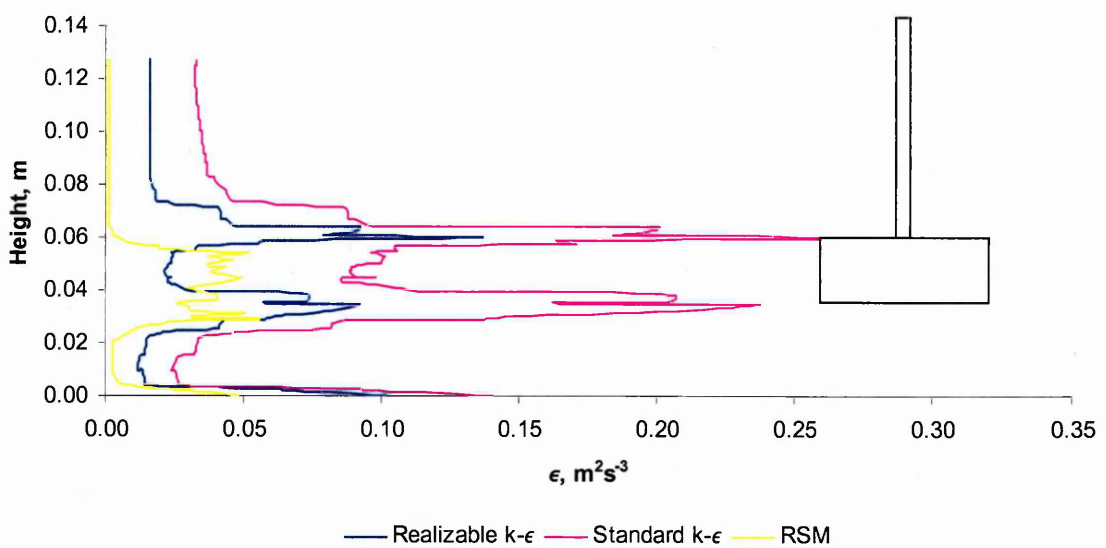


Figure 5-10: **Variation in turbulence dissipation rate at 200 rpm for different turbulence models.**

Figure 5-10 shows that all turbulence models produced maximum ϵ values at the top of the paddle (0.055m). The three model results all demonstrate little variation in ϵ values between 0.07m and top water level. Above and below the paddle, the models follow similar shapes and values. The RSM yields the lowest results throughout and exhibits a greater degree of variation in the vicinity of the paddle.

Whilst the model results all exhibit similar shapes, the same is not true of the magnitude of results arising from the models and, in particular, the standard k-ϵ model. The maximum ϵ values obtained for the three models are 0.3007 m^2s^{-3} (standard k-ϵ), 0.1369 m^2s^{-3} (realizable k-ϵ) and 0.0517 m^2s^{-3} (RSM). Therefore, the maximum ϵ value calculated using the standard k-ϵ model is some 5.8 times greater than the corresponding value calculated using the RSM. Occurrences of local velocity gradient values within the vessel, (defined as $G_L = \sqrt{\varepsilon/\nu}$) for the RSM and standard k-ϵ models are plotted on a cumulative basis at Figure 5-11. The disproportionate number of high G_L values obtained within the standard k-ϵ simulation is apparent. It is also clear that for the standard k-ϵ model there are no velocity gradient values below 200 s^{-1}, whereas the range for the RSM extends down to $50s^{-1}$.

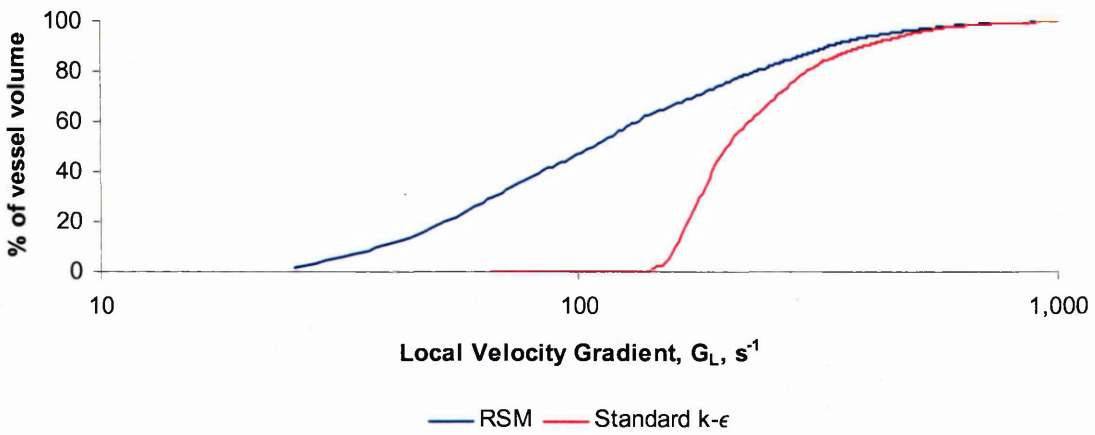


Figure 5-11: **Cumulative percentage of vessel volume containing G_L values less than the value shown, for RSM and standard k-ϵ turbulence models. N=200 rpm.**

5.2 Model Validation

5.2.1 Introduction

A CFD solution is a simulation of the flow field and therefore should, where possible, be validated by experimental evidence. The experimental evidence might be point measurement of physical quantities such as pressure or velocity components, measured

quantities such as residence time distributions, or comparison with an optical measurement technique such as PIV or LDA. It is accepted, however, that there are instances where validation is not possible. An example of such an instance is where CFD is used to determine the hydraulic characteristics of a situation where adjustment of variables is not permitted, *e.g.* the flocculator at Frankley WTW, described in Chapter 9 below. Indeed, this demonstrates one of the strengths of CFD, in that it can be used as a tool to assess unit process performance without necessitating removal of the process from duty.

5.2.2 Velocity Data

The cylindrical jar test CFD 100 rpm model results were compared with axial velocity data recorded as part of the LDA analysis. Data were recorded along a vertical axis at x=y=0.025m (*i.e.* r=0.5T) for the 100 rpm scenario and the results are presented at Figure 5-12

Numerical data are provided for the RSM and realizable k-ϵ (rk-ϵ) turbulence models, used in conjunction with both MRF and sliding mesh techniques, and also for the RNG turbulence model used with the sliding mesh technique. Good correlations between the observed and MRF RSM data are observed, particularly in the paddle region and below. There would appear to be some loss of accuracy around tank mid-depth and upwards for all models except the SM RSM simulation. This is likely to be as a result of vortexing within the vessel which was not modelled as part of the CFD exercise. The correlation between observed data and the realizable k-ϵ data (both MRF and SM) is rather more inferior, particularly for the MRF realizable k-ϵ simulation, with large errors found at mid-depth and also in the region below the paddle. The SM RNG models shows reasonable accuracy in the lower tank region, but this is lost in the paddle region and above.

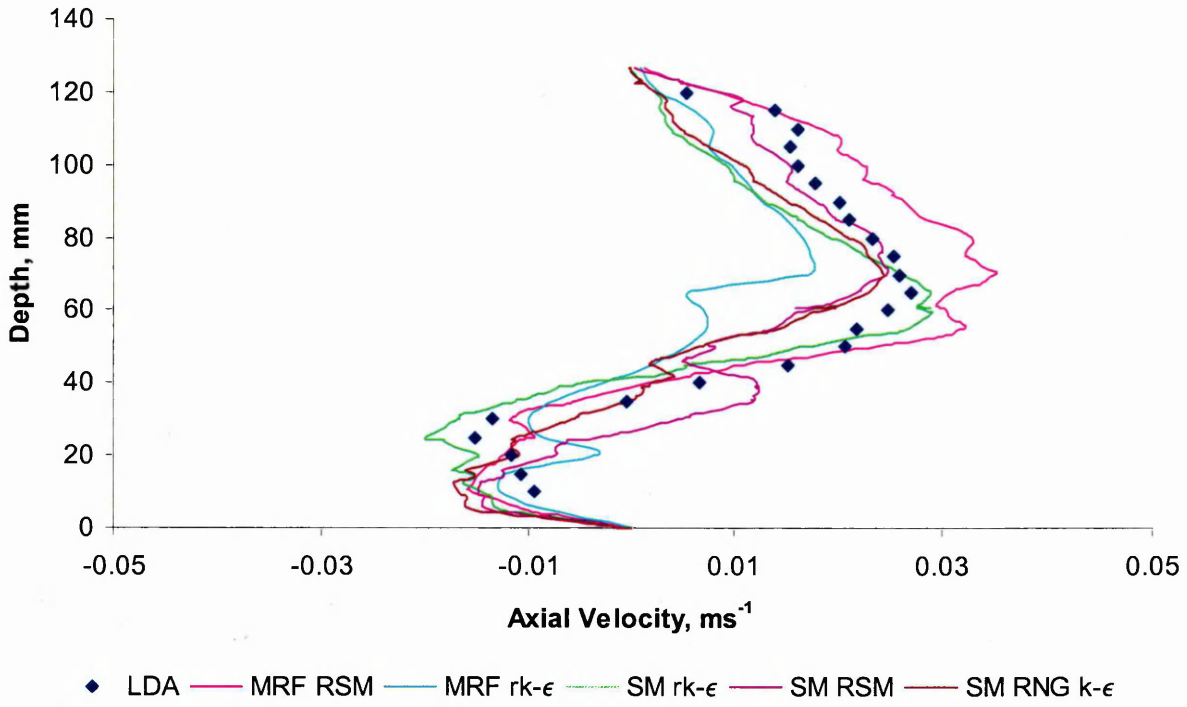


Figure 5-12: Simulated axial velocity profiles over tank depth for different turbulence models. (N = 100 rpm).

For each simulation shown at Figure 5-12, the magnitude of the differences between LDA and CFD data were calculated for 12 equally spaced points along the same vertical line as that used in Figure 5-12. The results are plotted at Figure 5-13. The data show that the MRF realizable k-ϵ simulation gave the greatest fluctuations from the LDA data, whilst the SM RSM simulation appears to have modelled the axial velocities with the greatest fidelity. This is unsurprising at this is the most robust of all the approaches adopted. The SM RNG data are surprisingly poor, bearing in mind the model's reported ability to deal with swirling flow (Fluent 2005). The model which offers the minimum variation from the LDA in the paddle area is the MRF RSM model.

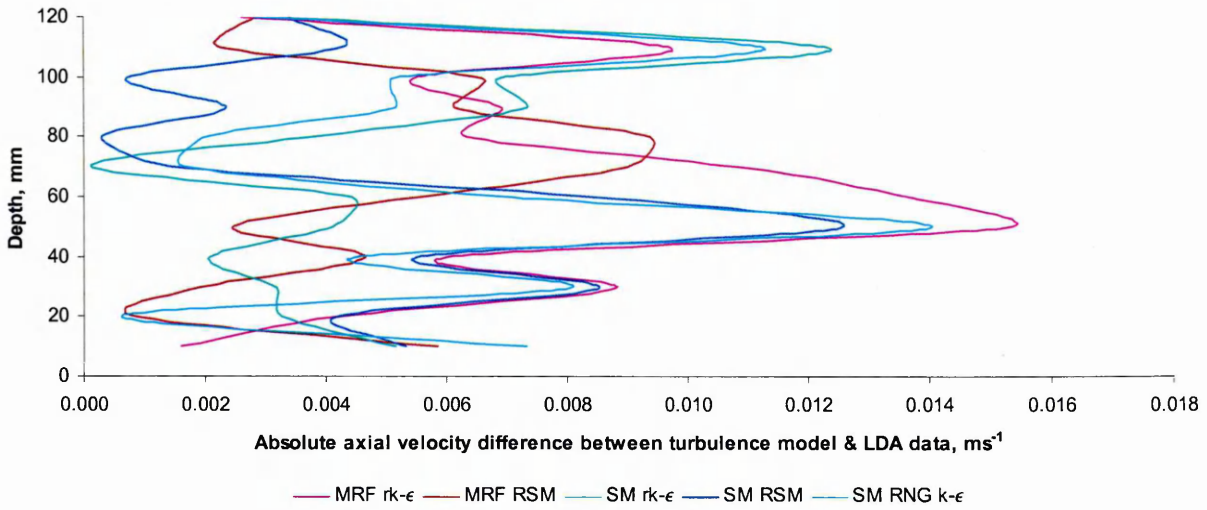


Figure 5-13: **Absolute difference between axial velocity values calculated using various turbulence models and those measured using LDA.**

5.2.3 Turbulence Data

The individual turbulence data arising from LDA analysis of each jar test scenario were not available, as described in Chapter 4. However, it was still possible to validate model results using experimental results. Using the energy dissipation rate calculated from the turbulence closure model, the overall power consumption was calculated for each mixing speed by numerically integrating the local power consumption over the entire vessel contents, expressed as

$$P = \rho \int \varepsilon \, dV \qquad \textbf{Equation 5-4}$$

This method has been found to be very dependent on the turbulent flow field obtained in the simulations and previous workers have reported varying degrees of success in applying this method to mixing scenarios of different scales. For example, Armenante *et al.* (1997) compared experimentally-derived power number values with those obtained from CFD models of the same mixing set-up using the standard k-ϵ and Algebraic Stress (ASM) turbulence models (Table 2-3 refers). At a mixing speed of 450 rpm, the ASM-derived Power number was just 45.3% of the experimentally-derived value. The standard k-ϵ model produced an improved result with a Power number of

71.9% of the experimental value. These results were obtained for a closed system; however, Ciofalo *et al.* (1996) reported a similar result for an open, unbaffled system, mixed with a Rushton turbine. Naude *et al.* (1998) concluded that any inaccuracy in the Power number calculation is not necessarily a result of the impeller modelled or the mesh applied in the modelling of the flow field, but rather the method of modelling the turbulence. Naude *et al.* suggested that the use of time averaged models in the simulation is a simplification which results in the reported inaccurate prediction of the Power number. Zhou and Kresta (1996) and Lee and Yianneskis (1998) suggested that any inaccuracies might arise as a result of anisotropic turbulence in the vicinity of the paddle. Again, this suggests that care must be taken over turbulence model selection. Nevertheless, Essemiani and de Traversay (2002a) obtained a very good correlation between experimental and numerical values of Power number and vessel average velocity gradient for a laboratory scale flocculator as discussed in Chapter 2.

In view of the concerns raised by previous workers about the importance of turbulence model selection, a sensitivity analysis was undertaken on various different models. Six numerical simulations were undertaken of the cylindrical vessel mixed at 100 rpm using a combination of turbulence models and approaches to modelling the rotating mesh; *viz.* MRF with standard k-ϵ, MRF with realizable k-ϵ, MRF with RSM, SM with RNG k-ϵ, SM with realizable k-ϵ and SM with RSM. The total power dissipated was calculated using Equation 5-4. Values for the vessel average velocity gradient were then calculated for both the experimental and CFD results using Equation 2-12, and the results are shown below at Figure 5-14 and Table 5-1. The MRF with standard k-ϵ solution is clearly wholly unrepresentative of the actual flow field. This modelling combination produced an average velocity gradient of $989s^{-1}$, compared to an experimentally-derived value of 104 s^{-1}. The realizable k-ϵ and RS models, used in combination with the MRF treatment for rotating meshes, produced reasonable results, certainly when compared to the work of previous authors. SM and realizable k-ϵ also produced acceptable results. However, it is very interesting to note that the SM RSM technique, representing the most rigorous and computationally demanding approach, significantly under-estimated the average G value.

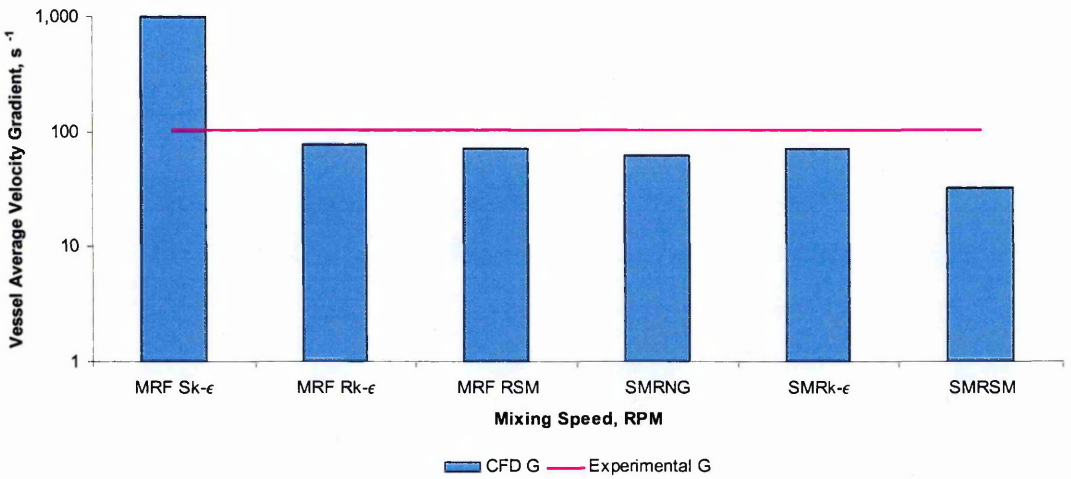


Figure 5-14: **Vessel average velocity gradient values calculated for various modelling approaches, compared to experimentally-derived value. N=100 rpm.**

Table 5-1: **Vessel average velocity gradient values, G s^{-1}, for cylindrical vessel. N=100 rpm.**

Exptl	MRF & Sk-ϵ	MRF & Rk-ϵ	MRF & RSM	SM & RNG	SM & Rk-ϵ	SM & RSM
104	989	77	71	62	72	33

5.3 Turbulence Modelling and Rotating Mesh Discussion

It is widely acknowledged that the Reynolds Stress Model is the most rigorous of the available models (Versteeg & Malalasekera, 1995), and this is demonstrated by the increased simulation time required when using this model (an additional 40-50% when compared to two-equation models and using the MRF approach). Fluent (2005) states that "use of the realizable k-ϵ model with multiple reference frames is not recommended". No reason for this statement is given in the documentation. Subsequent correspondence with Fluent (private communication) suggests that the effect of rotation on turbulent viscosity is not taken into account in the realizable k-ϵ model and hence it is not recommended for MRF problems.

Indeed, there is an inherent difficulty with all the two equation models when modelling this type of flow as they are all predicated on the assumption that turbulence is isotropic, meaning that the turbulent stress tensor is independent of direction (or, more precisely, invariant with respect to rotation and reflection of the coordinate axes of the coordinate

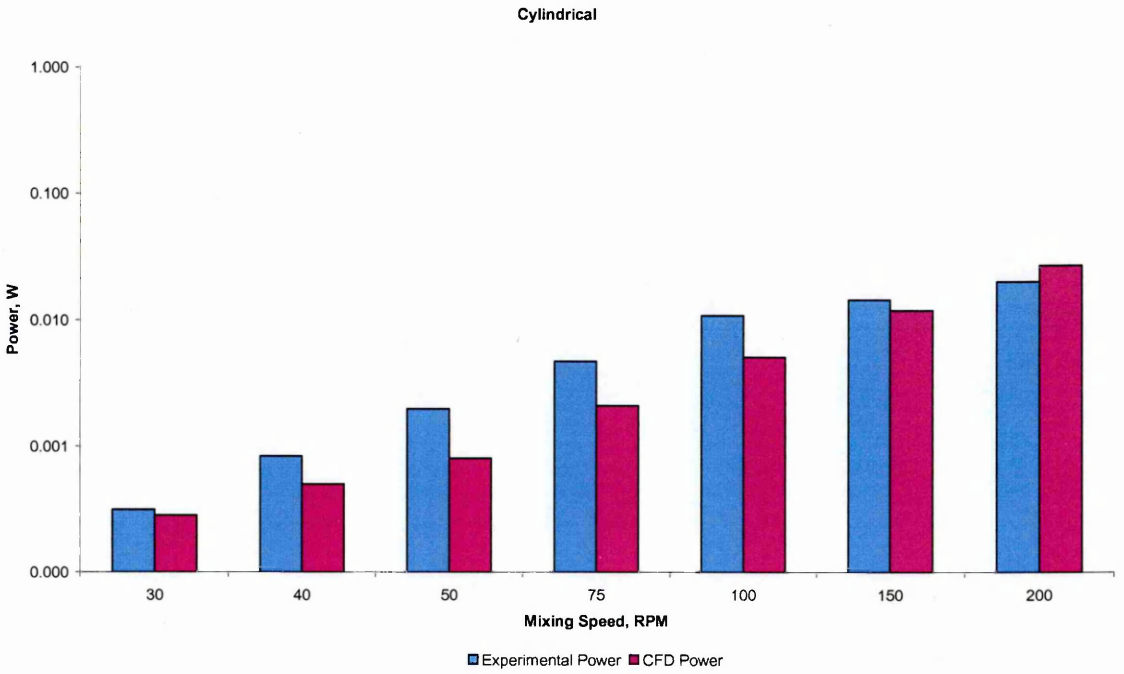
system moving with the mean motion of the fluid). This assumption is not true for swirling flow which is anisotropic in nature. For swirling flow, turbulence is generally more in the tangential and axial directions as compared to the radial direction. Thus, in order to capture this anisotropic nature of turbulence Fluent (2005) suggests that other models, such as the RSM should be employed as this solves the equations for all the stress components. Fluent (2005) states that "for highly swirling flows, the Reynolds stress model is strongly recommended. The effects of strong turbulence anisotropy can be modelled rigorously only by the second-moment closure adopted in the RSM."

The foregoing analyses confirmed the unsuitability of the standard k-ϵ turbulence model for simulation of an unbaffled stirred tank reactor. However, it is noted with interest that this is in contrast to the conclusions of Jaworski and Zakrzewska (2002). Korpijarvi *et al.* (1999) used the standard k-ϵ model to simulate an alternative flat paddle (Kemira Kemwater Mini Flocculator) unbaffled stirred tank reactor although the work reported here would indicate that it is unviable for highly swirling flows. It is also interesting to note that Korpijarvi *et al.* used a mesh considerably coarser than the one used in this research, but that they were able to obtain satisfactory correlation with experimental data with this coarse mesh. This research has shown that, certainly in the case of axial velocity, the coarsest mesh generated poor results compared to the other, finer, meshes at certain locations in the flow. It is possible that the results generated by the standard k-ϵ model which this research shows to be high in comparison to other, more refined models, are compensated for by coarse mesh quality, giving rise to a reasonable correlation with experimental data. However, without further detailed investigation into the work of Korpijarvi *et al.*, it is not possible to further this argument.

It is clear from Figure 5-12 and Figure 5-13 that the sliding mesh approach, coupled with the RSM, offers the greatest degree of accuracy for the determination of velocity data. However, that accuracy is paid for in terms of computational time and expense. Running this simulation on the high performance computing facility took approximately 17 hours to obtain a converged solution. Running the simulation on a laptop computer was not practical. The MRF RSM simulation offers reasonable correlation with the

LDA data and the numerically-derived power dissipation, at a substantially reduced computational cost. Consequently, in light of the good correlation found between the RSM results and the observed data, the limitations of two-equation models in predicting highly swirling flow patterns, and the expense of the SM approach, the RSM MRF combination was selected for all further jar test CFD models for both the cylindrical and Hudson vessels.

Power dissipated within each vessel for seven mixing speeds was calculated for the CFD simulations and were then compared to the power dissipation values calculated on the basis of experimental data. In addition, velocity gradient values were calculated for seven mixing speeds for both the cylindrical and Hudson vessels using power dissipation values derived from numerical data and Equation 5-4. These values were then compared to experimentally-derived values. The results are shown at Figure 5-15 and Figure 5-16.



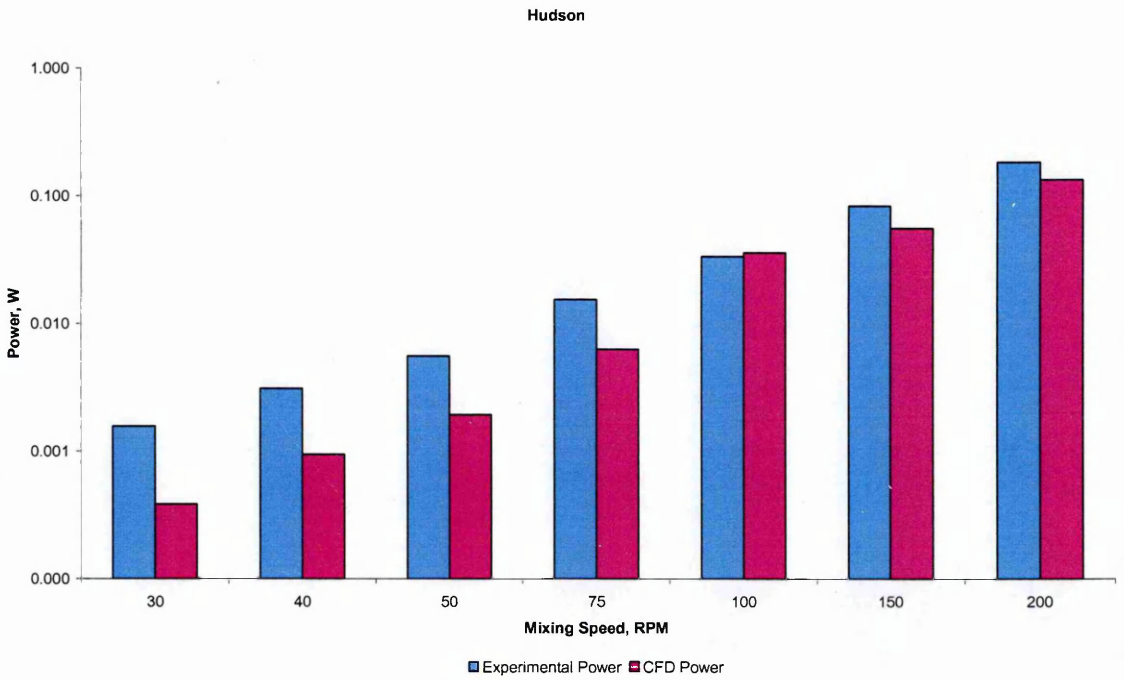


Figure 5-15: **Experimental and CFD-derived power dissipation values, W, at stated mixing speeds for (a) cylindrical vessel and (b) Hudson vessel.**

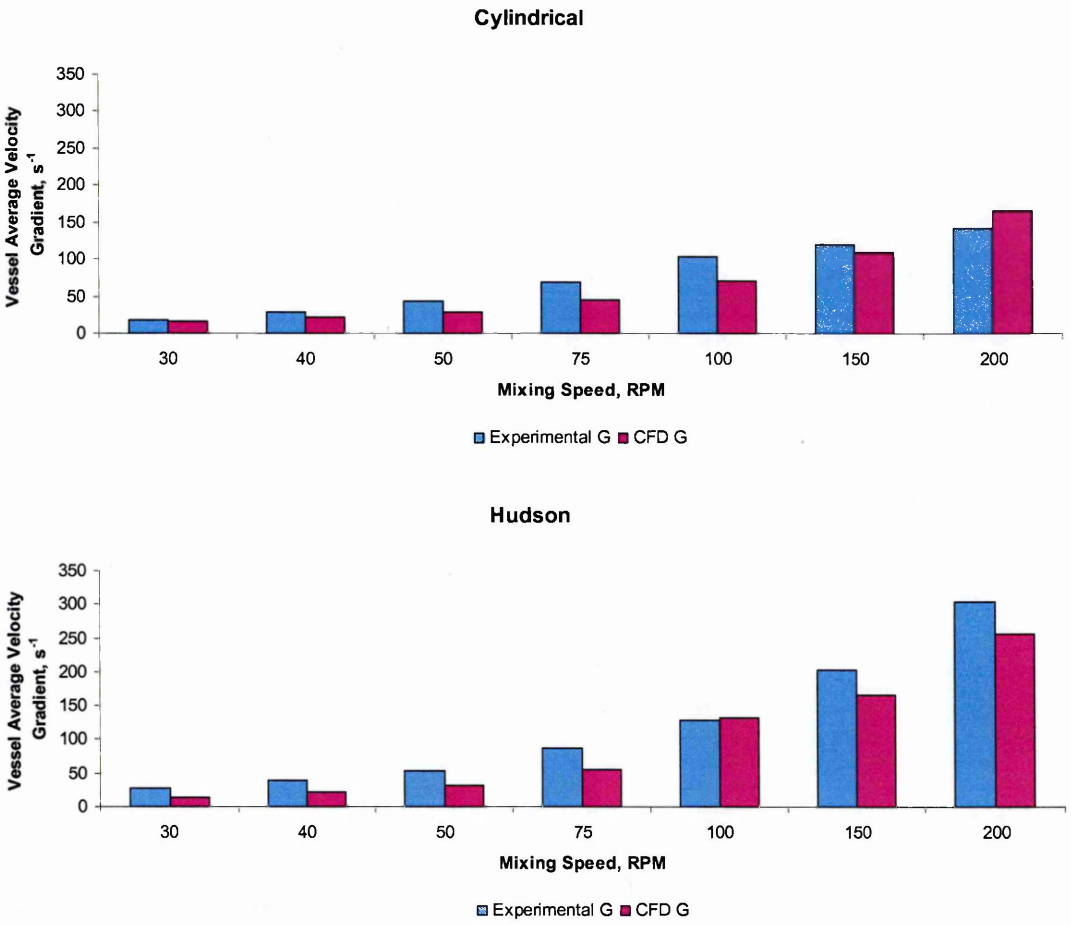


Figure 5-16: **Experimental and CFD-derived *G* values, s^{-1}, at stated mixing speeds for (a) cylindrical vessel and (b) Hudson vessel.**

The data shown in Figure 5-15 show that the CFD model generally underpredicts the total power dissipation in both the cylindrical and Hudson vessels. The degree of under-prediction is, as expected, greatest at the lower mixing speeds where the flow is transitional, as opposed to fully turbulent, and so the turbulence models are more challenged in replicating the scenario with complete fidelity. However, the degree of agreement between modelled and experimental data at mixing speeds of 100 rpm and above is good. For example, at 100 rpm, the discrepancy between modelled and experimental data is just 7% for the Hudson vessel. It is accepted that the degree of agreement is less good at low mixing speeds. However, this work is primarily focussed on an analysis of floc breakage mechanisms; phenomena which occur at higher mixing

speeds, and so it is important that these speeds are modelled with the greatest degree of accuracy. This has been achieved.

With regard to velocity gradients, in most instances, the CFD model is seen to under-predict the *G* value, irrespective of vessel shape or mixing speed (the exception being the cylindrical vessel mixed at 200 rpm). In percentage terms, the greatest degree of discrepancy between experimental and numerical data is found at mixing speeds between 40 and 75 rpm. As discussed previously, the flow is not fully turbulent at these mixing speeds, and so it is concluded that the turbulence models, which are strictly only valid for fully turbulent conditions, are not able to represent the flow with complete fidelity. In absolute terms, however, there is little difference between the CFD and experimental data. For the cylindrical vessel, the average discrepancy between numerical and experimental data is $16s^{-1}$, and the corresponding figure for the Hudson vessel is $24s^{-1}$. The maximum absolute difference occurs, unsurprisingly, at maximum mixing speeds ($46s^{-1}$ for the Hudson vessel) but the calculated value is within 18% of the measured value and is an improvement on similar work undertaken by others previously (*e.g.* Armenante *et al.*, 1997, Ciofalo *et al.*, 1996) although it is accepted that it is not as accurate as the results reported by Essemiani and de Traversay (2002a). The results of Essemiani and de Traversay (2002a) were based on the analysis of a significantly larger mixing vessel ($1m^3$), rather than the one or two litre vessels considered here and by others. It would appear, therefore, that CFD is better able to replicate the flow field in less constrained vessels where factors such as wall effects impinge less on the overall hydraulics.

Section 5.2 above shows that for this work, modelling the free surface of the cylindrical vessel as a symmetry plane yielded an acceptable correlation between numerical and experimentally-derived Power numbers, thus demonstrating that the magnitude and distribution of turbulence dissipation rate values was not adversely affected. It must also be borne in mind that the work reported in this thesis considers the impact of turbulence on floc formation and breakage. Stanley and Smith (1995) concluded that floc characteristics within the jar tester are governed by the hydrodynamic conditions found in the impeller zone. Therefore, an exact representation of the flow conditions at

the surface is not as significant in this work as an accurate representation of the flow characteristics in the impeller zone. For these reasons, it is considered that the limitation of modelling the free surface as a flat, no-shear plane can be accepted.

5.4 Summary

This section has demonstrated the key elements of developing and implementing a robust strategy for the CFD modelling of the jar test apparatus. The unsuitability of the standard k-ϵ turbulence model for modelling the highly swirling flow found in the circular jar tester has been demonstrated. The difficulties of using alternative two-equation models to simulate what is an anisotropic situation have also been demonstrated. The rigorous Reynolds Stress Model has been found to be the most effective means of modelling the flow field. The sliding mesh method of modelling rotating flows has been demonstrated to deliver slightly improved quality velocity data compared to the multiple reference frames approach, although the same is not true of turbulence dissipation data (judged using power dissipation as a surrogate). The sliding mesh method is computationally demanding and expensive, and the improvements in accuracy are not considered to be sufficient to warrant the additional time and expense. The density of the grid has been optimised such that the key features of the flow field are exhibited, without incurring additional and unnecessary computational expense.

6 Jar Test CFD Analyses of Cylindrical and Hudson Vessels: Flow Field Characteristics

6.1 Introduction

The previous chapters focussed on the development of models and the specifics of various CFD techniques. This chapter and subsequent chapters contain details and data arising from the use and application of these techniques.

Chapter 4 described the use of LDA and PIV techniques to demonstrate quantitative differences in velocity profiles between the cylindrical and Hudson vessels. It is of fundamental importance that these differences are quantified and understood. Jarvis *et al.* (2005a) provided a useful summary of jar test experiments and the energy requirements to bring about floc breakage. However, work which compares the results of jar test experiments has not accounted for the differences in configurations and the different hydrodynamic environments generated therein.

The CFD models of the cylindrical and Hudson vessels, described in Chapter 5, have been used to quantify these differences and to compare the results gained with previous, related work. In the first instance, differences in the velocities (magnitude, axial and tangential components) are discussed. Thereafter, the dissipation of turbulence energy is considered. As described in Chapter 2 and later in this chapter, the turbulence dissipation rate has a fundamental role in the flocculation process, and so an understanding of its variation within the two scenarios considered and between the two scenarios is most important. Later Chapters of this thesis explore floc trajectories in the cylindrical vessel and compare the experimental floc growth data of Jarvis (2004) with numerical data. No experimental floc size data was derived for the Hudson vessel and the CFD modelling of this vessel was undertaken simply for the purposes of examining differences in the hydraulic regimes found in the two different vessels.

6.2 Velocity Magnitude

The predicted flow field in the cylindrical jar tester at 200 rpm as obtained from the CFD analysis is shown in vector format at Figure 6-1. The high velocities in the region of the impeller which were noted in the LDA analysis are repeated here and the anticipated large circulation patterns above and below the impeller are also apparent. A similar flow pattern is also observed for the Hudson vessel at Figure 6-2. The results shown in Figure 6-2 also compare well on a quantitative basis with the PIV results shown at Figure 4-15 (a) giving confidence that the CFD model is representative of the physical flow characteristics. It is also noticeable that the average velocity magnitude in the cylindrical vessel is somewhat higher than that generated in the Hudson vessel (average velocity magnitudes are 0.409 and 0.217 ms^{-1} for the cylindrical and Hudson vessels respectively) although the Hudson vessel maximum exceeds that of the cylindrical vessel. In both scenarios it is clear that the maximum values occur, as is to be expected, in the immediate vicinity of the paddle (maximum velocity magnitudes are 0.844 and 1.064 ms^{-1} for the cylindrical and Hudson vessels respectively).

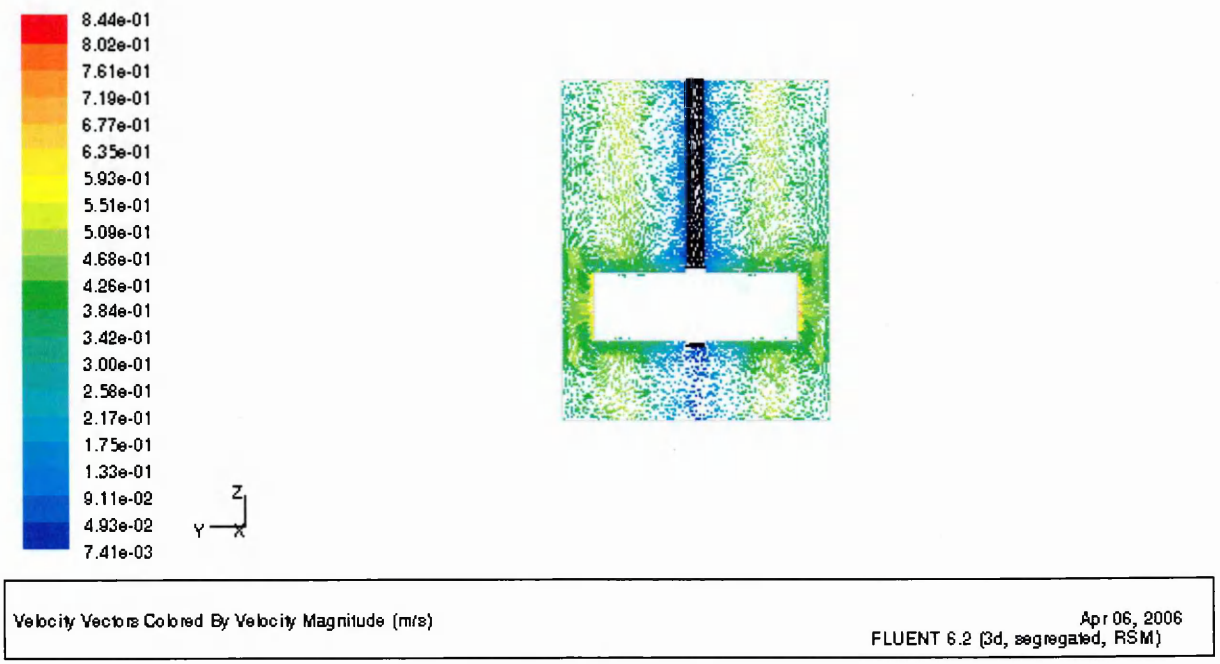


Figure 6-1: Velocity vectors generated in cylindrical vessel, N=200 rpm.

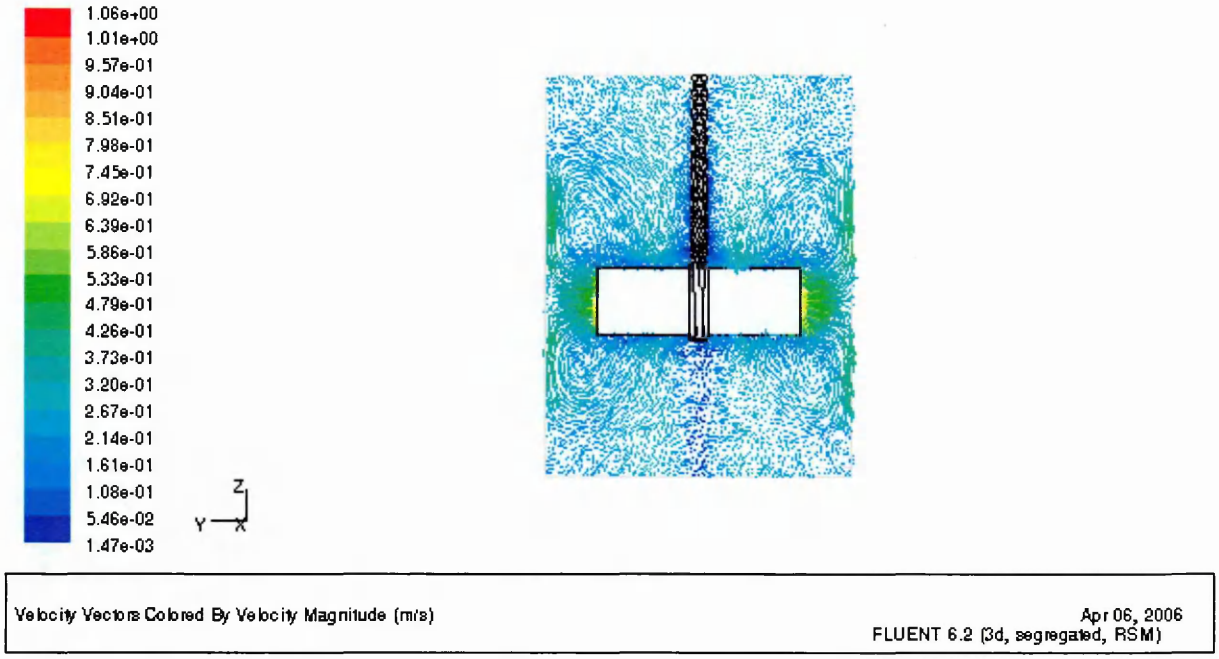


Figure 6-2: Velocity vectors generated in Hudson vessel, N=200 rpm.

Contours of velocity magnitude for the two vessels taken through vertical and horizontal planes are shown at Figure 6-3 to Figure 6-8 below. For both vessels it is apparent that the highest velocities are limited to the paddle tip zone. Areas shaded green through to red represent velocities which are greater than 50% of the vessel maximum. There is good coverage of green shading in the cylindrical vessel from the surface to just above the base. The same is not true of the Hudson vessel. Thus, there is an increased distribution of the higher velocities in the cylindrical vessel compared to the Hudson vessel. Considering the velocities taken through the horizontal plane at paddle mid-depth (Figure 6-4 and Figure 6-6 refer), again it is noticeable that the velocities are better distributed in the cylindrical vessel than the Hudson vessel. High values are apparent in the paddle wake for both scenarios, but they dissipate quickly in the Hudson vessel, with evidence of dead spots in the vessel corners. The implication of these observations is that the supplied mechanical energy (which is converted to velocity energy in the vessel) is dissipated throughout the majority of the cylindrical vessel, generating a greater degree of mass flow within it. The same is not true of the Hudson vessel and thus, it can be concluded that the mixing is better in the cylindrical vessel than the Hudson.

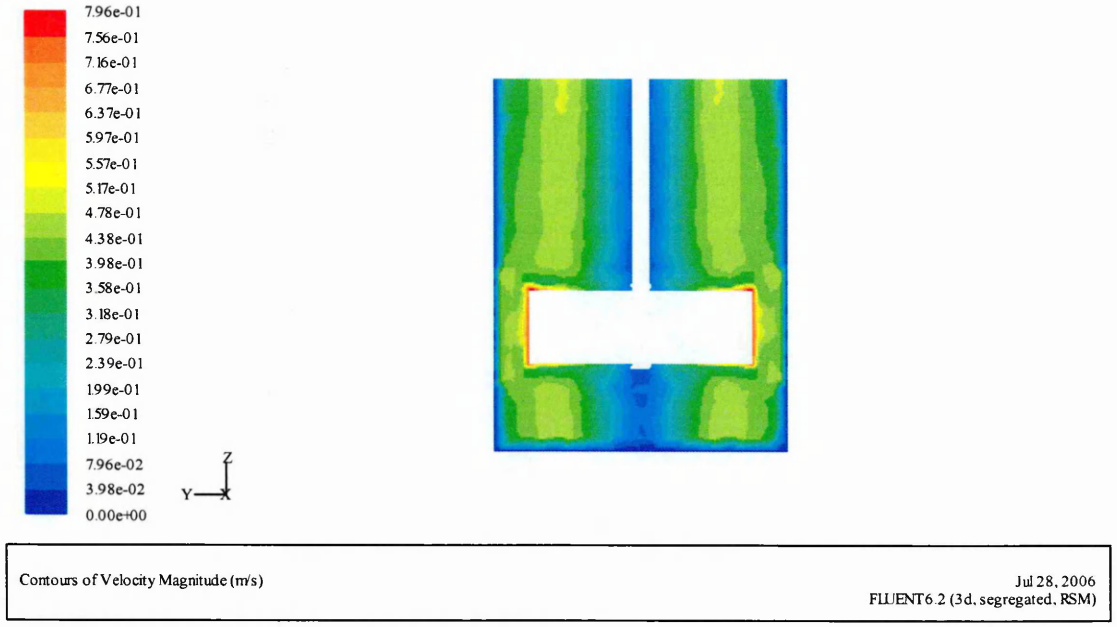


Figure 6-3: **Velocity magnitude contours taken through midplane of cylindrical vessel. Mixing speed = 200 rpm.**

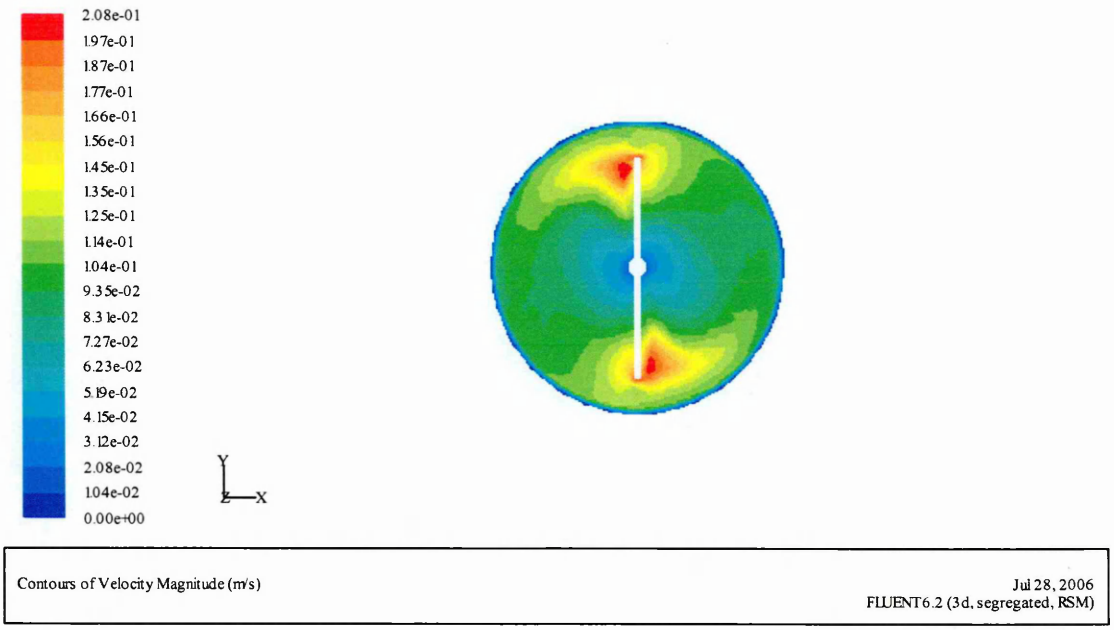


Figure 6-4: **Velocity magnitude contours taken through paddle centreline of cylindrical vessel. Mixing speed = 200 rpm.**

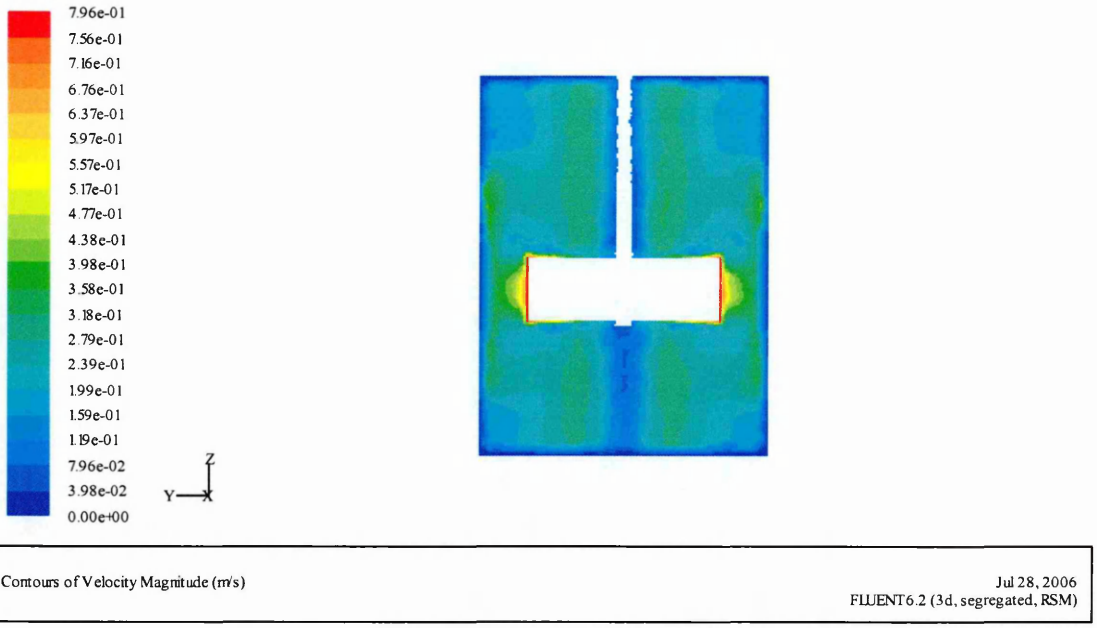


Figure 6-5: **Velocity magnitude contours taken through midplane of Hudson vessel. Mixing speed = 200 rpm.**

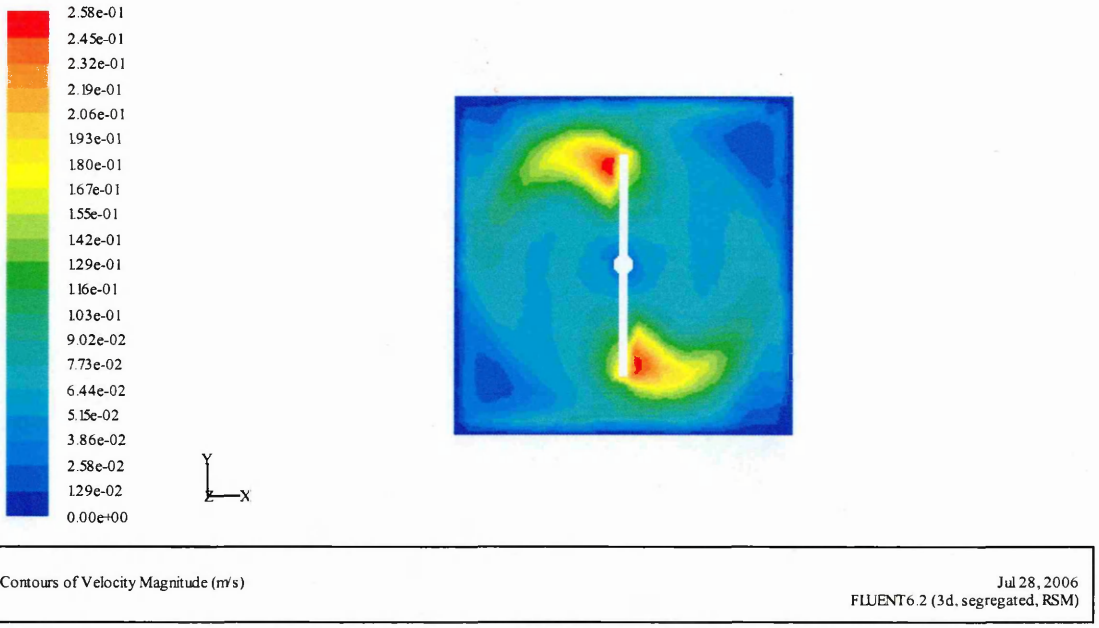


Figure 6-6: **Velocity magnitude contours taken through paddle centreline of Hudson vessel. Mixing speed = 200 rpm.**

Velocities calculated 2mm above the vessel bases at a mixing speed of 50 rpm are shown at Figure 6-7 and Figure 6-8. It can be seen that the velocities in the Hudson vessel are approximately 50% of those in the cylindrical vessel and there are significant dead spots in the Hudson vessel, once more implying less effective mixing.

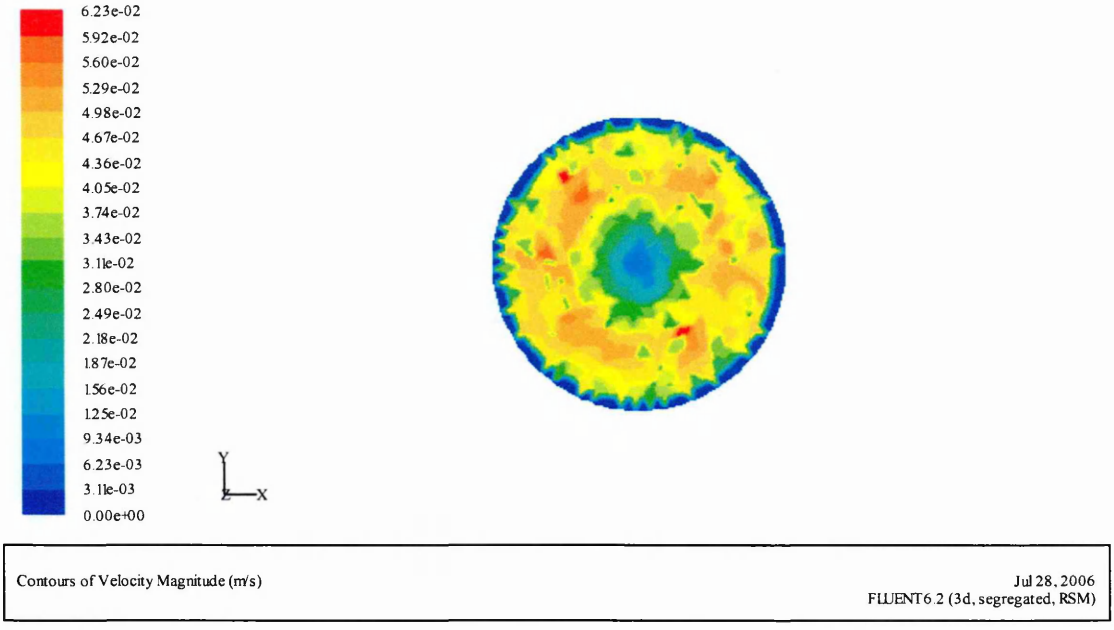


Figure 6-7: **Velocity magnitude contours taken 2mm above base of cylindrical vessel. Mixing speed = 50 rpm.**

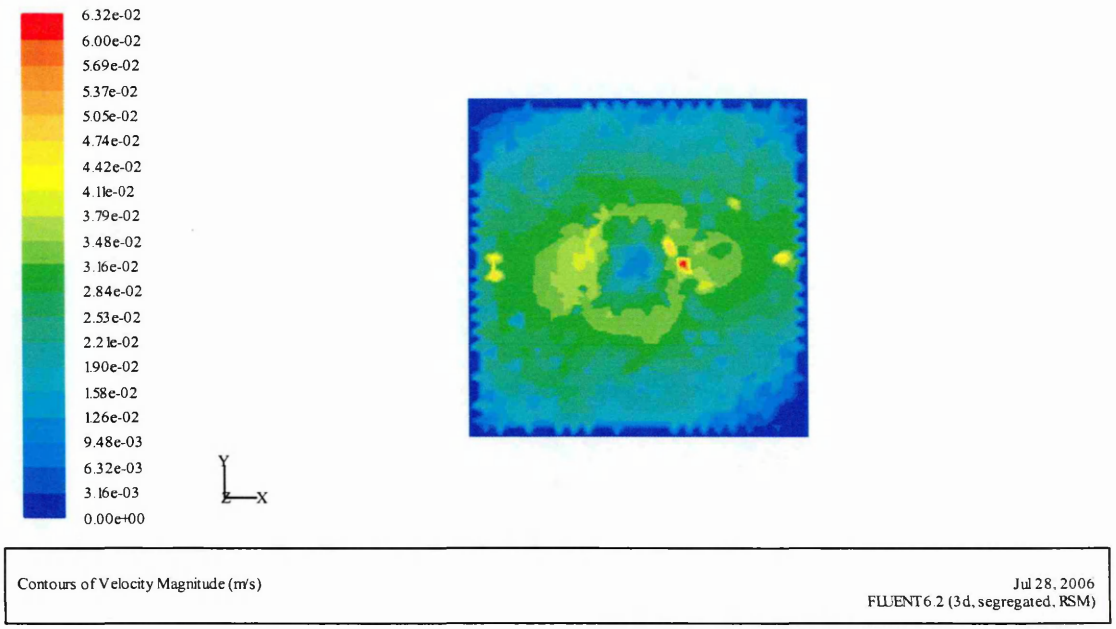


Figure 6-8: **Velocity magnitude contours taken 2mm above base of Hudson vessel. Mixing speed = 50 rpm.**

6.3 Axial and Tangential Velocities

Considering the cylindrical vessel, Figure 6-9 below shows the variation in axial velocity on an arc described by the paddle tip at rotational speeds of 100 and 30 rpm. The peak values of these two extremes of mixing speeds considered vary considerably (0.048 ms^{-1} and 0.008 ms^{-1} for 200 and 30 rpm respectively). However, it is interesting to note that the 200 rpm average axial velocity is just 0.0026 ms^{-1} greater than that of the 30 rpm value (0.0038 ms^{-1} and 0.0012 ms^{-1} respectively). This example highlights the instantaneous change in axial velocity brought about by an increase in mixing speed and suggests why flocs might be seen to break on exposure to higher mixing speeds. It also indicates the large variation in axial velocity components found at high mixing speeds, and the much reduced variation at lower speeds.

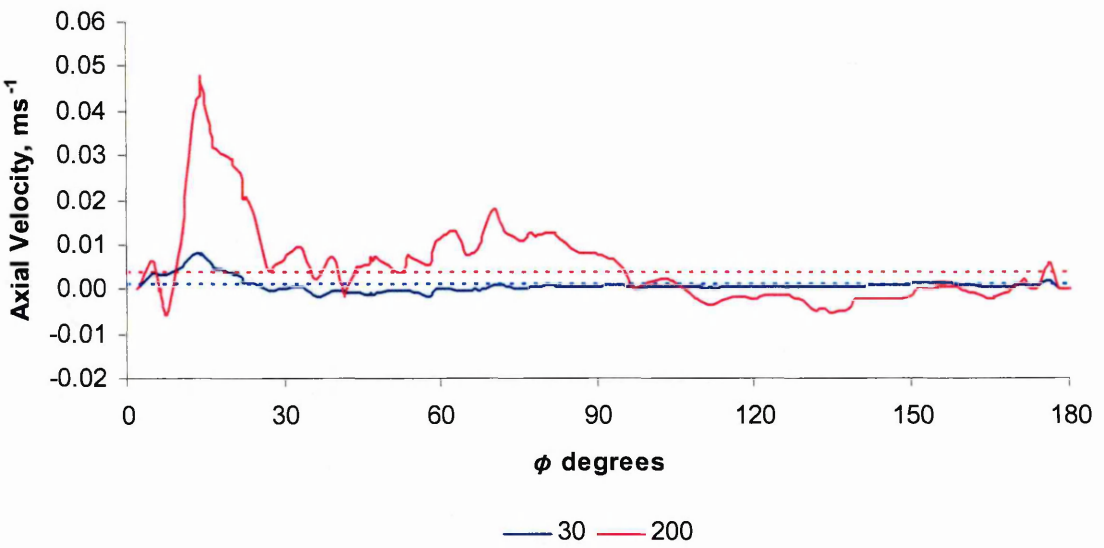


Figure 6-9: **Variation in axial velocity on an arc described by the impeller at N=100 and N=30 rpm for the cylindrical vessel.**

Again for the cylindrical vessel, Figure 6-10 shows the scaled mean radial velocities at different mixing speeds along the same axial profile. The profile was taken at a distance of 1.9 mm from the tip of the impeller (*i.e.* $2r/D = 1.05$). The results are consistent with previous studies of other impellers which found that the velocities scale on the impeller tip speed (*i.e.* πDN) as discussed in Chapter 4 (Nouri *et al.*, 1987, Zhou & Kresta,

1996). Scaled mean axial velocities are shown for the Hudson vessel at Figure 6-11. Again, the velocities are seen to scale reasonably well, although the 100 rpm data are somewhat out of line with the other data, particularly in the area above the impeller. It is also apparent that the scaled velocities between the two configurations are different. The maximum scaled velocity found for the cylindrical vessel is 0.2, whereas the corresponding value for the Hudson vessel is 1.75 times greater at 0.35, indicating the higher axial velocity values generated in the Hudson vessel. The scaled velocities for the Hudson vessel agree very well with data produced by Stanley and Smith (1995) who used LDA to physically measure the flows in the Hudson vessel at several mixing speeds. Stanley and Smith also found the maximum scaled velocity to be 0.35, thus providing additional physical evidence of the robustness of the CFD models developed in this work. Other scaling factors for this particular impeller were not found in the literature. However, several were found for the Rushton turbine (Nouri *et al.*, 1987, Wu and Patterson, 1989, Kresta and Wood, 1991). The scaling factors in these examples range from 0.5 to 1.2, with an average of 0.84. Clearly therefore they are considerably higher than the values for the scenarios examined here. It is believed that this difference can be attributed to the additional number and area of blades on the Rushton turbine compared to the paddle (six and two respectively).

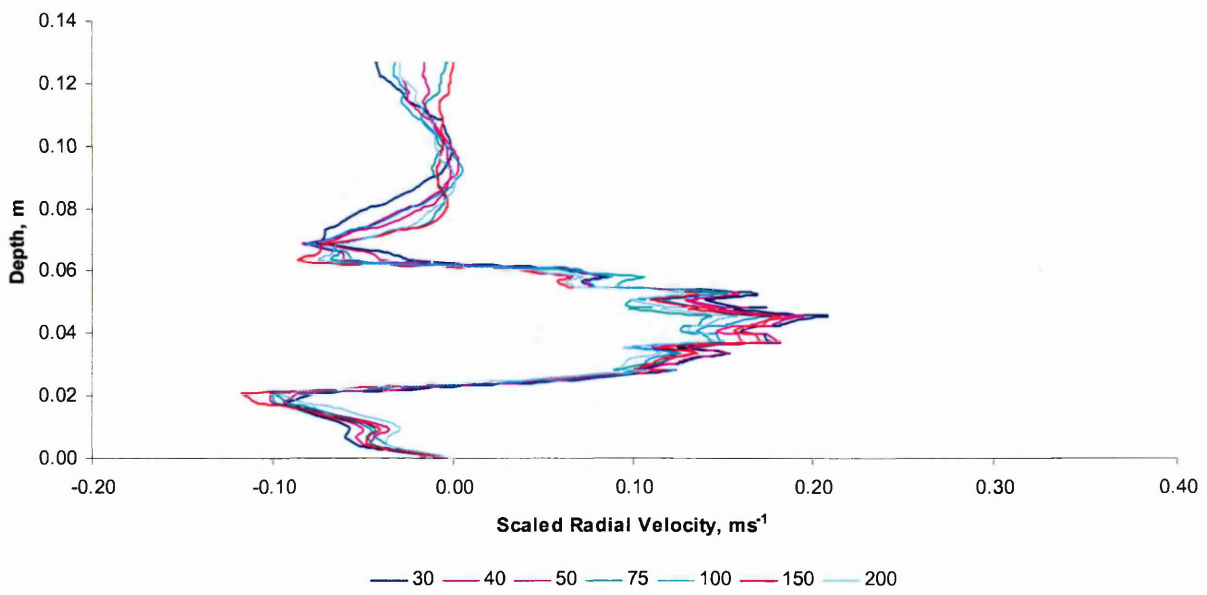


Figure 6-10: Cylindrical vessel scaled mean radial velocities at various mixing speeds.

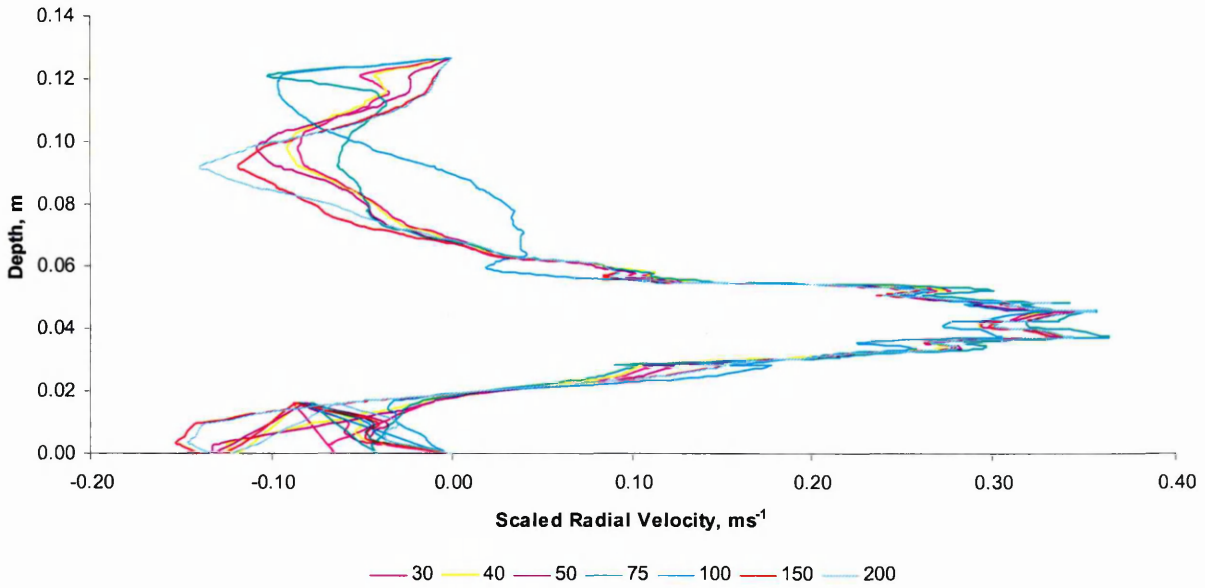


Figure 6-11: Hudson vessel scaled mean radial velocities at various mixing speeds.

Scaled mean axial velocities for the cylindrical vessel are shown below at Figure 6-12. It is interesting to note that the axial velocities do not scale as well as the radial velocities. It is also interesting to compare these data with the LDA-derived scaled axial velocity, as shown at Figure 4-10. It can be seen that the experimental data do not scale exactly, and that the range of values is also similar, with maxima ranging from -0.05 to 0.12 for the CFD data and from -0.04 to 0.10 for the LDA data. Thus, whilst the data do not scale, there is good agreement between the CFD and LDA data, giving additional confidence in the robustness of the models. Scaled mean axial velocities for the Hudson vessel are shown below at Figure 6-13 and it is clear that, as well as being larger in magnitude, the velocity scaling is better than that observed for the cylindrical vessel. As scaling is known to occur for turbulent flows, the implication to be drawn from this observation is that the flow within the Hudson vessel is more turbulent than that found in the cylindrical one. This observation is considered further in the following sections.

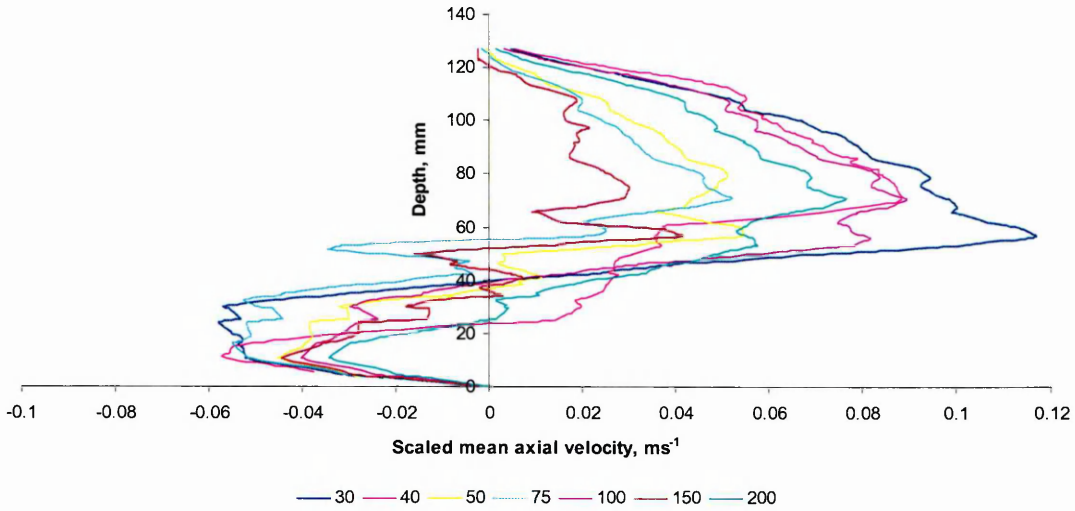


Figure 6-12: **Cylindrical vessel scaled mean axial velocities at various mixing speeds.**

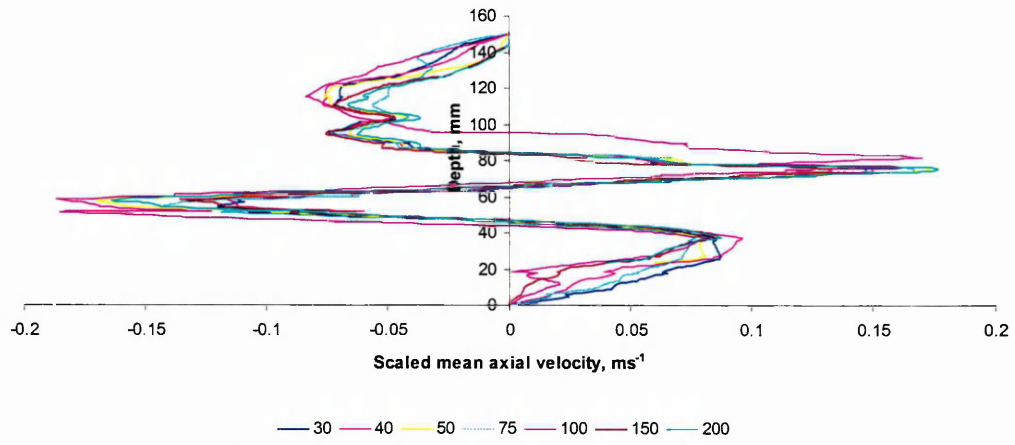


Figure 6-13: **Hudson vessel scaled mean axial velocities at various mixing speeds.**

6.4 Turbulence Dissipation Rate

6.4.1 Distribution of Turbulence Dissipation Rate

The importance of the turbulence dissipation rate, ϵ, in determining floc size was discussed in Chapter 2 above. A detailed and accurate understanding of ϵ is fundamental to the optimisation of a fluid mixing process. In particular, the maximum ϵ and its distribution within the mixing vessel are required to ascertain the degree of mixing imparted. Starting from the basis that floc size is a function of breakage (where negative breakage implies growth), Equations 2-32 and 2-35 established the role of ϵ in determining the floc breakage mechanisms in the viscous and inertial subranges. As a result, an informed understanding of ϵ in various different scenarios (*i.e.* test configurations and mixing speeds) can be used to develop important information with regard to floc behaviour. Baldi *et al.* (2004) discussed the difficulties inherent in the experimental determination of shear rates and associated values due to the small size of the dissipative scales to be resolved, but Hemrajani and Tatterson (2004) recognised the potential value of CFD in determining such characteristics. Consequently, plots of the variation of ϵ over the mid-planes of the two vessels were produced and these are shown at Figure 6-14 and Figure 6-15 below for the 200 rpm scenarios. Both Figure 6-14 and Figure 6-15 show a strong non-uniformity of turbulence dissipation throughout the vessel. In the impeller zone, the turbulent kinetic energy is highly dissipated, whereas outside of the impeller zone, the dissipation rate is reduced. The higher proportion of larger ϵ values in the Hudson vessel is clear. This is very much in line with the conclusions of Chapter 4 which presented the Power number for the Hudson vessel as being significantly higher than the cylindrical vessel.

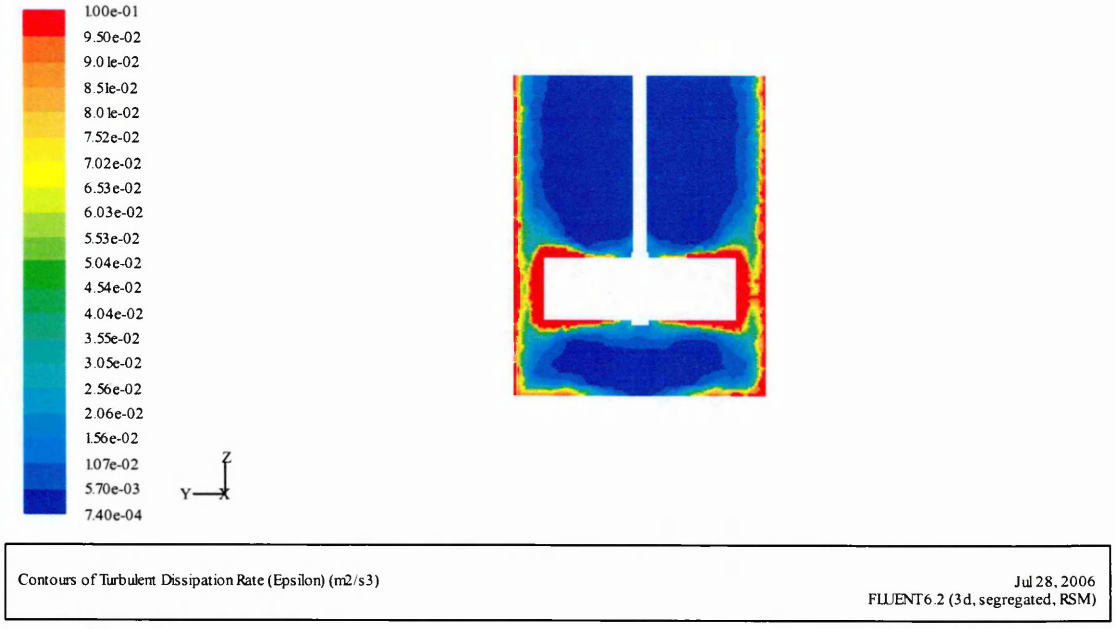


Figure 6-14: **Variation in turbulence dissipation rate across mid-plane at 200rpm for the cylindrical vessel.**

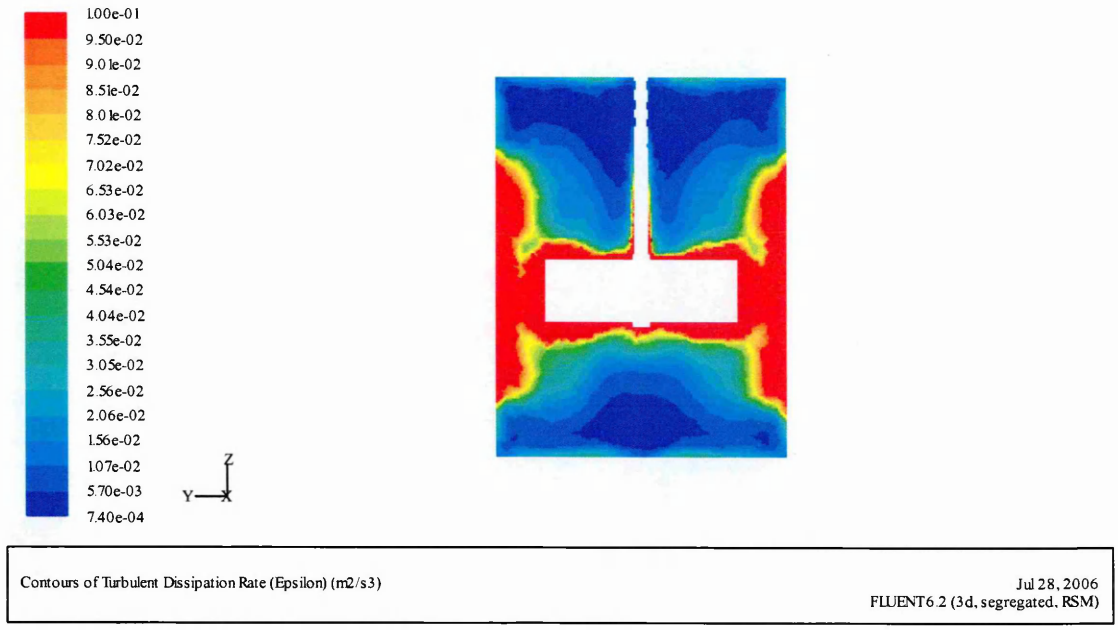


Figure 6-15: **Variation in turbulence dissipation rate across mid-plane at 200 rpm for the Hudson vessel.**

Using the CFD results, Figure 6-16 shows the variation in local turbulence dissipation rate at 200 rpm in the cylindrical vessel. Turbulence dissipation rate values were extracted from a plane in the wake of the paddle. It is immediately apparent that much of the turbulence dissipation takes place within, and immediately adjacent to, the impeller zone. A qualitatively similar result was obtained by Stanley and Smith (1995) when considering mixing in the Hudson vessel at 60 rpm.

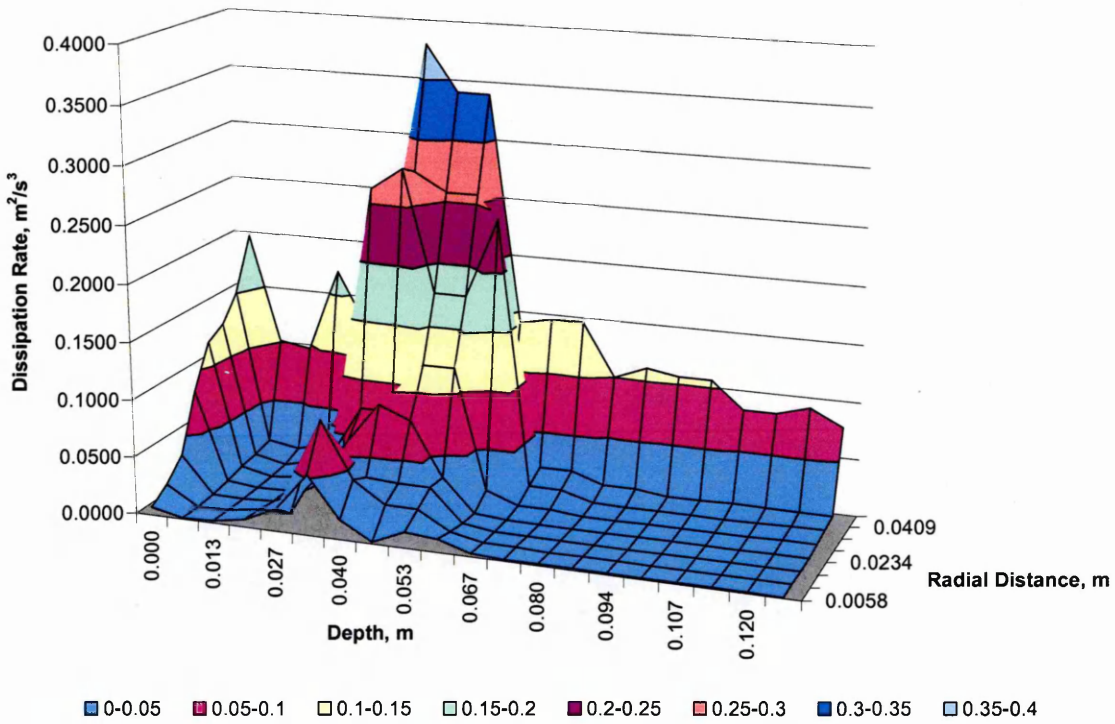
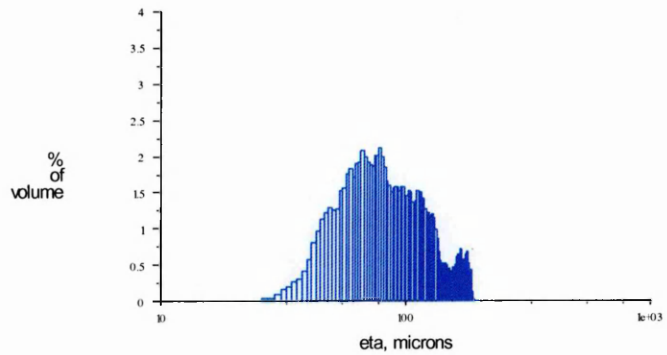


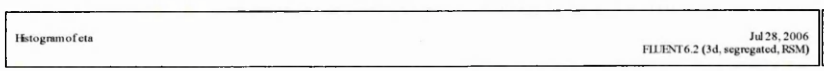
Figure 6-16: Variation in local turbulence dissipation rate in cylindrical vessel at 200 rpm.

Kolmogorov length scale values, η, were calculated according to Equation 2-8 and are presented for the two vessels and mixing speeds of 200 and 50 rpm at Figure 6-17 below. For both vessels, the maximum η value is seen to increase as the mixing speed decreases. Bimodal peaks, indicating non-uniformity of hydrodynamics, are particularly noticeable in the Hudson vessel plots. It is concluded that the first peak represents η values found in the impeller region, while the second peak is more indicative of a global average η value. These peaks are not as apparent in the cylindrical vessel plots, indicating a more even distribution of turbulence in that vessel.

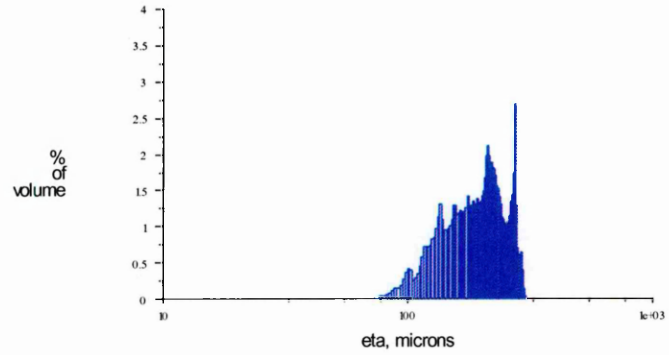
Therefore, it is concluded that the highest turbulence dissipation rate values (which might be considered to give rise to floc breakage) occur in the Hudson vessel. However, turbulence dissipation rate values are less well distributed in the Hudson vessel than in the cylindrical vessel. Consequently, although the potentially floc destructive, values occur, they are found only in the immediate vicinity of the paddle. Oldshue (1983) suggested that baffles in a mixer inhibit the overall motion of the fluid, whilst increasing power draw. The increased power draw in the Hudson vessel is apparent from Figure 4-7. The results shown here also corroborate the conclusions of Oldshue (1983). The increased volume of dead spots and lower distribution of the turbulence dissipation rate in the Hudson vessel compared to the cylindrical vessel demonstrate a reduction in mixing capacity of the Hudson vessel.

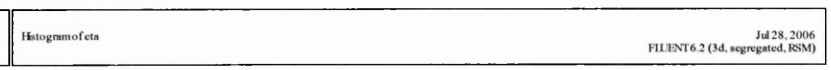
Cylindrical Vessel: N=200 rpm



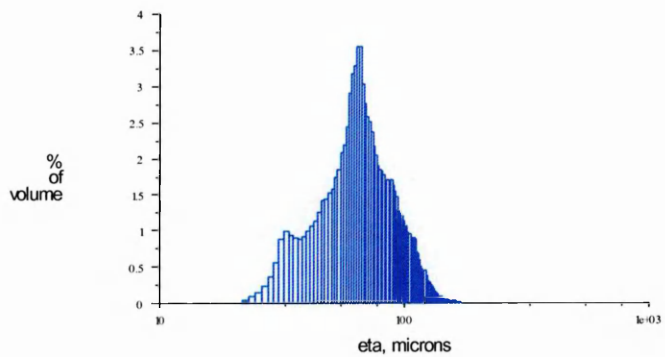


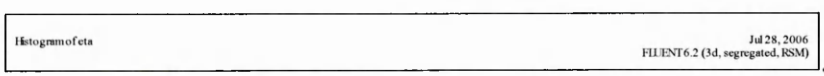
N=50 rpm



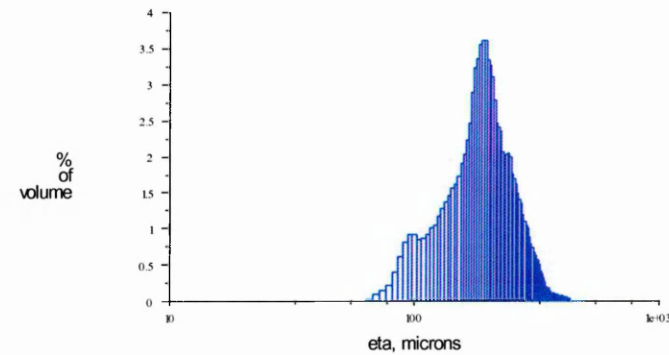


Hudson Vessel: N=200 rpm





N=50 rpm



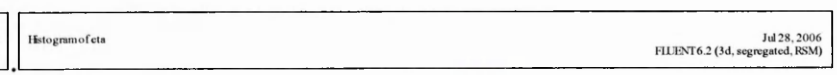


Figure 6-17: Kolmogorov length scale distributions in cylindrical and Hudson Vessels at 200 and 50 rpm.

6.4.2 Magnitude of Turbulence Dissipation Rate

In order to develop the understanding of the magnitude and distribution of the turbulence dissipation rate in each vessel further and to link this to impacts on floc breakage, for each of the two vessel models, four volumes of interest were identified and studied; specifically:

(i) vessel contents – *i.e.* all liquid in vessel

(ii) paddle swept volume (PSV) – *i.e.* volume of vessel traced by paddle

(iii) continuum – *i.e.* that part of the vessel not included within the paddle swept volume

(iv) paddle tip zone (PTZ) – *i.e.* an annulus extending 1.5mm beyond the paddle tip in both the radial and vertical directions.

In effect, this was an extension of the work of Tomi and Bagster (1978a & b) who originally identified the paddle swept and paddle tip zones as areas of interest. The relationships between the average turbulence dissipation rate values found in each of the four zones and the mixing speed are plotted at Figure 6-18. The turbulence dissipation rate volume averages for both mixing systems exhibit the hierarchy paddle tip zone > paddle swept volume > vessel > continuum. Good power curve correlations are observed between turbulence dissipation rate and mixing speed for all zones in both vessels. The resulting coefficient of determination, r^2, values are tabulated at Table 6-1.

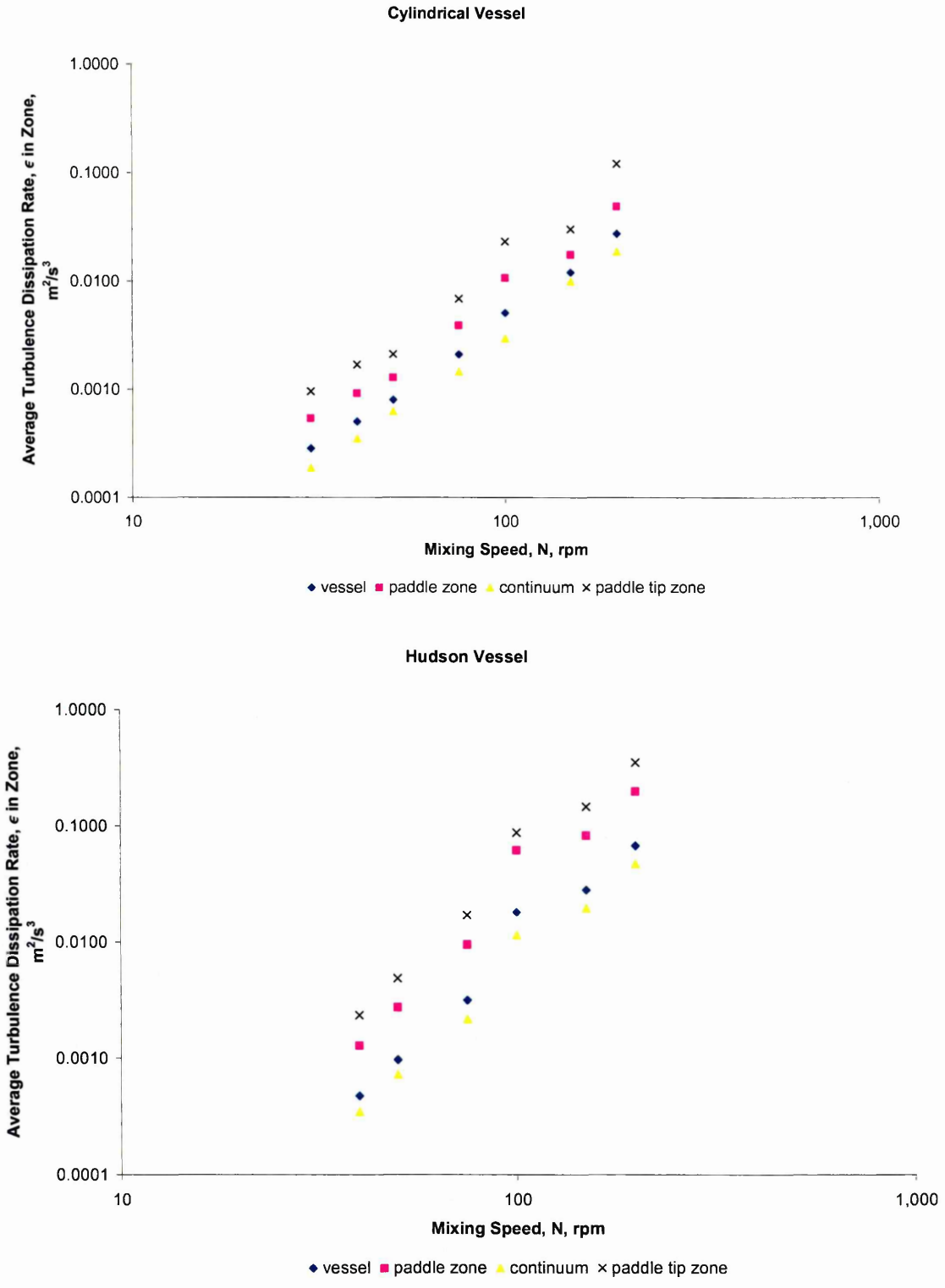


Figure 6-18: **Average turbulence dissipation rate, ϵ, in each of four zones, plotted against mixing speed for (a) cylindrical vessel and (b) Hudson vessel.**

Table 6-1: **Power curve coefficients of determination for turbulence dissipation rates and mixing speed from Figure 6-18**

Zone	Cylindrical Vessel	Hudson Vessel
Vessel	0.9972	0.9718
Continuum	0.9974	0.9778
Paddle Swept Volume	0.9883	0.9611
Paddle Tip Zone	0.9732	0.9767

Data for the two vessels are compared directly at Figure 6-19, where the results for the paddle tip zone and vessel averages are plotted together. It is apparent from Figure 6-19 that at the majority of mixing speeds, the Hudson vessel exhibits higher average turbulence dissipation rate values than the cylindrical vessel (the exception to this being the vessel data at 30 rpm). However, it is also clear that the rate of increase in ϵ with increasing mixing speed is greater in the Hudson vessel than in the cylindrical vessel; this observation being particularly true in the paddle tip zone. Stanley and Smith (1995) were able to develop similar shaped curves for the PSV and vessel for the Hudson vessel using LDA-derived data. However, it is also interesting to compare these curves with the results of Metzer and Taylor (1960) who demonstrated a linear relationship for various impeller types in a non-Newtonian fluid at various radial distances from the impeller.

The differences between the ϵ values found in the different zones are demonstrated at Figure 6-20. For the cylindrical vessel it can be seen that the average ϵ value in the paddle tip zone is 3.5 times greater than that found in the vessel overall. However, the corresponding relationship for the Hudson vessel shows that the average ϵ value in the paddle tip zone is 5.0 times greater than that found in the vessel overall. Using LDA-derived data, Stanley and Smith (1995) suggested that the value for the Hudson vessel at mixing speeds of 100 rpm and below should be between four and six, and so this result agrees well with the previous work. It is apparent from Figure 6-19 and Figure 6-20 that the degree of turbulence generated in the paddle tip zone in the Hudson vessel is significantly greater than the cylindrical vessel. However, it is interesting to note that for the continuum, the average ϵ value is half of that found in the vessel overall for both

vessels (*i.e.* $\epsilon_{continuum} / \epsilon_{vessel} = 0.5$). This result further confirms the conclusion drawn above that although higher ϵ values are generated in the Hudson vessel, they are less well dissipated than in the cylindrical vessel, and hence there is little difference between the ratios of the continuum average ϵ to the vessel average.

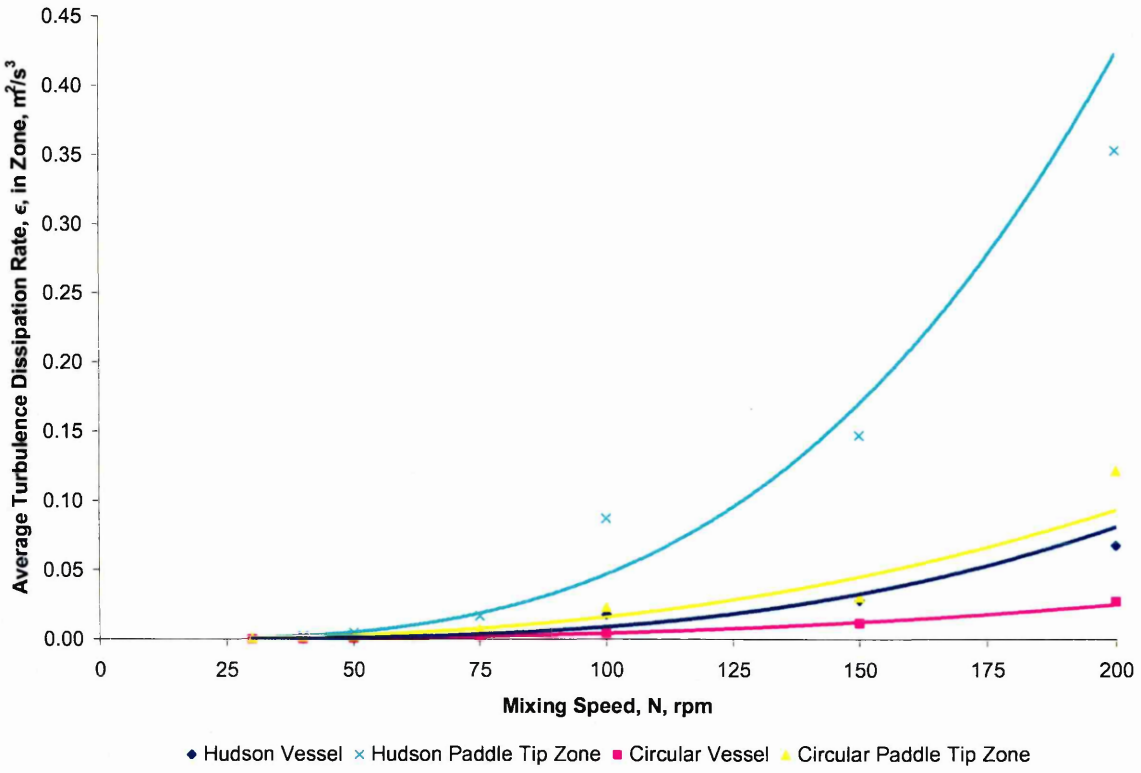


Figure 6-19: **Comparison of average turbulence dissipation rate in paddle tip zone and vessel for the cylindrical and Hudson vessels.**

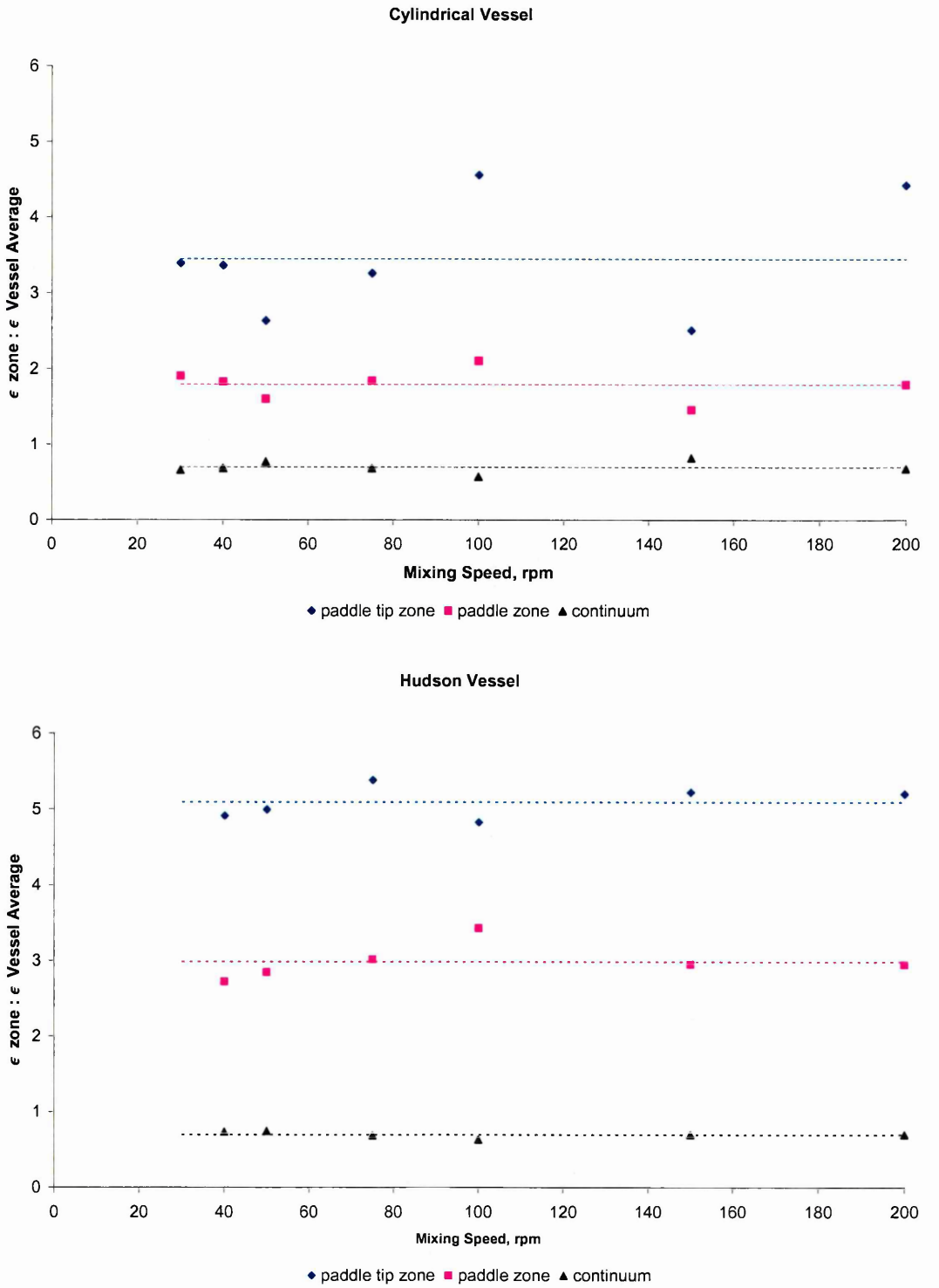


Figure 6-20: **Ratio of ϵ value in particular zone to vessel average ϵ value for cylindrical and Hudson vessels.**

6.5 Summary

Scaling of axial velocity components arising from the CFD model of the Hudson vessel showed good results, albeit with some scatter which is probably as a result of the presence of transitional flow regimes. The maximum scaled radial velocity for the Hudson vessel of 0.35 agreed well with that suggested by Stanley and Smith (1995) based on their LDA assessment of the same vessel and mixing configuration. A reduced maximum scaling constant of 0.20 was observed for the cylindrical vessel demonstrating the increased axial velocities generated in the Hudson vessel, particularly in the region between the paddle tip and vessel walls. Both values are substantially below recorded values for the Rushton turbine (range of reported values is 0.5 – 1.2, average 0.84).

The large instantaneous axial velocity increase brought about by an increase in mixing speed from 30 to 200 rpm and the large variability about the mean at 200 rpm have been demonstrated. An important element of the research that follows is an investigation into why flocs exhibit breakage at increased mixing speeds, and it is likely that breakage is, to some degree, a result of instantaneous changes in velocity and velocity gradients. This issue is discussed in greater detail in Chapters 7 and 8.

Very strong power curve relationships were demonstrated between the turbulence dissipation rate CFD data and mixing speed for both vessels. Strong relationships were observed for the vessel in its entirety, and also for various subsets of the vessel contents including the paddle swept volume and the paddle tip zone. Stanley and Smith (1995) had previously demonstrated similar shaped curves for the Hudson vessel at low mixing speeds. However, no previous data are available for the cylindrical vessel in similar circumstances, nor the Hudson vessel at high mixing speeds. The CFD analyses of the two vessels have shown that higher turbulence dissipation rates are to be found in the Hudson vessel than in the cylindrical vessel. In addition, the results show that the highest turbulence dissipation rate values are to be found in the region immediately adjacent to the paddle tip (referred to here as the paddle tip zone). Turbulence

dissipation rates in the paddle tip zone of the Hudson vessel were found to be some five times the vessel average values. The corresponding value for the cylindrical vessel was 3.5. However, the results also show that the bandwidth (*i.e.* distribution) of these high values is narrower in the Hudson vessel, indicating that the distribution of turbulence dissipation rates is greater in the cylindrical vessel than the Hudson vessel. Furthermore, it has been demonstrated that there is an increased amount of low velocity dead space in the Hudson velocity compared to the cylindrical vessel. Thus, it is concluded that the general degree of mixing is greater in the cylindrical vessel than the Hudson vessel, despite the presence of higher turbulence dissipation rates in the latter.

There is a significant range of velocities, and consequently velocity gradients, found in the two vessels, particularly the Hudson vessel, with the highest values found in the paddle swept volume and the paddle tip zone. It is likely therefore that the paddle has a significant impact on floc size, formation and breakage.

The jar test has been used effectively for considerable time in the water industry to determine optimum coagulant type, dose and pH for specific water types. However, the above results demonstrate that the hydrodynamic environments generated by the same paddle at the same mixing speeds but in different vessels are quite different. Consequently, the logical extension of this conclusion is that the jar tester does not represent the hydrodynamics of a full scale flocculator. As the literature review (Chapter 2) and the above results demonstrate, the hydrodynamic environment has a significant effect on floc formation and breakage. Thus, the use of the jar test to provide anything other than a coarse assessment of raw water flocculation characteristics must be questioned.

7 Cylindrical Jar Test Apparatus - CFD Particle Trajectory Analysis

7.1 Introduction

As discussed in Chapter 2, the design of flocculation tanks and their operating strategies depend on a good understanding of the flow and mixing characteristics of the mixing vessel. The ability to predict these turbulent flows with the necessary degree of accuracy is fundamental to the development and optimization of the flocculation process. The commercially-available CFD code, Fluent v6 (Fluent, Sheffield, UK) was used to model the flow field within a standard jar test apparatus as described in detail in Chapter 5 above.

Chapter 6 considered the bulk flow characteristics of two types of jar tester and also the local variations in key parameters (such as turbulence dissipation rate) and the impact that these might have on floc characteristics. This work provided a useful insight into the different mechanisms generated within the different flocculators and how these will affect jar test results. The work recorded in this chapter builds on the previous work, and the work of earlier researchers, by considering the effects of turbulence on individual particles. Previous workers have considered the bulk flow characteristics of specific vessels (Korpijarvi *et al.*, 1999 & 2000, Essemiani and de Traversay, 2002a & b) but none have extended their work to include particle transport analysis in flocculators (although Korpijarvi *et al.* recognised the need for the work). Thus, the particle trajectory analyses reported below represent a significant development in the understanding of floc transport in a jar test.

Using the MRF / RSM cylindrical vessel model, a series of simulations was undertaken in which the shaft rotational speeds were varied between 30 rpm and 200 rpm, resulting in Reynolds numbers of between 2,859 and 19,063. Fluent's Discrete Phase Model solver (described in section 7.2 below) was employed to study the predicted pathlines of

particles varying in both size and density injected into the vessel. Four particle diameters were considered (250, 500, 750 and 1,000μm) and up to four particle densities were considered for each particle, depending on its size. 11 different particle size / density combinations were considered for each of seven mixing speeds, giving 77 scenarios, as described at Table 7-1.

The difficulties inherent in the measurement of floc size and, perhaps more so, floc density, are well documented (Jarvis *et al.*, 2005b, Gregory and Nelson, 1986, Gregory, 1997). Further, flocs are irregular shaped, mass fractal objects and not spherical. Tang *et al.* (2002) recognised that floc settling behaviour is dependent on size, effective density and porosity. The fractal nature of flocs yields two potential effects on their settlement behaviour as their shape becomes increasingly non-spherical with growth. This deformation from spherical might be considered to increase the drag on the floc compared to a similarly sized solid sphere. However, Bushell *et al.* (2002) suggested that floc porosity can reduce drag by permitting advection of the suspending medium through the floc structure. Nevertheless, workers have successfully applied Stokes' law to the determination of floc settling velocity and fractal dimension (Miyahara *et al.*, 2002, Wu *et al.*, 2003, Gregory, 1989). Stokes' law was developed to characterise spherical particle settling velocity in terms of particle density relative to the surrounding liquid, particle size and velocity. However, Gregory (1997) suggested that it was adequate for use in floc settlement characteristics. Whilst the assumption that Stokes' law can be applied to flocs is open to debate, its application is widespread (Bache *et al.*, 1999, Gregory, 1997, Tang *et al.*, 2002, Jarvis *et al.*, 2005b). In view of the foregoing comments, the use of spherical solid particles in lieu of irregularly shaped flocs was deemed to be acceptable for the numerical analyses recorded here. The ranges of size and density used are indicative of those found in the literature.

Table 7-1: **Summary of particle size and density trajectories modelled (shading indicates analyses undertaken).**

N=30		Diameter, μm			
		250	500	750	1000
Density, kg/m³	1,000				
	1,250				
	1,500				
	2,000				

N=40		Diameter, μm			
		250	500	750	1000
Density, kg/m³	1,000				
	1,250				
	1,500				
	2,000				

N=50		Diameter, μm			
		250	500	750	1000
Density, kg/m³	1,000				
	1,250				
	1,500				
	2,000				

N=75		Diameter, μm			
		250	500	750	1000
Density, kg/m³	1,000				
	1,250				
	1,500				
	2,000				

N=100		Diameter, μm			
		250	500	750	1000
Density, kg/m³	1,000				
	1,250				
	1,500				
	2,000				

N=150		Diameter, μm			
		250	500	750	1000
Density, kg/m³	1,000				
	1,250				
	1,500				
	2,000				

N=200		Diameter, μm			
		250	500	750	1000
Density, kg/m³	1,000				
	1,250				
	1,500				
	2,000				

7.2 Modelling Particle Trajectories

The Fluent software has an in-built discrete phase model which can be used to model the trajectories of individual particles within a flow via integration of the force balance on a particle in a Lagrangian reference frame. Equating particle inertia with the forces acting on it, and applying a Cartesian co-ordinate system, yields:

$$\frac{du_p}{dt} = F_D(u-u_p) + \frac{g_x(\rho_p - \rho)}{\rho} + F_x \qquad \textbf{Equation 7-1}$$

where,

u is the fluid velocity,

u_p is the particle velocity,

μ is the dynamic viscosity of the fluid, and

ρ and ρ_p are the fluid and particle densities, respectively

$F_D(u-u_p)$ is the drag force per unit particle mass,

and $$F_D = \frac{18\mu}{\rho_p d_p^{\,2}} \cdot \frac{C_D \mathrm{Re}}{24} \qquad \textbf{Equation 7-2}$$

where d_p is the particle diameter, and Re is the relative Reynolds number, defined as:

$$\mathrm{Re} = \frac{\rho d_p |u_p - u|}{\mu}$$ **Equation 7-3**

For the work reported here, the drag coefficient, C_D, is defined as:

$$C_D = \alpha_1 + \frac{\alpha_2}{\mathrm{Re}} + \frac{\alpha_3}{\mathrm{Re}^2}$$ **Equation 7-4**

Where α_n are constants that apply to smooth spherical particles over several ranges of Re given by Morsi and Alexander (1972), cited in Fluent (2005).

A revised form of the drag coefficient is available in Fluent for sub-micron particles, but this has not been employed in this work as all particles studied were 1μm or greater in diameter.

The term F_x in Equation 7.1 relates to additional forces in the particle force balance that are relevant only under special circumstances. For the analyses undertaken as part of this work, F_x includes forces on particles that arise due to the rotation of the reference frame. Considering rotation about the z axis, the forces on the particles in the x and y directions may be expressed as:

$$\left(1 - \frac{\rho}{\rho_p}\right)\Omega^2 x + 2\Omega\left(u_{y,p} - \frac{\rho}{\rho_p}u_y\right)$$ **Equation 7-5**

where $u_{y,p}$ and u_y are the particle and fluid velocities in the y direction, and

$$\left(1 - \frac{\rho}{\rho_p}\right)\Omega^2 y + 2\Omega\left(u_{x,p} - \frac{\rho}{\rho_p}u_x\right)$$ **Equation 7-6**

where $u_{x,p}$ and u_x are the particle and fluid velocities in the x direction.

The discrete phase boundary conditions were set such that, on striking a boundary wall, the particles were reflected back into the flow.

7.3 Random Particle Analysis

7.3.1 Particle Trajectories and Fates

The predicted pathlines of spherical particles described at Table 7-1 when injected individually into the flow at a mid quadrant point at mid depth (*i.e.* x=y=0.0177m, z=0.0635m) were analysed. It is accepted that these trajectories might not define precisely the actual trajectories of all flocs, and nor does the discrete phase model consider inter-particle interaction (*i.e.* agglomeration and breakage); however, it is considered that the trajectories can be used to provide a good representation of the nature of turbulent effects and shear forces present locally within the vessel and to which a floc might be subjected. The trajectory of a neutrally buoyant 500μm diameter spherical particle injected into the vessel mixed at shaft rotational speed of 200 rpm is shown in Figure 7-1. Good coverage of the vessel was observed. With no baffles to encourage recirculation, the degree of particle transport shown in the vertical plane might not be expected. However, the particle was small and neutrally buoyant, and consequently it is concluded that the particle was following the flow field. Similar coverage of the vessel was observed for all particles and trajectories analysed. This demonstrates the good mixing characteristics of the cylindrical vessel which were anticipated on the basis of the distribution of the turbulence dissipation rate discussed in Chapter 6.

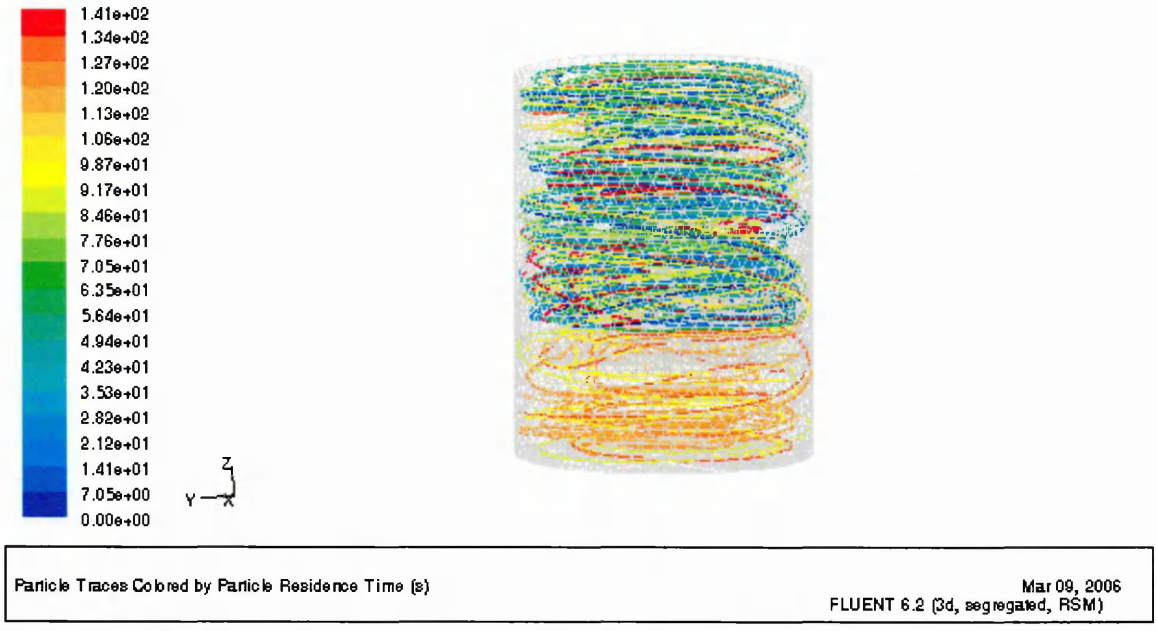


Figure 7-1: Particle trajectory: N=200rpm, ϕ=500μm, ρ=1,000 kg/m^3. Particle injected at mid-quadrant point at mid-depth.

7.3.2 Local Velocity Gradient Variation Along Trajectory

The local velocity gradient was calculated for each point along each particle's trajectory, (defined as $G_t = \sqrt{\frac{\varepsilon}{\rho}}$) and these values were then plotted against simulation time. (The formulation of G_t is the same as for the local velocity gradient, G_L; the difference being that G_t refers only to those local velocity gradient values experienced by a particle along a specific trajectory, whereas G_L can apply at any point within the vessel.) Plots for a neutrally buoyant 500μm particle subjected to five mixing speeds over 60 seconds duration are shown at Figure 7-2 and Figure 7-3. On each plot, the associated vessel average velocity gradient values are also shown.

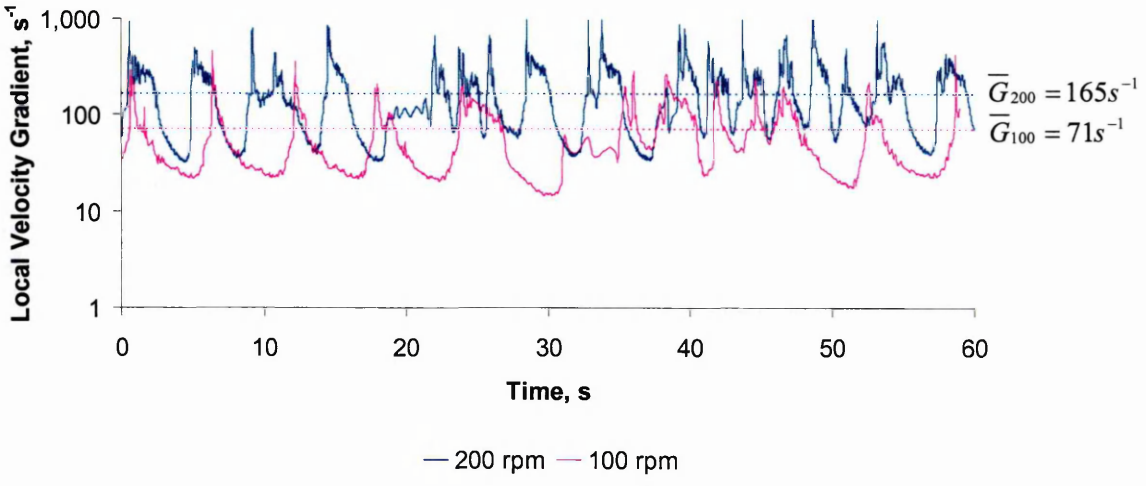


Figure 7-2: **Variation in local velocity gradient experienced by a 500μm neutrally buoyant particle subject to mixing speeds of 100 and 200 rpm.**

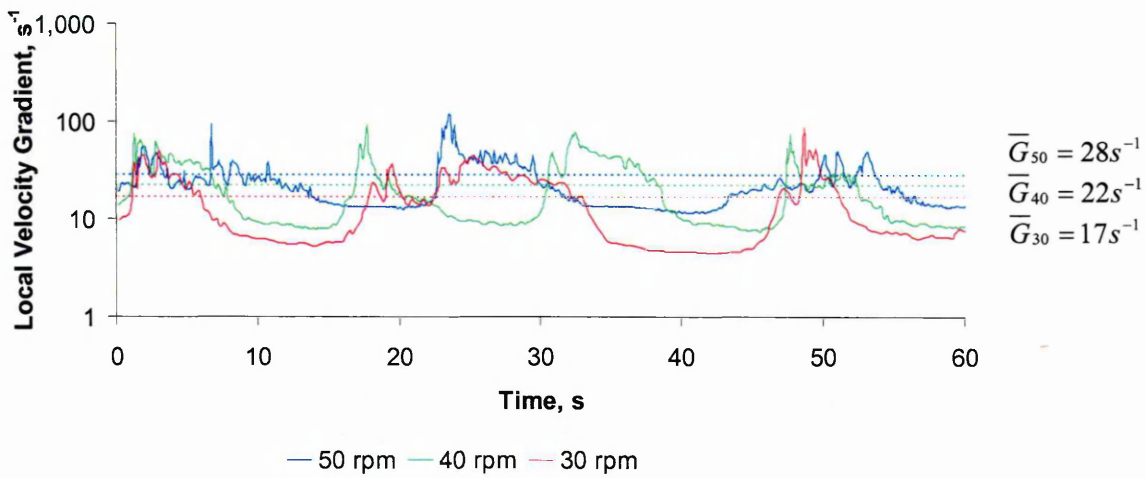


Figure 7-3: **Variation in local velocity gradient experienced by a 500μm neutrally buoyant particle subject to mixing speeds of 30, 40 and 50 rpm.**

For all five trajectories, it is clear that whilst there is a large number of local velocity gradient values which are significantly above the average value, the average value experienced by the particle along its trajectory, $\overline{G}_t$ is not dissimilar to the vessel average, $\overline{G}$. (The trajectory and vessel average values are tabulated below at Table 7-2 together with the maximum G_t value experienced.) This again demonstrates good

mixing of the particles throughout the vessel, covering areas of both high and low local velocity gradients.

Table 7-2: Comparison of vessel average, trajectory average and trajectory maximum velocity gradients for various mixing speeds.

N, rpm	Vessel Average Velocity Gradient, $\overline{G}$, s^{-1}	Trajectory Average Velocity Gradient, $\overline{G}_t$, s^{-1}	Trajectory Maximum Velocity Gradient, $G_{t\,max}$, s^{-1}	$G_{t\,max} / \overline{G}$
30	17	17	99	5.8
40	22	22	110	5.0
50	28	25	141	5.0
75	46	65	300	6.5
100	71	68	657	9.3
150	109	199	744	6.8
200	165	185	1551	9.4

However, although the average trajectory velocity gradient, $\overline{G}_t$, is similar to the vessel average (*i.e.* $\overline{G} \approx \overline{G}_t$), it is also evident that there are significant variations about the average for all mixing speeds. For example, in the 200 rpm case, whilst the average G_t value experienced by the particle over the first 60 seconds is $185s^{-1}$ (compared to a vessel average of $165s^{-1}$), there are 89 individual points within that period where G_t exceeds
$500s^{-1}$, and the maximum value the particle is subjected to is 1,551 s^{-1} (a factor of 8.4 greater than the $\overline{G}_t$ and 9.4 times greater than $\overline{G}$). This result is in agreement with Essemiani and de Traversay (2002a & b) who concluded that G_t takes into account local turbulence effects which are not included in the $\overline{G}$ calculation. It is apparent that these effects are large and potentially significant when considering the effects on floc structure. Korpijarvi *et al.* (1999 & 2000) and Essemiani and de Traversay (2002a & b) considered bulk flow patterns in a jar tester and pilot scale flocculator respectively. However, neither considered the shear forces applied to individual flocs. Whilst the magnitude of the G_t values are of interest, it is also interesting to consider the frequency of occurrence of these peaks. For the 200 rpm mixing scenario, peaks in excess of $500s^{-1}$ are observed at least every five seconds for the 60 second simulation period, whilst for the 100 rpm scenario this frequency reduces to one peak every 10 seconds.

The plots of G_t against time for the 40, 50 and 50 rpm scenarios are somewhat different to those for the 100 and 200 rpm scenarios. Peaks and troughs about the mean are again exhibited; however, the frequency of instantaneous peaks is much reduced. This is a significant observation as it indicates both a qualitative and quantitative difference in flow field characteristics between high and low mixing speeds. It is apparent from the data that as the mixing speed increases, the maximum G_t value experienced by the particle increases. However, in addition, these high G_t values are experienced on a more frequent basis. Thus, not only is a floc exposed to higher G_t values at higher mixing speeds, it is also exposed on a more frequent basis to G_t values which are greater than the vessel average. It is considered that both of these effects will have an effect on floc breakage.

For neutrally buoyant particles of various diameters, Figure 7-4 summarises the proportion of the 60s simulation time for which the particle was exposed to a G_t in excess of $\overline{G}$. The results demonstrate that irrespective of size and, to a lesser extent, mixing speed, the amount of time a particle experienced local velocity gradient values greater than the vessel average was broadly similar, and no discernible pattern or link could be derived between mixing speed and particle diameter. This result is unsurprising as one would intuitively expect these particles to behave in the same manner as they are all neutrally buoyant and relatively small.

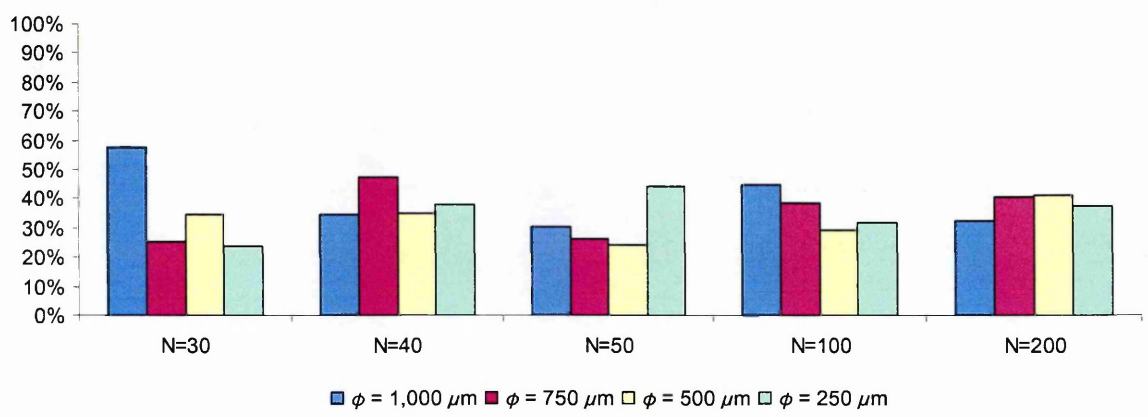


Figure 7-4: **Percentage durations for which neutrally buoyant particles (ρ=1,000 kg/m^3) experienced local velocity gradients in excess of the vessel average velocity gradient. Particle residence time = 60s.**

A similar analysis was undertaken for particles with a density of 1,250 kg/m^3, and the results are shown at Figure 7-5. In this situation, the overall result is somewhat different. At low mixing speeds, the smaller particles generally spent less time in regions of higher turbulence than the neutrally buoyant particles, (albeit the percentage differences are not great). However, once the mixing speed exceeded 50 rpm, the majority of the particles' exposure was to velocity gradients higher than the average for the majority of the simulation period. This is interesting as it demonstrates, for these somewhat random particles, a dependency on density and indicates that at high mixing speeds the denser particles spent more time in the turbulent, paddle region and did not occupy as much of the overall vessel as a neutrally buoyant particle did. This is of direct relevance to earlier work which has investigated floc density, such as Jarvis (2005), who presented structural data obtained during the coagulation of a NOM rich water source under optimum conditions for a range of coagulant systems. This evaluation of floc structure included traditional coagulants such as ferric sulphate and alum as well as novel treatment options such as polymers and ion exchange resin pre-treatment. For the latter, an anionic magnetic ion exchange resin (MIEX®) was used. Full details of MIEX® are to be found at Fearing *et al.* (2004); suffice to state here that MIEX® is a strong base anionic exchange resin of a macroporous structure. The ion exchange resin particles contain a magnetised component within their structure, allowing the particles to act as weak individual magnets, giving rise to agglomeration into flocs. In addition, the material is of high density which increases sedimentation rates. Jarvis (2005) demonstrated that floc settling velocities (and hence densities) were dependent upon treatment options, and found that the MIEX®-treated flocs had a settling velocity close to that of kaolin flocs, even though the Kaolin had a density of 2,600 kg/m^3, compared to an estimated humic density of 1,750 kg/m^3. Thus, it is concluded that within a jar test scenario, MIEX® flocs would be subjected to a greater degree of turbulence than other, less dense, flocs. It is of great interest therefore to note that Jarvis (2005) found the MIEX® flocs to be amongst the strongest studied. This density-related phenomenon observed in the CFD results suggests, therefore, that the strength of the MIEX® flocs has previously been understated as it has previously been assumed that flocs would be subjected to the same degree of turbulence, irrespective of size or density.

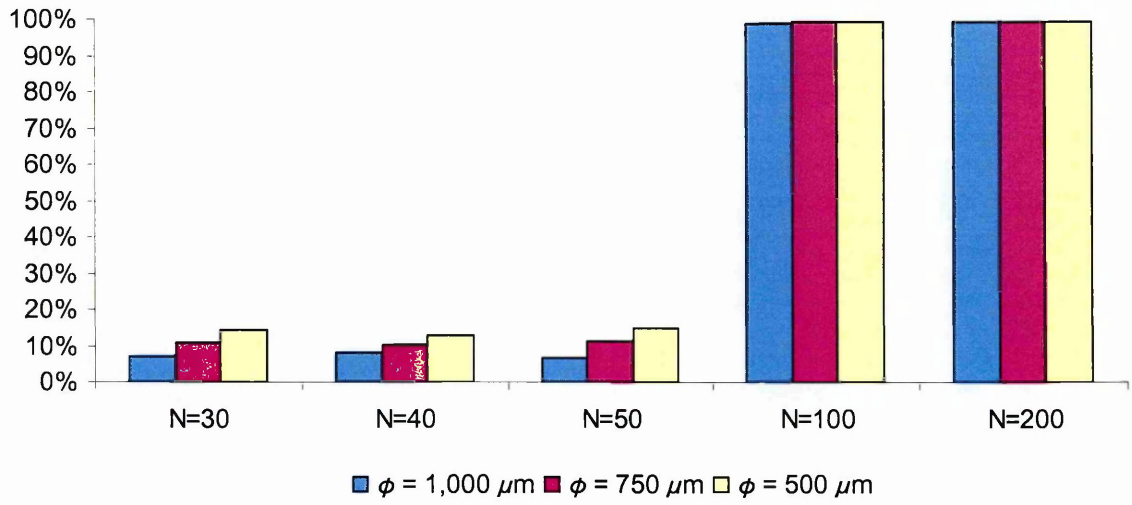


Figure 7-5: **Percentage durations for which non-neutrally buoyant particles (ρ=1,250 kg/m^3) experienced local velocity gradients in excess of the vessel average velocity gradient. Particle residence time = 60s.**

Figure 7-6 show plots of G_t with time for different density, same size particles mixed at 50 and 100 rpm (ϕ=250μm, ρ=1,000 kg/m^3 and 1,250 kg/m^3). Although the trajectories obviously differ, the profiles exhibit similarities as the range of the peaks and the troughs is the same. Therefore, whilst Figure 7-4 and Figure 7-5 demonstrate that varying density gives rise to different periods of exposure to G_t values which are greater than $\overline{G}$, Figure 7-6 shows that the extent of G_t values experienced at various mixing speeds is the same irrespective of density. Any effect that varying density has on the range of G_t values experienced is not evident.

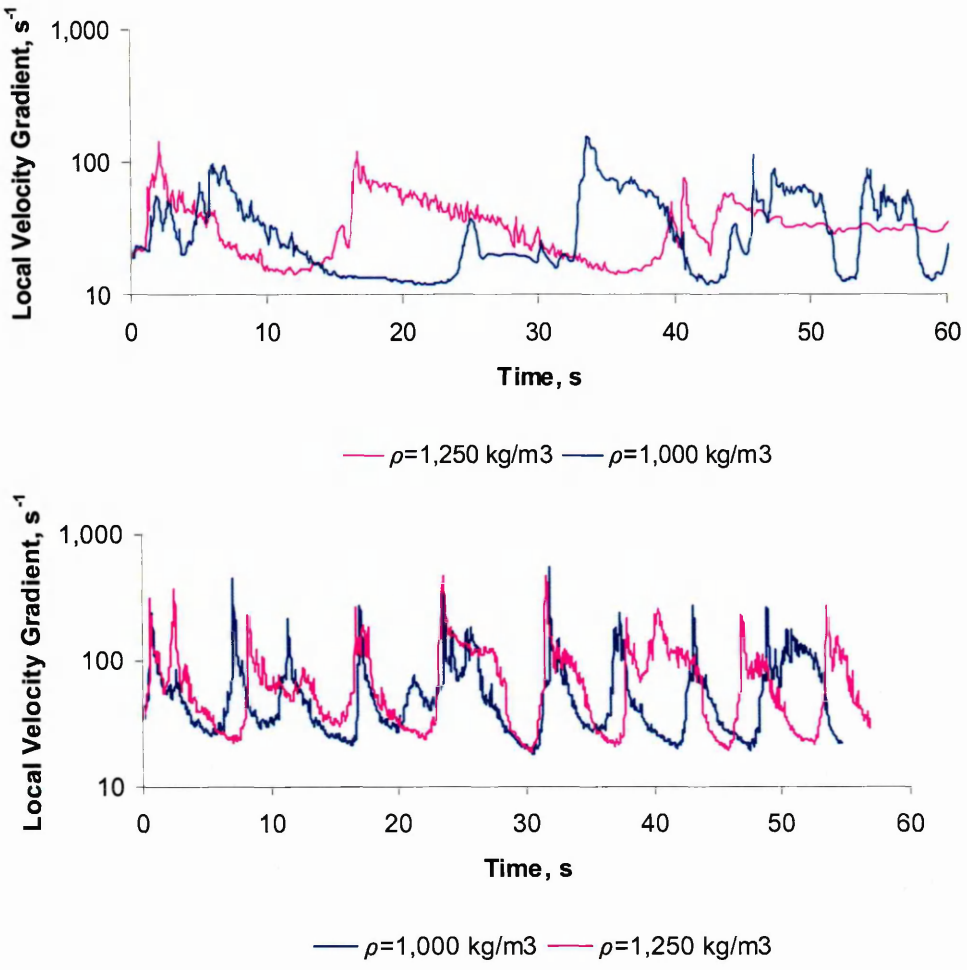


Figure 7-6: Variation in local velocity gradient with time for 250μm particles of different densities mixed at (a) 50 rpm and (b) 100 rpm.

7.3.3 Period of Exposure to Local Velocity Gradients

Whilst it is interesting and relatively straightforward to examine the profile of the local velocity gradient along the trajectory of a particle (or floc), further work is necessary to assist in the determination of the cause of floc breakage. Consequently, the model trajectory data were analysed further to determine the amount of time for which a particle was subjected to a given level of velocity gradient. For the 200 rpm, 500μm, 1,000 kg/m^3, 60 second simulation, Figure 7-7 shows ranges of G_t values on the

abscissa, with total time spent in each range (measured in seconds) on the left hand ordinate. Cumulative time spent in each range, as a percentage of the total simulation time considered, is displayed as a line against the right hand ordinate.

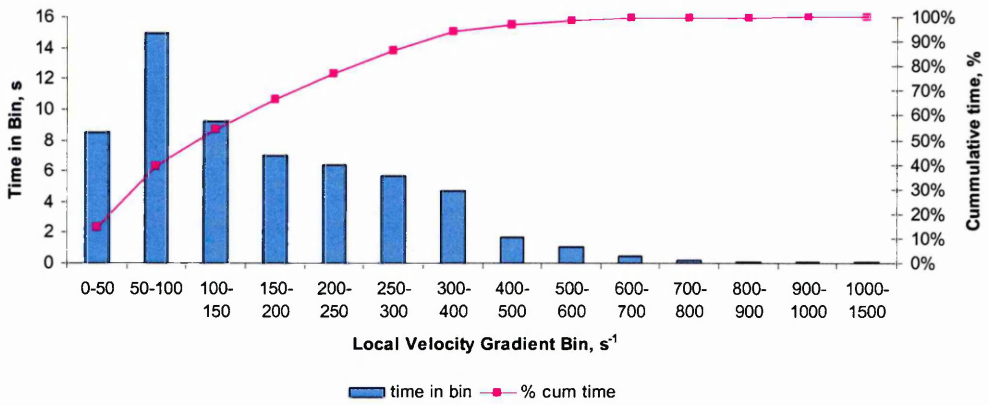


Figure 7-7: **Time spent by a particle experiencing ranges of local velocity gradient, N=200rpm, 500μm, 1,000 kg/m^3, 60s.**

It is clear from Figure 7-7 that the particle spends the majority of the simulation time shown being subjected to G_t values in the range 0-150 s^{-1}. In fact, the particle spends 54% of its time in this zone. However, in addition, the particle spends considerable time (42% of simulation) in the 150-500s^{-1} range. The $\overline{G}$ value for this scenario is 165s^{-1} and is therefore clearly unrepresentative of the magnitude of the degree of turbulence to which this random particle is subjected. Data for the 200, 100, 75, 50 and 30 rpm scenarios is shown in cumulative format at Figure 7-8. The plot shows a significant difference between the 50 and 30 rpm scenarios at the very low end of the scale (*e.g.* for the 50 rpm scenario, the particle experiences velocity gradients of 15s^{-1} and below for 35% of the time. The corresponding figure for the 30 rpm scenario is almost twice that at 61%). However, the two scenarios quickly converge, with neither giving rise to significant numbers of G_t values in excess of 100s^{-1}. There are noticeable differences between the 50 rpm and 75 rpm scenarios, and also between the 75 and 100 rpm scenarios and the 100 and 200 rpm scenarios. 96% of all trajectory G_t values are below 50s^{-1} for the 50 rpm scenario. The corresponding figures for 75, 100 and 200 rpm are 79%, 60% and 14% respectively.

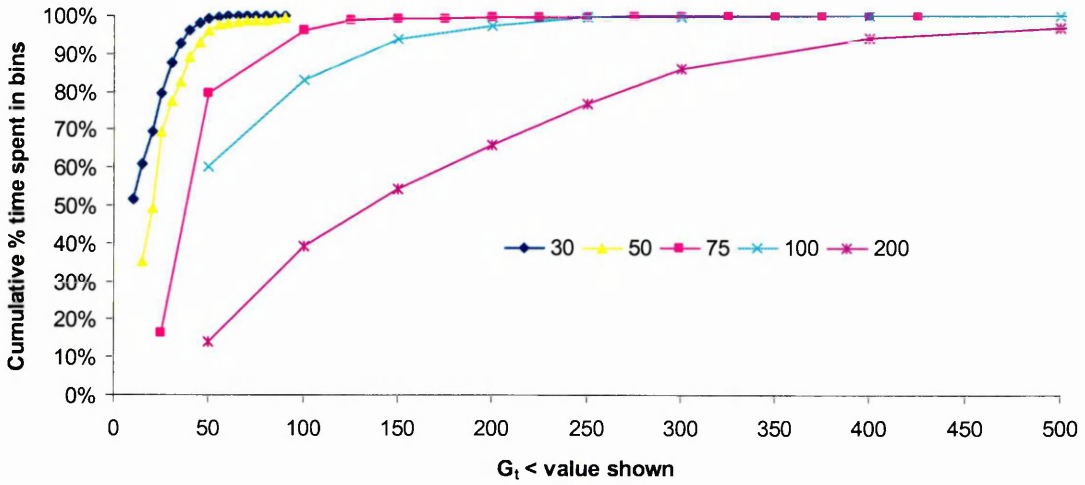


Figure 7-8: **Cumulative percentage time spent by a neutrally buoyant, 500μm particle experiencing ranges of local velocity gradient at various mixing speeds, 60s particle residence time.**

The shapes of the four curves in Figure 7-8 are significant as they demonstrate that at lower mixing speeds particles are subjected to lower G_t values for extended periods. At higher mixing speeds the situation is reversed with the particle experiencing high G_t values for the majority of the simulation period. For example, the 200 rpm scenario generated G_t>150s^{-1} for 50% of the simulation, whereas for the 50 rpm scenario, the corresponding figure is approximately 40 s^{-1}.

However, the analyses shown at Figure 7-7 and Figure 7-8 represent the total time spent in a particular zone over the 60s period considered, not the continuous time spent within that zone. When trying to elucidate the mechanisms by which flocs might break, it is important to consider whether breakage is brought about by instantaneous exposure to high velocity gradients, or prolonged exposure to lower values (and, clearly, definitions of "high" and "low" are open to some debate). Consequently, the data have been analysed to determine the continuous time a particle spends in a particular G_t range. For the 200, 100, 75 and 50 rpm scenarios, the maximum continuous time spent in each G_t range for a 500μm neutrally buoyant particle over a 60s mixing period are shown in Figure 7-9. Close inspection of Figure 7-9 is insightful as it demonstrates that a particle

typically spends less than one second in a G_t range which is higher than $\overline{G}$ at any one time. However, the total time spent in zones where the trajectory velocity gradient exceeds the vessel average is always greater than 5 seconds (and therefore significant) in each case. It is known (*e.g.* Jarvis *et al.*, 2004, Gregory, 2004) that flocs break when exposed to high mixing speeds. Therefore, the results obtained here would imply that any exposure to trajectory velocity gradients greater than the vessel average, irrespective of duration, might be significant in terms of floc breakage. This concept is developed further in Chapter 8 below.

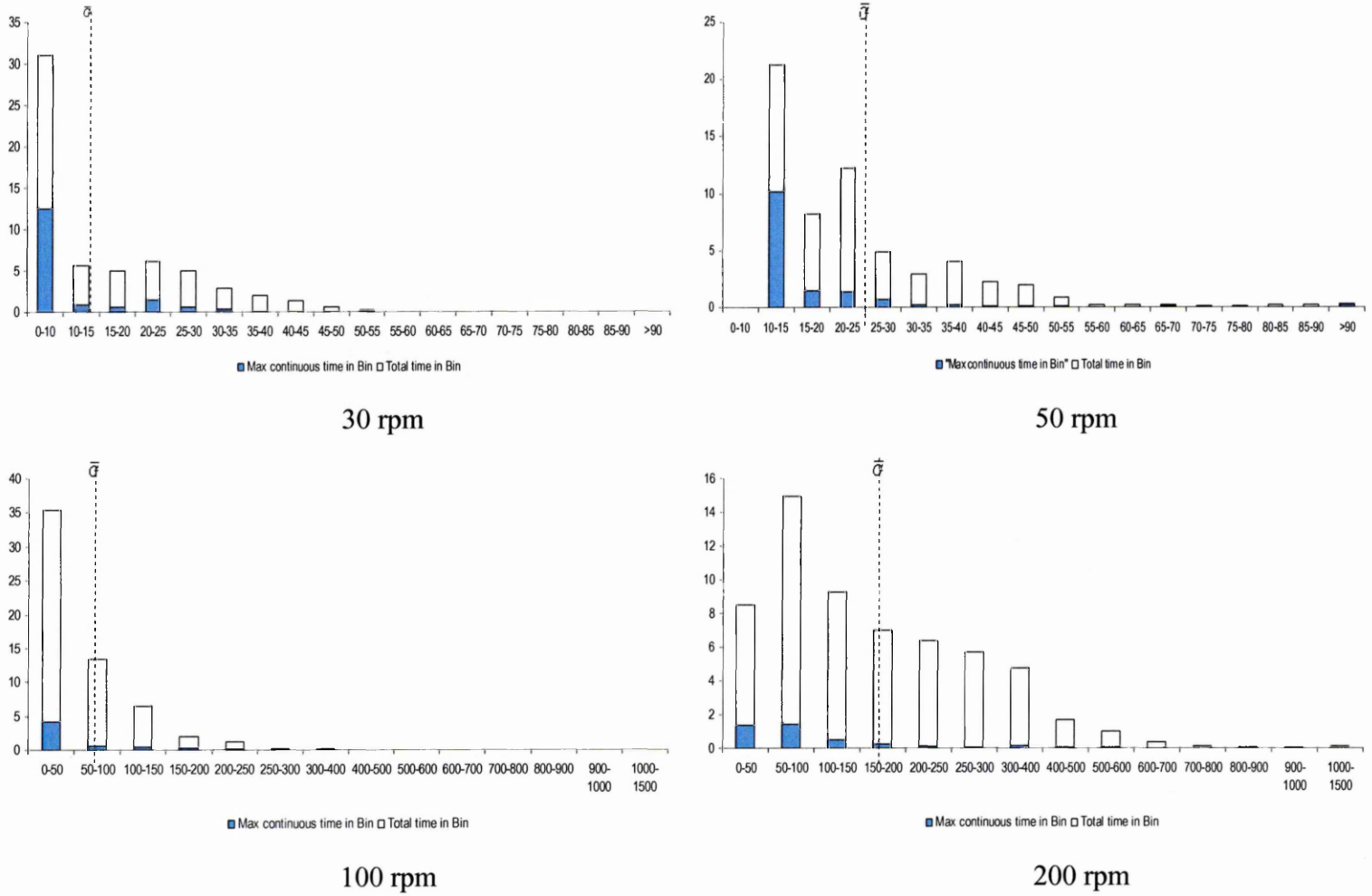


Figure 7-9: **Maximum continuous and total times for which a 500μm particle experiences specific velocity gradient ranges, 60 s particle residence time.**

The data from Figure 7-9 were extracted and the ratio of continuous time in bin to total time in each bin was calculated for each bin and each mixing speed. The results are plotted at Figure 7-10, and the $\overline{G}$ values for each mixing speed are also shown. This Figure presents some interesting results. It is apparent from Figure 7-10 that the curve shapes are broadly similar, irrespective of mixing speed. One can see that each curve is represented by an asymmetrical "U" shape, with a minimum value always being attained beyond the $\overline{G}$ value. The curves clearly shift to the right (*i.e.* higher G_t values) as the mixing speed increases. The increase after the minimum point is of interest. This demonstrates that the amount of continuous time spent in the highest G_t bins is high compared to the total time spent in these bins, and is, in relative terms, higher than in the lower G_t value bins. However, this can be readily explained by a closer examination of the data. As the G_t values increase, Figure 7-9 shows that the total time in those bins decreases to fractions of a second. Consequently, one would expect the particle to enter these bins on few occasions, and so, if the number of exposures to these high values is decreased, then the ratio of continuous time to total time spent in them must increase.

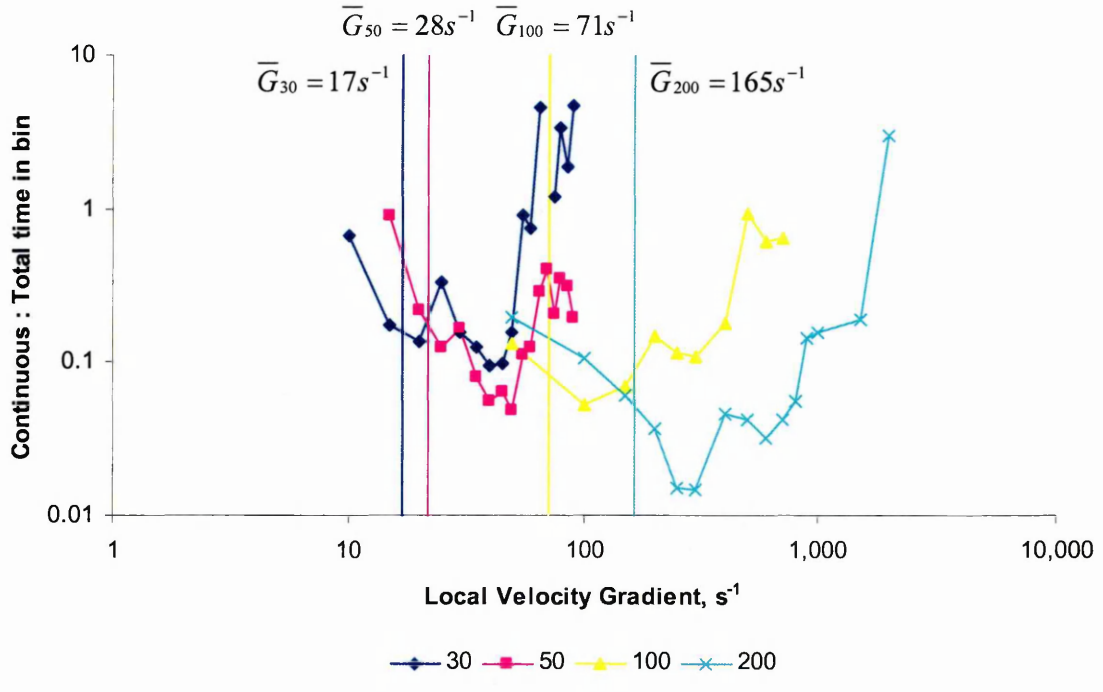


Figure 7-10: **Ratio of continuous time in bin to total time spent in bin plotted against velocity gradient.**

7.4 Summary

Considering the trajectories of random spherical particles with diameter and density fixed to replicate the characteristics of typical flocs subjected to 60s mixing in the cylindrical jar tester, it was found that, at a particular mixing speed, the average velocity gradient experienced by the particle along its trajectory was approximately equal to the vessel average velocity gradient for that vessel. This demonstrates that the two blade paddle and cylindrical vessel jar test configuration imparts a good degree of mixing to the liquid contents and further corroborates conclusions drawn in Chapter 6.

An analysis of the trajectories traced by particles demonstrates both a quantitative and qualitative difference in velocity gradient values experienced at different mixing speeds and, in particular, between high and low mixing speeds. At high mixing speeds (*i.e.* 100 rpm and above), local velocity gradients of up to ten times the vessel average are experienced at a rate of one or more every five seconds. The data show that as the mixing speed is decreased, so too is the magnitude of the peaks of velocity gradient experienced and the frequency with which these peaks are experienced.

The impact of particle size and density on trajectory and velocity gradient was considered via analyses of velocity gradients experienced along specific trajectories. It was found that neutrally buoyant particles experienced similar periods of exposure to trajectory velocity gradients which were higher than the vessel average, irrespective of diameter and, to a lesser extent, mixing speed. It was also found that the density of a particle affects the length of time for which a particle experiences velocity gradient values in excess of the vessel average. Viewed in conjunction with strength data developed by Jarvis (2005), it is concluded that the strength of MIEX® flocs has previously been understated. However, it was also found that changes in density did not have an effect on the range of the magnitude of local velocity gradient values experienced by the particle.

Increasing the mixing speed was found to increase the total amount of time for which a particle was exposed to higher velocity gradient values, but the maximum continuous

time for which a particle experienced values greater than the vessel average was always less than one second. As flocs are known to break at high mixing speeds, it is concluded that any exposure to velocity gradients in excess of the vessel average might be significant when considered in the context of floc breakage.

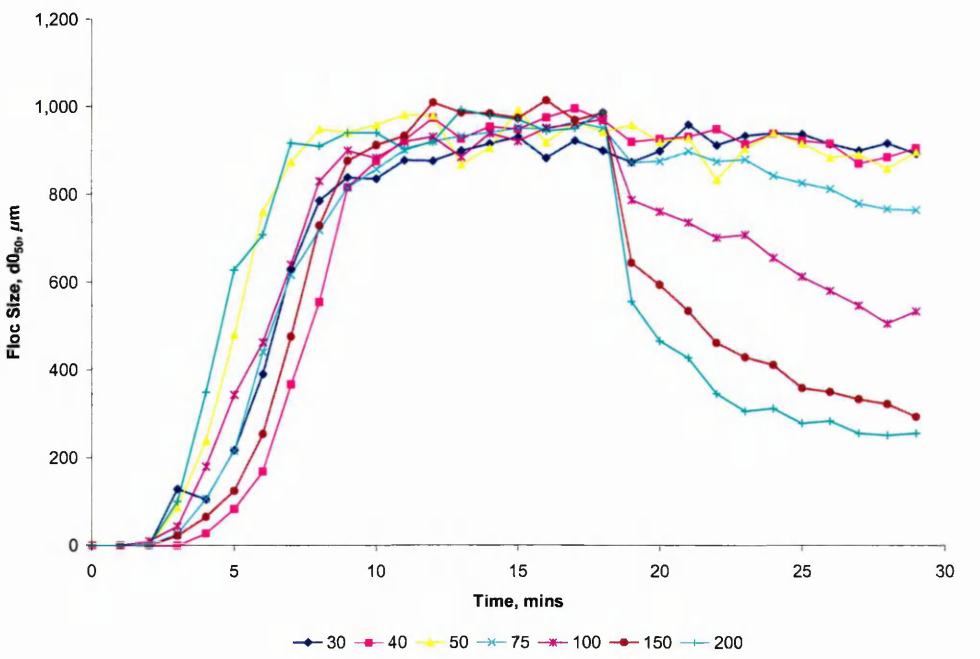
8 Comparison of Trajectory Data with Laboratory-Derived Floc Size Data

8.1 Previous Laboratory-Scale Work

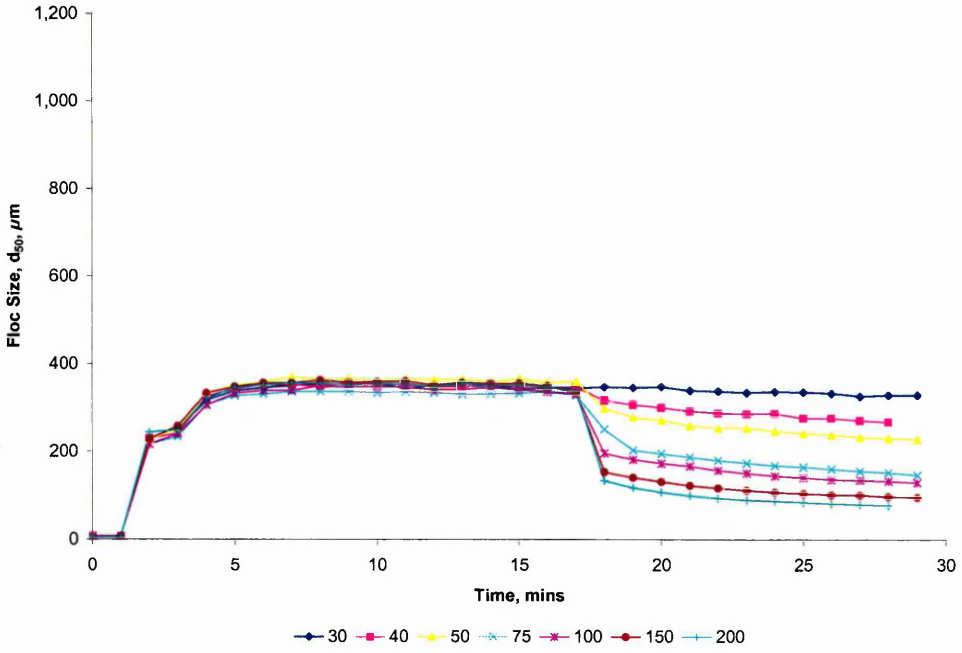
Having considered the trajectories of random particles designed to simulate a floc, the CFD analyses reported in previous chapters were extended in order to replicate laboratory scale flocculation experiments undertaken by Jarvis *et al.* (2004). Jarvis *et al.* undertook laboratory experiments using a cylindrical jar tester to compare the strength, breakage and re-growth characteristics of three different types of floc; specifically, coagulant precipitate (ferric hydroxide) flocs, turbidity flocs and organic matter flocs. Using a PB-900 variable speed jar tester (Phipps & Bird, Virginia, USA) and an unbaffled one litre cylindrical vessel, the authors developed flocs using a standard procedure (rapid mix at 200 rpm for 30s, followed by slow mixing at 30 rpm for 15 minutes) and then exposed the flocs to increasing levels of shear by increasing the mixing speeds, and observing any resulting changes in floc sizes.

As reported in the Literature Review (Chapter 2), Jarvis *et al.* (2004) found that the initial floc size (expressed as the median volumetric equivalent diameter, d_{50}) observed the hierarchy iron hydroxide > raw water > kaolin flocs. Increasing the mixing speed was found to decrease d_{50} in all cases until a steady state was reached some 30 minutes following the increase. The rate of degradation increased with the increase in mixing speed (*i.e.* a mixing speed of 200 rpm caused a faster rate of d_{50} decrease than a mixing speed of 50 rpm). Jarvis *et al.* reported that, upon exposure to increased mixing speeds (and so increased shear and velocity gradients), the kaolin and raw water flocs demonstrated a constant rate of degradation, whilst the iron hydroxide precipitate resisted shear levels induced at mixing speeds of 50 rpm and below. However, when mixed at speeds in excess of 75 rpm, the rate of degradation of the iron hydroxide precipitate flocs increased and the d_{50} was observed to diminish in size from 900μm to 250μm.

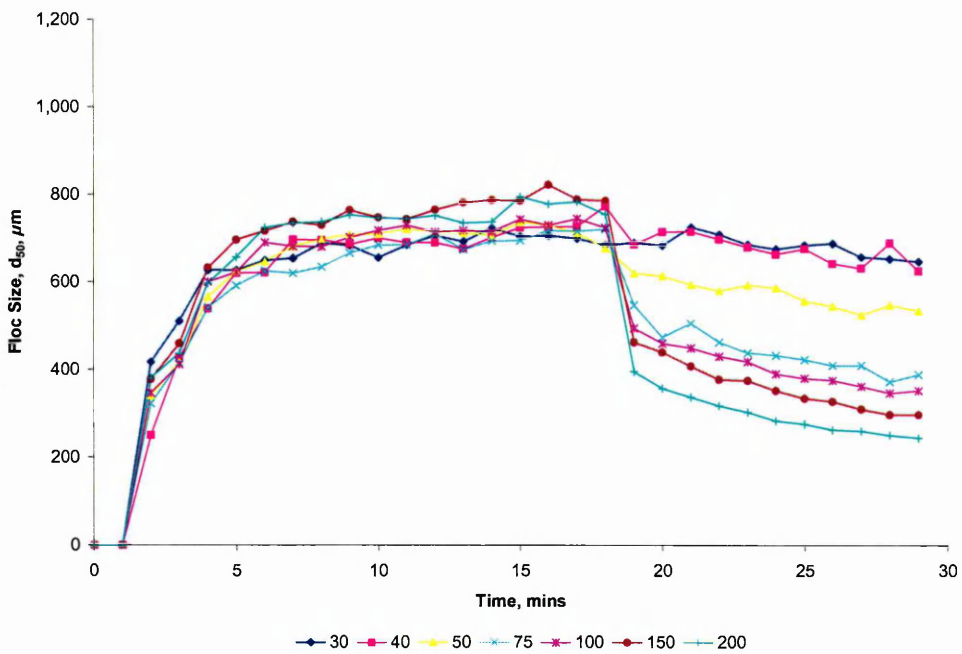
The development of the steady state values for all three suspensions is shown at Figure 8-1. For all suspensions, it is clear that within the first minute of increased mixing speed from 30 rpm to a speed equal to or in excess of 100 rpm, significant floc breakage occurred relative to the original floc size. For the ferric hydroxide flocs, a relatively high degradation rate was maintained, compared to the kaolin and raw water flocs which exhibited a reduced degree of floc breakage after the initial break. However, it is also clear that the iron hydroxide flocs were significantly larger at the onset of increased mixing speed. In this case, as time progressed, the rate of degradation was seen to decrease, despite the fact that the high mixing speeds were maintained. In order to investigate this further, a modelling exercise was undertaken to investigate the magnitude of shear forces to which flocs are exposed at the increased mixing speeds for the durations considered by Jarvis *et al.* (2004). In the first instance the iron hydroxide precipitate floc results were used for further investigation and analysis. In a process similar to that undertaken Chapter 7 above, the trajectories of a single particle, injected into the steady state flow induced at various mixing speeds were studied.



(a) Iron Hydroxide Precipitate



(b) Kaolin



(c) Raw water

Figure 8-1: **Floc size profiles during coagulation and flocculation, and after exposure to increasing levels of RPM, from Jarvis *et al*, 2004.**

8.2 CFD Results

8.2.1 Local Velocity Gradient Along Trajectory

8.2.1.1 Sample Particle Identification

The steady state models developed in Chapter 5 were used for the analyses and the development of the trajectory of a representative particle was the starting point for this work. For the 200rpm scenario, Jarvis *et al.* (2004) gave the average d_{50} for precipitate flocs after 18 minutes of slow mixing as 960μm. As part of an extensive particle counting exercise, Hamilton (2002) found that for a typical surface water, approximately 2,500 particles might be found in a 1 litre sample. Computational expense prohibited the modelling and analysis of such a large number of particles in all possible locations. (Theoretically, each particle could be located in any one of the 98,517 grid cells). Rather, a steady state flow field was developed for a mixing speed of 200 rpm and the trajectories of 500 neutrally buoyant discrete particles each of diameter 960μm were recorded and analysed. Neutrally buoyant flocs were considered appropriate for this study on the basis of existing published data (Bache *et al.*, 1999, Gregory, 1997) and the inherent difficulties and issues associated with the measurement and recording of accurate floc density data (Jarvis *et al.*, 2005b, Gregory 1997). 500 particles represent 20% of the total number of particles which, on the basis of the results of Hamilton (2002), might be expected to be present in the one litre sample.

Different starting positions were selected for each of the particles and these were spread over 50 depths (127mm – 1mm) and ten radial locations. For each point on a particle's trajectory, the G_t value was calculated and data were analysed for 60 seconds of mixing, representing the first minute following the increase in mixing speed from 30 rpm. The 60s time period was used as an appropriate simulation period as, within that time, a broad representation of maxima and minima G_t values were observed and the time was sufficient to allow good mixing within the vessel, as shown in Chapter 7. For each particle, the total time spent experiencing a range of G_t values was calculated and the

distribution of G_t values against times was broadly similar for all particles. The maximum difference in time spent in different G_t bins for different particles was no more than 15% across all 500 particles sampled.

Whilst the results gained from this are insightful in that they provide an indication as to the range of G_t values to which these random particles might be exposed and the time of that exposure, the results do not describe in quantitative terms the total shear to which the particles are exposed. In order to gain some insight into the degree of shear to which each particle was subjected over that first minute, the product of the local velocity gradient and time, $G_t.t$, was calculated by numerically integrating the local velocity gradient along the trajectory. Using the trajectories of the sample particles, 500 $G_t.t$ values were obtained for 60 seconds rapid mixing. The particle with the average $G_t.t$ value ($\overline{G}_t.\bar{t}$) closest to the average $G_t.t$ value of the whole sample was selected as the representative particle. As before, it is accepted that this single particle does not describe precisely the trajectory of any specific floc generated by Jarvis *et al.* (2004). However, it is believed that analysis of its trajectory and the shear applied to it provides a representation of the environment to which the flocs developed by Jarvis *et al.* were subjected. The distribution of G_t values over the 11 minute simulation period for this particle is shown at Figure 8-2 below, with 15% error bars to indicate the extent of variation about this line. A plot of G_t variation with time for the first 60s simulation period for this representative particle is shown at Figure 8-3 below.

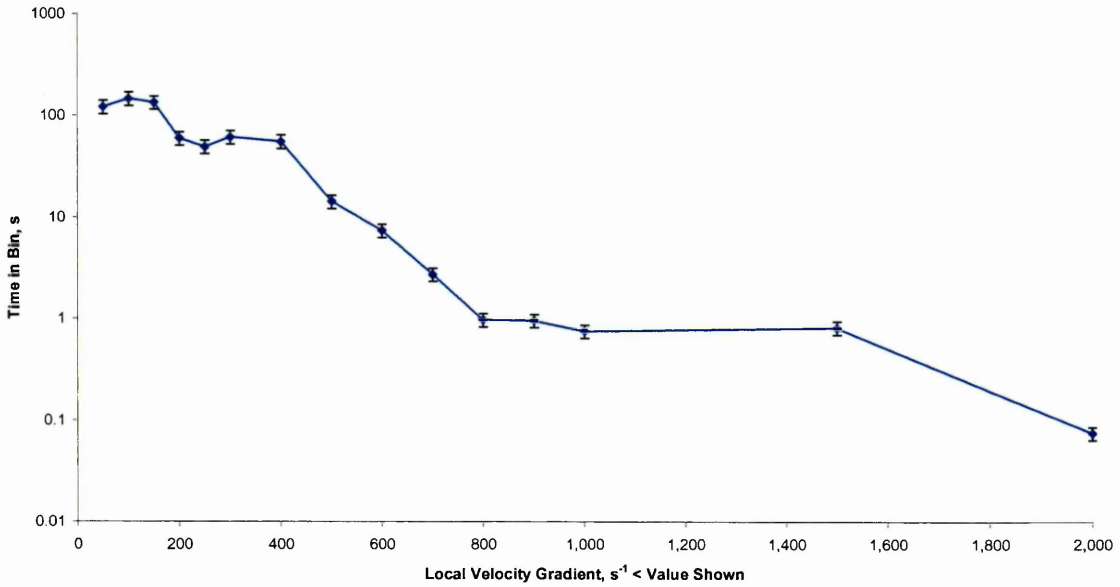


Figure 8-2: **Total time spent in bin, ϕ=960 µm, ρ=1,000 kg/m^3, N=200 rpm for representative sample. Error bars indicate 15% variation about mean, 660s analysis.**

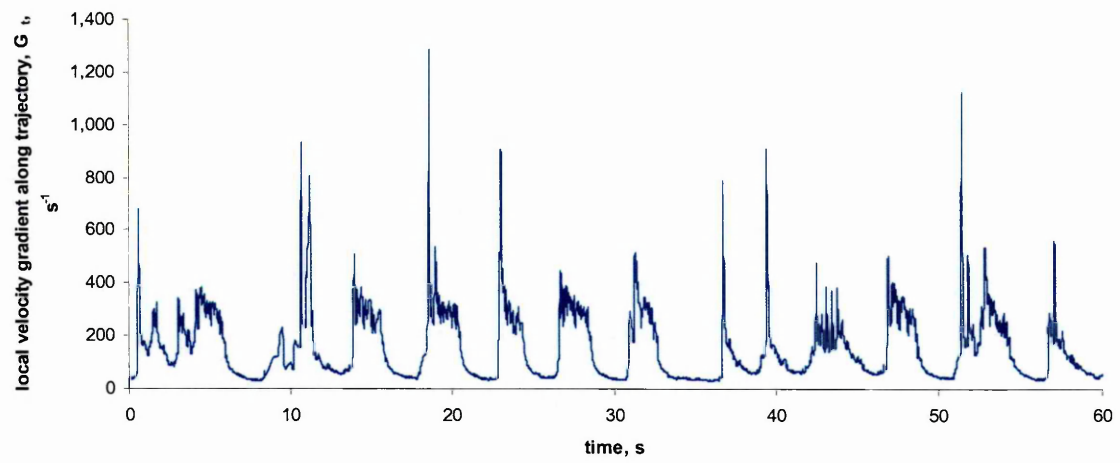


Figure 8-3: **Variation in G_t for a ϕ=960µm, ρ=1,000 kg/m^3 particle, N=200 rpm, 60s analysis.**

8.2.1.2 Floc Breakage and $G_t.t$

The physical data of Jarvis *et al.* and the numerical data obtained as part of this research were combined and are shown at Figure 8-4. This shows the floc size variations from Jarvis *et al.*, together with the $G_t.t$ values for the sample particle from the CFD models

of 30 and 200 rpm mixing over 29 minutes. Clearly, the CFD data can be taken as no more than an indication of $G_t.t$ values as, during the simulation, the particle diameter and density were held constant at 960μm and 1000 kg/m^3 respectively. In reality, the density will have decreased as the floc size increased due to the fractal nature and characteristics of the floc. The graph indicates that mixing at 30 rpm for 18 minutes caused the floc size to increase to 973 μm and that the total $G_t.t$ over this time was 14,424; *i.e.* it may be deduced that, assuming orthokinetic (*i.e.* shear-induced) flocculation dominates, a $G_t.t$ of 14,424 encouraged floc growth from zero to 973 μm. It is also clear that the bulk of the growth (from zero to 832μm) occurred in the first eight minutes of mixing. There was a much reduced rate of growth for the subsequent ten minute period during which time floc size developed from 832 to 973μm. This observation is discussed further below.

Figure 8-4 shows that increasing the mixing speed from 30 to 200 rpm at time t=18 minutes caused a significant rise in $G_t.t$ of 9,299 (14,425 to 23,724) over the first minute, and this was accompanied by a significant reduction in floc size. Therefore, it can be assumed that the application of a $G_t.t$ of 9,299 over 60s has caused the iron hydroxide precipitate floc to degrade in size from 989 to 557 μm; a size reduction of 43%. However, due to the low temporal resolution of the floc size measurements, it is not possible to determine if the floc broke immediately on increased shear (*i.e.* within the first few seconds) or in equal measure across the 60 second period. Over the full 11 minutes of mixing at 200 rpm, the d_{50} floc size reduces from 973 to 257 μm, a size reduction of 716μm (yielding a floc size equivalent to 26% of the original size). The corresponding $G_t.t$ in those 11 minutes has been calculated to be 95,700. Therefore, the first 60 seconds of rapid mixing has caused the floc to reduce in size by 42%, whilst the remaining size reduction has been brought about by ten further minutes of rapid mix, giving a final floc size some 26% of the original.

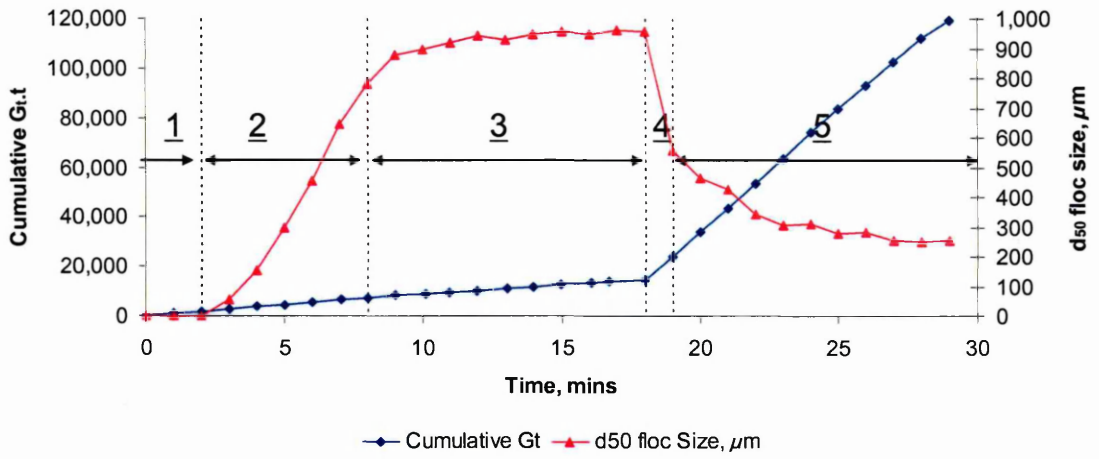


Figure 8-4: **Floc size (d_{50}) and local velocity gradient profiles at mixing speeds of 30 and 200 rpm.**

Considered in terms of total size reduction (rather than relative to starting size), the first 60 seconds is seen to generate 59% of total floc size reduction (432 of 732μm), with the remaining 41% of total floc size reduction (300 of 732 μm) occurring in the following 600s of mixing. These data are tabulated below at Table 8-1. In the period t=19 to t=29 minutes, the maximum level of floc breakage observed was 19% of the previous floc size, the minimum was -2% (indicating growth), and the average breakage was 10%. Thus, Figure 8-4 demonstrates that although rapid mixing caused an overall reduction in floc size, the greatest rate of breakage was observed within the first minute and whilst breakage continued throughout the ten minute period, the rate was significantly less. A similar result was found for the iron hydroxide precipitate floc at all other mixing speeds of 75rpm and above used by Jarvis *et al* (2004). Using data from Figure 8-1, the degree of breakage in the first minute, expressed as a percentage of the floc size at 18 minutes, for each of the mixing speeds is tabulated at Table 8-2.

Table 8-1: **Iron hydroxide precipitate floc size changes (d_{50}) after 1 minute and 11 minutes of increased mixing.**

	d_{50}, μm	Total Breakage, μm	Stage Breakage, μm	d_{50}, as % of d_{50} @ t=0	Total Breakage as % of d_{50} @ t=0	Stage Breakage as % of d_{50} @ t=0
t = 0	989	-	-	100%	0%	0%
t = 60s	557	432	432	56%	44%	44%
t = 660s	257	732	300	26%	74%	30%

Table 8-2: **Degree of floc breakage observed in the first minute of increased mixing for the iron hydroxide precipitate floc.**

Mixing Speed, rpm	Initial Floc Size, μm	Floc Size after 60s Increased Mixing, μm	Degree of Floc Degradation
200	989	557	44%
150	988	645	35%
100	973	789	19%
75	952	874	8%

Having ascertained that the highest rate of breakage occurred in the first 60 seconds of rapid mixing, an analysis was undertaken of the amount of time the particle was exposed to local velocity gradients of different magnitudes. For the 200 rpm scenario, Figure 8-5 shows the total time the particle was exposed to different ranges of velocity gradient during both the first 60 seconds of rapid mixing and the entire 11 minutes.

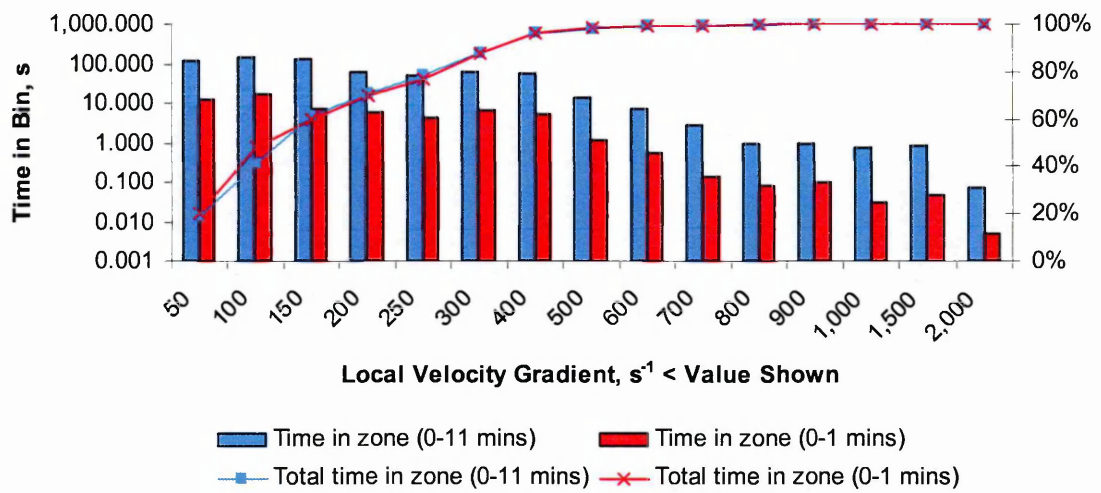


Figure 8-5: **Total and cumulative time of exposure to different ranges of local velocity gradient, ϕ=960um, ρ=1,000 kg/m^3, N=200 for representative sample, 660s and 60s analyses.**

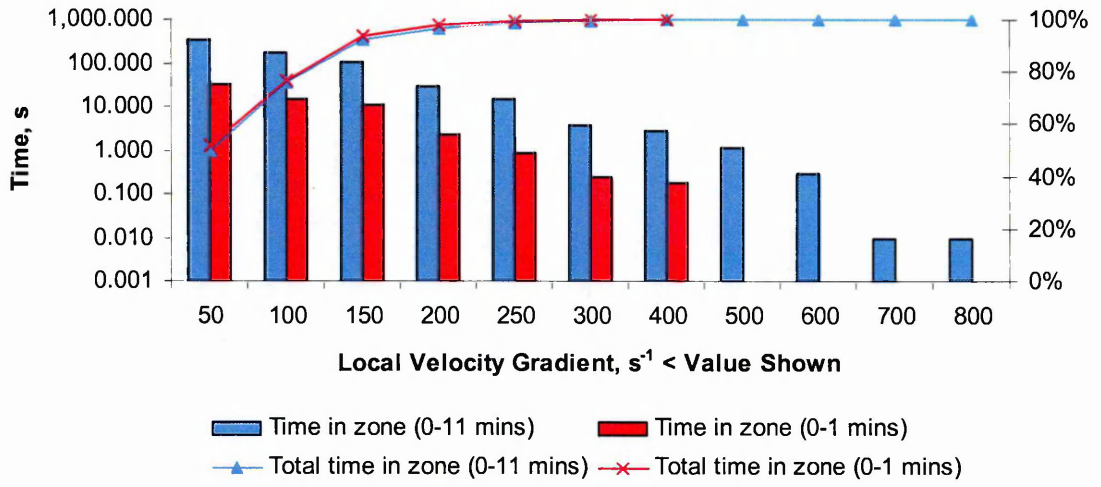


Figure 8-6: **Total and cumulative time of exposure to different ranges of local velocity gradient, ϕ=960um, ρ=1,000 kg/m^3, N=100 for representative sample, 660s and 60s analyses.**

It is clear from Figure 8-5 that the particle was exposed to G_t values of between 0 and 150s^{-1} for 60% (45s) of the first minute of increased mixing speed. The cumulative profiles for the first 60s and entire 660s are very similar with little discernible difference between the two lines. Corresponding data for the 100rpm scenario are shown below at Figure 8-6. There is a clear shift to lower G_t values in this scenario, with the particle exposed to G_t values of 0-100s^{-1} for 76% of the first minute.

Data for all mixing speeds are shown below at Figure 8-7, from which it can be seen that only particles mixed at speeds of 75 rpm and above experience G_t values in excess of 200s^{-1}. For the iron hydroxide precipitate flocs, Jarvis *et al.* (2004) noted a change in floc size response at mixing speeds greater than 75rpm, with floc breakage occurring much more rapidly at these speeds. Referring back to the conceptual description of floc breakage discussed in Chapter 2, it can be inferred that the threshold G_t value in this particular scenario (*i.e.* iron hydroxide precipitate flocs mixed in a cylindrical jar test vessel) is 200s^{-1}, with an increase beyond that threshold giving rise to rapid breakage.

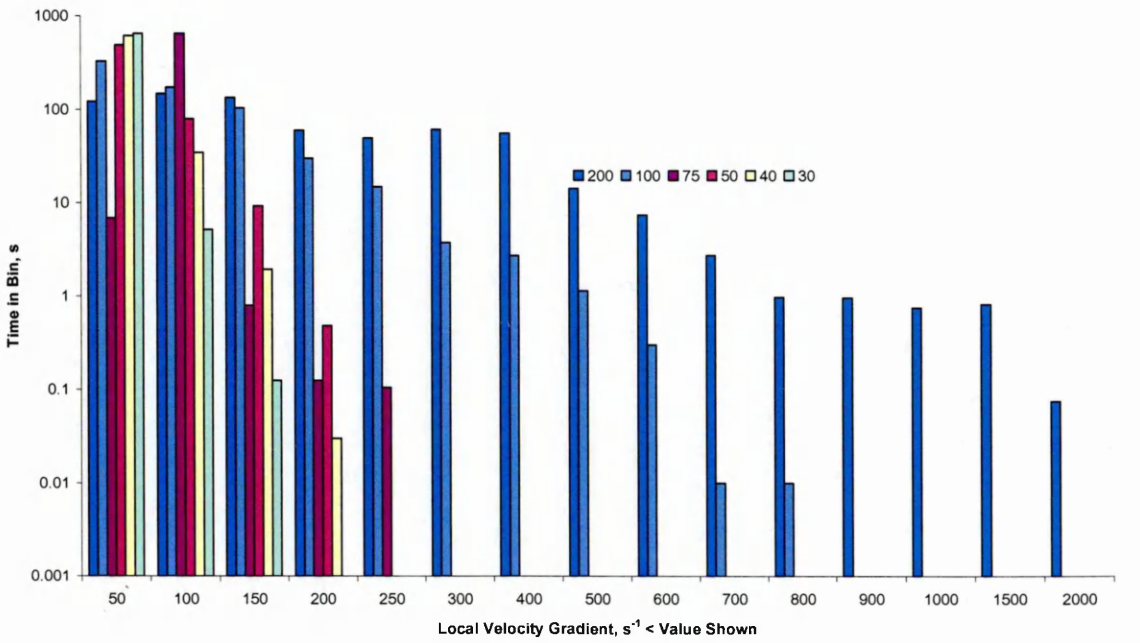


Figure 8-7: **Total time of exposure to different ranges of local velocity gradient, ϕ=960um, ρ=1,000 kg/m^3, 30<N<200 rpm for representative sample, 660s analysis.**

Whilst these observations are of interest, of equal interest is the maximum continuous time spent within a range of velocity gradient values. These results are shown below at Figure 8-8 for different mixing speeds. It is clear that for all mixing speeds, continuous periods for which the particle is exposed to G_t values greater than 100s^{-1} are less than one second.

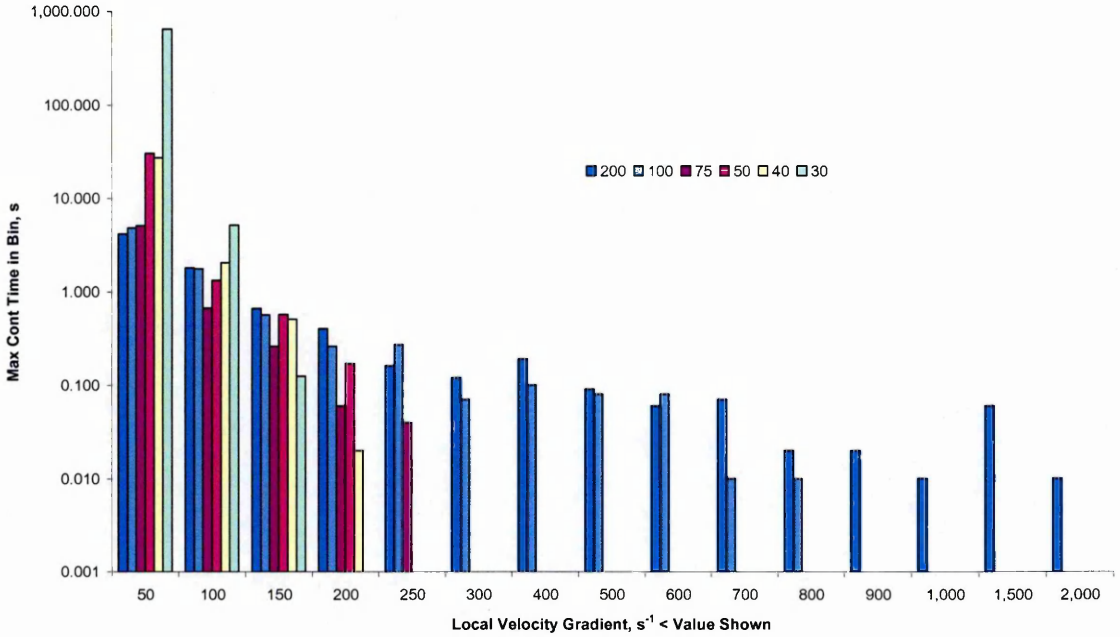


Figure 8-8: **Maximum continuous time spent in bin, ϕ=960um, ρ=1,000 kg/m^3, N=various for representative sample, 660s analysis.**

The iron hydroxide precipitate flocs began to exhibit significant floc breakage once the mixing speed was increased to 75 rpm and above. Figure 8-7 shows a threshold at N=75rpm, as no lower mixing speed gave rise to a G_t value of greater than 200s^{-1} or greater. It can be inferred, therefore, that a iron hydroxide precipitate floc mixed at 75rpm can withstand a G_t value of up to 200s^{-1} for up to 0.1s, without breaking. Once mixing speed is increased beyond 75rpm, the CFD model indicates that flocs will be exposed to G_t values of 300-800 s^{-1} for the 100 rpm scenario and 300-2,000s^{-1} for the 200 rpm scenario, and it is at these mixing speeds that significant breakage occurs. Flocs mixed at speeds of less than 75 rpm exhibited little breakage, with the majority of that occurring in the first minute of increased mixing speed. In these instances, it is concluded that it is the modest inertial increases brought about by increasing mixing speed which cause the small degree of breakage.

The breakage mechanisms for the NOM and kaolin flocs are significantly different to the ferric hydroxide floc breakage, as shown at Figure 8-1. The data suggest that the NOM flocs begin to break once a mixing speed of 50 rpm is applied; whereas the kaolin

flocs exhibit a noticeable degree of breakage at just 40 rpm. Figure 8-7 and Figure 8-8 show that the principal difference between mixing speeds of 30 and 40 rpm is the increased exposure to local velocity gradients above $50s^{-1}$, and the length of continuous exposure to all velocity gradients. At 30rpm, the CFD data presented in Figure 8-7 show that the particle spent 655 of the 660s simulation (*i.e.* 99%) exposed to G_t values of $50s^{-1}$ or below. At 40 rpm, the particle experienced G_t values of between 50 and $100s^{-1}$ for 35s (*i.e.* 6%) of the simulation period. In addition, the continuous time exposed to G_t values of $50s^{-1}$ or below reduced from 655s to just 27s (Figure 8-8 refers). As the amount of continuous time in the G_t $<50s^{-1}$ zone decreases significantly when considering the 40 rpm rather than the 30 rpm scenario, it is concluded that the kaolin flocs are vulnerable to instantaneous changes in G_t values above $50s^{-1}$, irrespective of time of exposure to the higher values.

The NOM floc breakage threshold was reached when the mixing speed was increased to 50rpm. At 50 rpm, the CFD data shows that for 84% of the 660s simulation time, the particle experienced G values below $50s^{-1}$; time spent exposed to G_t values of between 50 and 100 s^{-1} increased to 14%, and for approximately 1% of the time the particle was exposed to G_t values in excess of $150s^{-1}$ (with occasional, very short exposure to G_t values greater than $200s^{-1}$). For G_t values of below $200s^{-1}$, there was no significant difference between the maximum times spent in G_t value bins between the 40 and 50 rpm scenarios. Thus, it is possible to conclude that the NOM floc breakage was initiated by exposure to instantaneous exposure to G_t values of up to $150s^{-1}$ and some rather more prolonged exposure to G_t values of up to $100s^{-1}$. Relevant data are given at Table 8-3 below.

It is clear from Figure 8-5 and Figure 8-6 that exposure to the highest G_t values is not restricted to the first minute of rapid mixing. The numerical results from the first minute, when compared to the following ten minutes do not readily explain the higher breakage rate in the first minute. It is therefore considered likely that for the 200 rpm scenario it is the effect of the substantial inertial changes arising from increasing the average G_t from $12s^{-1}$ to 159 s^{-1} on the large, open flocs which causes them to break rapidly via fragmentation processes, rather than any noticeable difference between the

first and subsequent minutes of rapid mixing. An alternative viewpoint is that all the weaker bonds within the flocs are broken in the first minute, and so breakage via fragmentation was no longer possible, meaning that the only means by which flocs would be broken further is via surface erosion. Unfortunately, it is not possible to determine if the floc breakage occurred at the moment of increased mixing, or sometime during the first minute.

Considering the iron hydroxide precipitate floc suspension, cumulative $G_t.t$ values were calculated for particle trajectories for four additional increased mixing speeds. Again, combining laboratory and numerical data, Figure 8-9 shows the cumulative $G_t.t$ values plotted against the corresponding floc sizes for the period 1-11 minutes after mixing speed was increased. (Data from the first minute of increased mixing (*i.e.* zone 4) are shown as a dashed red line as it is not clear at which point within that minute breakage occurred). In all instances the initial floc size was between 900 and 989 μm. The plot demonstrates that, for mixing speeds of 100 rpm and above, floc size exhibits a strong power curve relationship with $G_t.t$ (r^2 values are given at Table 8-4). Furthermore, the shapes and slopes of the lines for speeds of 100, 150 and 200 rpm are similar, indicating that the rate of floc degradation, when expressed in terms of $G_t.t$ is similar, irrespective of applied mixing speed. This is a significant result as it demonstrates a strong link between floc size and total applied local shear. The relationship applies less well for a mixing speed of 75 rpm and does not apply for mixing speeds of 40 and 50rpm. However, this is to be expected as Figure 8-1 demonstrates the resistance of the iron hydroxide precipitate flocs to the shear forces applied by these lower mixing speeds. As the shapes of the curves are similar at mixing speeds of 100 rpm and above, it can be inferred that the rate of floc degradation is the same, regardless of mixing speed. The crucial factor in determining the overall floc breakage would appear to be the amount by which flocs break in the first minute of increased mixing. Breakage thereafter continues at a similar, diminishing, rate, irrespective of mixing speed. Consequently, the curves can be used as a predictor for floc breakage after the first, significant breakage episode has occurred. Clearly, however, there is a need to understand better the breakage mechanism in the first minute. In the absence of improved temporal resolution for floc breakage data, it is not currently possible to characterise this phenomenon accurately.

This piece of work features in the Recommendations for Further Work chapter of this thesis.

Similar plots have been obtained for NOM and alum floc degradation, as shown at Figure 8-10 and Figure 8-11 below. Again, good correlations were observed between applied $G_t.t$ and floc size. It is also clear that the correlations at lower mixing speeds are improved for the NOM and alum flocs when compared to the ferric hydroxide flocs. This is explained by the fact that these flocs were shown to be less resistant to lower mixing speeds (*i.e.* weaker) than the ferric hydroxide flocs. Coefficient of determination values (r^2) for all mixing speeds and floc suspensions are given at Table 8-4. Data analysis shows that linear relationships could also be demonstrated between floc size and $G_t.t$ for speeds of 75 – 200 rpm. However, unlike the power curves shown, linear models would not take account of the limiting floc size observed by Gregory (2003) and Jarvis *et al.* (2004). Both sets of authors found that mixing beyond a specific time period yielded no further floc degradation. The model curves shown in Figure 8-9, Figure 8-10 and Figure 8-11 accurately represent both observed floc degradation and also attainment of a limiting floc size.

Table 8-3: Actual and percentage times particles spent in G_t bins at 30, 40 and 50 rpm.

	Total						Continuous					
	G_t<50s^{-1}		50<G_t<100 s^{-1}		G_t>100 s^{-1}		G_t<50 s^{-1}		50<G_t<100 s^{-1}		G_t>100 s^{-1}	
	s	%	s	%	s	%	s	%	s	%	s	%
N = 30	655	99	5	1	0	0	655	99	5	1	0	0
N = 40	627	95	31	6	2	<0.1	26	4	2	<0.1	0.5	<0.1
N = 50	554	84	93	14	13	2	33	5	1	<0.1	0.6	<0.1

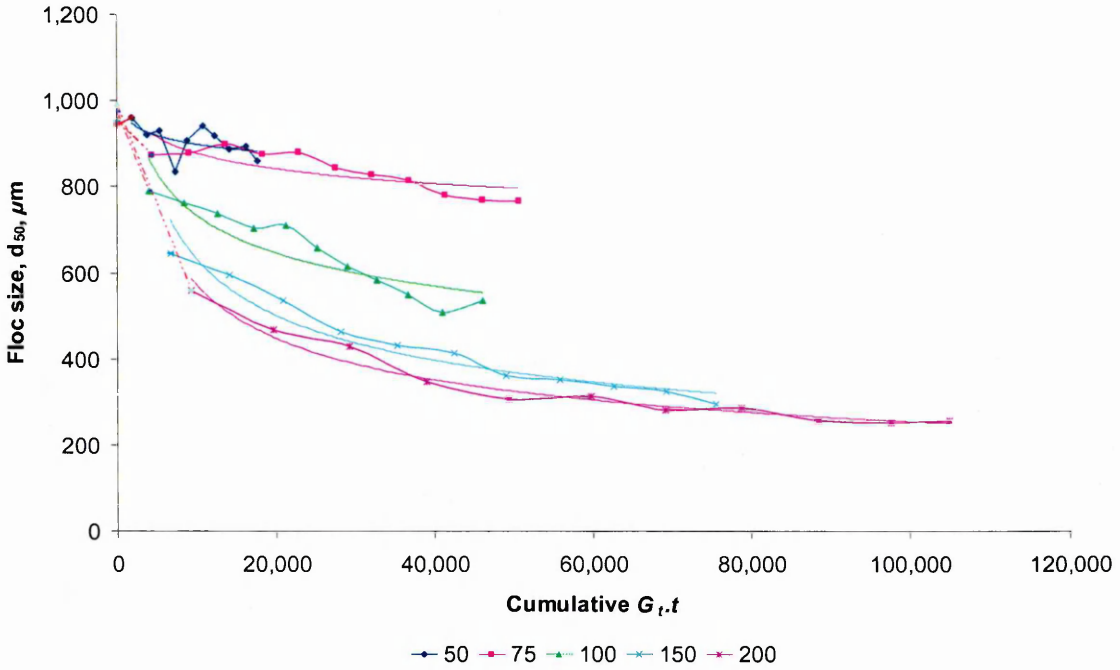


Figure 8-9: **Degradation of ferric hydroxide floc, expressed in relation to cumulative $G_t t$.**

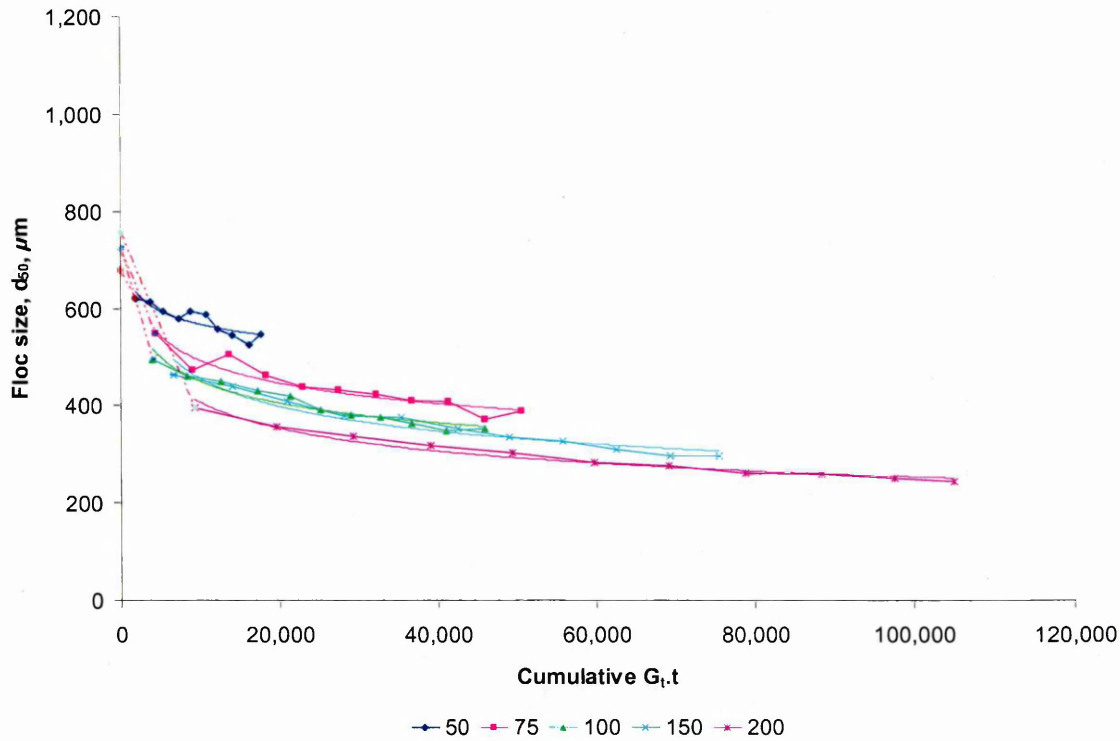


Figure 8-10: **Degradation of NOM floc, expressed in relation to cumulative $G_t t$.**

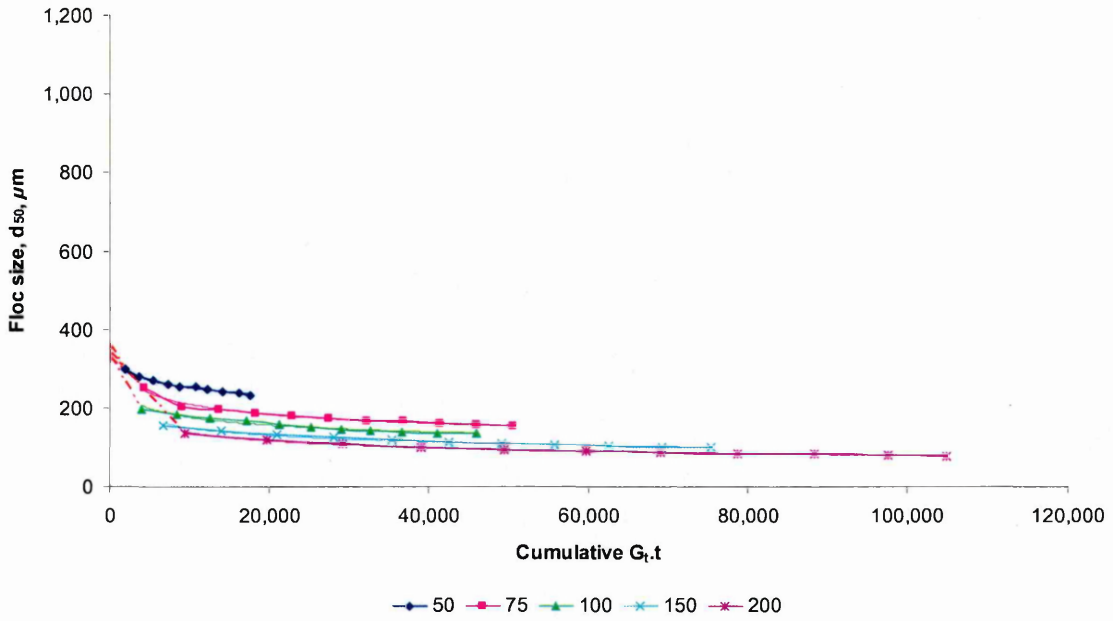


Figure 8-11: **Degradation of kaolin floc, expressed in relation to cumulative $G_t t$.**

Table 8-4: **r^2 values for power curves obtained from d_{50} vs. cumulative $G_t t$ plots.**

Mixing Speed, rpm	Iron Hydroxide Precipitate	NOM	Kaolin
50	0.2896	0.7809	0.9843
75	0.6065	0.8997	0.983
100	0.8028	0.9328	0.9582
150	0.9424	0.9400	0.9825
200	0.9710	0.9730	0.9924

The ratio of the post-breakage d_{50} floc size to the pre-breakage floc size d_{50} was compared with the vessel and paddle swept volume (PSV) average turbulence dissipation rates, and the results are plotted at Figure 8-12. The noticeable increase in the rate of change of PSV turbulence dissipation rate with mixing speed between 75 and 100 rpm is reflected in a corresponding increase in the rate of change of iron hydroxide precipitate d_2:d_1 with mixing speed at the same time, thus demonstrating the effect of the threshold G_t value (and hence threshold ϵ value) at this speed. Somewhat counter-intuitively, the NOM and kaolin flocs show a decline in the rate of change of d_2:d_1 value at this point. However, this is due to the fact that these flocs began degrading in size at much lower mixing speeds (50 and 40 rpm respectively) and so one would expect the rate of change ratio of their initial to final size to reduce with higher mixing speeds as significant degradation has already taken place.

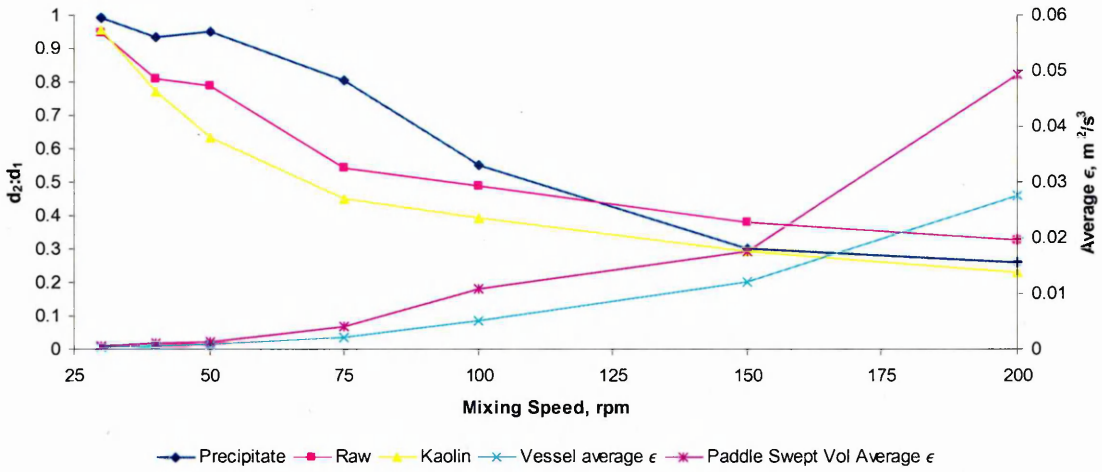


Figure 8-12: Ratio of final to initial floc size and turbulence dissipation rate vs. mixing speed.

Again combining laboratory-derived and numerical data sets, the vessel average turbulence dissipation rates were plotted against the post-breakage d_{50} values for each floc suspension, as shown at Figure 8-13. Lines equating to η and 6η are also shown. It is found that all d_{50} values fall within the $\eta<d_{50}<6\eta$. This is a somewhat narrower range than that found by Bache (2004) who used a larger data set to demonstrate a range of $0.9\eta<d_{50}<14\eta$. Interestingly, Muhle (1993) cited in Thomas *et al.* (1999) suggested that flocs which are above the microscale generally break by fragmentation as a result of fluctuating dynamic pressures, whereas below the microscale viscous forces predominate and flocs are broken by surface erosion. Although Figure 8-13 shows post breakage floc size only, it can be inferred that in all cases pre-breakage size was greater than the microscale, implying breakage via fragmentation processes.

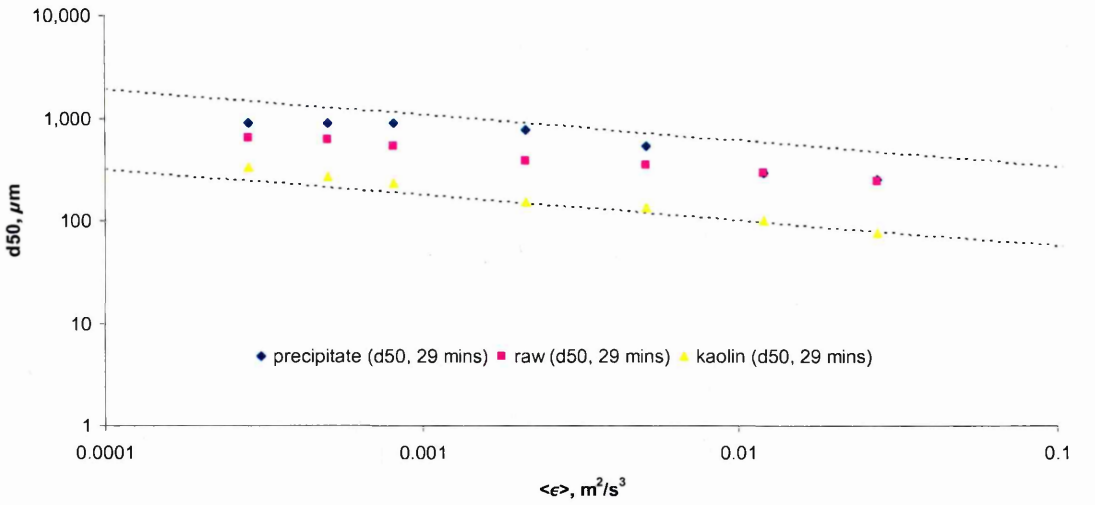


Figure 8-13: Post breakage floc size (d_{50}) vs. vessel average turbulence dissipation rate.

8.2.1.3 Floc Growth and $G_L.t$

Referring back to Figure 8-4, the lines depicting $G_t.t$ and d_{50} may be subdivided into five distinct regions. From this it can be seen that the average local velocity gradient in zone 1 had no effect on floc size in the suspension. Zones 2 and 3 encouraged floc growth, whilst the average local velocity gradients in zones 4 and 5 encouraged breakage, albeit at different rates. The average G_t values for each zone are readily calculated and are found to be as follows:

Table 8-5: Comparison of cumulative $G_t.t$, average G_t and observed floc behaviour.

Zone	Time (mins)	Cumulative G_t.t	Average G_t, s^{-1}, in zone	Floc behaviour
1	0-2	1,911	18	Stable
2	2-8	7,436	19	Growth
3	8-18	14,424	12	Growth
4	18-19	23,724	159	Breakage
5	19-29	119,424	172	Breakage

As the vessel is well mixed, even at low mixing speeds, the average G_t value is relatively constant throughout the low mixing speed period, with the result that the $G_t.t$ line is approximately linear. However, the floc growth data shows two different growth rates (zones 2 and 3 refer). Consequently, it can be deduced that the velocity gradients

induced at a mixing speed of 30 rpm are sufficient to encourage floc growth in the first instance, although previous work (Yukselen & Gregory, 2004, Jarvis *et al.*, 2005c) has shown that such velocity gradients will not always induce regrowth, post breakage. However, recalling the statement of Biggs and Lant (2000) as recorded in Chapter 2, that floc formation is a balance between the rate of aggregation and the rate of breakage, the data presented in Figure 8-4 and Table 8-5 demonstrate that once the flocs have developed to a certain size, (in this case, 876μm at nine minutes), their structural strength has reduced to an extent that the rate of breakage increases (and hence the growth rate decreases) even at the modest velocity gradient values generated at 30 rpm. Using the CFD data as a comparator, it can be concluded that for the raw water, coagulant and mixing conditions considered, a $G_t.t$ value of approximately 8,155 represents a point beyond which further mixing produces minimal additional benefit. This value is, of course, dependent on raw water quality and chemistry. The floc growth curves for the NOM and kaolin suspensions are shown, together with the coagulant precipitate curve at Figure 8-14. It is noted that the optimum $G_t.t$ values for floc growth are 6,715 for NOM and 3,800 for kaolin. These are important observations when considering how these data might be used to inform the design of a full scale flocculator. It is interesting to compare these values to the work of Camp (1955) who, on the basis of a review of various flocculator designs, suggested that a $G_t.t$ value of 23,000 to 210,000 was an appropriate figure for adequate flocculation. More recent texts have reduced this range significantly, *e.g.* 20,000-30,000 (Baruth, 2004), 36,000-48,000 (Crittenden, 2005), 10,000-100,000 (Droste, 1997). These recommended values are still considerably in excess of the values obtained here. However, as discussed in Chapter 2, the $G.t$ concept takes no account of particle concentration.

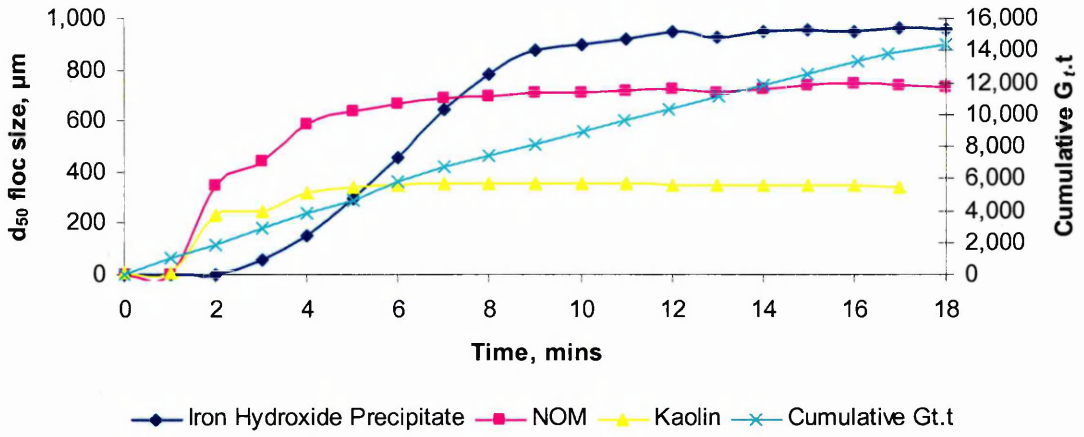


Figure 8-14: Floc growth curves in relation to applied $G_r t$.

8.3 Summary

Combining the CFD data generated as part of this work with laboratory-derived breakage data, it has been possible to postulate threshold local velocity gradient values at which floc breakage might be expected to occur for three different floc suspensions. Threshold velocity gradients are suggested as follows:

Iron Hydroxide Precipitate flocs:	$200s^{-1}$ (instantaneous)
Kaolin flocs:	$50s^{-1}$ (instantaneous)
NOM flocs:	$150s^{-1}$ (instantaneous), $100s^{-1}$ (continuous)

This is a most important advancement as the results can be used to assess the performance of existing flocculators, or as design guidance for new installations.

Although the threshold values for each suspension have been determined using a jar tester and CFD analyses, they are based on the flocs' resistance to induced velocity gradients. This is a significant result as any previous breakage thresholds have always been expressed in terms of mixing speed and consequently are meaningless when applied to any situation other than that in which they were developed. The results shown here can be adopted for use in other situations, and not just as applied to one

specific jar test configuration. Therefore, these breakage thresholds could be used to assess the performance of existing flocculators or to design new installations. For example, if a new flocculator was to be designed and constructed, CFD and jar test data could be combined for the specific raw water and coagulant dose proposed and a breakage threshold found. The proposed flocculator could then be modelled using CFD to determine the overall G_L value distribution and the likelihood of floc breakage. In this way, it is suggested that flocculator design can be optimised via use of CFD and a jar tester in combination.

Over the duration of an 11 minute mixing period, the maximum continuous exposure of a floc to a velocity gradient in excess of $100s^{-1}$ was found to be always less than one second.

A linkage between floc size and applied local shear was confirmed and expressed in terms of the numerical integral of the product of local velocity gradient and time of exposure. Model equations were developed to express the rate of floc degradation as a function of $G_t.t$. It was found that at mixing speeds of 100 rpm and above, the rate of floc degradation, when expressed in terms of $G_t.t$, was the same. It was deduced that the key factor in determining the total degree of floc breakage was the extent of breakage which occurred in the first minute. The lack of temporal resolution in the laboratory data collection exercise precluded the development of a robust model to replicate this sudden breakage phenomenon.

Floc growth was also studied in relation to applied $G_t.t$. It was found that the applied $G_t.t$ to attain maximum floc size was significantly less than that recommended in both current and historic texts. This implies some degree of over-treatment in full scale flocculators constructed on the basis of recommended $G.t$ values. This concept is developed further in later chapters of this thesis.

9 Frankley WTW Flocculator CFD Analyses

9.1 Introduction

Much work has been carried out in recent years examining floc formation and breakage at laboratory scale using the jar test apparatus (*e.g.* Jarvis *et al.*, 2005a, Gregory, 2004). This work has enabled conclusions to be drawn with regard to average power dissipation and average velocity gradient which (a) encourage flow formation and (b) give rise to floc breakage. The analyses described in Chapters 6, 7 and 8 above have extended this further via a consideration of the local turbulence conditions to which a floc might be exposed using CFD. However, whilst the jar test is widely used to determine optimum pH and coagulant type and dose to effect good coagulation and flocculation for specific raw waters, it does not necessarily accurately reflect a full scale flocculator. Consequently, while the jar test can be used to optimise the chemical aspects of coagulation and flocculation, on its own it provides little information of value regarding the hydrodynamics of a flocculator, as discussed in earlier chapters.

Chapters 6, 7 and 8 have provided an indication of the hydrodynamic conditions necessary to bring about both floc growth and breakage. The individual unit processes at water treatment works should be designed such that floc breakage is minimised. However, this can never be achieved with complete success, and areas of high shear will be found at weirs, adjacent to baffles and blades in flocculators and within DAF plants. Boller and Blaser (1998) demonstrated that particle removal efficiency decreases with a reduction in particle size and so it is important that flocs are able to withstand any high shears imparted to them and that particularly high velocity gradient values are avoided. Furthermore, an inherent difficulty associated with the optimisation of a full scale water treatment plant is that it is often not possible to attempt changes to operation or design without potentially jeopardising the quality of the final water.

With these factors in mind, work has been undertaken to use CFD to model numerically the hydrodynamic conditions within a full scale flocculation vessel. The work reported here has two principal aims; firstly, to assess the perceived benefits of using CFD to model the hydraulic performance of the flocculation process at one of the UK's largest surface water treatment works. Secondly, consideration has been given to the possibility of using CFD and jar test results in combination to consider the flocculation performance of full-scale flocculation vessels. This work has considered the results and conclusions of the previous laboratory scale work in the context of a full scale plant treating a similar (*i.e.* upland) raw water. Improved understanding of flocculator hydrodynamics can only serve to improve design procedures and standards for future installations.

9.2 Frankley WTW

Originally commissioned in 1904, Frankley WTW has been serving the city of Birmingham and its surrounding environs for over 100 years. The upland source produces soft raw water which, for the period January 2003 to September 2005, displayed the following characteristics:

Table 9-1 **Frankley WTW average raw water characteristics – January 2003 to September 2005.**

Average colour	13.97 ^{O}Hazen
Average turbidity	0.67 NTU
Average TOC	2.61 mg/l
Average alkalinity	12.38 mg/l as $CaCO_3$

Raw water is stored in two open reservoirs; Frankley and Bartley. Recent raw water data have been collected and are shown at Figure 9-1 below.

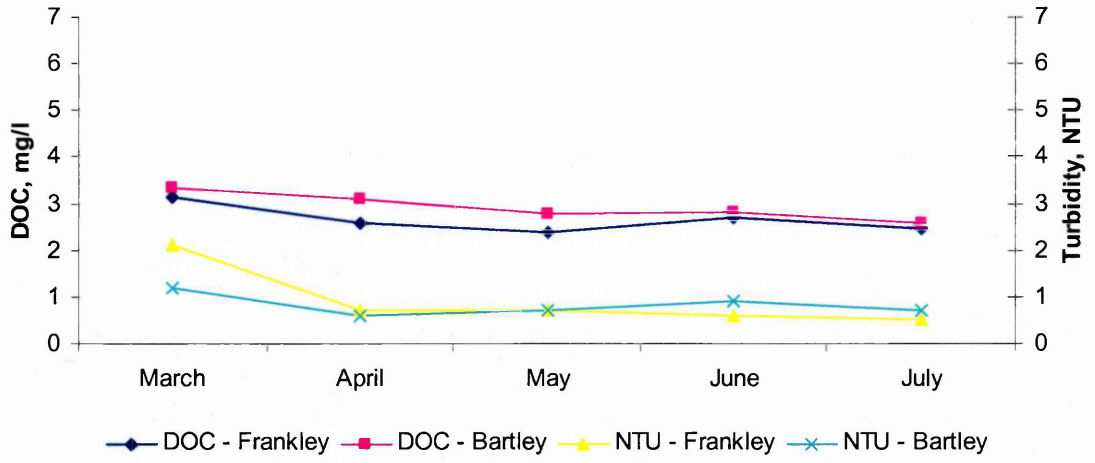


Figure 9-1: Frankley and Bartley reservoir raw water characteristics – March to July 2006.

Following partial treatment (screening, coarse filtration, pH adjustment and fluoridation) at Elan WTW in the Welsh valleys, the water flows 75 miles by gravity to the two raw water storage reservoirs at Frankley WTW. The treatment train for Frankley WTW, shown at Figure 9-2, comprises two identical streams, each of 220 Ml/d capacity. A pH adjustment stage (effected via lime dosing) is followed by coagulation and mechanical tapered flocculation upstream of clarification via dissolved air flotation. Coagulant is dosed in the form of ferric sulphate and mixing is achieved hydraulically via flow over a thin plate weir. Frankley WTW operates a system of tapered flocculation through 20 lanes, each lane comprising three identical vessels and paddles rotating at different speeds. In this way the designers anticipated that the tapered flocculation so provided would enhance the production of high density flocs quickly in the first cell, and encourage growth rather than breakage in the subsequent cells, with a minimum amount of turbulence generated in the final cell to avoid floc breakage but to maintain suspension in the flocculator. Each cell comprises a rectangular section vessel, 6.4m x 7.0m x 4.75m deep, within which a four blade, 6.0m diameter rake (or picket fence) paddle rotates slowly. A photograph of an empty flocculation vessel is shown at Figure 9-3. The clarified water is subsequently filtered and disinfected before entering an on-site treated water storage facility from where it either gravitates or is pumped into supply depending on its destination. The work reported here focuses on the hydraulic performance of the flocculation process.

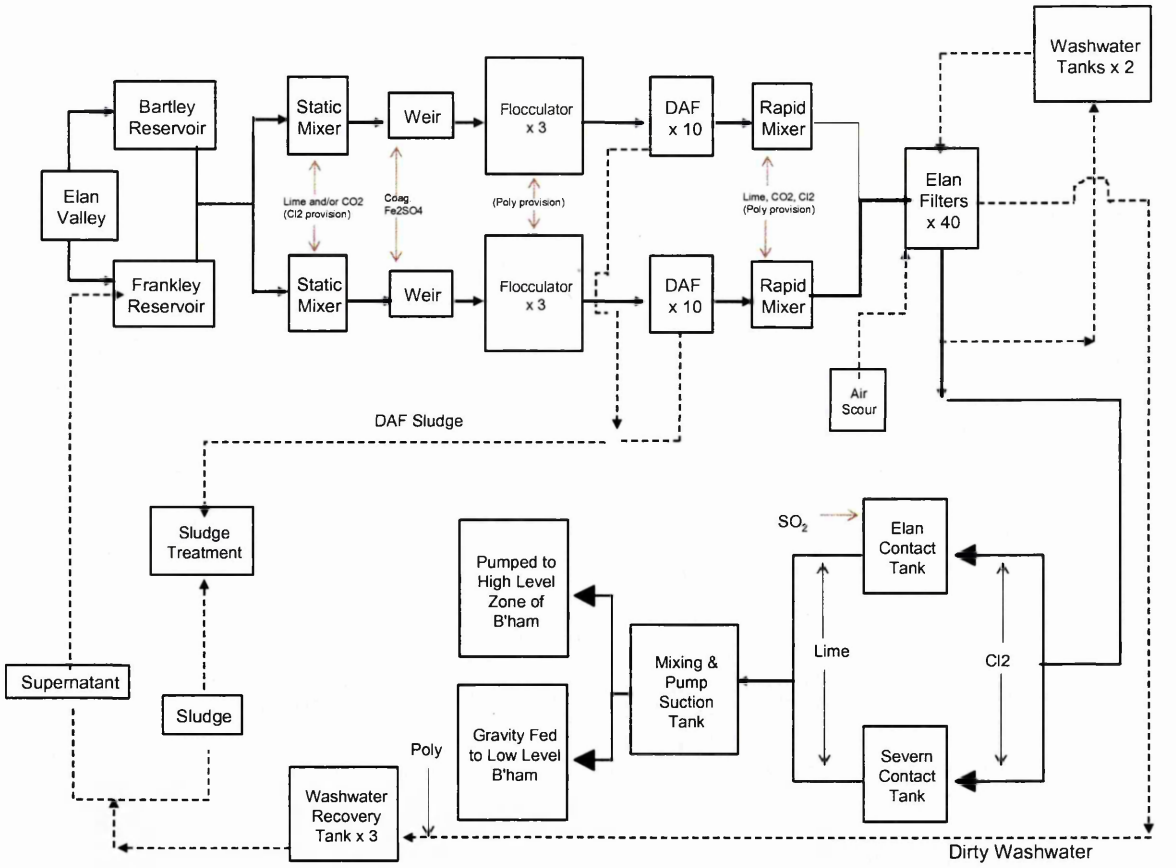


Figure 9-2: **Schematic of treatment processes at Frankley WTW.**



Figure 9-3: **Empty flocculation vessel at Frankley WTW.**

9.3 Modelling Strategy

The commercial software packages, Gambit and Fluent (Fluent Inc, Sheffield, UK) were used to generate the mesh and solve the equations of flow within one flocculation vessel. The mesh comprised 338,213 cells, with refinements made in the vicinity of the paddles and the inlet. Plan and sectional views of the mesh are shown at Figure 9-4. Appropriate boundary conditions were specified; in particular, free slip conditions at the top water level, no slip conditions at the walls, standard logarithm wall boundary layer profile, normal velocity inlet and pressure outlet. The two-equation realizable k-ϵ model was used to characterise turbulence within the flocculator. The selection of the realizable k-ϵ model in favour of other turbulence models was made on the basis of its suitability to round jets, such as may be found at the flocculator inlet (Fluent, 2005). A description of the realizable k-ϵ model is provided in Chapter 2 of this thesis.

The Literature Review (Chapter 2) showed that there are no published examples of CFD models of full scale mixing units such as this. Consequently, it is not possible to benchmark the approach against that of others. However, good modelling practice has been observed throughout. Previous work has been limited to laboratory scale (Korpijarvi *et al.*, 1999 & 2000) and pilot scale (Essemiani and de Traversay, 2002a & b), both of whom used the standard k-ϵ turbulence model. A description of the standard k-ϵ turbulence model was provided in Chapter 2 and its application to swirling flow scenarios was discussed in Chapter 5. Suffice to reiterate here that its use in such circumstances is not recommended. Nevertheless, for the work recorded here, the rotating flows were first modelled using the standard k-ϵ turbulence model and the multiple reference frames method to generate an initial solution. (Convergence criteria were set at 1×10^{-5}). These data were then interpolated into a sliding mesh version of the mesh and the analysis refined using that method of solution. 100 time steps per revolution were specified, and, in the first instance, 15 revolutions were specified in order to ensure a steady solution had been reached (Fluent, 2005). Point velocities and pressures were monitored to ensure that a time-independent solution had been reached.

The standard k-ϵ turbulence model was then replaced by the realizable k-ϵ turbulence model and a converged solution obtained once more.

To reduce computational expense, just one vessel was modelled at any one time, and each of the three mixing speeds (3.2, 2.4 and 1.6 rpm) were simulated. As previously discussed, the sliding mesh method is computationally expensive. To develop a converged solution for one flocculation cell over 15 revolutions using either the standard k-ϵ or realizable k-ϵ model took approximately five days CPU time using the high performance computing facility at Cranfield University. The work undertaken here made use of the University's Sun cluster grid, comprising 19 2x3.06 dual processor computers, each with 6GB RAM available, all managed by the Sun grid engine from which 100% of a processor could be made available for up to five days at a time (Cranfield University, 2006). Consequently, modelling in excess of one vessel at any one time was not achievable with the available resources. The high CPU usage of the model also precluded mesh density sensitivity analyses from being undertaken. However, it is believed that the mesh density used is adequate for the analyses undertaken. Indeed, the density is comparable to, if not finer than, examples of similar-sized unit processes found in the literature (*e.g.* Brouckaert & Buckley, 1999, Van der Walt, 2002). For each mixing speed, three different flow rates were simulated (21.1, 24.0 and 16.0 Ml/d) representing the average, maximum and minimum flows through the vessels. Thus, nine separate simulations were undertaken.

The high CPU usage of this model also brings into question the possibility and practicalities of widespread CFD use in industry for applications such as this. This work began using modest computing facilities (*i.e.* laptop computer). However, whilst this was adequate for jar test simulations using the MRF technique, it became apparent that it was totally inadequate for the Frankley model using either MRF or sliding mesh. As an experiment, a Frankley model run was initiated on the laptop. After 14 days of continuous use, the computer had solved less than two complete revolutions of the paddle. Thus, it is clear that the use of basic computing facilities is precluded by a model of this size and complexity. This restriction will have an impact on water companies and consultants wishing to adopt CFD as an analysis tool in-house. Few

commercial organisations have either the necessary high performance computer facilities, or the resources to invest in them. In addition, the financial cost of running a model for such a long time (five days) is significant, if not prohibitive. Furthermore, model development and data analysis requires trained staff, which adds further to the overall cost of CFD analyses.

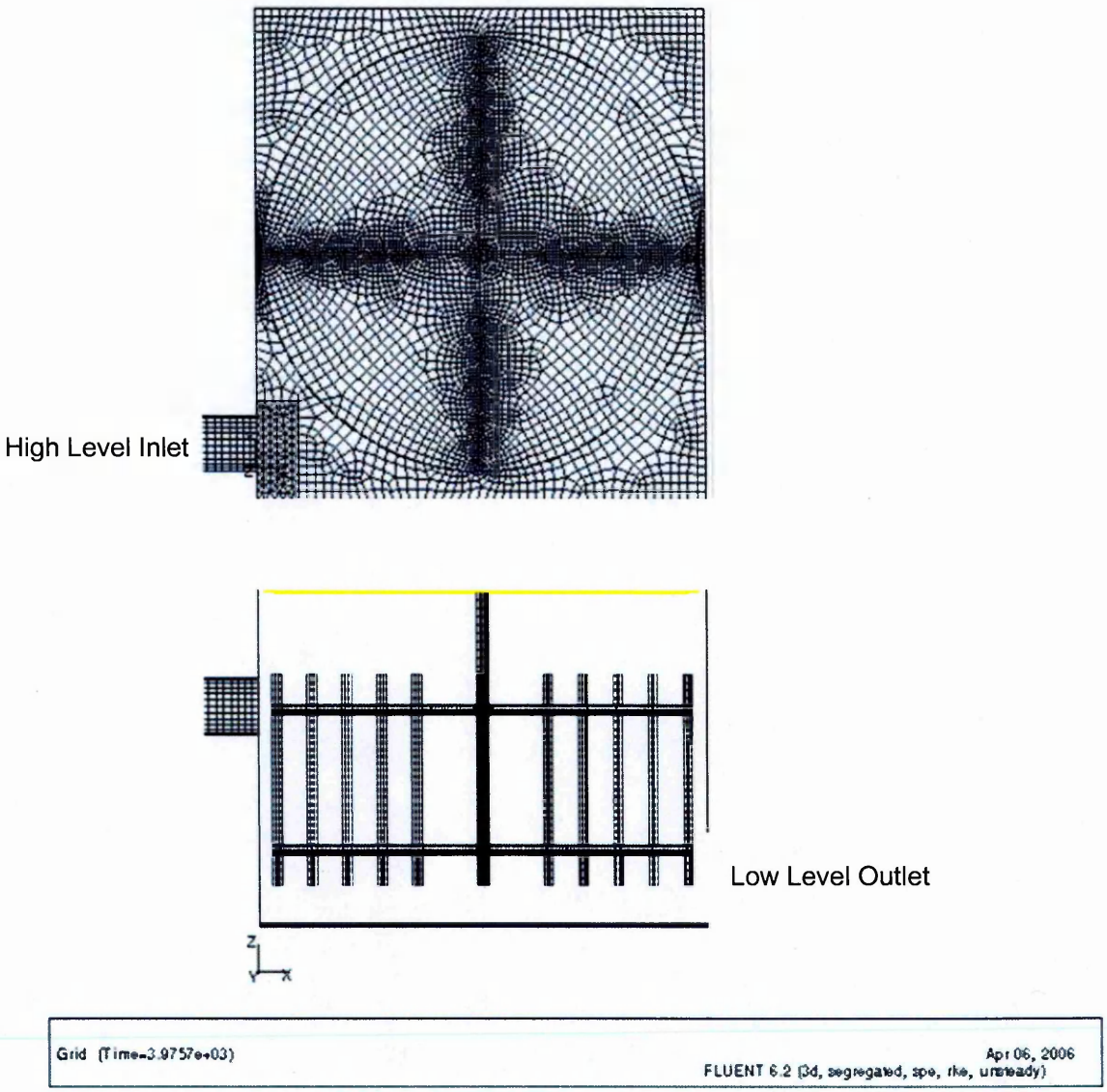


Figure 9-4: Plan and sectional views of meshed flocculation vessel.

As it was not permissible to remove a flocculator from service, it was not possible to develop an experimental residence time distribution to validate the model. Consideration was given to adopting the numerical integration of turbulence dissipation rate, as decribed in Chapter 5. However, this was not appropriate as all motors on the

flocculator paddles are rated the same (3.7KW), irrespective of mixing speed. Consequently, any comparison between power based on numerical integration of CFD data with pump rating would be meaningless.

9.4 Results

9.4.1 Velocity Profiles

The simulated velocity vectors and contours measured in the horizontal plane 3m above floor level (corresponding to the centreline of the inlet) at a mixing speed of 2.4 rpm (in the anticlockwise direction) are shown at Figure 9-5 and Figure 9-6. Some small dead spots at the vessel corners and around the shaft are apparent in the contour plot; otherwise there is a reasonable degree of movement within the vessel. Both figures indicate that the highest velocity vectors are located towards the tips of the paddles. The velocity varies from 0 to 0.89 ms^{-1} within the vessel; the upper limit being some 1.83 times greater than the inlet velocity of 0.486 ms^{-1}. These, and the corresponding data for the 1.6 and 3.2 rpm scenarios, are tabulated at Table 9-2 below.

Table 9-2: Minimum and maximum velocities found in vessel at stated mixing speeds. Flow rate = 21.1 Ml/d.

Mixing Speed, rpm	Min velocity, U_{min}, ms^{-1}	Max velocity, U_{max}, ms^{-1}	Inlet velocity, U_{inlet}, ms^{-1}	U_{max}/U_{inlet}
1.6	0	0.60	0.486	1.23
2.4	0	0.89	0.486	1.83
3.2	0	1.18	0.486	2.42

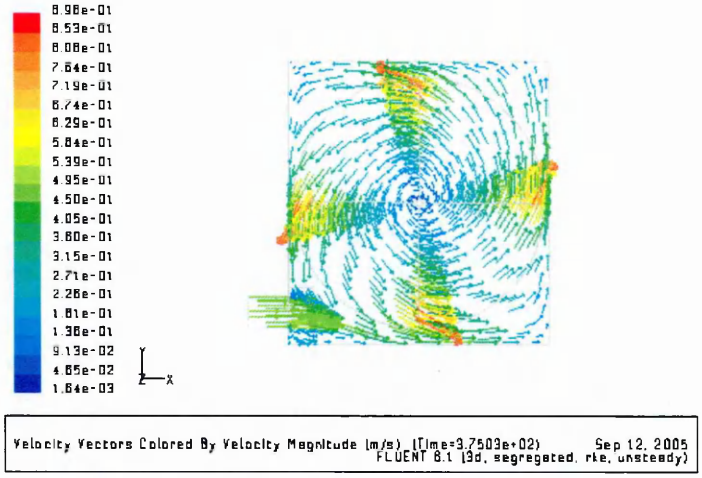


Figure 9-5: **Velocity vectors in horizontal plane (z=3.0m). N=2.4 rpm.**

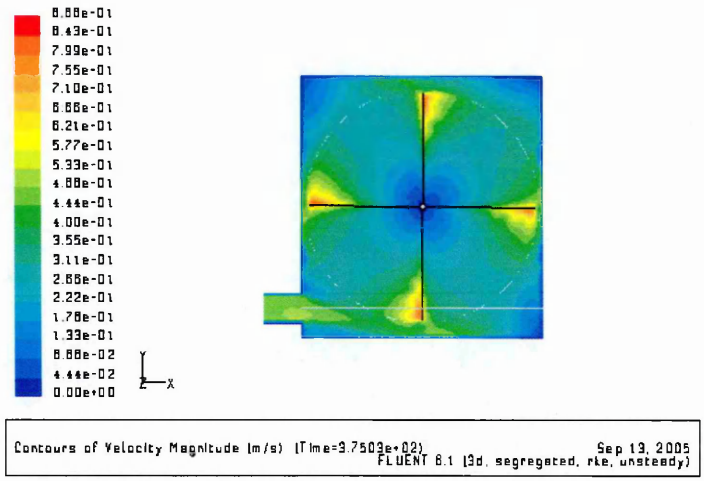


Figure 9-6: **Velocity contours in horizontal plane (z=3.0m). N=2.4 rpm.**

9.4.2 Particle Trajectory Analysis

For the 21.1 Ml/d, 2.4 rpm simulation, the injection into the flow of 50 particles (ϕ = 500μm, ρ = 1,000 kg/m^3), was modelled using the discrete phase model as described in Chapter 7. Bache and Rasool (2001) presented a variety of maximum size data for flocs encountered at seven different water treatment works treating typical upland waters (*i.e.* significant colour, low turbidity, low alkalinity), and showed a wide variation in size, depending on water quality and coagulation approach. From these data, a floc size of 500µm was considered to be appropriate for Frankley WTW. Neutrally buoyant flocs were also considered appropriate on the basis of published literature (Gregory, 1997). The particles were injected at the inlet with flow rate set to 21.1 Ml/d and mixing speed

at 2.4 rpm and the particles' trajectories were traced. The results are displayed at Figure 9-7. Just 45 seconds of trajectory tracking is shown in Figure 9-7, yet it is clear that a number of particles are seen to leave the vessel within that time period; this despite the fact that at a flow rate of 21.1 Ml/d, the vessel has a theoretical retention time, τ, of 14.5 minutes. Therefore, this small sample would appear to indicate some degree of short-circuiting within the vessel.

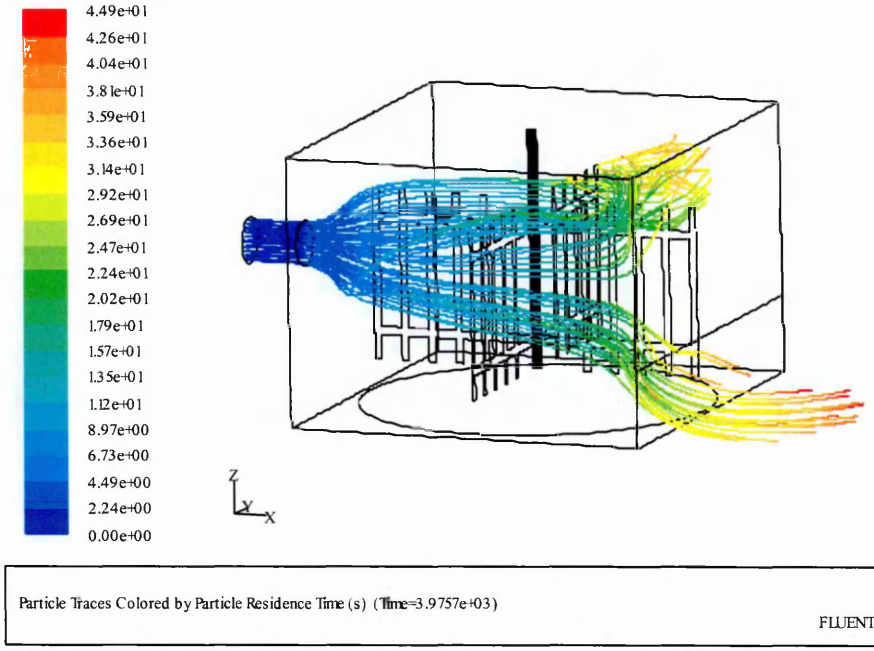


Figure 9-7: **Trajectories of 50 particles injected into the flow. ϕ = 0.5mm, ρ= 1,200 kg/m^3. Flow rate = 21.1Ml/d. Mixing speed = 2.4 rpm.**

9.4.3 Residence Time Distributions (RTD)

Using CFD it is possible to employ the discrete phase model to undertake a Lagrangian particle tracking analysis on a number of particles to determine overall residence times. However, this method requires a large number of particles to be analysed in order for the results to be statistically valid (certainly more than the 50 particles presented as an example above). This introduces significant additional computational expense and time to a model which has already taken approximately twelve days' CPU time to generate a converged solution. (Convergence being a three stage process: 1) MRF & *sk*-ϵ: ~ 2 days, 2) SM & *sk*-ϵ: ~ 5 days, 3) SM & *rk*-ϵ: ~ 5 days). An alternative approach is to treat a tracer fluid as a continuum by solving a transport equation for the tracer species.

This latter approach was adopted here. The transport and decay of a chemical species in a flow can be described by a general convection/diffusion equation:

$$\rho\frac{\partial\phi}{\partial t}+\rho u_i\frac{\partial\phi}{\partial x_i}-\left(\rho D_\phi+\frac{\mu_t}{\sigma_\phi}\right)\frac{\partial^2\phi}{\partial x_i^{\,2}}=S \qquad \textbf{Equation 9-1}$$

where ϕ is any scalar variable, D_ϕ is the molecular diffusivity of the scalar, σ_ϕ is the turbulent Schmidt number of the scalar, and S is the source / sink term for the scalar variable (= 0 for tracer transport).

As discussed in Chapter 2, the residence time distribution (RTD) is a measure or indication of the bulk flow patterns (*i.e.* macromixing) in a vessel and is defined such that the RTD function represents the fraction of fluid at the outlet that has a residence time in the vessel of between t and t+δt. Consequently,

$$\int_0^\infty E(t)dt=1 \text{ and } \int_{t_1}^\infty E(t)dt=1-\int_0^{t_1}E(t)dt \qquad \textbf{Equation 9-2}$$

Essentially, an RTD is simply the distribution of particles leaving a mixing system or, viewed from an alternative perspective, the distribution of life expectancies for particles entering the system.

A small amount of non-reactive tracer (approximately 1m^3, representing 0.5% of the flocculation cell volume), with fluid properties set to the same as water, was "injected" into the flow via the inlet. All reactions between the species and bulk flow were turned off, and the species concentration was monitored at the outlet. The tracer flow curves and normalised residence distribution curves for the three mixing speeds and the three flow rates are shown at Figure 9-8 to Figure 9-13. The tracer study data was normalised according to the method of Crittenden *et al.* (2005) on the basis of $\bar{t}$ and C_N. where

$$\bar{t}=\frac{\int_0^\infty Ct\,dt}{\int_0^\infty C\,dt}\approx\frac{\sum\overline{Ct}\,\Delta t}{\sum\overline{C}\,\Delta t} \qquad \textbf{Equation 9-3}$$

$$C_N=\int_0^\infty Cd\left(\frac{t}{\bar{t}}\right)=\frac{\int_0^\infty Cdt}{\bar{t}}\approx\frac{\sum\overline{C}\Delta t}{\bar{t}} \qquad \textbf{Equation 9-4}$$

$$E(\theta)=\frac{C}{C_N} \qquad \textbf{Equation 9-5}$$

where $\bar{t}$ = mean residence time in vessel,

C = concentration exiting vessel at time t,

t = time since addition of tracer pulse to vessel.

The results for all flow rates and mixing speeds are presented below at Table 9-3 and are presented for each scenario as time for concentration of species at outlet to reach 10%, 50% and 90% of the total measured output concentration.

The RTD curves demonstrate that regardless of flow rate, the time before tracer is first measured at the outlet is approximately one minute. After this, the flow curves rise steeply to attain maximum tracer flow values. Flows for all mixing speeds and flow rates all exhibit some shouldering, indicating a degree of recirculation. All curves then drop sharply, thereafter taking a more exponential shaped profile, indicating that the tracer has reached an approximately uniform distribution throughout the tank. At all flow rates, $\bar{t}$ decreases with increasing mixing speed, as do t_{10}, t_{50} and t_{90}, indicating a retention time dependency on mixing speed and not simply flow rate. A modest increase in the $t_n / \bar{t}$ ratio with increasing mixing speed is observed for all flow rates, indicating that the reduction in $\bar{t}$ outweighs any corresponding reduction in t_n. The implications of these times on floc formation and growth are discussed below.

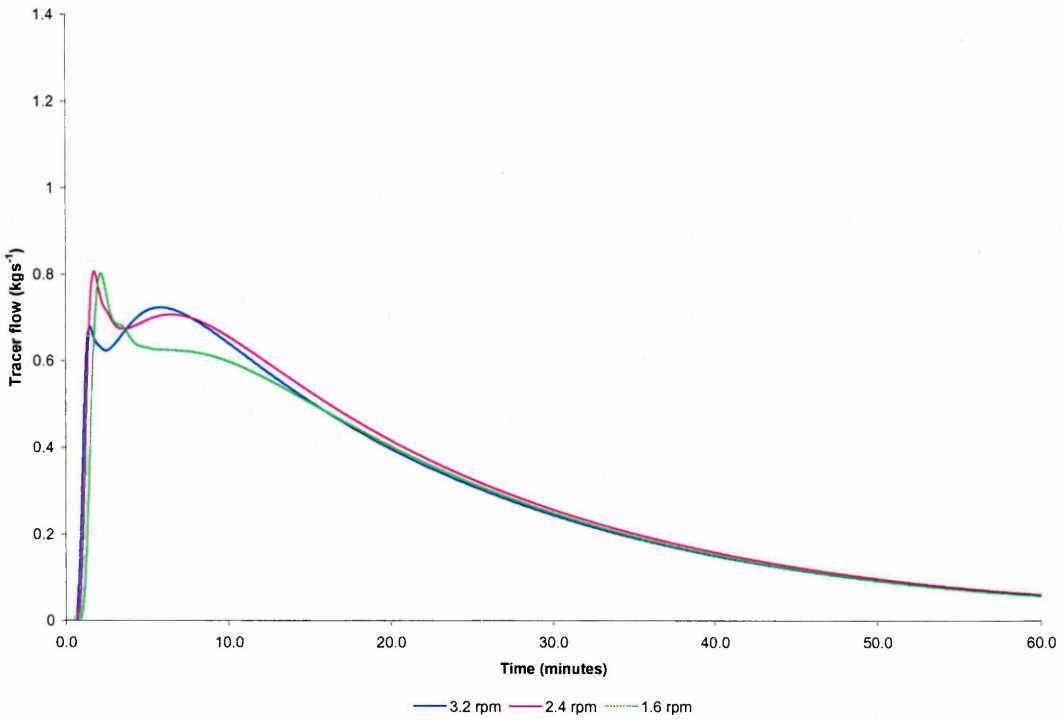


Figure 9-8: Outlet measured tracer flow rate at 16 Ml/d.

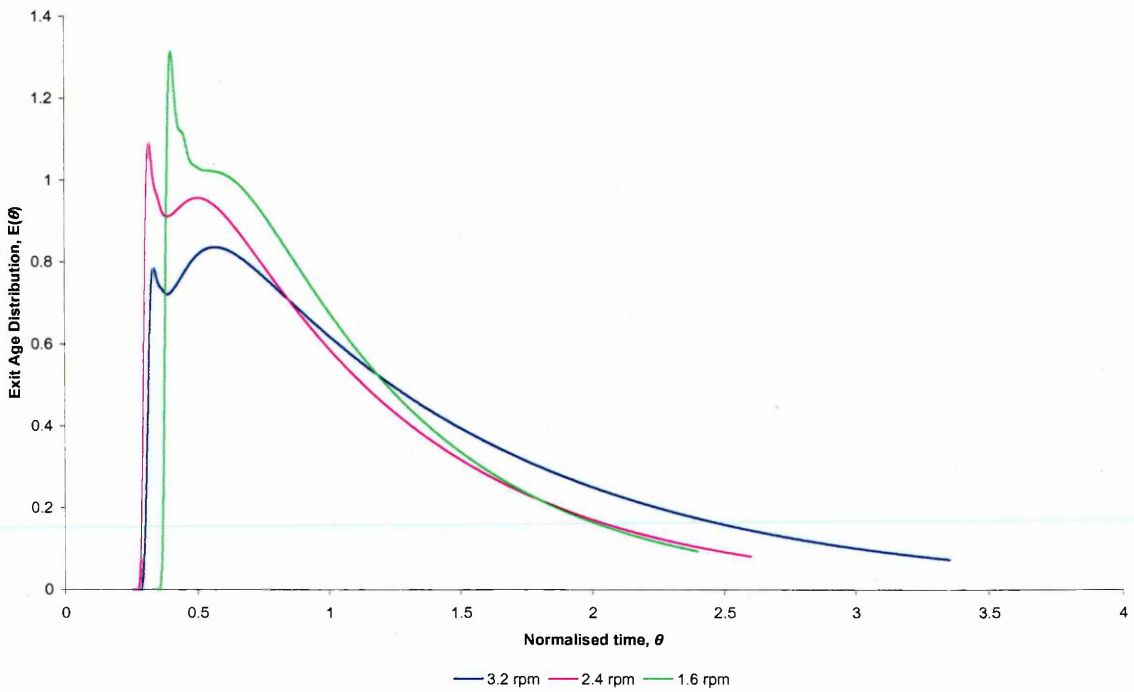


Figure 9-9: Normalised residence time distribution curve at 16 Ml/d.

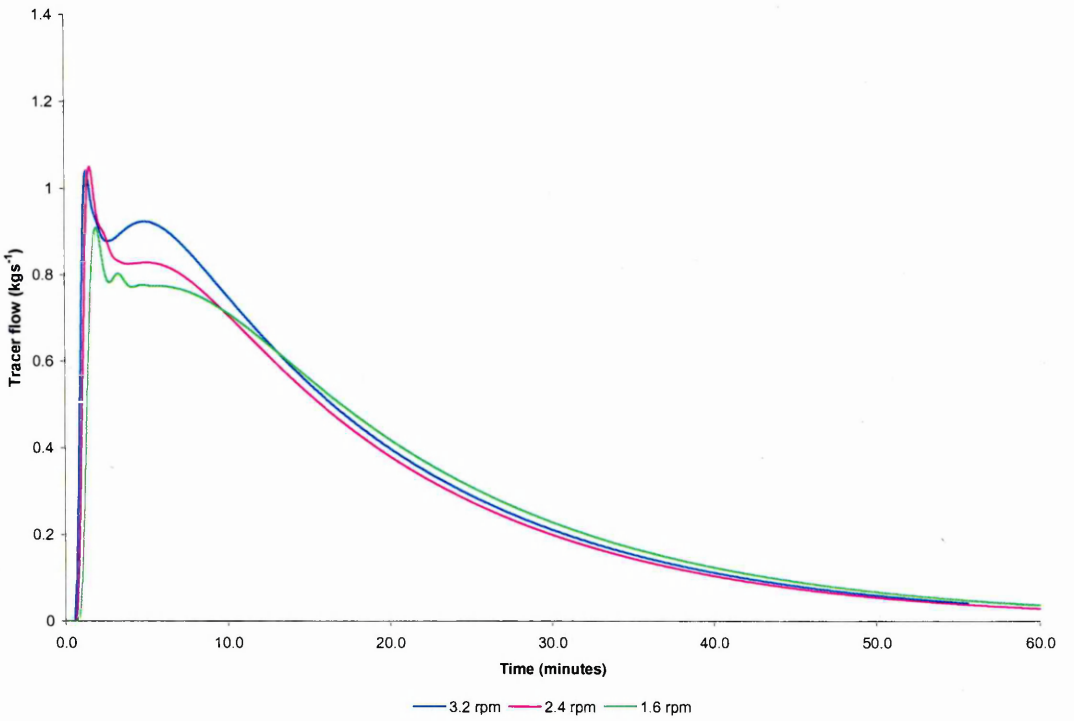


Figure 9-10: Outlet measured tracer flow rate at 21.1 Ml/d.

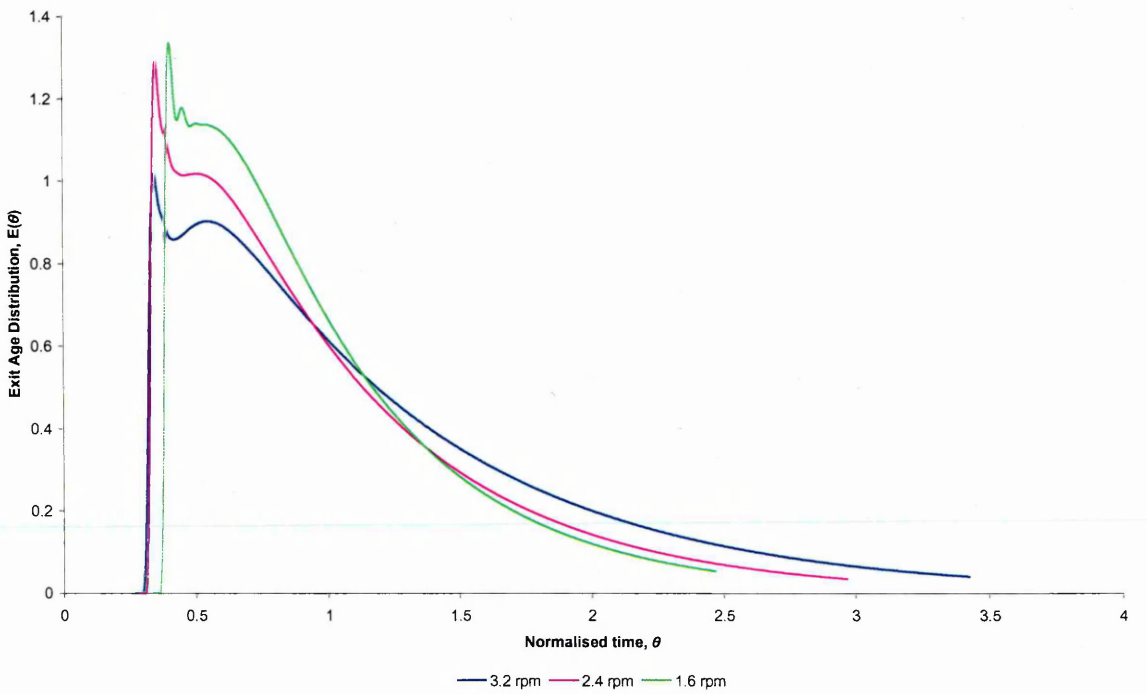


Figure 9-11: Normalised residence time distribution curve at 21.1 Ml/d.

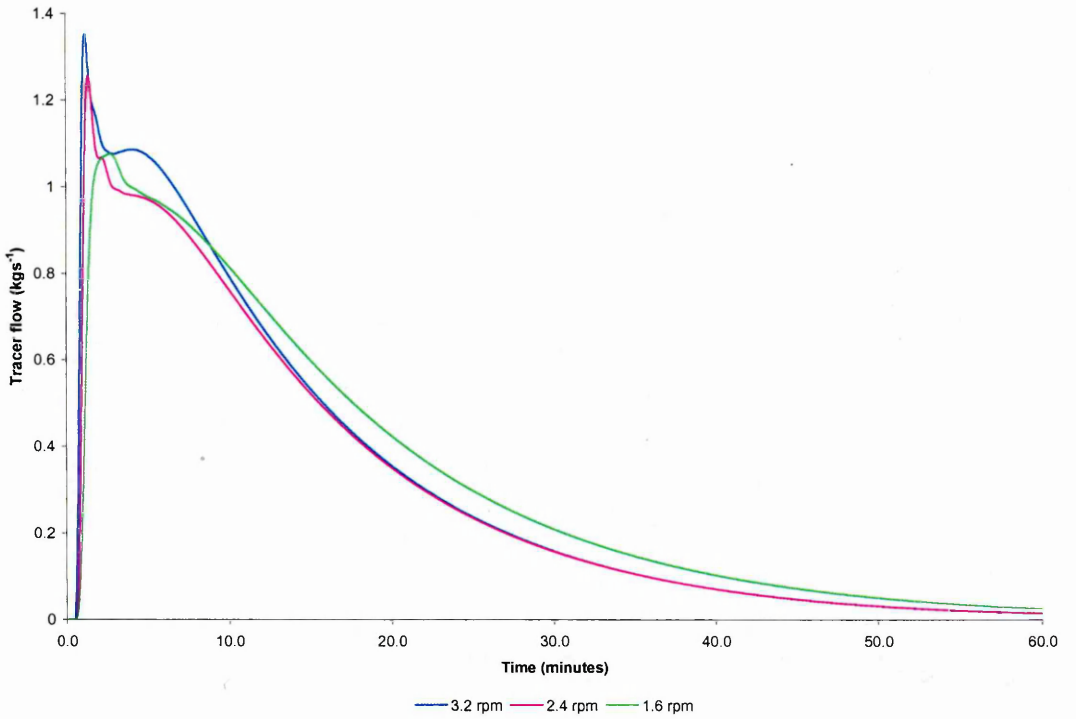


Figure 9-12: Outlet measured tracer flow rate at 24.0 Ml/d.

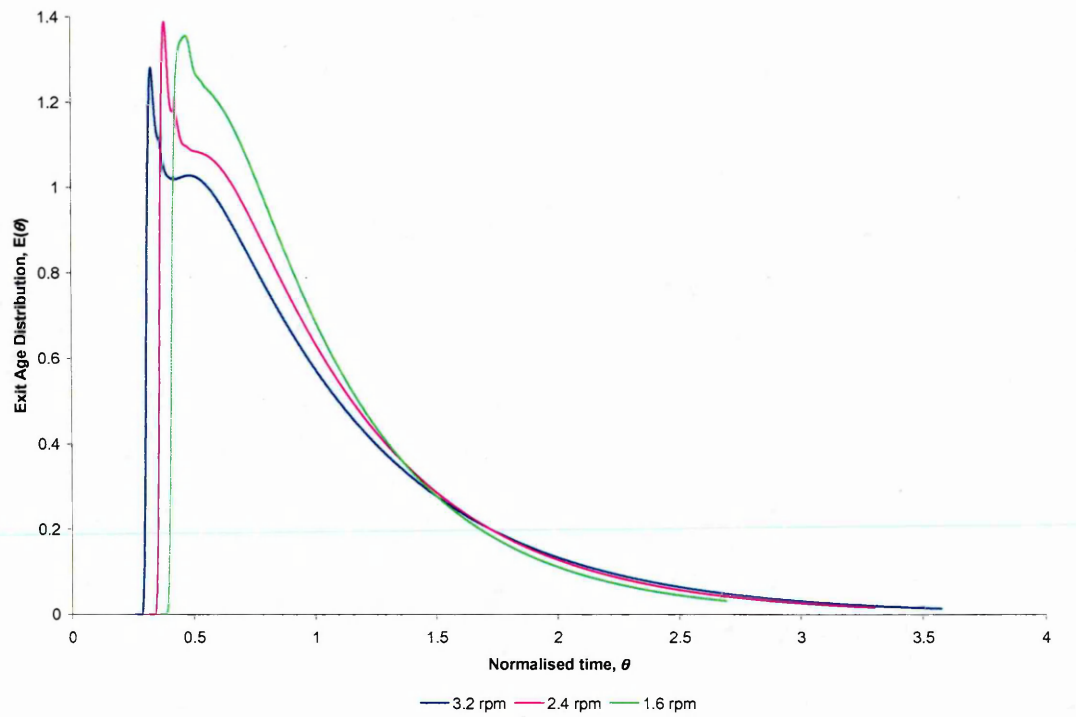


Figure 9-13: Normalised residence time distribution curve at 24.0 Ml/d.

Table 9-3: Frankley WTW Residence Time Distribution Results.

Flow Rate, Ml/d	Mixing Speed, rpm	Theoretical Ret'n Time, τ, mins	Mean Residence Time, $\bar{t}$, mins	t_{10}, mins	t_{50}, mins	t_{90}, mins	$t_{10}/\bar{t}$	$t_{50}/\bar{t}$	$t_{90}/\bar{t}$	t_{50}/t_{10}	t_{90}/t_{10}
16.0	1.6	19.15	28.96	3.89	16.02	41.19	0.13	0.55	1.42	4.12	10.60
	2.4	19.15	25.50	3.77	10.65	40.85	0.15	0.61	1.60	4,12	10.83
	3.2	19.15	23.72	3.8	15.23	40.59	0.16	0.64	1.71	4.01	10.68
21.1	1.6	14.52	28.14	3.59	14.32	39.95	0.13	0.51	1.42	3.99	11.12
	2.4	14.52	22.35	2.94	12.51	34.74	0.13	0.56	1.55	4.25	11.80
	3.2	14.52	20.71	2.94	12.35	34.82	0.14	0.60	1.68	4.20	11.85
24.0	1.6	11.61	25.79	3.09	12.29	34.88	0.12	0.48	1.35	3.97	11.27
	2.4	11.61	20.08	2.53	10.58	29.74	0.13	0.53	1.48	4.19	11.77
	3.2	11.61	18.11	2.37	10.12	29.15	0.13	0.56	1.61	4.28	12.33

9.4.4 Average Velocity Gradient, Local Velocity Gradient and Turbulence Dissipation Rate

For a flocculation system of this type, Armitharajah *et al.* (1991) stated that the vessel average velocity gradient be calculated on the basis of power applied as:

$$G = \sqrt{\frac{1.1x10^{-3}.C_D.(1-k_2)^3.N^3.\Sigma Ar_b^{\ 3}}{\mu V}} \qquad \textbf{Equation 9-6}$$

where, C_D = drag coefficient (=1.8 for flat blades)

k_2 = ratio of fluid velocity to blade velocity

N = mixing speed

A = area of paddle

r_b = distance from shaft to centreline of blade

ΣAr_b^3 = the sum of Ar_b^3 values for all paddles.

Applying Equation 9-6, the vessel average velocity gradient, $\overline{G}$ has been calculated for each mixing speed, and these values are tabulated at Table 9-4. Water at Frankley WTW is treated via tapered flocculation, and consequently, the total $\overline{G}.t$ applied to the water is the sum of the $\overline{G}.t$ applied at each mixing speed. The total $\overline{G}.t$ applied is 67, 292 (at 16 Ml/d), 84,158 (at 21.1 Ml/d) and 110,993 (at 24 Ml/d). This observation is discussed further below.

Table 9-4: **Calculated average velocity gradient and $\overline{G}.t$ values.**

N, rpm	$\overline{G}$, s^{-1}	Design $\overline{G}.t$ 16 Ml/d	21.1 Ml/d	24 Ml/d
1.6	19.4	22,291	16,901	13,514
2.4	31.8	36,538	27,704	22,152
3.2	45.4	52,165	39,552	31,626
$\Sigma\overline{G}.t$		67,292	84,158	110,993

The G values and other relevant design parameters are compared with those recommended by Crittenden *et al.* (2005) at Table 9-5. It is found that $\overline{G}$, N and

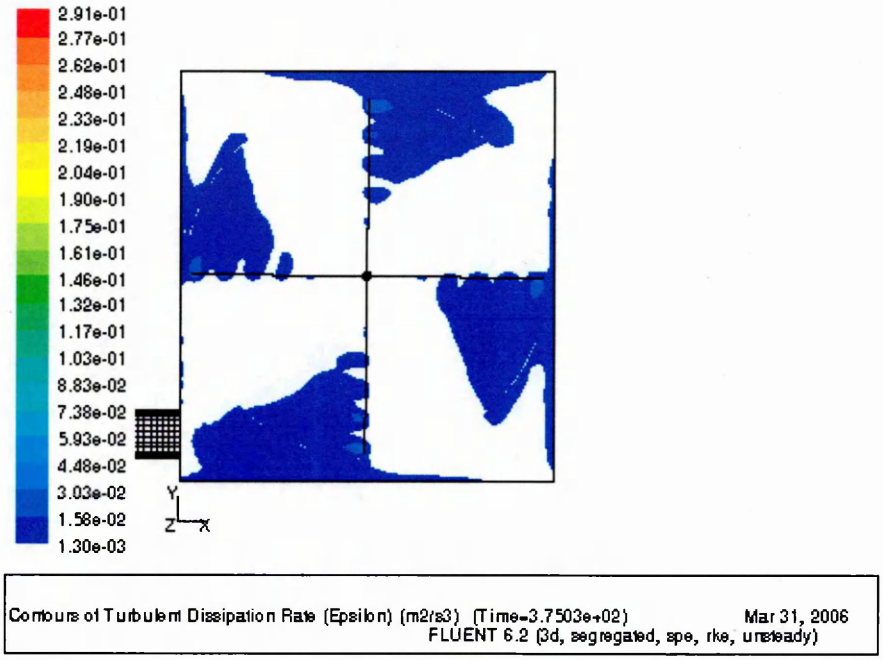
number of cells values all lie within the recommended ranges, whilst tip speed and cell size are outside the recommended range, albeit the latter only slightly so.

Table 9-5: **Comparison of Frankley design parameter values with those recommended by Crittenden *et al* (2005).**

Design Parameter	Recommended Range	Frankley Value(s)
$\overline{G}$, s^{-1}	10-80	19-45
N, rpm	1-5	1.6-3.2
Paddle tip speed, ms^{-1}	1	0.25-0.5
Flocculation cell size, m	3-6 x 3-6	6.4 x 7
No. of cells	2-6	3

Using the CFD data, vessel average values for local velocity gradient $(\overline{G_L})$ and turbulence energy dissipation rate $(\overline{\varepsilon})$ for N = 2.4 rpm at a flow rate of 21.1 Ml/d were calculated as 30.4 s^{-1} and 1.36 x 10^{-3} m^2s^{-3} respectively, and it is noteworthy that in this situation, the vessel average velocity gradient calculated on the basis of power drawn is similar to the average calculated by averaging the individual local velocity gradients at each location in the grid ($31.8s^{-1}$) . Previous workers (*e.g.* Cleasby, 1984, Graber, 1994, Jones, 1999) have expressed significant concern with regard to the viability of the vessel average velocity gradient, $\overline{G}$, (as formulated by Camp and Stein, 1943) as a robust design parameter, and the results of the jar test CFD simulations presented above would appear to verify the assertion that $\overline{G}$ does not reflect the significant variations found in the local velocity gradients throughout the jar test vessel. However, for this full scale facility, there is little discernible difference between the "traditional" $\overline{G}$ value and the value based on the average of all local velocity gradients, $\overline{G}_L$.

Considering the 2.4 rpm, 21.1 Ml/d simulation, Figure 9-14 and Figure 9-15 show contours of turbulence dissipation rate and local velocity gradient in the vertical and horizontal planes for values which are in excess of the vessel averages. As would be expected, the values greater than the average are generally to be found around the paddle edges and in the wake of the paddle.



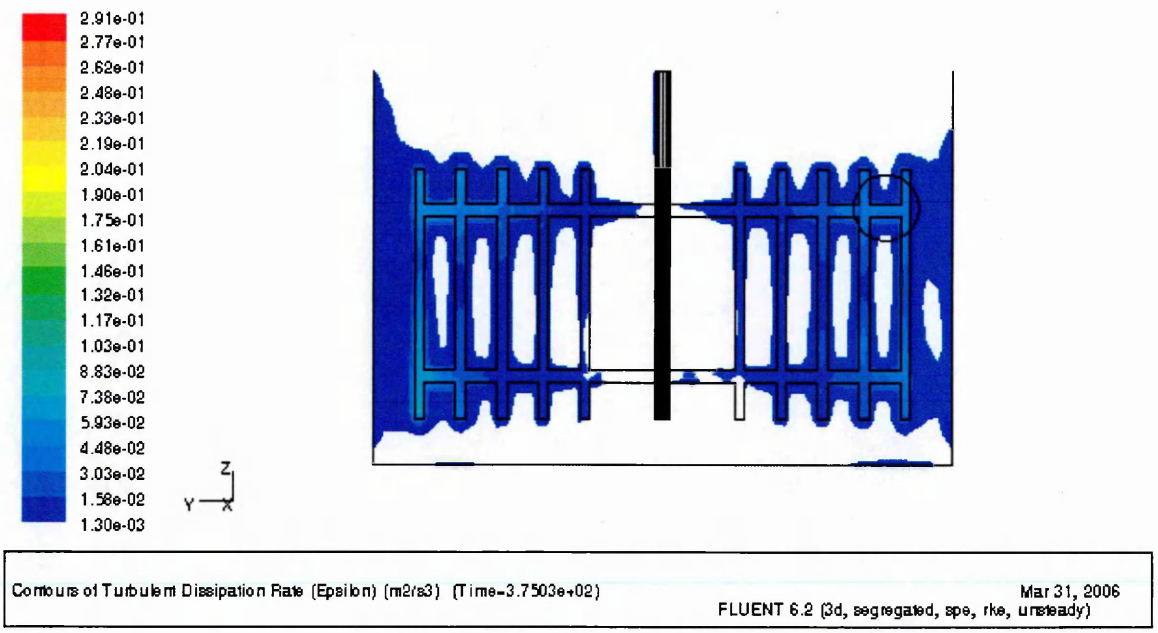
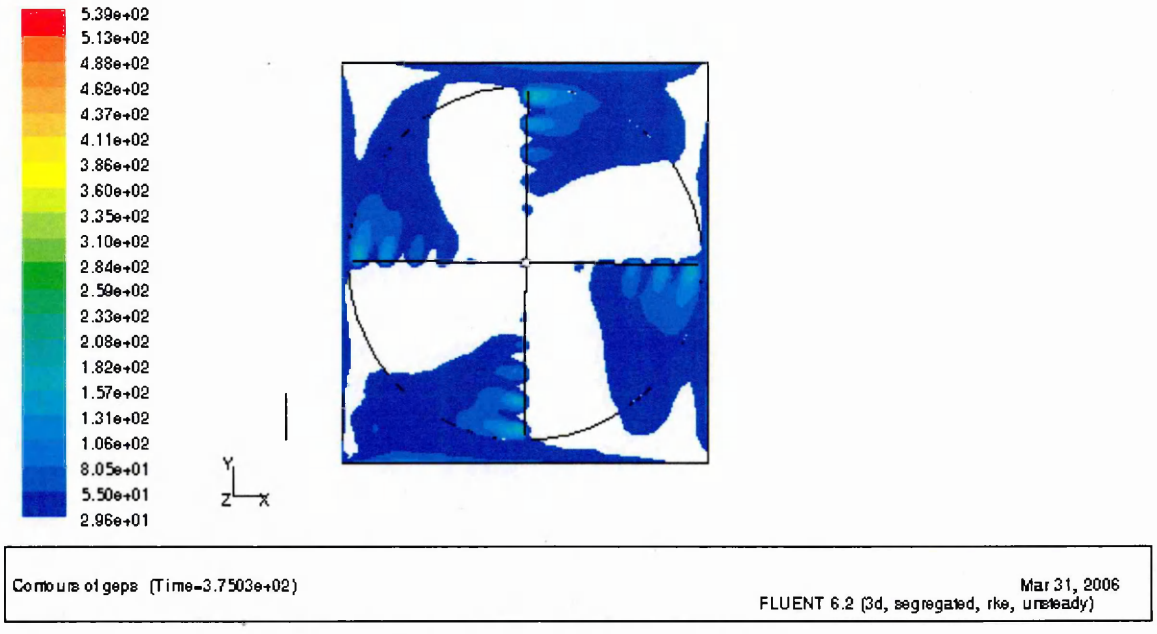


Figure 9-14: **Contours of turbulence dissipation rate, ϵ greater than vessel average value taken through (a) z = 3.0m and (b) paddle section. N = 2.4 rpm, flow rate = 21.1 Ml/d.**



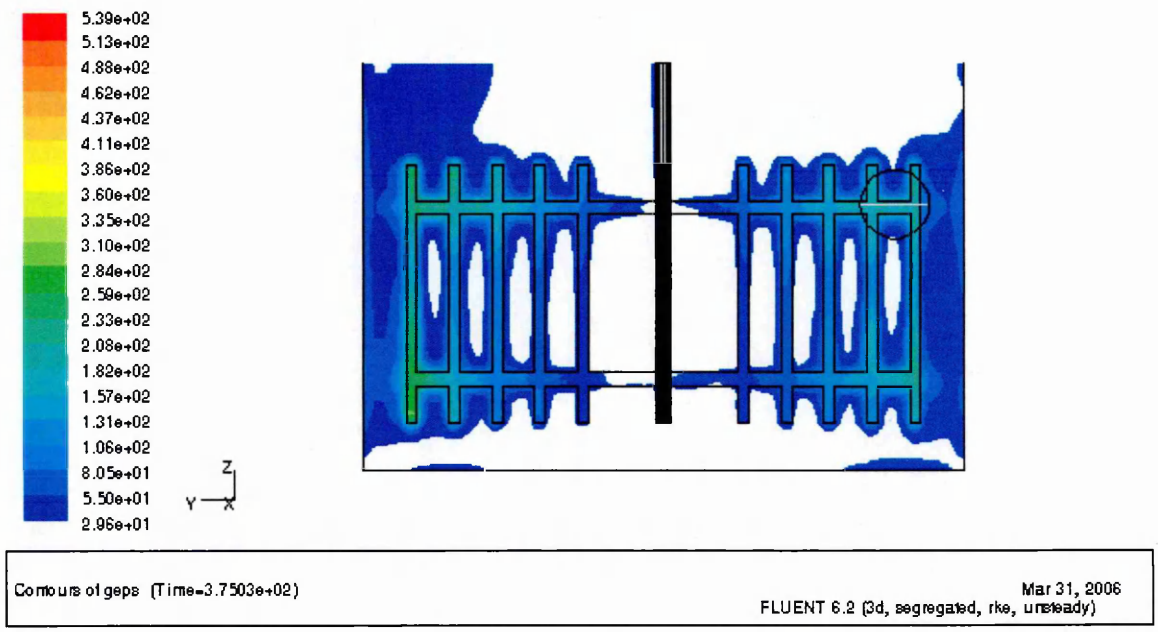


Figure 9-15: **Contours of local velocity gradient, G_L, greater than vessel average value taken through (a) z = 3.0m and (b) paddle section. N = 2.4 rpm, flow rate = 21.1 Ml/d.**

In order to relate the results of the Frankley models to those generated from the jar test model, the average and maximum local velocity gradients, $\overline{G_L}$ and G_{Lmax} respectively, and average turbulent eddy dissipation, $\bar{\varepsilon}$, values were calculated for each mixing speed and flow rate and the results are shown at Table 9-6. It is apparent that both the average and maximum local velocity gradients are affected by the mixing speed, but are

effectively independent of flow rate at each mixing speed. The data for the 21.1 Ml/d simulation are plotted at Figure 9-16 (the other data sets have been excluded for clarity of presentation). It is also clear from Table 9-6 and Figure 9-16 that the ratio of maximum local velocity gradient to average local velocity gradient is similar for each flow rate at a specific mixing speed, yet the ratio is seen to increase with increasing mixing speed. With just three data points for each data set, it is difficult to draw a robust conclusion from this observation. However, the data points show that the proportional increase in G_{Lmax} is greater than the proportional increase in $\overline{G_L}$ each time the mixing speed is increased. The consequence of this is that the G_{Lmax}:$\overline{G_L}$ ratio rises as the mixing speed is increased. Histograms of the volumetric distribution of local velocity gradient within the vessel for the three mixing speeds at a flow rate of 21.1 Ml/d are shown at Figure 9-17. As the mixing speed increases, there is an extension in the distribution towards higher local velocity gradient values in that there are increased maxima but similar minima. Therefore it is assumed that the increases in G_{Lmax} brought about by increasing mixing speed are not sufficiently well-distributed to cause a corresponding increase in $\overline{G_L}$.

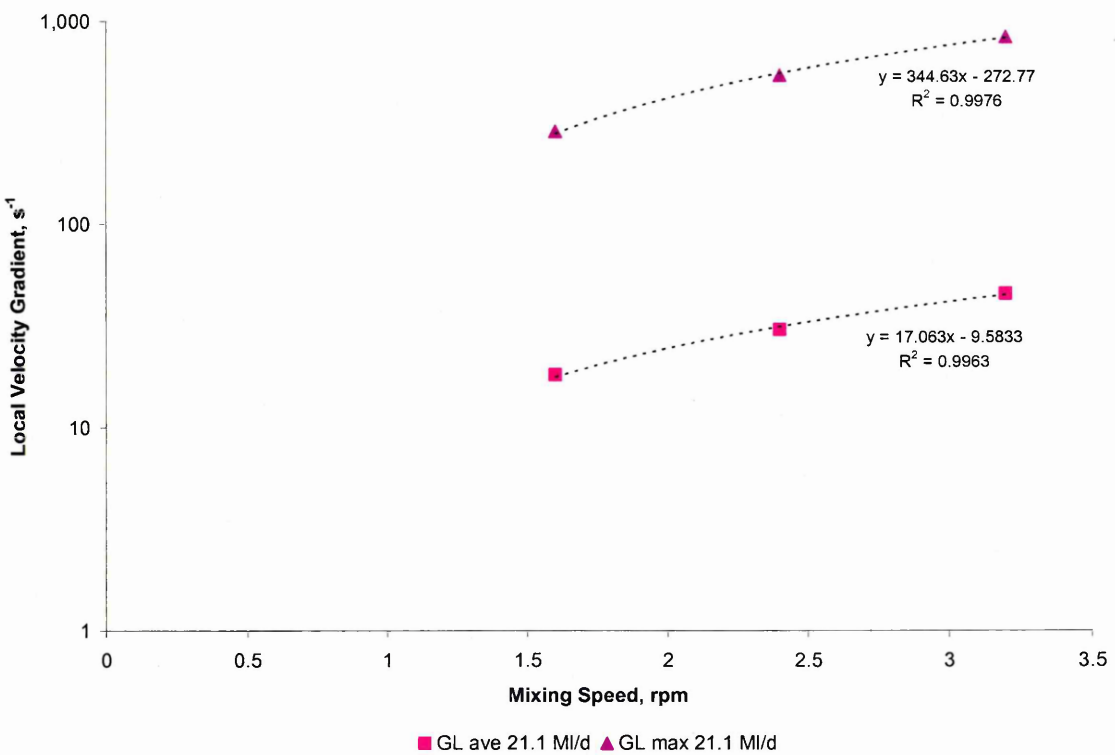
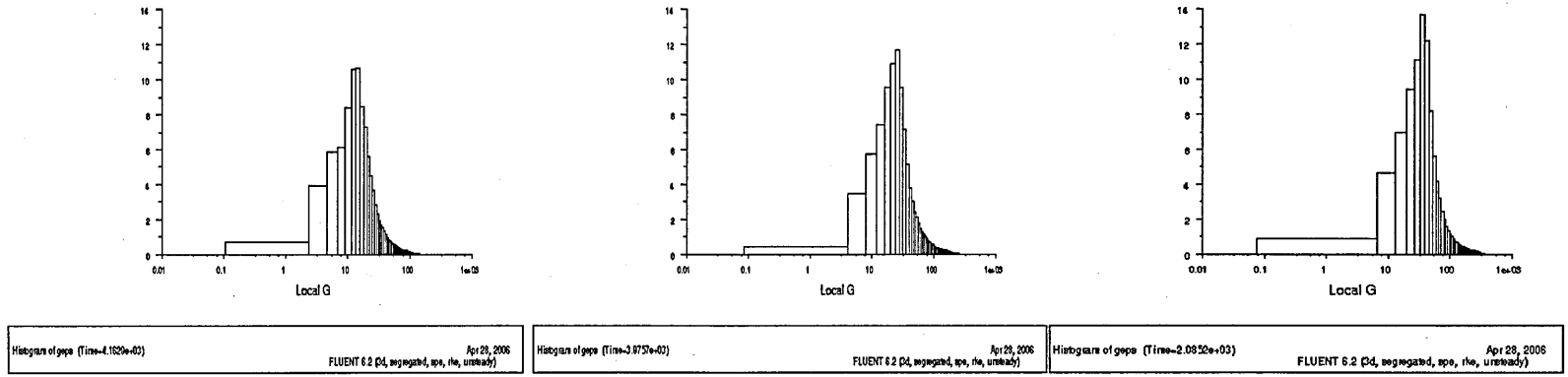


Figure 9-16: Average and maximum local velocity gradient values at stated mixing speeds

Table 9-6: Average turbulence dissipation rates and average and maximum values of local velocity gradient at stated mixing speeds.

Flow Rate, ML/d	3.2 rpm				2.4 rpm				1.6 rpm			
	ϵ x 10^{-3}, m^2s^{-3}	$\overline{G_L}$, s^{-1}	$G_{L\max}$, s^{-1}	$\frac{G_{L\max}}{\overline{G_L}}$	ϵ x 10^{-3} m^2s^{-3}	$\overline{G_L}$, s^{-1}	$G_{L\max}$, s^{-1}	$\frac{G_{L\max}}{\overline{G_L}}$	ϵ x 10^{-3} m^2s^{-3}	$\overline{G_L}$, s^{-1}	$G_{L\max}$, s^{-1}	$\frac{G_{L\max}}{\overline{G_L}}$
16.0	3.07	44.9	839.9	18.7	1.31	29.6	544.3	18.4	0.42	16.9	268.7	15.9
21.1	3.11	45.5	837.9	18.4	1.36	30.4	538.6	17.7	0.48	18.2	286.5	15.7
24.0	3.19	46.5	832.8	17.9	1.45	31.6	526.0	16.6	0.53	19.2	289.6	15.1



N = 1.6 rpm N = 2.4 rpm N = 3.2 rpm

Figure 9-17: Local velocity gradient distribution.

It is clear from Figure 9-17, however, that for all mixing speeds, there is only a small percentage of the overall volume where the velocity gradient value exceeds $100s^{-1}$. To facilitate an improved analysis, the cumulative distributions of local velocity gradient values for the three mixing speeds are shown at Figure 9-18. It can be seen from Figure 9-18 that at a mixing speed of 1.6 rpm, the vessel has a 90% coverage of G_L values below $50s^{-1}$, and 95% coverage of G_L values of 65 s^{-1} or below. The three curves are all of a similar shape, but shift towards higher G_L values as the mixing speed increases. For the 3.2 rpm simulation, 90% vessel coverage is attained at a G_L value of $117s^{-1}$, and 95% coverage is attained at a G_L value of $170s^{-1}$.

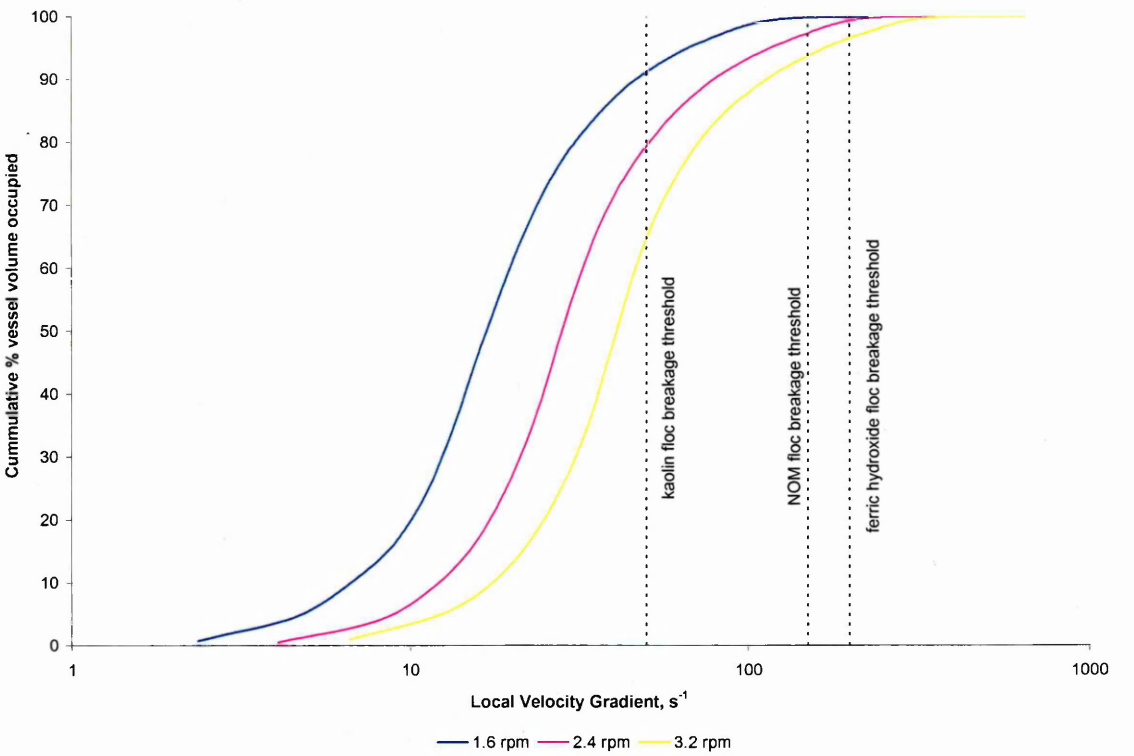


Figure 9-18: Cumulative distribution of local velocity gradient at different mixing speeds. Flow rate = 21.1 Ml/d.

It is both interesting and instructive to consider the data of Figure 9-18 alongside the floc breakage data and CFD analyses provided in Chapter 8 above. Therefore, the postulated breakage thresholds for each of the three suspensions studied by Jarvis *et al.* (2004) are shown on Figure 9-18, with the weak kaolin flocs having a breakage threshold of $50s^{-1}$, NOM flocs having a breakage threshold of $150s^{-1}$ and the coagulant

precipitate flocs breakage threshold being $200s^{-1}$. From the perspective of hydrodynamics alone (*i.e.* ignoring residence time), the plot shows clearly that irrespective of floc type the three mixing speeds used at Frankley will generally encourage floc growth (or, at least, stability) rather than breakage. At the highest mixing speed, approximately 33% of the vessel has a local velocity gradient value above the breakage threshold for kaolin flocs. The corresponding values for NOM and coagulant precipitate flocs are 6.3% and 3.4% respectively. These data, and the relevant data for the other two mixing speeds, are given below at Table 9-7.

Table 9-7: Percentage of vessel volume experiencing local velocity gradient values in excess of postulated breakage threshold.

	% of tank volume greater than breakage threshold G_L		
Mixing Speed, rpm	**Kaolin**	**NOM**	**Coagulant Precipitate**
3.2	33%	6%	3%
2.4	20%	3%	1
1.6	8%	<1%	<1%

The above data would appear to demonstrate that, as currently designed and operated, the Frankley system of flocculation provides a good hydrodynamic environment to assist in the flocculation process for NOM flocs, whereas the shears are too great for the kaolin flocs, particularly in the 3.2 and 2.4 rpm mixing zones. However, one should recall that these values take no account of residence time and the residence time distribution curves demonstrated that some flocs will have a significantly reduced $G_t.t$ compared to others. Data from Table 9-4 shows that the total design $\overline{G}.t$ values to which the water is subjected all fall within the range postulated by Camp (1955). However, the jar test results given in Chapter 8 above, suggested that a much lower $\overline{G}.t$ value would be sufficient to ensure adequate flocculation, and this is backed up by the theoretical approach of Lawler and Nason (2004). It is accepted that the jar test simulation used a different raw water (albeit it was a similar, upland water) and different coagulant dose and type. However, the jar test CFD results inferred that a $G_t.t$ value of approximately 14,500 was adequate to form flocs of a large, open (and hence weak) nature. Considering the appropriate elements of Table 9-4 and Table 9-6, it is possible to determine the Camp number in terms of the mean residence time, $\bar{t}$, and $\overline{G_L}$ for each cell and the complete flocculation process (three cells in series), and to

compare these to the design values shown in Table 9-4. These data are shown below at Figure 9-19. It is immediately apparent that $\overline{G_L.t}$ is greater than $\overline{G}.\tau$ in all cases, thus indicating a greater degree of flocculation in each cell than originally intended by the plant designers.

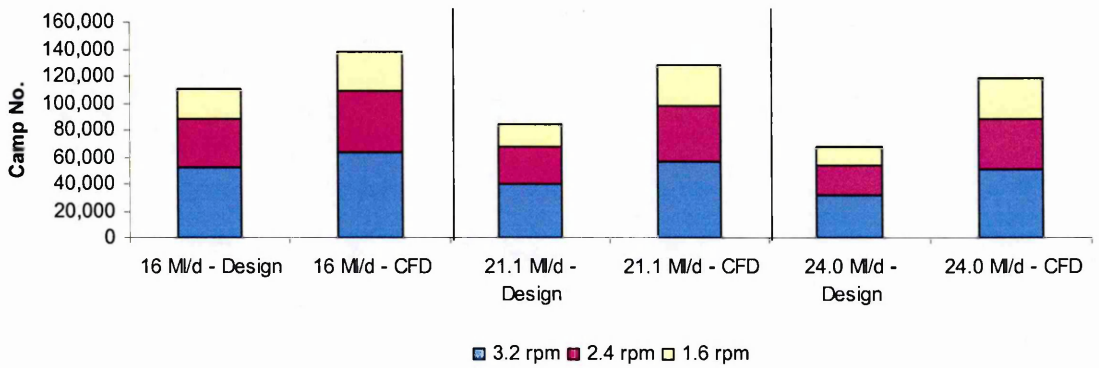


Figure 9-19: Camp numbers for each flow rate based on design parameters and CFD results.

It is concluded that the flocculators at Frankley WTW are, in effect, over-treating the water and applying a *G.t* value in excess of that which is actually necessary for effective flocculation. The likely outcome of such over-treatment is floc breakage to a minimum size. However, the operators at Frankley WTW have not reported any serious under-performance of the downstream DAF process arising as a result of ineffective flocculation. Consequently, it may be concluded that the DAF process is capable of removing flocs which are smaller than the maximum possible. Indeed, Bache and Rasool (2001) reported an instance of successful DAF plant operation in the absence of correctly-functioning flocculation upstream. Whilst this apparent over-treatment at Frankley may not have an immediate operational impact on the works, there are clearly long term effects (*e.g.* unnecessary power consumption) which will have an impact on the overall profitability of the treatment works, particularly when considered in the context of forecast increased energy costs and the economic regulator's requirement for increased operational efficiency.

9.5 Summary

CFD has been used to analyse the flow field generated within a flocculator cell at the Frankley WTW in Birmingham, UK. Turbulence closure was achieved via use of the realizable k-ϵ turbulence model, and the rotating flow was solved using the computationally-expensive, but robust, sliding mesh method. The high CPU usage of a model of this size and complexity precludes its use in most commercial environments and may limit the use and application of complex CFD analyses within the water industry.

The CFD analysis of the Frankley flocculator has facilitated an insight into the hydrodynamic environment generated across the full range of flow rates and mixing speeds which are found at the treatment works and, in turn, this has enabled the user to derive a set of data would not otherwise have been easily obtained. In particular, the species transport function was used to develop residence time distributions for average, minimum and maximum flow rates at each of the three prescribed mixing speeds. Some short-circuiting was found in all cases. Irrespective of flow or mixing speed, the time for 10% of the tracer to exit the flocculator was in the region of 3-4 minutes of the total retention time. The times for 10%, 50% and 90% of the tracer to exit the vessel (t_{10}, t_{50} and t_{90} respectively) all decreased with flow rate, as expected. Mixing speed was found to exert an influence on the mean residence time, with increased mixing speed giving rise to reduced retention. The velocity field analyses demonstrated that there are some localised areas of stagnation within the vessel, particularly in the corners and the immediate vicinity of the shaft. However, overall a reasonable degree of mixing was observed.

A comparison of the average velocity gradient calculated on the basis of power drawn by the impeller and the equivalent value calculated as the average of individual velocity gradients within each cell yielded consistent results. Analyses of the distribution of local velocity gradients within the flocculator showed that the magnitude of these gradients is generally less than that found in the jar tester at all but the lowest mixing

speed. In addition, the distribution of local velocity gradients is not as great as that found in the jar tester, thus corroborating a conclusion of Stanley and Smith (1995) that floc characteristics within the jar tester are governed by the hydrodynamic conditions found in the impeller zone.

A comparison was made between the velocity gradients (magnitude and distribution) in the full-scale plant with the laboratory and CFD data from the jar test apparatus. In particular, the performance of the Frankley flocculator was viewed in terms of the breakage thresholds postulated in Chapter 8. It is concluded that the velocity gradients generated in the Frankley flocculator are conducive to floc growth or stability. However, it was also demonstrated that the $\overline{G}.\tau$ value to which the water (and hence flocs) are subjected is significantly less than the $\overline{G_L.t}$ value developed using CFD and RTD, but is greater than the $G_t.t$ value developed for a similar raw water using the laboratory data of Jarvis *et al.* (2004) and a CFD model. It is concluded that, as the $\overline{G_L.t}$ value is so much greater than that found necessary for effective flocculation in the jar tester, the floc size at Frankley is not maximised. Whilst this does not appear to have had detrimental impact on the performance of the downstream clarification process, there are potential long term issues for the operators with regard to power consumption, increasing energy costs and a reduced opportunity for efficiency savings.

The analysis undertaken here has demonstrated how the design and operation of an existing flocculator can be assessed using CFD in combination with jar test data. A knowledge of floc strength (expressed in terms of threshold velocity gradient values) has been applied to the hydrodynamics of the flocculator to elucidate an understanding of the flocculator's performance. In a similar manner, the same approach could be adopted to the design of new flocculators. Jar test experiments and CFD analyses could be undertaken on the particular raw water and the results combined to develop threshold velocity gradient values as shown in the foregoing chapters. A CFD model could then be constructed based on an outline flocculator design and the flow patterns and turbulence characteristics identified. Thus designs could be verified in advance of construction and without scale model manufacture and testing, potentially generating savings as experienced and reported by Andoh (2006).

10 Bamford WTW Flocculator CFD Analysis

10.1 Introduction

Whilst the literature contains a number of examples of CFD analyses of full scale water treatment unit processes, there are very few examples of numerical studies of hydraulic flocculators. It is true that in the UK the number of mechanical installations outnumber the number of hydraulic ones; however, on a global scale it is somewhat surprising to find that this example of a unit process has received such little attention, or at least, has so few publications associated with it. Indeed, a thorough search of the literature found just two published, peer-reviewed articles relating to the performance of a full scale hydraulic flocculator; those being the papers of Haarhoff and van der Walt, (2001) and Haarhoff (1998). Van der Walt (2002) also includes details of the same analyses.

Despite the apparent lack of attention paid to CFD studies of hydraulic flocculators, it was considered appropriate for this research project to consider one such installation in order that its design and operation might be considered in relation to the mechanical design which is installed and operated at Frankley WTW. Severn Trent Water operates just one hydraulic flocculator; that being at its Bamford WTW in Derbyshire. The WTW takes water from an upland source and so its characteristics are similar to those found at Frankley WTW and also to the upland water used by Jarvis *et al.* (2004) in their jar test experiments.

Hydraulic flocculation is perceived as offering certain advantages over mechanical flocculation; specifically offering relatively simple operation and maintenance (and hence low operating costs). However, hydraulic flocculators generally occupy a larger footprint and are limited in their ability to adjust the degree of mixing.

10.2 Bamford WTW

Bamford WTW, situated to the west of the city of Sheffield in the UK, takes water from the three large impounding reservoirs (Ladybower, Derwent and Howden) to the north of the works. The three reservoirs are arranged in series and have a combined storage of approximately 306,000Ml. Of these, Ladybower offers the maximum storage (approximately 287,000Ml), with Derwent and Howden having approximately 9,600Ml and 9,000Ml storage respectively.

The water treatment works has a capacity of 198 Ml/d, but treats an average of 160-165 Ml/d on a regular basis with little deviation either above or below this narrow band. Treated water is fed into the strategic Derwent Valley Aqueduct which subsequently feeds large areas of Derbyshire, Nottinghamshire and Leicestershire. However, the configuration of Severn Trent Water's strategic grid system means that water treated at Bamford can, in theory, be pumped into parts of Warwickshire and beyond.

The catchment area for the treatment works is predominantly peaty moorland which is used extensively for grazing purposes, and this is reflected in the raw water characteristics, as shown below. Heavy rainfall events are known to exacerbate colour difficulties with the raw water, with values in excess of 300°H being observed. Table 10-1 provides average raw water quality data for the period up to December 2000, whilst Figure 10-1 shows DOC and turbidity data for the period February to July 2006.

Raw water is treated at Bamford via coarse screening, pH correction, coagulation and flocculation, clarification, filtration and disinfection, as shown on the process schematic at Figure 10-2. Bamford WTW operates a rudimentary system of coagulation and hydraulic flocculation through a mixing chamber and single baffled channel. Ferric sulphate (12.5% w/w as iron solution) is dosed into a flash mixer where it is mixed into the main flow. The original intention was that mixing be induced via a submerged mixer. However, at the time of this investigation, no mixer was present. Consequently, for the purposes of this exercise, no mixing, other than that generated by the mixing of

the three inlets within the chamber, has been modelled (*i.e.* no mechanical mixing has been simulated so that the work provides an assessment of current operation). The impact of this is discussed below. The channel is 2.5m wide, 4.165m deep and approximately 50m in length. Vertical baffles are positioned at regular intervals along the length of the channel, causing the flow to move in an "up and over" serpentine manner. The work reported here focuses on the performance of the flocculation process.

Table 10-1: Raw Water Characteristics and Target Final Water Quality Standards for Bamford WTW.

Parameter	Units	Raw	Final Target	Operating Maximum
Average colour	°Hazen	60	2	
Average turbidity	NTU	1.3	3	
Average Iron (total)	µg/l	340	50	
Average Aluminium (total)	µg/l	200	50	
Average Manganese (total)	µg/l	40	20	
Total THMs	mg/l			40
Final chlorine residual	mg/l		0.6	0.8
pH			9	9.5

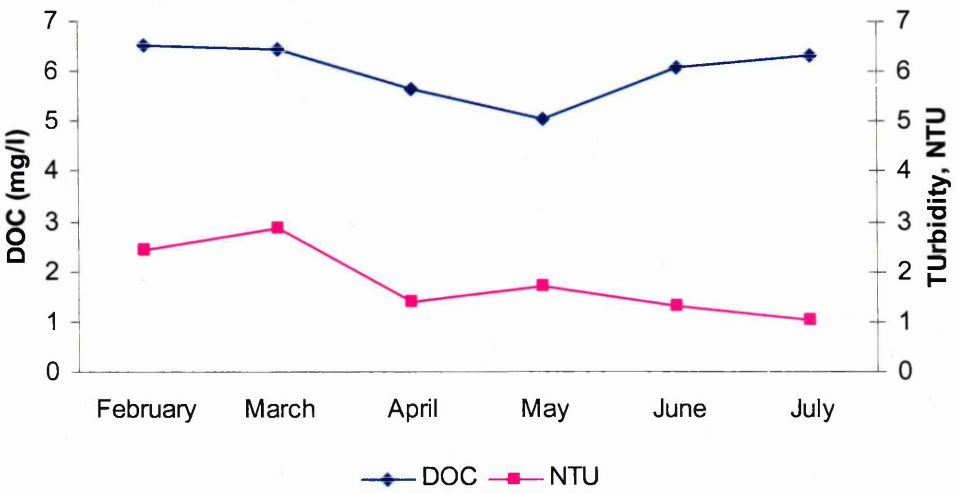


Figure 10-1: Bamford WTW raw water characteristics – February to July 2006.

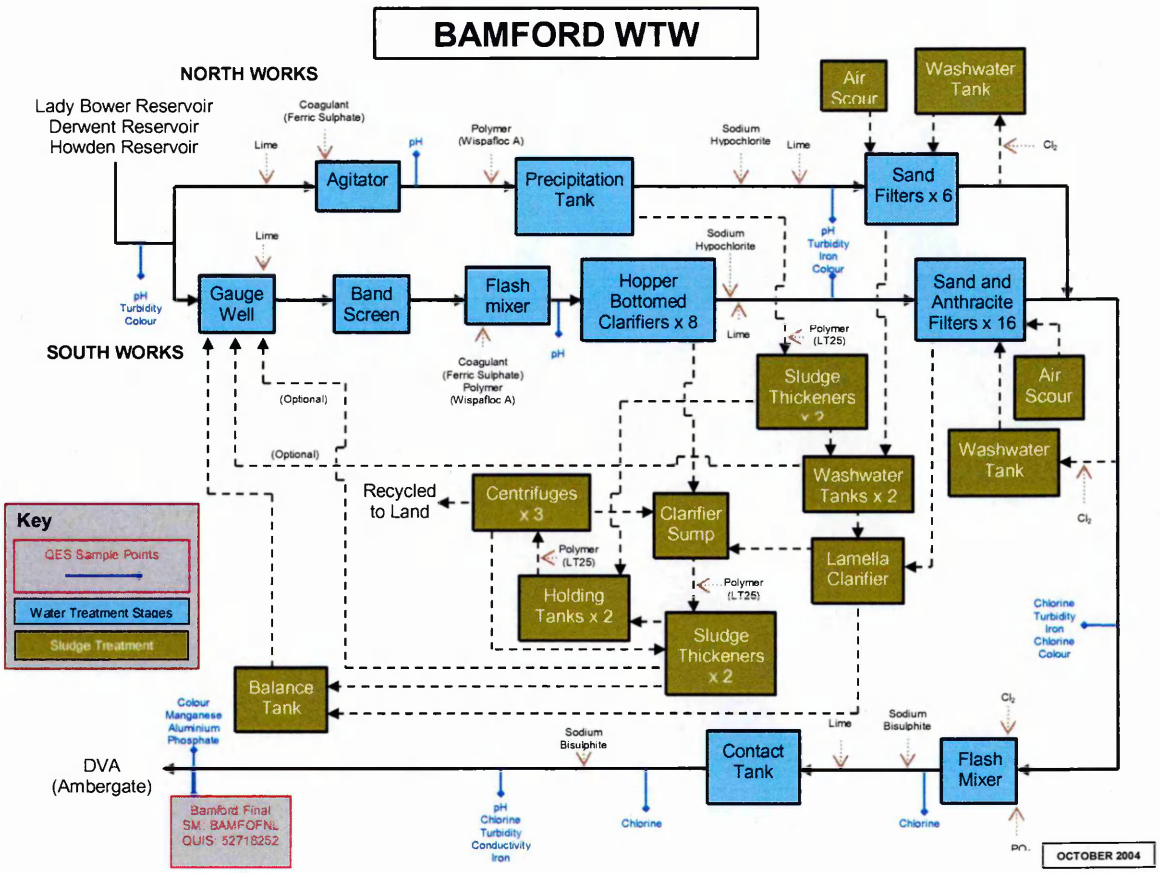


Figure 10-2: Bamford WTW Process Schematic.

10.3 Modelling Strategy and Validation

10.3.1 Grid Density

As with all other models produced as part of this work, the commercial software packages, Gambit and Fluent (Fluent Inc, Sheffield, UK) were used to generate the mesh and solve the equations of flow. The standard k-ϵ model was used to characterise turbulence within the flocculator. The decision to use the standard k-ϵ model was based on a study of previous work undertaken on similar structures, such as an hydraulic flocculator and several contact tanks and service reservoirs. (Haarhoff and van der Walt, 2001, Morrison, 1999, Yeung, 2001, Hannoun *et* al, 1997, Wang and Falconer, 1998), coupled with the fact that the flow would not follow a swirling path which would necessitate the use of a more rigorous approach such as the Reynolds Stress Model. As the works runs at average output for the majority of the time of the time, just one flow

rate was modelled; that being 160 Ml/d. Plan and isometric views of the flocculation channel (mesh removed) are shown at Figure 10-3.

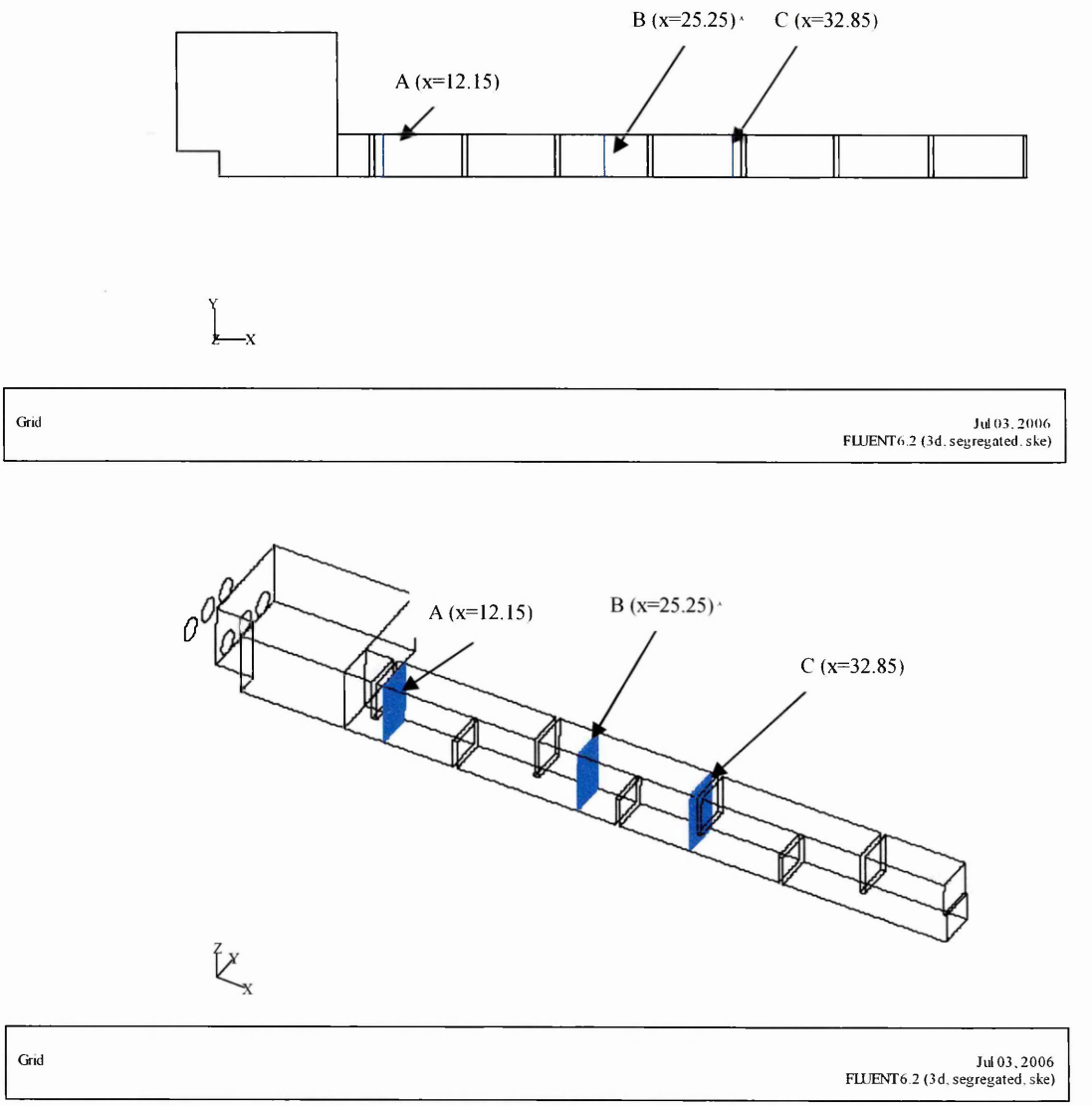
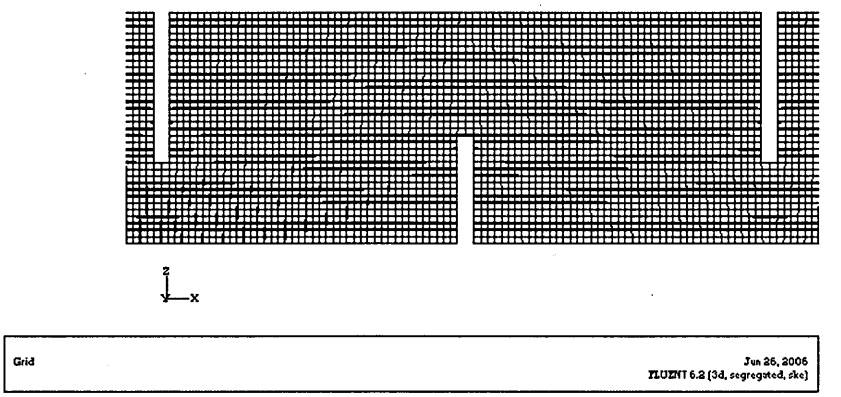


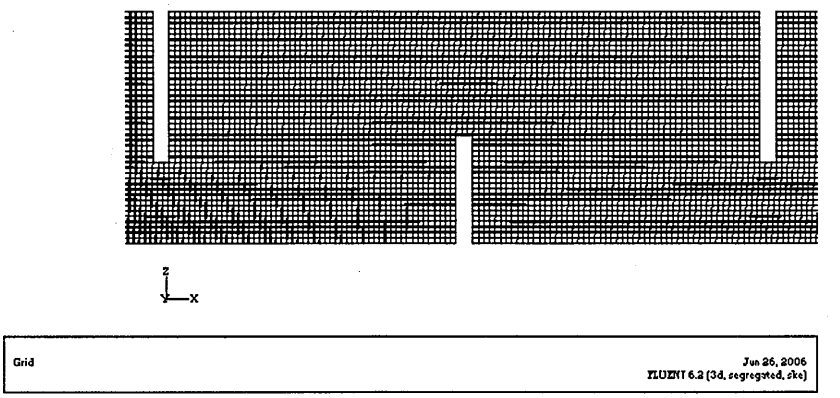
Figure 10-3: Plan and isometric views of flocculator channel (shaded areas indicate planes used for model validation).

Boundary conditions were established such that free slip conditions were specified at the top water level with no slip conditions specified at the walls. The standard (logarithmic) wall function was specified for the wall boundary layer profile, with constants as stated in Chapter 5.

Two grids were developed and a mesh density sensitivity analysis was undertaken. The first, coarse mesh comprised 395,328 cells, whilst the finer mesh comprised 776,187 cells. A cross-section through the two meshes between three consecutive baffles is shown at Figure 10-4. Using the high performance computer facility at Cranfield University, a converged solution was obtained for the coarser mesh in approximately six hours. The additional CPU time required for the finer mesh was approximately 100% at 12.25 hours. Velocity data were extracted from the two models and compared with measured data as part of the model validation exercise.



(a)



(b)

Figure 10-4: Cross-sections through two meshes (a) 395,328 cells, (b) 776,187 cells.

10.3.2 Model Validation

10.3.2.1 Velocity Data

Although access to the flocculation channel at Bamford WTW is not straightforward, the site did present an opportunity to undertake a degree of model validation which had not been possible or permissible at Frankley WTW. Model validation was achieved using the method described by Haarhoff and van der Walt (2001) in which an OTT turbine meter was suspended above the channel, velocity profiles obtained and compared to the CFD simulation results. However, Haarhoff and van der Walt selected only one location (the fourth turn) as representative of the whole flocculation channel and took profiles at various points at that turn. Haarhoff and van der Walt gave no justification for choosing that location as representative. For the purposes of this research, three locations were selected along the length of the channel and velocities measured at specified depths along the centreline of the channel and also 500mm from the channel walls. The velocity measurement locations are shown on Figure 10-3 as A, B and C. Velocity measurement was undertaken in a manner similar to that of Haarhoff and van der Walt. An OTT turbine meter was located in the flow (orientated perpendicular to the flow) and velocities measured at 500 mm depth intervals (giving nine readings for each profile). It became apparent from visual inspection of the flow that some degree of flow reversal was occurring in the channel. This presented a problem with regard to velocity measurement as the turbine meter was effectively insensitive to flow direction. Flow measurements were averaged over 60 second periods and repeated four times. From these, nine profiles of velocity were developed which were then used to compare with CFD results.

Profiles for three of the nine locations are shown at Figure 10-5. In each case it can be seen that there is satisfactory correlation between the measured and CFD data, to the extent that either set of model data could be considered to be representative of the actual flow in the channel. In absolute terms, there is little difference between the velocity data for the two models. At a distance of 0.5m from the channel walls, the data are

almost identical. Along the channel centreline, there is a discrepancy, but this is a maximum of just 0.03 ms^{-1} at approximately 0.7m depth.

Local velocity gradient data were calculated and extracted for each cell from the two models and plotted, on a cumulative percentage volume occupancy basis at Figure 10-6. It is clear from a visual inspection that there is very little difference in local velocity gradient distribution between the two models. Consequently, in view of the additional computational expense required by the finer mesh, and the lack of discrepancy between the two sets of model results, the coarser mesh was judged to be satisfactory for the further analyses and CFD exercise.

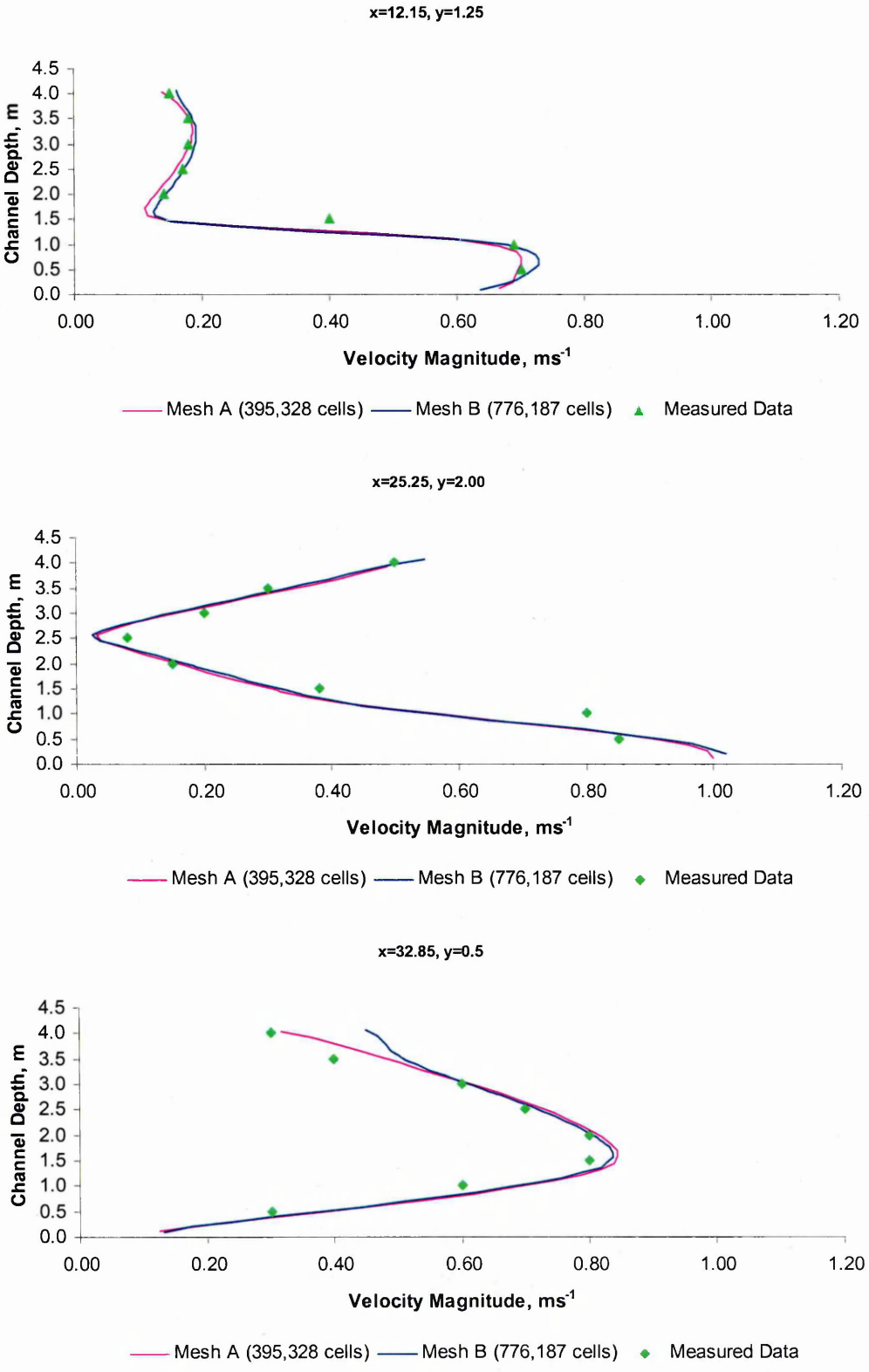


Figure 10-5: Comparison between measured and modelled velocity profile data.

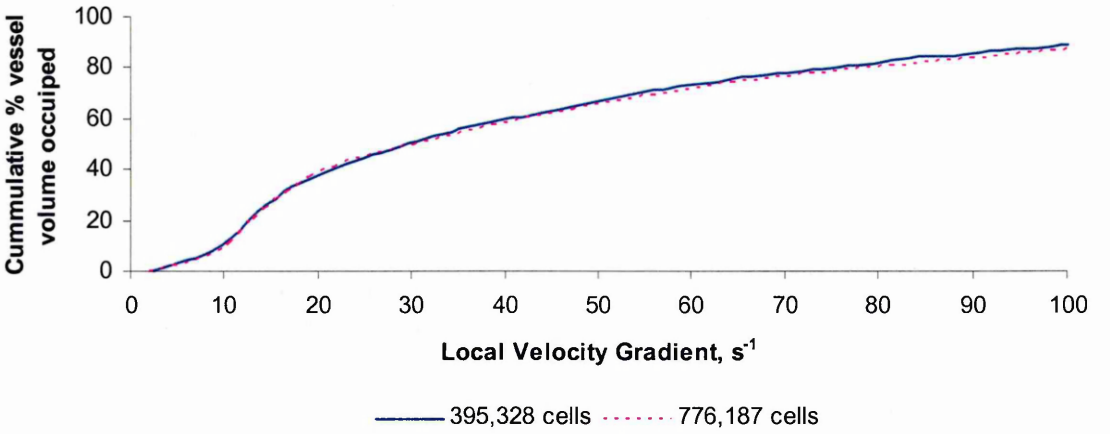


Figure 10-6: Local velocity gradient distribution – comparison between two grids.

10.3.2.2 Turbulence Data

The power dissipated across an hydraulic flocculator can be expressed as

$$P = Q\rho gh \qquad \textbf{Equation 10-1}$$

where Q is the flow rate and h is the headloss across the flocculator.

Measurements of top water level were taken between baffles so that the total headloss across the flocculator could be determined. With the works running at 160 Ml/d, a total headloss of 90mm was observed across the flocculation channel. Applying these values to Equation 10-1 yields a total power dissipation across the flocculator of 1,635W. The CFD model turbulence dissipation rate volume integral was derived and the total power dissipation calculated (according to Equation 5-4) as 1,574W. Thus, there is excellent agreement between the measured and modelled power dissipation giving confidence in the model output.

10.4 Results

10.4.1 Velocity Profiles

A plot of velocity vectors calculated on a vertical plane along the centreline of the channel is shown at Figure 10-7. Working from the left hand side of the plot, it is apparent that the flow at the surface strikes the baffle wall and is deflected vertically downwards. A significant proportion of the flow continues under the baffle wall and into the next cell. However, it is also clear that in each cell a recirculation loop is set up, with a proportion of the flow returning, at low speed along the top or bottom of the vessel. This recirculation flow pattern is observed in all flocculation cells of the channel.

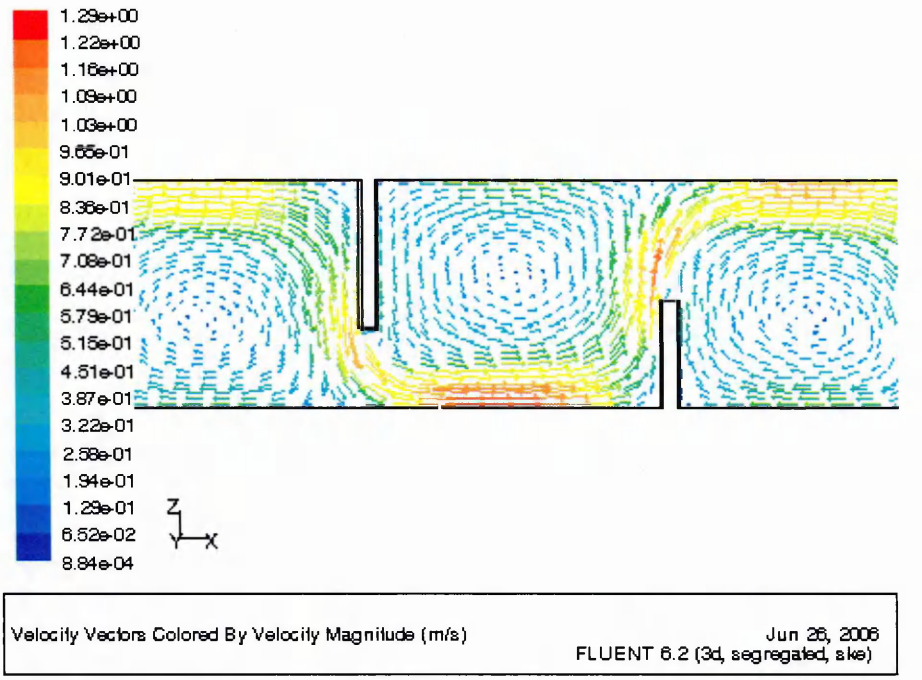


Figure 10-7: Velocity vectors along centreline of channel.

Contours of velocity magnitude are plotted at Figure 10-8. Dead areas are apparent within each cell, primarily located at the centres of the cells (*i.e.* at the centres of the recirculation zones), but also at the upper and lower corners. The maximum velocity calculated in the channel was 1.27 ms^{-1} at the edges of baffle walls, with areas of zero velocity also being evident. The variation of turbulent kinetic energy, relating to the

production of turbulence, is shown for a four baffle section of flocculator at Figure 10-9 It is noted that turbulence is generated as the fluid is guided around a bend. The variation of local velocity gradient (which, in effect, mirrors the variation in turbulence dissipation rate) is shown for the same four baffle section at Figure 10-10 Variations in the velocity gradient are significant, ranging from 2 to 400s^{-1}, implying that the use of a vessel average value would be unrepresentative of the actual values found.

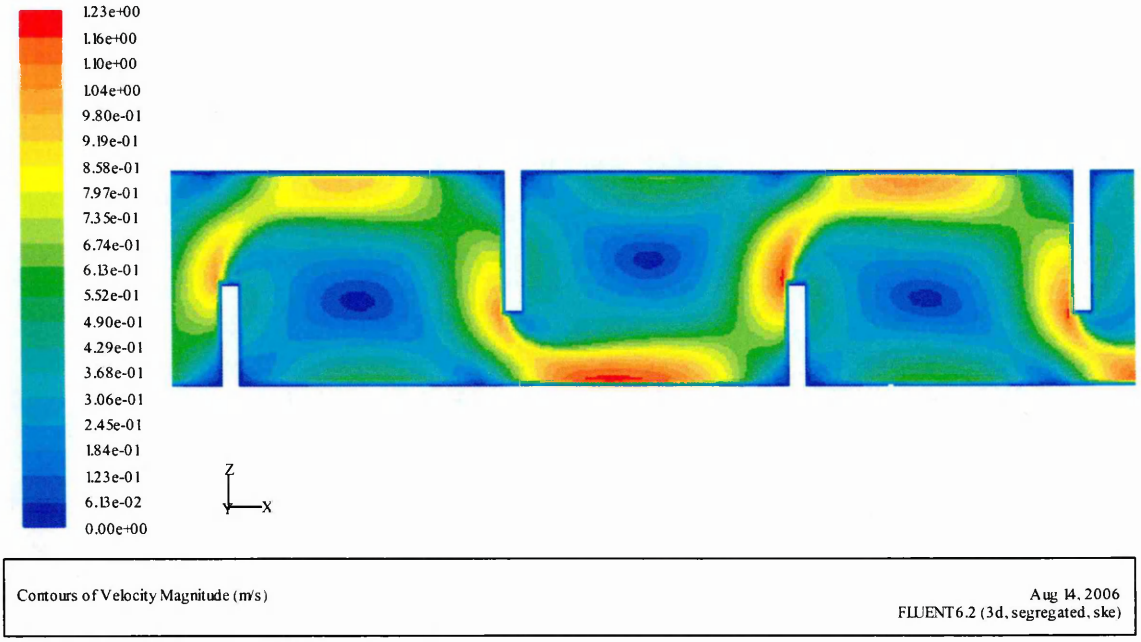


Figure 10-8: Contours of velocity magnitude.

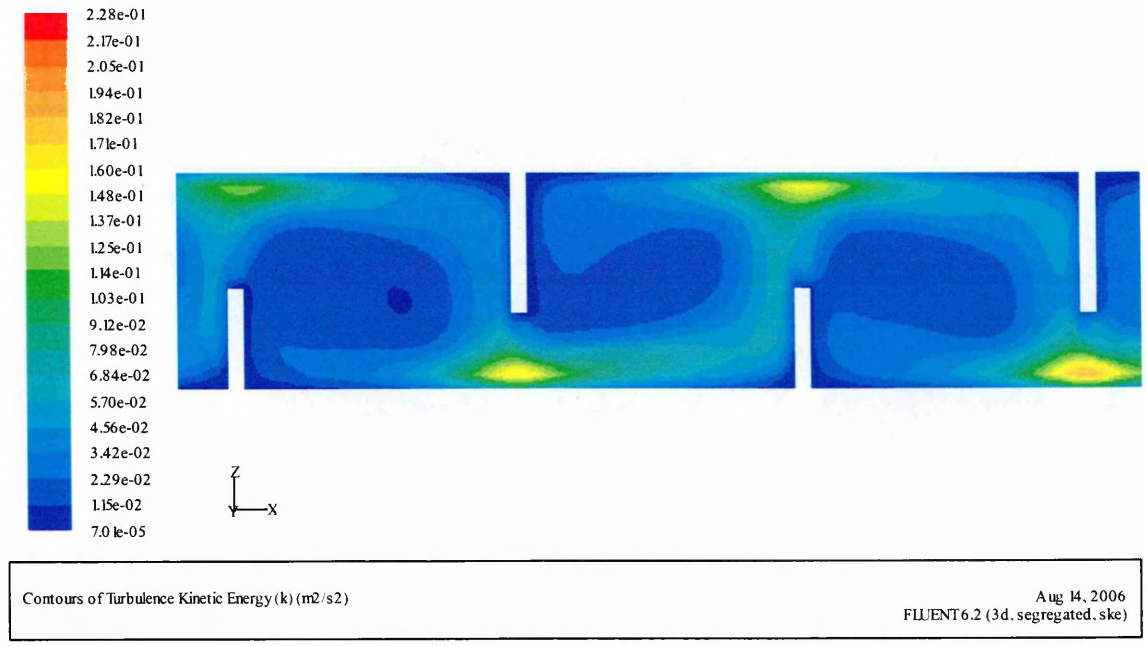


Figure 10-9: Contours of turbulent kinetic energy.

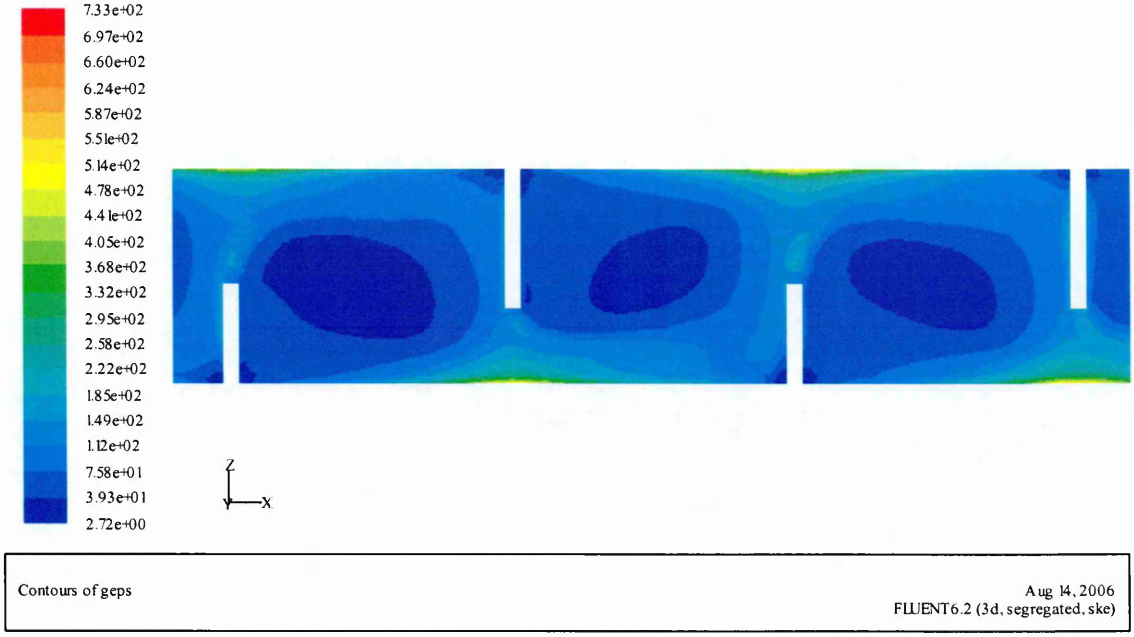


Figure 10-10: Contours of local velocity gradient.

10.4.2 Residence Time Distribution

A residence time distribution (RTD) analysis was undertaken using the coarser of the two meshes, developed in a manner similar to that adopted in the Frankley WTW flocculator study; *i.e.* the flow of a known volume of non-reactive tracer was simulated by linking a scalar equation to the momentum equations. The tracer curve is shown at Figure 10-11 and the normalised Exit Age Distribution curve is shown at Figure 10-12. Key data pertaining to the RTD analysis are given at Table 9-3.

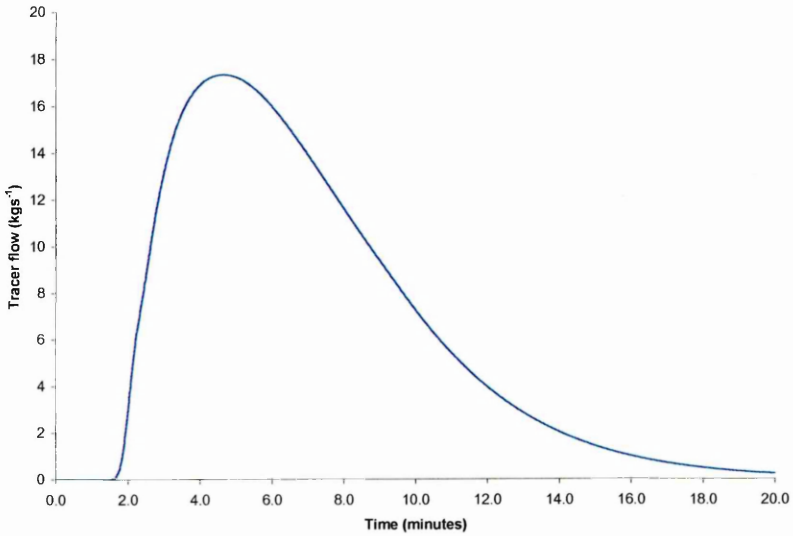


Figure 10-11: **Bamford WTW CFD flow tracer study – tracer curve.**

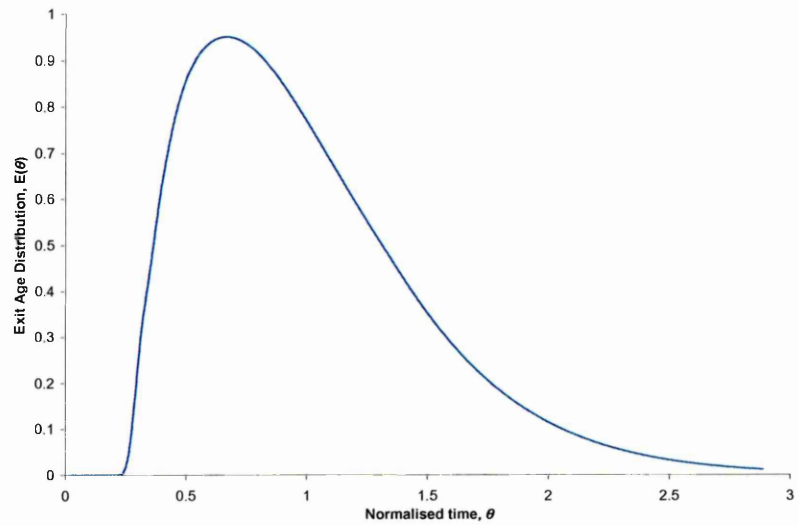


Figure 10-12: **Bamford WTW CFD flow tracer study - exit age distribution curve.**

Table 10-2: Bamford WTW Residence Time Distribution Results.

Flow Rate, Ml/d	Theoretical Ret'n Time, τ, mins	Mean Residence Time, $\bar{t}$, mins	t_{10}, mins	t_{50}, mins	t_{90}, mins	t_p, mins	$t_{10}/\bar{t}$	$t_{50}/\bar{t}$	$t_{90}/\bar{t}$	t_{50}/t_{10}	t_{90}/t_{10}
160.0	6.69	6.95	3.25	6.30	11.55	4.63	0.47	0.91	1.66	1.94	3.55

Table 10-3: Average turbulence dissipation rates and average and maximum values of local velocity gradient.

	Flow Rate, ML/d	$\epsilon \times 10^{-3}$, m^2s^{-3}	$\overline{G_L}$, s^{-1}	$G_{L\max}$, s^{-1}	$G_{L\max} / \overline{G_L}$
Flocculation channel & mixing chamber combined	**160.0**	4.11	45.7	734.9	16.1
Mixing chamber	**160.0**	0.270	14.6	152.2	10.4
Flocculation channel	**160.0**	7.24	71.1	734.9	10.3

10.4.3 Average and Local Velocity Gradients

For a flocculation system of this type, Armitharajah *et al.* (1991) stated that the vessel average velocity gradient be calculated on the basis of power applied as:

$$G = \sqrt{\frac{\rho g h}{\mu t}} \qquad \textbf{Equation 10-2}$$

where, h = headloss across the flocculator

t = retention time

With the works running at 160 Ml/d, top water levels were recorded within each flocculation cell and a total headloss of 90mm observed across the flocculation channel. Using the theoretical retention time, τ, the average velocity gradient was calculated for the flocculation channel and mixing chamber combined and for the flocculation channel alone. These data are compared with the average of the local velocity gradient values in each cell of the CFD model and are given below at Table 10-4.

Table 10-4: Average velocity gradient.

	Flow Rate, ML/d	$\overline{G_{ave}}\ s^{-1}$	Design *G.t*	$\overline{G_L}\ , s^{-1}$ *(CFD)*
Flocculation channel & mixing chamber combined	**160.0**	46.6	18,705	45.7
Flocculation channel	**160.0**	62.7	13,882	71.1

Excellent agreement is observed between the vessel average velocity gradient calculated on the basis of overall head loss and the average local velocity gradient value calculated using CFD. Furthermore, the G values found in Table 10-4 are within the recommended range as shown at Table 9-5. However, the design $G.t$ values are low compared to recommended values and this is discussed in Section 11 below.

A histogram showing the volumetric distribution of the local velocity gradients within the channel at a flow rate of 160 Ml/d is shown at Figure 10-13. In common with the Frankley flocculator, there is only a small percentage of the overall channel volume where the local velocity gradient exceeds $100s^{-1}$. The same data are shown in a cumulative manner at Figure 10-14 and this shows that some 82% of the channel has a

local velocity gradient of $100s^{-1}$ or less. The cumulative local velocity gradient distribution curves for Frankley WTW flocculator at three mixing speeds are also plotted at Figure 10-14. Comparison of the Bamford curve with the three Frankley curves is interesting. At low (*i.e.* less than $15s^{-1}$) velocity gradient values, the Bamford velocity gradient distribution is approximately midway between the Frankley 1.6 and 2.4 rpm scenarios. However, beyond $15s^{-1}$, the rate of change of volume decreases, indicating that a greater volume of higher local velocity gradient values are found within the channel. For example, at Bamford, 47% of the channel has a local velocity gradient of $26s^{-1}$ or below and the corresponding figure for Frankley (2.4 rpm) is 49%. However, at Bamford, 73% of the channel has a local velocity gradient of $61s^{-1}$ or below and the corresponding figure for Frankley (3.2 rpm) is 59%. Like Frankley, it is apparent that the vast majority of the velocity gradient values within the Bamford flocculation channel are at or below the three postulated breakage thresholds.

Both Van der Walt (2002) and Haarrhoff and Van der Walt (2001) chose to consider the local velocity gradient using the 95th percentile of the normalised G_L value distribution (*i.e.* $\overline{G}_{95} = \frac{G_{95}}{\overline{G}}$). The authors considered that values in excess of $\overline{G}_{95}$ would give rise to floc breakage. However, this standard appears to be completely arbitrary and not based on any fact or observation. In fact, no justification is given for the selection of this value. In the case of the Bamford flocculator, the 95th percentile value is $169s^{-1}$, a value which is almost four times the vessel average ($47.5\ s^{-1}$), more than double that found in the flocculation channel ($71.1s^{-1}$), and in excess of the NOM breakage threshold ($150s^{-1}$). It is believed that the threshold value approach developed in Chapter 8 of this thesis offers a far more robust approach to the assessment of flocculator hydrodynamics and its impact on floc formation, growth and breakage.

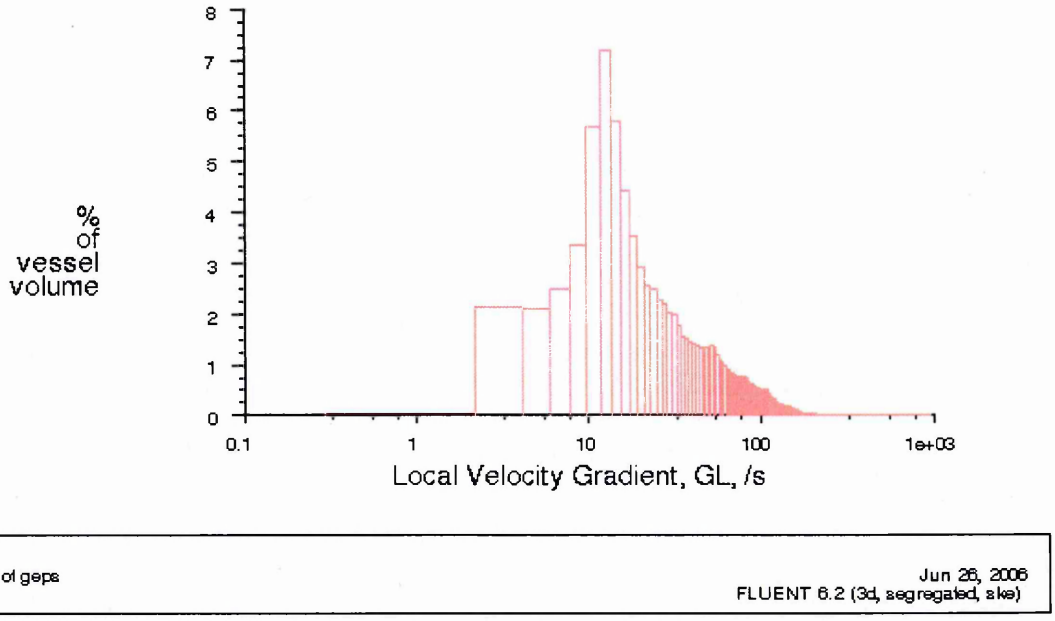


Figure 10-13: Histogram of local velocity gradient distribution throughout flocculation channel and upstream mixing chamber.

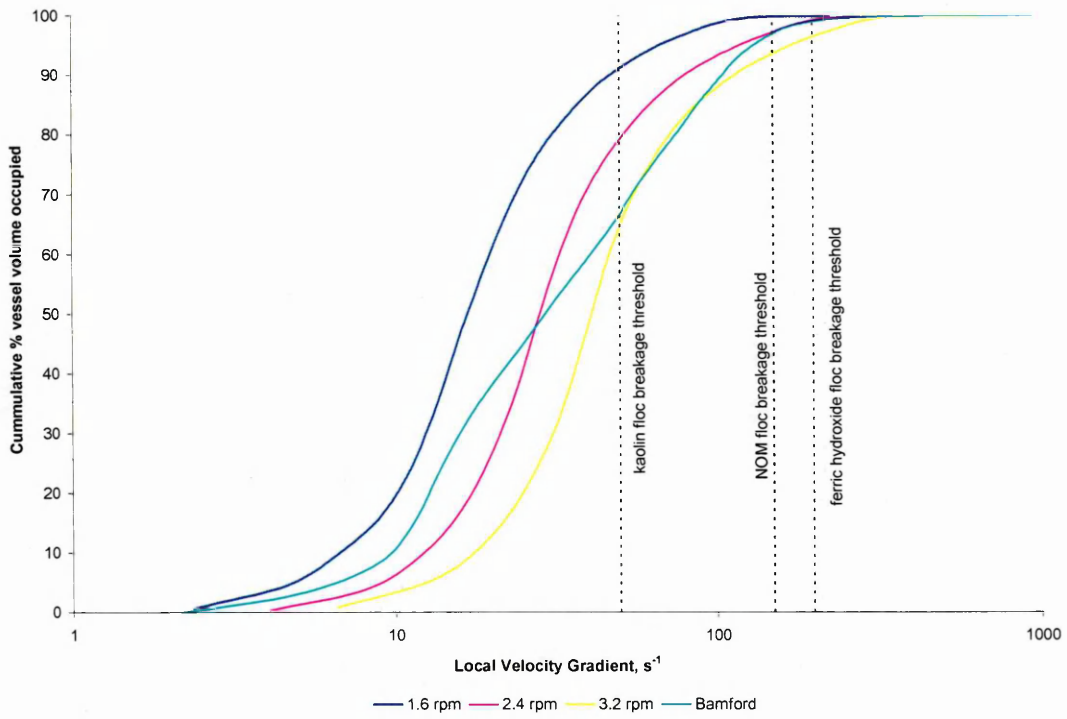


Figure 10-14: Cumulative distribution of local velocity gradient for Bamford WTW and Frankley WTW at different mixing speeds.

Average and maximum local velocity gradient values for both the mixing chamber and flocculation channel are shown at Table 10-3. These data are very interesting as they

show the impact of the removal of mechanical mixing from the mixing chamber. It is clear that the turbulence dissipation rates and hydraulic gradient values are less in the mixing chamber than in the flocculation channel. Obviously, this would not occur if the original flash mixer was still installed in the channel. The CFD data for Bamford indicate that the mixing chamber generates G_L values with an average of just $15s^{-1}$. Standard texts suggest that coagulation is best undertaken at velocity gradients of $300s^{-1}$ to $1{,}000s^{-1}$ for between 30 seconds and two minutes, although G_L values for static mixers will be significantly higher with reduced time of exposure (Amirtharajah *et al.*, 1991). Effective coagulation requires the dispersion of the coagulant within a few seconds in order that the particles are destabilised. Therefore, it is clear that this current mode of operation is not generating velocity gradient values of a sufficient magnitude to effect adequate coagulation. This inadequacy in the process will have a consequential impact on the flocculation process. Indeed, it is likely that much of the mixing one would expect to find in the mixing chamber is actually taking place in the flocculation channel itself.

It is also necessary to consider the length of time the water spends in the mixing chamber and flocculation channel. The combined theoretical retention time is 6.69 minutes (Table 10-2 refers) and the calculated mean residence time from the CFD model is close to this at 6.95 minutes. The theoretical retention time in the mixing chamber is 3.00 minutes and 3.69 minutes in the flocculation channel. Referring back to the laboratory work of Jarvis *et al.* (2004) which used a similar upland water; the authors simulated coagulation for 30 seconds by mixing in the jar tester at 200 rpm, and then simulated flocculation by mixing in the jar tester at 200 rpm for 10 minutes. The results of Jarvis *et al.* (2004), as reported in Chapter 8 show that no particles were formed for the first two minutes, and then there was steady growth in floc size to a maximum. The time taken to develop the maximum floc size was a function of raw water type and coagulant. However, in the case of the raw upland water (Figure 8-1 (c)), the time taken was approximately 10 minutes. Using the jar test apparatus, Fearing (2004) showed a strong relationship between pH and coagulation / flocculation time and flocculation index (FI, used as a surrogate for floc size), with higher pH (up to 6.3) shortening the time before an increase in size was observed. Even at the highest pH

values, the time taken for flocs to show an increase was approximately 200 seconds (*i.e.* more than three minutes). It would appear, therefore, that the hydrodynamic environments induced in the mixing chamber and flocculation channel are inadequate for both coagulation and flocculation purposes. Neither the necessary energy for coagulation nor time for flocculation are applied to allow either process to be performed adequately.

10.5 Financial Implications

It is interesting to note that the site uses a starch-based flocculant aid to encourage the development of stronger flocs, giving rise to enhanced settlement and filtration. It is possible that the need for this flocculant aid is necessitated by the inadequate basic coagulation and flocculation facilities. Data provided by Severn Trent Water indicates that the flocculant aid costs £1.36 / kg. Exact dose rates were not available from the Works Manager, but in the past it is known that they have been as high as 1.5 mg/l. The table below shows the range of costs incurred by the Company in dosing the flocculant aid at several different dose rates. The flow rate remains constant at 160 Ml/d throughout.

Table 10-5: Impact on operating budget of varying flocculant aid dose.

Dose Rate, mg/l	£ per annum
0.1	7,942
0.5	39,712
1.0	79,424
1.5	119,136
2.0	158,848

The impact of high dose rates of flocculant aid is immediately apparent, as are the savings to be made if the dose rate can be reduced from, say, 1.5 mg/l to 0.5 mg/l. For example, adopting a 5% discount rate over a 20 year period, the net present value of dosing at 1.5 mg/l is £1,484,698. The corresponding figure for dosing at 0.1 mg/l is £98,980. In the short term, coagulation could be improved via the reinstatement of the flash mixer in the mixing chamber. However, adequate flocculation time cannot be provided without a complete redesign or replacement of the flocculation channel. Such

replacement would be extremely capital-intensive. Previous work undertaken by the Consulting Engineer Binnie, Black and Veatch (BBV), 2001, suggested that reconstruction of the inlet works at Bamford WTW, including the replacement of the existing flocculation channel and replacement with two mechanically-mixed flocculation would cost £577,000 (at 2001 price base date) with no impact (either positive or negative) on operating costs. Clearly, if modifications to the coagulation and flocculation stages will incur capital costs with no positive impact on operating budget, then the need has to be questioned, unless it can be shown that downstream processes, such as filtration are suffering as a result of the poor performance (and the impact of this performance measured in either or both financial and treated water quality terms). However, if the mixing arrangements were to be improved and the retention time increased, it is hard to understand how chemical usage would not be reduced on the works. At this stage it is not possible to quantify the extent of savings to be made, and it is assumed that this is why BBV chose not to attempt any quantification of savings to be made. Nevertheless, Chapter 1 of this thesis discussed the importance of mixing in water and waste water treatment. This simple financial analysis of a live situation bears out the importance of the role of mixing.

10.6 Summary

CFD analysis of the hydraulic flocculator at Bamford WTW has enabled the author to develop a greater understanding of the hydrodynamic regime which exists in the flocculation channel at average flow. The raw water treated has similar characteristics to the raw water treated at Frankley WTW and also to the water used by Jarvis *et al.* (2004) in their jar test experiments. Thus, this section of work has enabled the author to compare the performance of an hydraulic flocculator with a mechanically mixed one, when treating similar types of water.

Two meshes were developed for the CFD simulations; the finer of the two having 776,187 cells, and the other having 395,328 cells. The standard k-ϵ turbulence model

was used for all model runs as previous work on serpentine tanks had yielded positive results using this model and anisotropic turbulent flow conditions were not anticipated.

Mesh sensitivity analyses were undertaken using both velocity and local velocity gradient data. Velocity data from both grids were compared with velocity data measured in the channel using a turbine meter. Good correlation was observed between the measured and both sets of numerically-derived data. Good agreement was also observed between power derived from headloss across the flocculator and the value obtained from the CFD model. Little discernible differences were noticed between the two sets of CFD data. The finer of the two meshes incurred double the amount of CPU time to derive a converged solution. Considering the degree of uniformity between the results of the two models, the coarser of the two was selected for further use.

Inspection of velocity data extracted from the CFD model showed the development of a flow recirculation loop between each baffle. Maximum velocities were noted at the edges of the baffles, with dead spots at the centre of each recirculation loop and also at the corners of each compartment.

A residence time distribution analysis was undertaken on the flocculation channel at an average flow rate of 160 Ml/d. The mean retention time was found to be close to the theoretical hydraulic retention time (6.95 minutes and 6.69 minutes respectively). The times for 10, 50 and 90% of tracer to pass through the vessel were calculated as 47%, 91% and 166% of the mean residence time.

Similar to the results arising from the Frankley flocculator CFD analysis, a comparison of the average velocity gradient calculated on the basis of head loss across the flocculator and the equivalent value calculated as the average of individual velocity gradients within each cell yielded consistent results. The distribution of local velocity gradients within the Bamford flocculation showed that the magnitude of these gradients is generally less than that found in the jar tester at all but the lowest mixing speed. At first sight, it might be considered that the very low velocity gradient values found throughout the channel would minimise floc breakage. However, inspection of the

velocity gradient values in the mixing chamber and the flocculation channel indicate that insufficient energy is imparted into the water for adequate coagulation of flocculation to occur. Indeed, in the absence of any mechanical mixing device in the mixing chamber, the velocity gradients are of a lower magnitude in the mixing chamber than in the flocculation channel. In addition, the time allowed for coagulation and flocculation is unlikely to be sufficient to generate an optimum size floc. Using a similar raw water and coagulant dose, Jarvis *et al.* (2004) found that approximately eight minutes flocculation (mixing at 30 rpm in a jar tester) was required to achieve a maximum floc size. Fearing (2004) found that floc formation was pH dependent, but that even at the fast-reacting high pH values, no significant floc development was noticed within the first 3.5 minutes of flocculation. The CFD model results show that at Bamford, there is just 6.95 minutes retention in the combined coagulation and flocculation vessels, of which just 3.95 minutes is spent in the flocculation channel. It is clear that such time will be insufficient to generate a maximum floc size. Flocculation performance is enhanced at Bamford via the addition of a starch-based flocculant aid. High doses of this flocculant aid have been required at the works historically. A financial analysis has demonstrated the positive effects that adequate coagulation and flocculation would have on the works operational budget, with the potential to realise savings in excess of £110,000 per annum in flocculant aid alone. However, this saving would need to be balanced against the capital cost of improved coagulation and flocculation.

Previous CFD analyses of an hydraulic flocculator (Haarhoff & Van der Walt, 2001) used the 95 percentile G_L value to characterise floc breakage. The work undertaken here has shown that approach to be unrepresentative of the actual floc breakage thresholds found for a similar water in the jar tester. The validity of the G_{95} value is therefore questioned.

CPU usage for this analysis was significantly less than that required for the mechanically mixed flocculator at Frankley; this being a result of the absence of rotation in the solution. It is clear that modelling an hydraulic flocculator is much more

within the reach of commercial organisations than a more complex mechanical installation.

11 Discussion

11.1 Introduction

An experimental investigation into the flow fields generated by two different jar test configurations has been undertaken using Laser Doppler Anemometry (LDA) and Particle Image Velocimetry (PIV). Subsequently, the same scenarios have been modelled using a variety of CFD techniques, including single and dual phase modelling, steady and unsteady flow and residence time distributions. These analyses have facilitated further insights into the hydrodynamic environments which exist within the two configurations at different mixing speeds. The numerical data have been compared with laboratory-derived data, from which a greater, in-depth understanding of the hydraulics dictating floc breakage and formation has been developed.

CFD models have been constructed of two full scale flocculation installations. The model results have been used to assess the hydraulic performance of the flocculators and also to assess the degree of turbulence developed under various operating regimes. Results and conclusions from the jar test modelling work have been applied to those scenarios, from which knowledge of flocculation performance has been developed further.

The following discussion focuses initially on the development and application of a robust modelling strategy for characterising swirling flow found in a jar test apparatus. This included consideration of the mesh density, turbulence model selection and physical treatment of the rotating flow. Thereafter, the practical implications of the main findings and outcomes of the experimental and modelling work presented in this thesis are discussed. These findings are summarised as:

- Used carefully, CFD can be used effectively to model, and characterise the flow fields generated in, laboratory and full scale flocculators. However, for certain

large scale, complex applications, the cost to industry could ultimately prove to be prohibitive.

- Using data derived from the modelling studies, floc growth and breakage can be quantified in terms of exposure to local velocity gradients.
- Laboratory and numerical jar test data can be used in combination to develop guidelines for the design of full scale mechanical and hydraulic flocculators.

11.2 Flow Visualisation

LDA and PIV techniques have been applied to the cylindrical and Hudson jar test vessels respectively. Both techniques are used extensively in academic mixing studies (*e.g.* Armenante, 1997, Baldi *et al.*, 2004, Bhattacharya & Kresta, 2002, Ducoste & Clark, 1998a & b, Jaworski & Zakrzewska, 2002), but have been applied to the jar test apparatus to only a limited degree (Buoyer *et al.,* 2001 & 2005, Korpijarvi *et al.*, 1999 & 2000, No Suk Park, 2003). Both techniques yield data which is used to describe the hydrodynamic environments generated. However, as the PIV technique develops a 2D representation of a cross-section of the flow field, a significant volume of data is generated. In this study of just one vessel mixing at six speeds, more than 15GB of data were generated. Such a volume of data is unwieldy at best. However, using this data, it was possible to produce accurate figures of the 2D flow field; something which was not possible using LDA. It is unfortunate that previous authors have not disclosed the size of data sets and the extent of computing power required to analyse these data. The work reported here suggests that it is only heavily computer-intensive environments (such as those found in academia) which are able to provide the facilities and space to manage cumbersome datasets.

Although the LDA data does not describe the complete flow field, it is very useful for assessing the nature of flow within the vessels and has been used to good effect both here and in previous studies (*e.g.* Korpijarvi *et al.*, 1999 & 2000). The data produced are much smaller in size and hence easier to manipulate than PIV-produced data. It is

also straightforward to use LDA data to validate CFD models in a quantitative as well as qualitative manner.

As described in Chapter 4, LDA analysis yields a single point time series measurement of one, two or three velocity components (the third being inferred), depending on system configuration. From these data, mean and RMS velocities can be extracted, together with spectral information and, in the case of two-component measurements, Reynolds stresses. LDA measurements are used extensively for the validation of CFD models, with velocity measurements often being compared directly with LDA data, as has been done in this work. Mean velocity components can be used to validate circulation patterns (Figure 4-9, Figure 4-11, Figure 4-13 and Figure 4-14 refer). In addition, if available, the RMS velocity components can be combined for comparison with the modelled turbulent kinetic energy, k. It is apparent from the literature that many, if not most, workers in this area have used axial and tangential velocity profiles (absolute and scaled) to validate their CFD models. Examples of this include Bhattacharya and Kresta (2002), Decker & Sommerfeld (1996) and Oshinowo & Bakker (2002). Some others have used velocity profile data in conjunction with calculations of Power number and Pumping Number to validate models (*e.g.* Montante & Magelli, 2005, and Essemiani and de Traversay (2002a). Jaworski & Zakrzewska (2002) considered velocity profile data for CFD model validation, but also extended their analyses to include axial profiles of turbulent kinetic energy, k, calculated as $k = \frac{1.5}{2}(u_\theta'^2 + u_z'^2)$ where it was assumed that the third energy component was equal to the mean value of the two measured components (tangential and axial).

The literature also shows that LDA has been used to characterise turbulence dissipation in the impeller region of mixing vessels. Adopted approaches range from the use of dimensionally-based relationships, founded on isotropic turbulence assumptions, of the form $\varepsilon = \frac{A.u^3}{L}$ (Zhou & Kresta, 1996), to the use of 4 channel LDA to measure Reynolds stress gradients (Baldi *et al.*, 2004), and this is still an area of active research.

In this work, it was only the ensemble-averaged axial and tangential velocity data which were obtained. With hindsight, this was a limitation, as it precluded the development of turbulent kinetic energy profiles, similar to those produced by Jaworski & Zakrzewska (2002). The direct measurement of velocity gradients, as undertaken by Baldi *et al.* (2004) was not possible due to resource and financial limitations. Nevertheless, using the ensemble-averaged data, it was possible to provide satisfactory evidence of velocity component validation for the cylindrical jar test models. Furthermore, satisfactory turbulence validation was inferred from consideration of the overall power dissipation, derived experimentally from torque measurements and computationally from numerical integration of the turbulence energy dissipation rate over the complete vessel volume.

Both LDA and PIV measurements are costly to undertake. The capital cost of equipment can be up to £100,000 and owners are understandably keen to recoup a proportion of that investment via high rental and subcontract charges. Indeed, LDA measurements on the Hudson vessel were not possible for this research as a direct consequence of cost. It is considered likely that these high costs will preclude the general use of these visual flow measurement techniques within the water industry for any purpose other than specialised research.

11.3 Jar Test CFD Modelling Strategy

CFD has been used to model successfully the hydrodynamics of mechanically mixed systems used in water treatment processes at different scales. However, the work has demonstrated that care must be exercised in the selection of modelling strategy.

Different modelling strategies, each with varying degrees of computational complexity and expense are available for modelling mixing systems. However, much of the small scale mixing work found in the literature and, in particular, that related to the jar tester, does not consider the modelling strategy in any detail (Korpijarvi *et al.*, 1999, 2000, Essemiani & de Traversay, 2002a & b); the primary exceptions to this being Armenante *et al.*, 1997 and Jaworski & Zakrzewska, 2002. Table 11-1 compares approaches found

in the literature with those used in this work. It is clear that this work has examined alternative modelling strategies to a greater degree than other work.

The modelling philosophy adopted should be appropriate to the system and governed by the needs of the modeller. It is intuitively obvious that the greater the degree of detail and resolution required, the more demanding the strategy and methodology must become. The purpose of the jar test modelling work undertaken here was to consider and develop an appreciation of the magnitude of shear zones and turbulent effects within the system. When considering the treatment of rotating flow fields in that context, the computational expense of the sliding mesh technique was found not to be necessary. Whilst the sliding mesh technique may produce a more accurate representation of the velocity components of the flow, there was little improvement in the accuracy of turbulence characteristics and the results produced by the simpler Multiple Reference Frames (MRF) technique were quantitatively similar and adequate for the purpose. This was sufficient to develop an understanding of the magnitude of velocity gradients to which a particle (floc) may be subjected within the vessel. Where the sliding mesh technique is required, (*e.g.* for unsteady simulations, or situations where impeller / baffle interactions are significant), the complexities in modelling justify the need for high performance computing and preclude the use of modest computing hardware for all but the most straightforward applications. This is significant as, in the author's opinion, it will tend to preclude the widespread use of CFD in the water industry, forcing the industry to make use of specialist consultants or the academic sector, or to forgo the potential benefits offered by CFD. (This observation is developed further in 11.7 below).

The models developed to study the laboratory and full scale flocculators have provided a framework within which to investigate the complex hydrodynamic environments generated therein. Due to a combination of a lack of uptake of CFD in the water industry and the complexity of the scenarios, there has been little previous published work in this field.

Using LDA experimental data in conjunction with CFD analysis, and also by comparing experimental and numerical energy dissipation values, it has been shown that, for highly swirling flows (such as those found in a cylindrical jar tester) the standard k-ε turbulence model can yield turbulence dissipation results which are erroneous by an order of magnitude. This is of great concern as some of the limited published data which exists used the standard k-ε model in this laboratory scale situation (Korpijarvi *et al.*, 1999 & 2000, Jaworski and Zakrzewska, 2002) and also at pilot scale (Essemiani and de Traversay, 2002). The results presented here have demonstrated that the standard k-ε model is, in fact, wholly inappropriate for the cylindrical vessel.

When using a high performance computing facility to model the jar tester, the additional computational expense required by the more rigorous anisotropic Reynolds Stress Model (RSM) was easily accommodated. It is noteworthy that the realizable k-ε model was found to produce reasonable results in this situation, despite the fact that its use with the multiple reference frames approach is not recommended (Fluent 2005). The other turbulence models considered (RNG k-ε, k-ω and SST k-ω) performed less well, and it is interesting to note that no previous published work exists which used the ω-based turbulence models in similar scenarios. However, Jones (1999) used the k-ω model for mixing within a static mixer. These observations underline the fact that no single turbulence model is specifically appropriate for a particular scenario, and that care must always be taken in turbulence model selection. However, where time and computing facilities permit, use of the RSM is recommended.

Using the RSM in conjunction with the MRF technique, the numerically-derived velocity components and power dissipation agreed well with experimental results for both the Hudson and cylindrical vessels when mixed at high speeds. Power dissipation agreement was less good at the lower mixing speeds, where the flow was not fully turbulent. In this work, the minimum discrepancy between modelled and experimental data was just 7% for the Hudson vessel when comparing values obtained at a mixing speed of 100 rpm. This rose to 70% at the lowest mixing speed (30 rpm). However, at this speed, power dissipation was extremely small, and so any differences between figures measured on a percentage basis are likely to be large. Previous workers (*e.g.*

Ciofalo *et al.*, 1996, Armenante *et al.*, 1997 and Essemiani and de Traversay 2002a) have reported varying degrees of success in obtaining agreement between numerical and experimental power dissipation values, with Armenante *et al.* finding differences of between 45.3% and 71.1% (depending on turbulence model selection) and Essemiani and de Traversay closing the difference to 10%. In this work, at the highest mixing speeds, the differences range from 7% for the Hudson vessel at 100 rpm (which is an excellent correlation) to 30% at the same mixing speed for the cylindrical vessel. Whilst not perfect, these data are certainly within the range of values obtained by others working in the field, and serve to show the current limitations of turbulence modelling, particularly with regard to highly swirling flow.

Table 11-1: Comparison of modelling approaches for small scale, mechanically mixed scenarios.

Reference	Configuration	Moving Mesh Treatment	Flow Regime	Turbulence Model
Armenante *et al.*, 1997	PBT in cylindrical vessel	3D, LDV experimental values,	Turbulent	Standard k-ϵ, RSM
Bakker *et al.*, 2000	PBT in cylindrical vessel	3D, SM	Laminar	LRN k-ϵ
Daskopoulos & Harris, 1996	Rushton turbine & PBT	LDV experimental values, SM, MRF	Turbulent	Standard k-ϵ, RNG k-ϵ, RSM
Ducoste & Clark, 1999	Rushton turbine & Lightnin A310 in square vessels	LDV experimental values	Turbulent	Standard k-ϵ
Essemiani & de Traversay, 2002a & b	Mixel TT axial impeller in rectangular vessel	3D, MRF	Turbulent	Standard k-ϵ
Jaworski & Zakrzewska, 2002.	PBT in cylindrical vessel	3D, MRF	Turbulent	Standard k-ϵ, RNG k-ϵ, Realizable k-ϵ, RSM
Kee & Tan, 2002	Lightnin R100 (6 blade turbine) & Lightnin A310 (3 blade propeller) in cylindrical vessel	2D	Turbulent	Standard k-ϵ
Korpijarvi *et al.*, 1999 & 2000	Kemira Kemwater mini-flocculator in cylindrical vessel	3D, SM	Turbulent	Standard k-ϵ, RNG k-ϵ, RSM
This work	2 blade paddle, cylindrical & Hudson vessels	3D, MRF & SM	Transitional & turbulent	Standard k-ϵ, Realizable k-ϵ, RNG k-ϵ Standard k-ω, SST k-ω, RSM

11.4 Hydrodynamics of the Jar Test Apparatus

One of the principal requirements of the jar test modelling work was to gain further understanding of floc strength through response to shear. Stanley and Smith (1995) had recognised this need, stating that "there is a need for better understanding of the effects of local hydrodynamics on floc characteristics and process performance...". There are extensive published data drawing conclusions about floc formation and breakage; much of which is based on different test configurations (Jarvis *et al.*, 2005a and Gregory, 2004 both provide useful summaries of this work). However, the experimental and numerical work undertaken here indicate that the hydrodynamics of jar test vessels will change significantly depending on the test configuration and, in particular, the size and shape of vessel. Experimentally-derived power draw figures were developed as part of the work reported in this thesis and these have facilitated the calculation of vessel average velocity gradient, $\overline{G}$, values for two different jar test configurations using the same impeller and mixing speeds. Whilst the average Power number, P_o, for the cylindrical vessel in the turbulent zone was 0.46, for the Hudson vessel the corresponding value rose to 2.31, thus demonstrating the additional power required to motivate the water when it is retarded by the flat walls which provide a baffling effect. Nevertheless, both values are less than recorded values for other impellers. Bates (1963) gave the Power number of a Rushton Turbine as approximately seven, with disk, flat and curved blade turbines between two and five. P_o and $\overline{G}$ are implicitly linked via Equations 2-12 and 2-13. Although this thesis questions the validity of the $\overline{G}$ value as a parameter to characterise flocculation processes, differences in this value between different vessels do indicate the presence of different hydrodynamic environments which may affect floc formation and breakage mechanisms.

To this end, the CFD models were used to explore possible relationships between the turbulence dissipation rate and mixing speed for both vessels. Very strong relationships were observed between the two parameters for the vessels in their entirety, and also for various subsets of the vessels' contents including the paddle swept volumes and the paddle tip zones. Higher turbulence dissipation rates were found in the Hudson vessel than in the cylindrical vessel with the highest values found in the paddle tip zone, which

is in qualitative agreement with data found in Francois (1987). However, it is interesting to compare the turbulence dissipation rates between the two vessels, a task which hitherto had not been undertaken. Turbulence dissipation rates in the paddle tip zone of the Hudson vessel were found to be some five times the vessel average values (so agreeing with the range suggested by Stanley and Smith (1995) of four to six) whilst the corresponding value for the cylindrical vessel was 3.5 times. The results also demonstrated the distribution of the turbulence dissipation rate values, indicating that their distribution is broader in the cylindrical vessel than the Hudson vessel. A greater proportion of dead spots was also identified in the Hudson vessel. Thus, it was concluded that the general degree of mixing is greater in the cylindrical vessel than the Hudson vessel, despite the presence of higher values in the latter. This observation has implications for the wealth of literature which compares floc size and strength results obtained from different jar test scenarios (*e.g.* Gregory, 2004, Jarvis *et al.*, 2005a, Bache & Rasool, 2001) as the validity of conclusions drawn must be queried in light of the hydrodynamic differences.

There are numerous instances of floc breakage reported in terms of applied mixing speed, with no account taken of the impact of shape and volume of vessel or of impeller type on the results (*e.g.* Gregory, 2004, Jarvis *et al.*, 2004, Bouyer *et al.*, 2001). Chapters 4 and 5 have demonstrated that even where geometric similarity was maintained, the scaling of both experimental and numerically-derived velocity components still produced a degree of scatter not seen in other work (Nouri *et al.*, 1987, Patterson & Zipp, 1999, Zhou & Kresta, 1996, Kresta & Brodkey, 2004). It is likely that this scatter was due to the presence of transitional flow regimes, as opposed to fully turbulent ones, and further reinforces the care that must be taken when extrapolating results from one jar test to another. It is clear that the shape of jar test apparatus (*i.e.* circular or square on plan) and nature of flow regime (*i.e.* turbulent, transitional or laminar) all affect the resultant hydrodynamic environments and will consequently yield different flocculation performance and results; an observation which appears to have gone unnoticed or been dismissed by workers in this field until now.

11.5 Effect of Jar Test Flow Regime on Flocs

In order to consider the effects of induced flow fields on flocs, a series of Lagrangian particle analyses was undertaken using the Fluent software's in-built discrete phase model. Little information was found in the literature regarding Lagrangian analyses of particle transport in mixing systems. Stovin and Saul (1996 & 1998) published data relating to sediment transport in sewerage systems; however, the density of particles analysed was significantly different to those of flocs and the type of flow was also different to that found in a jar tester. The need to assess floc transport in laboratory and small scale environments has previously been recognised (Korpijarvi *et al.*, 1999 and Luo, 1997), but seemingly not developed. Here, CFD was used to model the trajectories and fates of particles designed to mimic flocs in mixing vessels. This analysis was then used to develop an understanding of the relative impact and importance of particle size and density. This was of particular significance since flocs are mass fractal particles whose density is generally found to decrease as size increases (Gregory, 1997 & 1998). Neither changes to mixing speed nor changes in particle size were found to affect greatly the amount of time for which a neutrally-buoyant particle was exposed to velocity gradients which exceeded the vessel average (*i.e.* at 200 rpm, neutrally buoyant particles ranging in size from 250 to 1,000μm all experienced velocity gradients in excess of the vessel average for between 35 and 40% of the simulation period). Some density-related effects were noticed, however. Increasing floc density was found to result in increased exposure to higher velocity gradient values. Jarvis (2005) found that MIEX® flocs were larger, denser and stronger than other flocs tested. Therefore, it can be concluded that this increased strength is, in fact, somewhat greater than previously believed, as the floc will have been subjected to an increased level of shear compared to other, less dense, flocs subjected to the same test which Jarvis (2005) demonstrated were weaker. The observed density-dependent nature of floc mixing shows that higher density flocs receive an increased degree of shear. Consequently, it is concluded that the jar test understates the strength of denser flocs and it is not appropriate to compare strengths solely on the basis of a d_2:d_1 ratio as others have done previously (Francois, 1987, Fitzpatrick *et al.*, 2004, Jarvis *et al.*, 2005a).

It was found that the turbulent flow characteristics in a circular section jar tester at high mixing speeds (>75 rpm) exhibit quantitative and qualitative differences to flow fields generated at lower mixing speeds, and these differences were quantified using CFD. A wide range of peak local velocity gradient values was found over the range of mixing speeds, with values greater than $1{,}300s^{-1}$ found at a mixing speed of 200 rpm. This is to be compared with a vessel average value of just $165s^{-1}$. At high mixing speeds (*i.e.* 100 rpm and above), local velocity gradients of up to ten times the vessel average were observed at a frequency of one or more every five seconds. The peak values of velocity gradient decreased with mixing speed, as did the frequency at which these peaks were observed. As well as indicating the range of local velocity gradients experienced by a floc in the jar tester, this analysis demonstrated that $\overline{G}$ is not representative of the magnitude of localised turbulent effects found within a mixing vessel and so is in agreement with the conclusions of previous authors in this field (Cleasby, 1984, Hanson & Cleasby 1990, Graber 1997). In the context of flocculation, this is important as effective design should minimise the likelihood of breakage and hence exposure to high velocity gradients. Standard texts (*e.g.* Crittenden *et al.*, 2005, Baruth, 2005) offer design recommendations in the form of $\overline{G}$ and $\overline{G}.t$. However, the range of local velocity gradient values identified demonstrated that these traditional design methods may not necessarily achieve optimum floc sizes. This observation is discussed further below.

Nevertheless, considering the trajectories of notional spherical particles with diameter and density set to replicate the characteristics of typical flocs subjected to one minute of mixing in the cylindrical jar tester, it was found that, at a particular mixing speed, the average velocity gradient experienced by the particle along its trajectory was approximately equal to the vessel average velocity gradient for that vessel. This demonstrated that the two blade paddle and cylindrical vessel jar test configuration imparts a good degree of mixing to the liquid contents and that, despite its critics (*e.g.* Cleasby, 1984, Hanson & Cleasby 1990, Graber 1997) the average velocity gradient has value as a flow field descriptor, provided that its limitations are recognised.

Korpijarvi *et al.* (1999 & 2000) recognised the potential benefits of the use of the local velocity gradient to represent localised shear conditions to which particles (flocs) are

exposed. In the work recorded here, a $G_t.t$ term (*i.e.* the product of the local velocity gradient along a particle trajectory and time) was developed by numerically integrating the velocity gradient along the trajectory. As a result, it was possible to develop an understanding of the total shear effect to which a particle was subjected over a known mixing period. In particular, results from cylindrical jar test analyses were used to examine floc formation and degradation at specific mixing speeds. The same experiments were replicated numerically using CFD. Comparison of the two data sets enabled conclusions to be drawn with regard to the magnitude of G_t and $G_t.t$ to which a floc could be subjected without breakage. This facilitated an extension of previous laboratory-based work (Gregory, 2004, Jarvis *et al.*, 2004 & 2005d, Yukselen & Gregory, 2002 & 2004) which had considered floc breakage and regrowth only as a function of mixing speed. Experimental data showed that a floc formed by the addition of iron hydroxide to an upland water could withstand mixing speeds of less than 75 rpm. CFD analysis showed a step change in G_L values occurring in the mixing vessel at the 75 rpm threshold. Consequently, it was possible to describe the strength of this floc in terms of turbulence dissipation rate and local velocity gradient; parameters which are meaningful across a range of scenarios, unlike mixing speed which is applicable only to the test configuration in which the results were obtained.

For the three different floc suspensions studied by Jarvis *et al.* (2004), model equations were developed to express the rate of floc degradation as a function of $G_t.t$. It was found that at mixing speeds of 100 rpm and above, the rate of floc degradation, when expressed in terms of $G_t.t$, was the same. For all suspensions, the degree of breakage, expressed as a percentage of the initial floc size, was greatest at 200 rpm and observed the hierarchy 200 > 150 > 100 > 75 rpm. It was deduced that the key factor in determining the total degree of floc breakage was the extent of breakage which occurred in the first minute. A similar observation may be inferred from the results of others (Fitzpatrick *et al.*, 2004, Gregory, 2004, Gregory & Rossi, 2001, Gregory & Dupont 2001). However, that work all made use of the flocculation index (as described in Chapter 2) rather than actual floc size. The lack of temporal resolution in the laboratory data collection exercise precluded the development of a robust model to replicate this

sudden breakage phenomenon. There is a clear need for further work, at a finer temporal resolution, to investigate this breakage phenomenon further.

For three different floc suspensions, the rate of floc breakage, when expressed in terms of applied $G_t.t$ has been shown to display a strong power curve relationship with floc size. For the iron hydroxide suspension, robust relationships were observed at mixing speeds of 100 rpm and above. The r^2 values were found to decrease with mixing speed, demonstrating the flocs' increasing resistance to shears imposed at the lower mixing speeds. The power curve models give a good representation of floc degradation, but also account for the steady state floc size following sustained rapid mixing which was observed by Jarvis *et al.*, 2004.

The large instantaneous velocity increase brought about by an increase in mixing speed from 30 to 200 rpm was demonstrated in Chapter 5. Jarvis *et al.* (2004) showed that the rate of floc breakage for precipitate flocs was higher in the first minute of increased mixing than in any of the subsequent minutes. However, CFD analysis has shown that the degree of intensity of the highest local velocity gradients ($>150s^{-1}$) to which a particle is exposed does not necessarily decrease after the first 60 seconds. Over 11 minutes of mixing, the maximum continuous exposure of a floc to a velocity gradient in excess of $100s^{-1}$ was found to be always less than one second. Increasing the mixing speed was found to increase the total amount of time for which a particle was exposed to higher velocity gradient values, but the maximum continuous time for which a particle experienced values greater than the vessel average was always less than one second. However, this observation does not appear to fit neatly with the fact that the rate of degradation after the first minute was reduced. Combining numerical data with physical results suggests that floc breakage is a function of water chemistry and vessel hydrodynamics. (This is obvious for if water chemistry exerted little or no effect, flocs formed under different raw water and / or coagulant dose and type conditions would all break in the same manner). The results demonstrate that iron hydroxide flocs will break at instantaneous velocity gradient values of $200s^{-1}$ or greater. However, NOM flocs exhibit breakage either when exposed to instantaneous G_L values of $150s^{-1}$ or when experiencing sustained exposure to G_L values of $100s^{-1}$. Previous work has

demonstrated the fragility of kaolin flocs (Jarvis *et al.*, 2004) and this work identified that they are broken at instantaneous G_L values of $50s^{-1}$ and above. Earlier work has considered floc breakage mechanisms in detail (Gregory, 2004, Mikkelsen & Keiding, 2002, Yeung *et al.*, 1997, Boller & Blaser, 1998). The addition of this CFD data to our current understanding leads to the conclusion that no single dominant force exists to bring about floc breakage. Rather, floc breakage occurs as a result of short (<1s) exposure to very high shear, or prolonged exposure to lower shear values. This is evidenced by the fact that the rate of degradation dropped off following the first 60 seconds, despite the fact that in the subsequent ten minutes, the particle was exposed to some very high G_L values, for very short (<1s) periods. Consequently, it is concluded that flocculators should be designed to minimise the areas of high shear within the mixing vessel, and also to optimise the retention time to avoid longer than necessary exposure to potentially damaging shear levels; *i.e.* flocculators should be designed to both G_L and $G_t.t$ criteria. The subject of retention period is discussed further below.

An understanding of the changes in the profile of the local velocity gradient distribution within a jar test at different mixing speeds has enabled the development of the concept of a "breakage threshold"; that being a local velocity gradient value which would appear to be of sufficient magnitude to give rise to floc breakage. Breakage threshold values were developed for three separate floc suspensions as follows:

Table 11-2: Threshold local velocity gradient values for various floc types.

Floc Type	Threshold Local Velocity Gradient, s^{-1}
Iron Hydroxide	200
NOM	150
Kaolin	50

The above data imply that the strength hierarchy is iron hydroxide > NOM > kaolin. Previously this has been expressed only in terms of mixing speed. However, this work has enabled floc strength to be characterised on the basis of breakage threshold and so be used for as a basis for full scale flocculator design.

Although the threshold values for each suspension have been determined using a jar tester and CFD analyses, they are based on the flocs' resistance to induced velocity gradients. Therefore, they can be adopted for use in other situations, and not just as applied to one specific jar test configuration. This is a significant result as any previous breakage thresholds have always been expressed in terms of mixing speed and consequently are meaningless when applied to any situation other than that in which they were developed.

11.6 Implications for Full Scale Flocculation

CFD models have been developed for two full scale flocculator installations; one mechanically mixed, the other hydraulically mixed. The results were considered in the light of results obtained from the jar test numerical analyses and, in particular, the floc breakage threshold values. The sites were carefully selected as the raw water treated at each is similar in nature to that used by Jarvis *et al.* (2004). The models were used to develop numerical residence time distributions for the full scale flocculators at various flow rates and mixing speeds as appropriate. The ability to develop accurate computer models of these processes is significant as they enable a works manager to understand and assess the efficiency of the unit process without first having to stand it down from duty; something which would not be possible in the case of the two flocculators considered. However, the complexity and size of some models may well preclude their use in certain situations, as discussed elsewhere. Little full scale flocculation CFD modelling has been undertaken (or, at least, published) for either mechanical or hydraulic flocculators (Haarhoff, 1998, Haarhoff & Van der Walt, 2001).

11.6.1 Frankley WTW

For the mechanically-mixed flocculator, CFD was used to analyse the flow field generated within a flocculator cell at the Frankley WTW in Birmingham, UK. Turbulence closure was achieved via use of the realizable k-ϵ turbulence model, and the rotating flow was solved using the computationally-expensive, but robust, sliding mesh

method. Inspection of the velocity vectors and contours showed that there were some localised areas of stagnation within the flocculation cell, particularly in the corners and the immediate vicinity of the shaft. In a rectangular shaped tank this is to be expected and largely unavoidable. The volume of stagnation was not large enough to be of concern. Some short-circuiting was evidenced via the residence time distribution analysis. However, in such a large vessel, the concept of ideal flow is something of an aspiration rather than a reality and this is why certain designers maintain the need for flocculation cells in series, such as those found at Frankley (Polasek & Mutl, 1996, Baruth, 2005, Crittenden *et al.*, 2005).

Changes to the flow rate were found to have only a small impact on the distribution of local velocity gradient values. Changes to the mixing speed were found to exert a noticeable influence on the magnitude of turbulence dissipation rate and hence local velocity gradient, which is to be expected as the jar test work discussed here and undertaken by others (Stanley & Smith, 1995) demonstrated the dependency of $\bar{\varepsilon}$ on mixing speed, as shown at Table 11-3. However, even at the highest mixing speed, local velocity gradients within the majority of the vessel contents were below the breakage threshold values derived from the CFD analyses of the jar tester. As a result, it was concluded that the magnitudes of velocity gradients induced in the three tapered flocculation stages at Frankley WTW are acceptable for adequate flocculation.

Table 11-3: Mixing speed and corresponding velocity gradient increases.

	N % increase	$\bar{\varepsilon}$ increase	$\bar{\varepsilon}$ factor increase
Stanley & Smith, 1995 (Hudson)	100% (50 – 100 rpm)	0.012 – 0.1	8.33
This work (cylindrical jar test)	100% (50-100 rpm)	$8.1\text{x}10^{-4} - 5.11\text{x}10^{-3}$	6.33
	100% (100-200 rpm)	$5.11\text{x}10^{-4} - 2.75\text{x}10^{-3}$	5.38
This work (Frankley WTW)	100% (1.6-3.2 rpm)	$4.83\text{x}10^{-4} - 3.11\text{x}10^{-3}$	6.43

However, it was also demonstrated that the calculated $\overline{G_L}.t$ value to which the water (and hence flocs) are subjected is significantly greater than the design $G.\tau$ value which is, in turn greater than the $G_t.t$ value developed using CFD results and the laboratory data of Jarvis *et al.* (2004). This can be seen clearly from Figure 11-1 which shows the variation in G, t and $G.t$ for the three jar test suspensions and the nine Frankley

flocculator cells. The left hand axis shows G and $G.t$ values, whilst the right hand axis shows retention time, t. Also shown are the total $G.t$ values for each flow rate at Frankley and the shaded area depicts the "optimum" Camp number range as recommended by various texts (Crittenden *et al.*, 2005, Baruth, 2005). It is clear that the degree of flocculation in the jar tester is an order of magnitude less than that provided in each of the individual cells at Frankley. $G.t$ for the individual cells is generally in line with the published recommendations, but the total generally exceeds the recommendations. The reduction of retention time with an increase in mixing speed at constant flow rate is also apparent.

However, an additional key observation from Figure 11-1 is that the reason for the increase in Camp number between the jar test and Frankley analyses is not the applied velocity gradient, but rather the flocculation time. In their critique of the G value, Lawler *et al.* (1983) stated that "The primary role of mixing in flocculation basins might not be to bring about particle contact directly, but to keep particles in suspension so that collisions brought on by Brownian motion and differential settlement can occur. If this is true, flocculation might be improved by reducing the velocity gradient ... to a level just sufficient to keep the particles in suspension." However, the foregoing does not consider retention period. The data of Figure 11-1 show that the G_L values in the three flocculation cells at Frankley are satisfactory, but that the retention is greater than necessary. Indeed, the retention time and G_L in just one cell are sufficient to meet standard text recommendations and are in excess of those required to generate maximum floc size, assuming an equivalent raw water and coagulant dose to those used in the jar tester. The clear implication of this is that the flocculation process at Frankley is over-treating the water. The analyses of Chapter 6 concluded that floc breakage was brought about by short exposure to high velocity gradients and more prolonged exposure to lesser values. Therefore, retention periods in excess of that necessary to maximise floc size, such as those at Frankley, would only serve to reduce the floc size. It is suggested that, as the $\overline{G}_L.t$ value is so much greater than that found necessary for effective flocculation in the jar tester, that the floc size at Frankley is not maximised. Bache and Rasool (2001) reported floc data from a range of water treatment works in Scotland showing large variations in size and strength, yet all operators reported

adequate performance of the DAF. Indeed, the authors reported the case of one water treatment works where the mechanical flocculator was not functioning, and yet the DAF units still performed adequately. Whilst the apparent over-treatment at Frankley does not appear to have had detrimental impact on the performance of the downstream DAF clarification process, there are potential long term issues for the operators with regard to power consumption (and operational efficiencies) and for designers with regard to efficient capital and operational design.

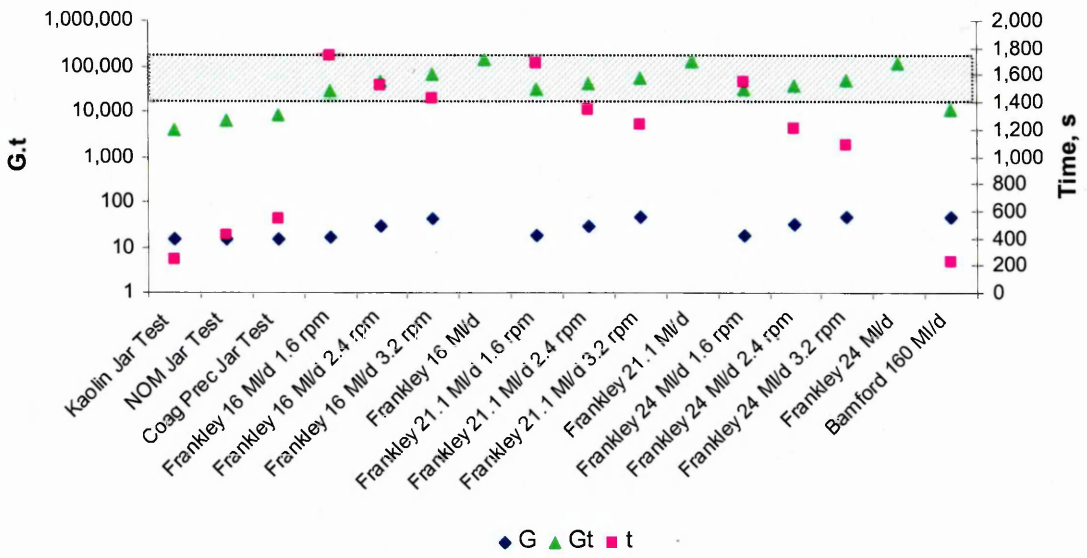


Figure 11-1: **Variations in velocity gradient, Camp number and retention time for jar tester, Frankley and Bamford WTW. (Shaded area indicates the recommended Camp No. optimum range for effective flocculation, from Crittenden *et al.*, 2005, Baruth, 2005).**

However, one must also consider what the optimum floc size should be for a process, as it will not necessarily be the maximum. Edzwald (1995) recommended that DAF used for drinking water applications should be fed with a strong floc in the size range 10-30μm. This is in contrast to Fukushi *et al.* (1995) who suggested the use of larger flocs. Valade *et al.* (1996) recommended that flocculator retention time be reduced to five minutes in view of the fact that the coagulation chemistry has a stronger influence on DAF performance than physical flow parameters; however, this is in stark contrast to Eades and Brignal (1995) who maintained the need for 20 – 30 minutes multi-stage mechanical flocculation upstream of a DAF process. Finally, Bache and Rasool (2001)

found that DAF units operate satisfactorily irrespective of floc size, thus further questioning flocculator design philosophy and parameters. Flocculator design has traditionally been based on empiricism due to a lack of accurate flocculation models (Thomas *et al.*, 1999, Lawler, 1993, Lawler and Nason, 2004). Thus the velocity gradient breakage threshold concept established here, used in conjunction with CFD analyses, offers benefits over the more traditional approaches.

11.6.2 Bamford WTW

For the hydraulically-mixed flocculator at Bamford WTW, the standard k-ϵ turbulence model generated satisfactory numerical results. The numerical data were validated by considering velocity profiles at various sections in the flocculation channel and comparing them with directly measured values. In addition, power dissipation across the flocculator was calculated from the measured headloss and compared favourably with the numerical power dissipation calculated from the turbulence dissipation rate integral. In this instance, the use of the standard k-ϵ model was appropriate as there was little evidence of highly swirling flow and this turbulence model has been used successfully by others for similar scenarios (Wang and Falconer, 1999, Haarhoff & Van der Walt, 2003). The distribution of local velocity gradients was found to be centred on the lower end of the scale, with most values being similar to those found in the jar tester at a mixing speed of 30rpm. However, the flocculator was found to be volumetrically undersized. Data from Fearing (2004) and Jarvis (2005) showed that for a NOM floc, three minutes was required for the coagulation phase, with a further five minutes for flocculation. A longer period is required for iron hydroxide flocs; although the smaller kaolin flocs attained their maximum limiting size after approximately five minutes of coagulation and flocculation. Thus, the retention time at Bamford is inadequate to ensure adequate flocculation even accounting for possible reductions in flocculation time as discussed above. This is demonstrated graphically at Figure 11-2. At an average flow rate of 160 Ml/d, the mean retention time was found to be close to the theoretical hydraulic retention time (6.95 minutes and 6.69 minutes respectively), with t_{10}, t_{50} and t_{90} determined as 47%, 91% and 166% of the mean residence time. Velocity vectors between each baffle indicated the presence a flow recirculation loop and

velocity maxima were identified at the edges of the baffles, with dead spots (*i.e.* zero velocity) at the centre of each recirculation loop and also at the corners of each compartment. The lines depicting t_{10} and t_{50} for Frankley relate to one of three cells only; thus further demonstrating the apparent over-treatment.

The absence of any mechanical mixing for coagulation gave rise to the somewhat perverse situation where velocity gradients generated in the flocculation stage were actually higher than those generated in the coagulation stage. It is clear that this element of the process is sub-optimal and the cost implications of chemical dosing in this environment have been shown to be significant.

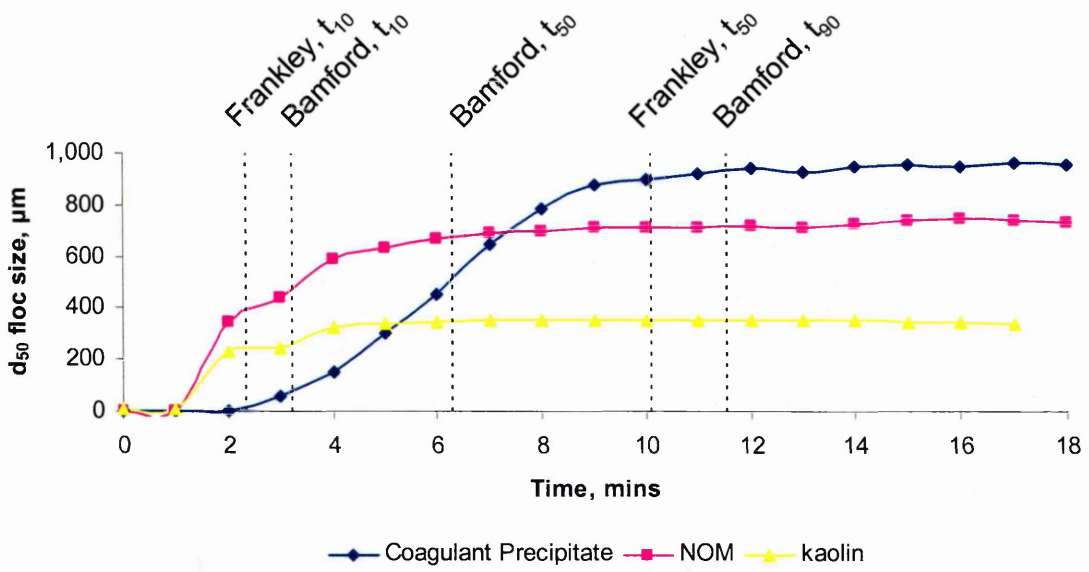


Figure 11-2: Floc growth with time for various suspensions, showing Frankley and Bamford retention times.

11.7 The Use of CFD in the Water Industry

As part of this work, a number of CFD simulations of laboratory and full scale unit processes commonly found at water treatment works have been undertaken. The early work (multiple reference frames, two-equation modelling of jar testers) was undertaken using a 1.4GHz, 250MB RAM laptop computer. The most straightforward of these runs

took at least 12 hours CPU time to obtain a converged solution and it became apparent that the modelling of anything more complex would require significantly improved computing facilities. As a result, the high performance computing (HPC) facility at Cranfield University was used for the more complex jar tests scenarios (sliding mesh and Reynolds stress modelling) and all Frankley and Bamford simulations. Even using the HPC, Frankley sliding mesh simulations still required up to 12 days' CPU usage. As a test, an attempt was made to run the same model on a laptop. The test was abandoned after two weeks of continuous running, with the solution still distant from convergence.

Articles have been published in trade magazines espousing the benefits of CFD to the water industry (Hamill, 1998, Shilton *et al.*, 1999, Harwood, 2001, Andoh, 2006) and it is accepted that the cost of undertaking simple CFD modelling has fallen in real terms as the cost of basic hardware and memory has fallen (although annual licence fees for commercially-available codes remain high at £3,500 per annum for an academic Fluent licence). However, this work has shown how modest computing hardware is not capable of running anything other than the most straightforward of models. Indeed, even when runs are possible on such machines, the machine is redundant for all other purposes during that time. This observation leads one to question the appropriateness and the place of CFD in the general water industry. Accepting the fact that complex modelling can only be undertaken by skilled operatives using HPC facilities, one must consider the costs involved. Unfortunately, no commercial rate for the Cranfield University was available; however, Oswald (2006) advised that charging for HPC usage was a deterrent to use. This author believes that traditional commercial IT management in the water industry perceive HPC systems to be a niche environment, and so will not be disposed to significant capital investment, or the training of staff, in that area. This is borne out to some extent by the fact that in the UK, it is only Anglian Water and Thames Water which are known to have specialist CFD capabilities; this, from a cohort of ten major water and sewerage companies. It is less surprising to note that the water-only companies have no specialist in-house CFD expertise. This issue was also raised by Morvan (2005) who stated that "CFD requires a background knowledge whose cost is still high to industrialists for whom CFD only provides either an occasional tool or a

tool that is too sophisticated to be used in its most general form in their daily business". Gujer (2006) also questioned the likelihood of widespread CFD modelling in the water industry and wrote "... to what extent this ever more detailed research will lead towards models that will be applicable in daily consulting business. Who can afford to identify accurately parameters that are subject to high sensitivity but are only amenable to expensive and time-consuming analytical procedures?" This is at odds with the thoughts of Fawcett (1991) who wrote that "In the near term, it is likely that CFD will become commonplace in the design office, as well as the research and development laboratory". Fifteen years later, this author believes that the water industry in particular is still some way from adopting CFD as a "commonplace" design tool, this despite Morvan's work on developing "front-end" applications for non-expert users to exploit the benefits of CFD without the requisite background knowledge (Morvan, 2005). Indeed, this author would counsel against the use of CFD by non-expert users as the complexity of the software and algorithms contained therein raise the likelihood of misuse and the production of incorrect data sets and results.

Although CFD offers undoubted benefits for those seeking to understand better the flow in and around complex geometries, the level of complexity demands extensive computing power and trained staff to such an extent that this author believes its widespread use outside academic and specialised consultancies is unlikely. Nevertheless, this work has demonstrated clearly the benefits to be gained from this powerful tool.

12 Conclusions

12.1 Modelling Strategy and Methods

- For straightforward unbaffled paddle mixing in a small vessel, the computational expense of the sliding mesh technique to model rotating flows was found not to be necessary where the user's scope of interest is limited to a broad consideration and appreciation of the magnitude of shear zones and turbulent effects within a mixing system. The multiple reference frames approach was found to be sufficient to develop an understanding of the magnitude of velocity gradients to which a particle (floc) may be subjected within the vessel.

- For highly swirling flows the standard k-ε turbulence model was found to yield turbulence dissipation results which were erroneous by an order of magnitude. The unsuitability of this turbulence model for highly swirling flows is confirmed. Other models produced results of variable quality. Where time and computational expense permit, use of the Reynolds Stress Model is recommended. Even using this robust turbulence modelling approach, whilst velocity components were faithfully replicated across the range of mixing speeds, turbulent effects were less well reproduced at lower mixing speeds, where the flow was not fully turbulent.

12.2 Hydrodynamics of the Jar Test Apparatus

- Experimental and numerical vessel average velocity gradient values for two different jar test configurations using the same impeller and mixing speeds were found to vary significantly. The degree of variation increased with mixing speed.

- CFD analysis showed that for the jar test simulations, the ratio of turbulence dissipation rate in the paddle volume to the total volume was constant, irrespective of mixing speed. However, the constant was found to change with vessel configuration; the square section vessel constant being 1.75 times greater than the circular one.

- CFD analysis has demonstrated that, when the jar test vessel contents were mixed at the same speed, the turbulence dissipation rates generated in a square section vessel were significantly higher than those found in a circular section vessel, albeit they were less well-distributed.

12.3 Particle Trajectory Analysis in the Cylindrical Jar Tester

- Despite recent criticism in the literature, the vessel average velocity gradient concept has value as a flow field descriptor, provided that its limitations are recognised.

- Turbulent flow characteristics in a circular section jar tester at high mixing speeds ($\geq$100 rpm) were found to exhibit quantitative and qualitative differences to flow fields generated at lower mixing speeds. Peak values of local velocity gradient decreased with mixing speed, and the frequency of occurrence of these peaks also decreased.

- For a range of mixing speeds, the $G_t.t$ value (*i.e.* the product of the local velocity gradient along a particle trajectory and time) for a circular section jar tester was shown to be similar to the traditional $\overline{G}.t$ value for a specific mixing speed and configuration.

- CFD analysis demonstrated that the degree of intensity of the highest local velocity gradients (>150 s^{-1}) to which a floc is exposed did not necessarily decrease after the first 60 seconds of increased mixing.

12.4 Floc Breakage Mechanisms and Criteria

- Floc breakage was found to occur as a result of short (<1s) exposure to very high shear, or prolonged exposure to lower shear values.

- Changes in the profile of the local velocity gradient distribution within a jar test at different mixing speeds enabled the development of the concept of a "breakage threshold"; that being a local velocity gradient value which is of sufficient magnitude to give rise to floc breakage. Breakage threshold values were developed for three separate floc suspensions as follows:

Iron Hydroxide flocs:	$200s^{-1}$
Kaolin flocs:	$50s^{-1}$
NOM flocs:	$150s^{-1}$ (instantaneous), $100s^{-1}$ (continuous)

- For three different floc suspensions, the rate of floc breakage, when expressed in terms of applied $G_t.t$ displayed a strong power curve relationship with floc size. The r^2 values decreased with mixing speed, demonstrating the flocs' increasing resistance to shears imposed at the lower mixing speeds. The power curve models gave a good representation of floc degradation, but also accounted for the steady state floc size which was observed following sustained rapid mixing.

12.5 Floc Growth Mechanisms and Criteria

- Considering modelled $G_t.t$ values for particles in the cylindrical jar tester, it was found that the applied $G_t.t$ to attain maximum floc size was significantly less than that recommended in both current and historic texts, implying a degree of over-treatment in full scale flocculators constructed on the basis of recommended $\overline{G}.t$ values.

12.6 Flocculator Assessment and Design Guidance

- An evaluation of the extent of floc growth and breakage demonstrated that these processes cannot be judged solely on the basis of applied G_t values. Flocculators should be designed to minimise the areas of high shear within the mixing vessel, and also to optimise the retention time to avoid longer than necessary exposure to potentially damaging shear levels; *i.e.* flocculators should be designed to both G_L and $G_L.t$ (or $G_t.t$) criteria. However, account must also be taken of the optimum floc size required for the downstream clarification process.

12.6.1 Frankley WTW Mechanical Flocculator

- Changes to the flow rate were shown to exert only a small influence on the distribution of local velocity gradient values. Changes to the mixing speed did impose a significant impact on the local velocity gradient distribution, over the 1.6 – 3.2 rpm operational band.

- The majority of the vessel contents were found to experience local velocity gradients below the breakage threshold values derived from the CFD analyses of the jar tester.

- Some short-circuiting was evidenced via the residence time distribution analyses.

- Despite the short-circuiting, the RTD analyses demonstrated that the tapered flocculation system over-treated the water when the $\overline{G}.t$ value was compared to the $\overline{G}.\tau$ value and the $\overline{G}_L.t$ values developed for jar test simulations

12.6.2 Bamford WTW Hydraulic Flocculator

- The magnitudes of local velocity gradients were found to be similar to those found in the jar tester at a mixing speed of 30 rpm.

- It was demonstrated that the Bamford flocculator is volumetrically undersized, with a retention time which is inadequate to ensure adequate flocculation.

- Large recirculation loops and dead spots were identified in flocculation cells between baffles.

- Coagulant mixing arrangements were found to be insufficient and ineffective.

12.7 The Use of CFD in the Water Industry

- Using modest computing hardware (*e.g.* desktop personal computers) CFD modelling is restricted to the analysis of relatively simple flows. More complex scenarios, such as rotating meshes, require greater computing power which is not generally found outside academic environments or highly specialised consultancies. CFD modelling also requires trained staff to generate robust models and solutions. The combination of these two factors is likely to preclude the widespread use of CFD in most water companies and mainstream consultancies in the foreseeable future.

13 Recommendations for Further Work

The described work has presented a range of models which assess flow characteristics in a range of flocculators at laboratory and full scale. By understanding the hydrodynamics of such vessels, and coupling the results with floc strength data, improvements can be made to the way in which flocculation vessels are assessed and new installations designed. However, more research is required in this area and should concentrate on the following topics.

- This work presented numerically-derived velocity gradient threshold data for three types of floc; (iron hydroxide flocs, turbidity flocs and organic matter flocs). Further work is required to extend the work further to consider alternative raw waters and coagulant types.

- This work has considered floc fate from the perspective of particle trajectory and an assessment of the turbulent environment which is likely to give rise to growth, stability or breakage. Further work should be undertaken to apply the velocity gradient threshold concept developed here to numerical modelling of the flocculation process itself (*i.e.* growth and breakage).

- Further work is required to determine the type and extent of floc breakage in the first minute of increased mixing in the jar tester. Further experimental work should be undertaken, at a refined temporal resolution (*i.e.* floc size measured every few seconds), the results of which could then be fed into an appropriate numerical model.

- This work has shown that the degree of flocculation required (expressed as $G_t.t$) to develop a steady state floc size is considerably smaller than that recommended by standard texts. Actual floc sizes produced at the water treatment works considered here and by others in associated projects should be measured and compared to values obtained in the jar tester. This could reduce

the flocculation time at water treatment works, thus offering water companies an opportunity to reduce operational costs.

References

Adrian, RJ, 1991, "Particle imaging techniques for experimental fluid mechanics", *Annu. Rev. Fluid Mech.*, 23, 261-304.

Alex, J, Kolisch, G and Krause, K, 2002, "Model structure identification for wastewater treatment simulation based on computational fluid dynamics", *Water Science and Technology*, 45, 4-5, 325.334.

Amirtharajah, A, 1978, "Design of rapid mix units", In: Sanks, RL (Ed), *Water treatment plant design*, 131-147, Butterworth Heinemann.

Amirtharajah, A, Clark, MM, and Trussell, RR, 1991, "*Mixing in coagulation and flocculation*", AWWARF, Denver, Co, USA.

Anderson, JD 1995, "*Computational Fluid Dynamics*", McGraw Hill

Andoh, R, 2006, "CFD saves $50,000 in design of stormwater separator", *Fluent News*, XV, 2, 35 – 37.

Armenante, PM, Luo, C, Chou, C-C, Fort, I and Medek, J, 1997, "Velocity profiles in a closed, unbaffled vessel: comparison between experimental LDV data and numerical CFD predictions", *Chemical Engineering Science*, 52, 20, 3483-3492.

Bache, DH, 2004, "From rupture to structure: the physical character of flocs", *Water Science and Technology*, 50, (12), 55-62.

Bache, DH, Johnson, C, McGilligan, FJ, and Rasool, E, 1997, "A conceptual view of floc structure in the sweep floc domain", *Water Science and Technology*, 36 (4), 49-56.

Bache, DH and Rasool, ER, 2001, "Characteristics of Alumino-Humic Flocs in Relation to DAF Performance", *Water Science and Technology* 43 (8), 203-208.

Bache, DH, Rasool, E, Moffatt, D, and McGilligan, FJ, 1999, "On the Strength and Character of Alumino-Humic Flocs", *Water Science and Technology*, 40 (9), 81-88.

Bakker, A, LaRoche, RD, Wang, MH and Calabrese, RV, 2000, "Sliding Mesh Simulation of Laminar Flow in Stirred Reactors", "The Online CFM Book", http://www.bakker.org/cfm. (accessed 21st September 2006).

Baldi S, Ducci A, Yianneskis M, 2004, "Determination of dissipation rate direct measurement of fluctuating in stirred vessels through velocity gradients", *Chemical Engineering and Technology*, 27 (3), pp 275-281

Baruth, EE, 2005, "*Water treatment plant design*", McGraw-Hill, 4th Edition.

Bates, RL, Fondy, PL, and Corpenstein, RR, 1963, "Examination of some geometric parameters of impeller power", I&EC Process Design & Development, 2, 4, 312 – 314.

Bayley R, Ta, CT, Sherwin, CJ, Renton, PJ, 2001, "Traditional and novel reservoir management techniques to enhance water quality for subsequent potable water treatment" *Water Science and Technology: Water Supply,* 1, 1, 1-16.

Bechtel TB, 2003, "Laminar pipeline flow of wastewater sludge: Computational fluid dynamics approach", *Journal of Hydraulic Engineering –ASCE*, 129 (2), pp 153-158

Bechtel TB, 2005, "A computational technique for turbulent flow of wastewater sludge", *Water Environment Research*, 77 (4), pp 417-422

Bell, B, 2004, "Case studies on using the turbulence models in Fluent 6", Presented to CFD Training Summit, June 10th,

http://www.fluentusers.com/support/ugm04/auto/2004-UGM-TRAINING-BB-9.pdf, accessed 4th July 2006.

Bhattacharya, S and Kresta, SM, 2002, "CFD simulations of a three-dimensional wall jets in a stirred tank", *Canadian Journal of Chemical Engineering*, 80, 4, 695-709.

Biggs, CA and Lant, PA, 2000, "Activated Sludge Flocculation: On-Line Determination of Floc Size and the Effect of Shear", *Water Research* 34 2542-2550.

Binnie, Black and Veatch, 2001, "Bamford WTW General Improvements Feasibility Study", Volume 1 of 2, confidential report produced for Severn Trent Water Ltd.

Boller, M and Blaser, S, 1998, "Particles Under Stress", *Water Science and Technology*, 37, 10, 9-29

Bouyer, D, Coufort, C, Liné, A and Do-Quang, Z, 2005, "Experimental analysis of floc size distributions in a 1-L jar under different hydrodynamics and physico-chemical conditions", *J.Colloid Interface Sci*, 292, 413-428.

Bouyer, D, Escudié, R and Liné, A, 2005, "Experimental analysis of hydrodynamics in a jar-test", *Transactions of the Institution of Chemical Engineers* 83 (B), 22-30.

Bouyer, D, Lainé, A, Cockx, A and Do-Quang, Z, 2001, "Experimental Analysis of Floc size Distribution and Hydrodynamics in a Jar Tester," *Transactions of the Institution of Chemical Engineers* 79 (A), 1017-1024.

Brouckaert, CJ and Buckley, CA, 1999, "The use of computational fluid dynamics for improving the design and operation of water and wastewater treatment plants", *Water Science and Technology,* 40, 4-5, 81 - 89.

Brown, DAR, Jones, PN, and Middleton, JC, 2004, "Measuring tools and techniques for mixing and flow visualisation techniques", In: "*Handbook of industrial mixing: science and practice*", edited by Paul, EL, Atiemo-Obeng, VA and Kresta, SM, pp 145-201.

Bujalski, W, 2006, *Personal communication.*

Bushell, GC, Yan, YD, Woodfield, D, Raper, J and Amal, R, 2002, "On techniques for the measurement of the mass fractal dimension of aggregates", *Advances in Colloid and Interface Science*, 95, 1, 1-50.

Byun, S, Oh J, Lee BY, and Lee S, 2005, "Improvement of coagulation efficiency using instantaneous flash mixer (IFM) for water treatment", *Colloids and Surfaces A-Physicochemical and Engineering Aspects*, 268 (1-3), pp 104-110

Camp, TR, 1955, "Flocculation and flocculation basins, ASCE Transactions, 120, 1-16. (Reprinted in Civil Engineering Classics: Outstanding papers of Thomas R Camp, ASCE, 1973).

Camp, TR and Stein, PC, 1943, "Velocity gradients and internal work in fluid motion", *Journal of the Boston Society of Civil Engineers*, XXX, 4 219-237.

Chadwick, A and Morfett, J, 1998, "*Hydraulics in civil and environmental engineering*", E & F Spon, 3rd edition.

Chaignon, V, Lartiges, BS, El Samrani, A and Mustin, C, 2002, Evolution of Size Distribution and Transfer of Mineral Particles Between Flocs in Activated Sludges: an Insight into Floc Exchange Dynamics. *Water Research* 36 676-684.

Chataigner, O, Gatel, D and Cavard, J, 1999, "Chlorine disinfection: From CT requirements to clearwell design", *Water Supply*, 17, 3/4, 191 - 197.

Chow, VT, 1986, "*Open channel hydraulics*", McGraw-Hill, 22nd printing

Chu, CP, Chang, BV, Liao, GS, Jean, DS and Lee, DJ, 2001, "Observations on changes in ultrasonically treated waste-activated sludge", *Water Research*, 35, 1038 – 1046.

Ciofalo, M, Brucato, A, Grisafi, F and Torraca, N, 1996, "Turbulent flow in closed and free-surface unbaffled tanks stirred by radial impellers" *Chem .Engng Sci.* 51(14), 3557-3573.

Clark, MM, 1985, "Critique of Camp and Stein's RMS velocity gradient", *J. Environmental Engineering*, 111(6), 741-754.

Cleasby, JL, 1984, "Is velocity gradient a valid turbulent flocculation parameter?", *J. Environmental Engineering,* 110(5), 875-897.

Coufort, C, Bouyer, D and Liné, A, 2005, "Flocculation related to local hydrodynamics in a Taylor-Couette reactor and in a jar", *Chemical Engineering Science*, 60, 2179 – 2192.

Craig, K, De Traversay, C, Bowen, B, Essemiani, K, Levecq, C, and Naylor, R, 2002, "Hydraulic study and optimisation of water treatment processes using numerical simulation", *Water Science and Technology: Water Supply*, 2 5-6, 135-142.

Cranfield University, 2006, "High performance computing, 2005-2006", http://www.cranfield.ac.uk/ccc/information/high_performance_computing_2005.pdf, accessed 6th October 2006.

Crittenden, JC, Trussell, RR, Hand, DW, Howe, KJ, Tchobanoglous, G, 2005, "*Water Treatment: Principles and Design*", 2nd Edition, John Wiley & Son.

Crow, D, Yeung, H and O'Neill, S, 1997, "Chlorine contact tanks, hydraulic performance and retrofit manual", United Utilities, R97/196/B.

Danckwerts, PV, 1953, "Continuous flow systems – distribution of residence times", *Chemical Engineering Science*, 2 (1): 1-13, cited in Naumann, 2004.

Daskopoulos, PH and Harris, CK, 1996, "Three dimensional CFD simulations of turbulent flow in baffled stirred tanks: an assessment of the current position", In: *IChemE Symposium Series No 140, Fluid Mixing 5*, Edited by Benkreira, H, 1-13.

Decker, S and Sommerfeld, M, 1996, "Calculation of particle suspension in agitated vessels with the Euler-Lagrange approach", In: *IChemE Symposium Series No 140, Fluid Mixing 5*, Edited by Benkreira, H, 71-82.

Do-Quang, Z, Cockx, A, Laine, J-M, and Roustan, M, 2000, "Applying CFD modelling to enhance water treatment reactors efficiency: example of the ozonation process", *Proceedings of the 1st World Water Congress of the International Water Association, 3-7 July, Book 2, Drinking Water Treatment,* 50-55.

Droste, RL, 1997, "Theory and practice of water and wastewater treatment", Wiley.

Duan, J and Gregory, J, 1996, "Influence of soluble silica on coagulation by aluminium sulphate", *Colloids and Surfaces, A: Physicochemical and Engineering Aspects*, 107, 309-319.

Duan, J and Gregory, J, 1998, "The influence of silicic acid on aluminium hydroxide precipitation and flocculation by aluminium salts", *J. Inorganic Biochemistry*, 69, 193 – 201.

Ducoste, JJ and Clark, MM 1998a, The Influence of Tank Size and Impeller Geometry on Turbulent Flocculation: I Experimental. *Environmental Engineering Science* 15 (3), 215-224.

Ducoste, JJ and Clark, MM, 1998b, "The influence of tank size and impeller geometry on turbulent flocculation: II. Model", *Environmental Engineering Science*, 15, 3, '225-235.

Durbin, PA, 1995, "Separated flow computations with the k-ϵ-v^2 model", *J.AIAA*, 33, 4, pp659-664.

Durst, F, Melling, A and Whitelaw, JH, 1976, "Principles and practice of laser Doppler anemometry", Academic Press, London.

Eades, A and Brignal, WJ, 1995, Counter-current dissolved air flotation / filtration", *Water Science and Technology*, 31, 3-4, 173-178.

Edzwald, JK, 1995, "Principles and applications of dissolved air flotation", *Water Science and Technology*, 31, 3-4, 1-23.

Essemiani, K and de Traversay, C, 2002a, "Optimisation of the flocculation process using computational fluid dynamics", in *Chemical Water and Wastewater Treatment VII, Proceedings of the 10th Gothenburg Symposium*, Hahn, HH, Hoffmann, E & Odegaard, H, (Eds), IWA Publishing.

Essemiani, K and de Traversay, C, 2002b, "Optimum design of coagulation / flocculation vessels", *WQTC 2002 conference*, Seattle, USA.

Faram, MG and Harwood, R, 2003, "A method for the numerical assessment of sediment interceptors", *Water Science and Technology*, 47, 4, 167.

Fawcett, NSJ, 1991, "Getting started with CFD", *paper presented to Environmental Engineering Group of the Institution of Mechanical Engineers meeting, 26th November,* London.

Fawcett, NSJ, 1997, "The hydraulics of flotation tanks: computational modelling", In: "*Dissolved Air Flotation", International Conference*, London, April, CIWEM, 51 - 71.

Fearing, DA, 2004, "Process Options for the Treatment of Humic Rich Waters", PhD Thesis, Cranfield University.

Fitzpatrick, CSB, Fradin, E, and Gregory, J, 2004, "Temperature Effects on Flocculation Using Different Coagulants", *Water Science and Technology*, 50, 12, 171 – 175.

Fluent Inc., 2005, *Fluent 6 Users' Guide.*

Fluent Inc., 2003, *MixSim 2.0 Users' Guide.*

Francois, RJ, 1987, "Strength of Aluminium Hydroxide Flocs", *Water Research*, 21, 9, 1023-1030

Freitas, CJ, 1995, "Perspective: Selected Benchmarks From Commercial CFD Codes", *J. Fluids Engineering.* 117, 210-218.

Frost, W and Moulden, TH, 1977, *Handbook of turbulence. Vol. 1, Fundamentals and applications*, Plenum Press, London and New York.

Fukushi, K, Tambo, N and Matsui, Y, 1995, "A kinetic model for dissolved air flotation in water and wastewater treatment", *Water Science and Technology*, 31, 3-4, 37-47.

Glover, GC, Printemps, C, Essemiani, K and Meinhold, J, 2006, "Modelling of wastewater treatment plants - how far shall we go with sophisticated modelling tools?", *Water Science and Technology*, 53, 3, pp 79–89

Graber, SD, 1994, "A critical review of the use of the *G*-value (RMS velocity gradient) in environmental engineering", *Dev. Theor. Appl. Mech.*, 17, 533-556.

Greene, DJ, Haas, CN and Farouk, B, 2002, "Numerical simulation of chlorine disinfection processes", *Water Science and Technology*, 2, 3, 167-173.

Greene, DJ, Farouk, B and Haas, CN, 2004, "CFD design approach for chlorine disinfection processes", *J.AWWA*, 96 (8), 138-150.

Gregory, J, 1997, "The density of particle aggregates", *Water Science and Technology*, 36, 4, 1-13.

Gregory, J, 1998, "The role of floc density in solid-liquid separation", *Filtration and Separation*, May, 367 – 371.

Gregory, J, 2004, "Monitoring floc formation and breakage", *Water Science and Technology*, 50, 12, 163-170.

Gregory, J and Dupont, V, 2001, "Properties of flocs produced by water treatment coagulants", *Water Science and Technology*, 44, 10, 231-236.

Gregory, J and Nelson, D, 1986, Monitoring of Aggregates in Flowing Suspension. *Colloids and Surfaces,* 18 175-188.

Gregory, J and Rossi, L, 2001, "Dynamic testing of water treatment coagulants", *Water Science and Technology: Water Supply*, 1, 4, 65-72

Gujer, W, 2006, "Activated sludge modelling: past, present and future", *Water Science and Technology*, 53, 3, 111-119.

Haarhoff, J, 1998, "Design of around-the-end hydraulic flocculators", *J Water Supply: Research and Technology-AQUA*, 47, 3, 142-152.

Haarhoff, J and van der Walt, JJ, 2001, "Towards optimal design parameters for around-the-end hydraulic flocculators", *J Water Supply: Research and Technology-AQUA*, 50, 3, 149-159.

Hague, J, Ta, CT, Biggs, MJ, and Sattary, JA, 2001, "Small scale model for CFD validation in DAF application", *Water Science and Technology*, 43, 8, 167-173

Hamill, N, 1998, "CFD - the key in design cycles", *Waste and Water Treatment*, June, 20.

Hamilton, P, 2002, "Using particle monitors to minimise *Cryptosporidium* risk", PhD Thesis, Cranfield University.

Hannoun, IA and Boulos, PF, 1997, "Optimizing distribution water storage quality: a hydrodynamic approach", *Applied Mathematical Modelling*, 21, 495-502.

Haque, JN, Mahmud, T and Roberts, KJ, 2006, "Modelling flows with free-surface in unbaffled agitated channels", *Ind. Eng. Chem. Res.*, 45, 2881-2891.

Harwood, R, 2001, 2001, "Embracing a super modeller", *Water and Waste Treatment*, September, 22-24.

Hemrajani and Tatterson, 2004, "Mechanically stirred vessels", In: "*Handbook of industrial mixing: science and practice*", edited by Paul, EL, Atiemo-Obeng, VA and Kresta, SM, pp345 – 390.

Hillis, P, Padley, MB, Powell, NI and Gallagher, PM, 1998, "Effects of backwash conditions on out-to-in membrane microfiltration", *Desalination*, 118, 197-204.

Hope, C, 1996, "Design software for process engineering seminars", presentation at the Kensington Park Thistle Hotel, London. Cited in: Morrison, 1999.

Huang, T, Brouckaert, CJ, Docrat, M and Pryor, M, 2002, "A computational fluid dynamic and experimental study of an ozone contactor", *Water Science and Technology*, 46, 9, 87 - 93.

Huang TH, Brouckaert CJ, Pryor M, and Buckley, CA, 2004, "Application of computational fluid dynamics modelling to an ozone contactor" *Water SA,* 30 (1), pp 51-56.

Hudson, HE, 1981, "Water Clarification Processes: Practical Design and Evaluation". Van Nostrand Reinhold Co., New York.

Hudson HE and Wagner, EG, 1981, "The conduct and use of jar tests", *J.AWWA*, 73(4): 218-223.

Iaccarino, G, 2000, "Prediction of the turbulent flow in a diffuser with commercial CFD codes", Centre for Turbulence Research Annual Research Briefs, 271 - 278.

Ives, KJ, 1968, "Theory of operation of sludge blanket clarifiers", *Proc. ICE*, 39, 243.

Ives, KJ, 1978, "Rate theories", In: "The scientific basis of flocculation", Ed: KJ Ives, Sijthoff and Noordhoff International Publishers, The Netherlands, pp 37-62.

Janex, ML, Savoye, P, Do-Quang, Z, Blatchley, E and Laine, JM, 1998, "Impact of water quality and reactor hydrodynamics on wastewater disinfection by UV, use of CFD modelling for performance optimisation", *Water Science and Technology*, 38, 6, 71.

Jarvis, P, 2005, "The Impact of Natural Organic Matter on Floc Structure", PhD Thesis, Cranfield University.

Jarvis, P, Jefferson, B, and Parsons, SA, 2004, "The duplicity of floc strength". *Water Science and Technology*, 50, 63-70.

Jarvis, P, Jefferson, B, Gregory, J and Parsons, SA, 2005a, "A review of floc strength and breakage", *Water Research*, 39, 3121-3137.

Jarvis, P, Jefferson, B, and Parsons, SA, 2005b, "Measuring floc structural characteristics", *Reviews in Environmental Science and Bio/Technology*, 4: 1–18.

Jarvis, P, Jefferson, B, and Parsons, SA, 2005c, "How the natural organic matter to coagulant ratio impacts on floc structural properties", *Environmental Science and Technology*, 39 (22): 8919-8924

Jarvis, P, Jefferson, B, and Parsons, SA, 2005d, "Breakage, Regrowth, and Fractal Nature of Natural Organic Matter Flocs", *Environmental Science and Technology*, 39, 2307-2314.

Jaworski, Z and Pianko-Oprych, P, 2002, "Two-phase, laminar flow simulations in a Kenics static mixer. The standard Eulerian and Lagrangian approaches", *Trans IChemE,* Vol *80, Part A*, 910 - 916.

Jaworski, Z and Zakrzewska, B, 2002, "Modelling of the turbulent wall jet generated by a pitched blade turbine impeller. The effect of turbulence model", *Trans IChemE*, Vol 80, Part A, 846 – 854.

Jefferson, B, Jarvis, P, Sharp, E, Wilson, S and Parsons, SA, 2004, "Flocs through the looking glass", *Water Science and Technology*. Accepted for publication, (presented at IWA Micro and Nano Particles in Water Treatment, Zurich, Switzerland, 2003).

Jones, SC, 1999, "Static mixers for water treatment. A computational fluid dynamics model", PhD Thesis, Georgia Institute of Technology.

Jones, SC, Amirtharajah, A, Sotiropoulos, F, and Skeens, BM, 2000, "Using static mixers to mix coagulants: CFD modelling and pilot-plant experiments", in *Chemical*

Water and Wastewater Treatment VI, Proceedings of the 9th Gothenburg Symposium, Hahn, HH, Hoffmann, E and Odegaard, H, (Eds), Springer, 79-88.

Kaneda, Y, Ishihara, T, Yokokawa, M, Itakura, K and Uno, A, 2003, "Energy dissipation rate and energy spectrum in high resolution direct numerical simulations of turbulence in a periodic box", *Physics of Fluids*, 15, 2, 21-24.

Karama, AB, Onyejekwe, OO, Brouckaert, CJ and Buckley, CA, 1999, "The use of computational fluid dynamics (CFD) technique for evaluating the efficiency of an activated sludge reactor", *Water Science and Technology*, 39, 10-11, 329-332.

Keane, RD and Adrian, RJ, 1992, "Theory of cross-correlation analysis of PIV images", *Applied Scientific Research*, 49, 191-215.

Korpijarvi, J, Ahlstedt, H, Saarenrinne, P, and Renanen, J, 1999, "Modelling of flow field in the mini-flocculator", In: *IChemE Symposium Series No 146, Fluid Mixing 6*, Ed. Benkreira, H, 361-372.

Korpijarvi, J, Laine, E, and Ahlstedt, H, 2000, "Using CFD in the study of mixing in coagulation and flocculation" in *Chemical Water and Wastewater Treatment VI, Proceedings of the 9th Gothenburg Symposium*, Hahn, HH, Hoffmann, E and Odegaard, H, (Eds), Springer, 89-99.

Kresta, SM and Brodkey, RS, 2004, "Turbulence in mixing applications", In: "*Handbook of industrial mixing: science and practice*", edited by Paul, EL, Atiemo-Obeng, VA and Kresta, SM, pp 19 – 87.

Kresta, SM and Wood, PE, 1991, "Prediction of the three dimensional turbulent flow in stirred tanks", *J.AIChE.*, 37, 448-460.

Lai, RJ, Hudson, HE and Singley, JE, 1975, "Velocity gradient calibration of jar test equipment", *J.American Water Works Association*, 67(10), 553-557.

Lainé, S, Phan, L, Pellarin, P, and Robert, P, 1999, "Operating diagnostics on a flocculator-settling tank using FLUENT CFD software", *Water Science and Technology,* 39 4 155-162.

Langelier, WF, 1921, "Coagulation of water with alum by prolonged agitation", *Eng. News-Record*, 86, 924-928.

Launder BE and Spalding, DB, 1972, "*Lectures in mathematical models of turbulence*", Academic Press, London, UK.

Lawler, DF, 1993, "Physical aspects of flocculation: from microscale to macroscale", *Water Research*, 27, 164-180.

Lawler, DF, Izurieta, E and, Kao CP, 1983, "Changes in particle size distributions in batch flocculation", *J.AWWA*, 75 (12): 604-612.

Lawler, DF and Nason, JA, 2004, "The scientific basis of flocculator design", *Water Science and Technology*, 50, 12, 155-162.

Lee, BCT, Croft, TN, Hayes, CR and Said, R, 2006, "Computational fluid dynamics (CFD) modelling of disinfection tanks and water storage structures", *paper presented to "Disinfection for water supply – UV or not UV?"*, CIWEM, 17th October.

Lee, KC and Yianneskis, M, 1998, "Turbulence properties of the impeller stream of a Rushton turbine, *AIChE Journal*, 45, 209-221.

Leentvaar, J and Rebhun, M, 1983, "Strength of Ferric Hydroxide Flocs", *Water Research* 17 895-902.

Levenspiel, O, 1972, "Chemical Reaction Engineering", 2nd Edition, Wiley, cited in Brown *et al.*, 2004.

Liu, Y and Ducoste, JJ, 2006, "Numerical simulation of chloramines formation in turbulent flow using a multi-fluid micromixing model", *Environmental Modelling and Software*, 21, 1198-1213.

Lourenco, LM, Krothopalli, A, and Smith, CA, 1989, "Particle image velocimetry", In: *Advances in fluid mechanics measurements*, Springer-Verlag, Berlin, p 127.

Luo, C, 1997, "Distribution of velocities and velocity gradients in mixing and flocculation vessels: comparison between LDV data and CFD predictions", PhD Thesis, New Jersey Institute of Technology.

Luo, JY, Issa, RI and Gosman, AD, 1994, "Prediction of impeller induced flows in mixing vessels using multiple frames of reference", In: *IChemE Symposium Series No 136*, 549-556.

Marshall, EM, and Bakker, A, 2004, "*Computational Fluid Mixing*", In: "*Handbook of industrial mixing: science and practice*", edited by Paul, EL, Atiemo-Obeng, VA and Kresta, SM, pp257-343.

Matko T, Fawcett N, Sharp A, Stephenson T, 1996, "Recent progress in the numerical modelling of wastewater sedimentation tanks", *Process Safety and Environmental Protection*, 74 (B4), pp 245-258.

Melling, A, 1997, "Tracer particles and seeding for particle image Velocimetry", *Meas. Sci and Technol.*, 8 (12), 1406-1416.

Menter, FR, 2003, "Turbulence modelling for turbomachinery", *QNET-CFD Network Newsletter*, 2, 3, December, 10-13. Accessed 23rd September 2006. http://www.qnet-cfd.net/newsletter/7th/n7_10.pdf.

Metcalf and Eddy, 2003, "*Wastewater Engineering: Principles and Design*", 4th Edition, McGraw Hill.
Metzer, AB and Taylor, JS, 1960, "Flow patterns in agitated tanks", *AIChEJ*, 6, 109.

Mhassalker, VA, Paramasivan, P and Bhole, AG, 1991, "Optimizing physical parameters of rapid mix design for coagulation-flocculation of turbid waters", *Water Research*, 25, 43-52.

Mikkelsen, LH and Keiding, K, 2002, "The Shear Sensitivity of Activated Sludge: an Evaluation of the Possibility for a Standardised Floc Strength Test", *Water Research* 36 2931-2940.

Miyahara, K, Adachi, Y, Nakaishi, K and Ohtsubo, M, 2002, "Settling Velocity of a Sodium Montmorillonite Floc under High Ionic Strength", *Colloids and Surfaces A: Physicochemical Aspects* 196 87-91.

Moin, P and Kim, J, 1997, "Tackling turbulence with supercomputers", *Scientific American*, 276, 1, 62-68.

Montante, G and Magelli, F, 2005, "Modelling of solids suspensions in stirred tanks: analysis of simulation strategies and comparison with experimental data", *International Journal of Computational Fluid Dynamics*, 19, 3, 253-262.

Morsi, SA and Alexander, A, 1972, "An investigation of particle trajectories in two-phase flow systems", *J. Fluid Mechanics*, 55 (2), 193-208.

Morrison, DJ, 1999, "Experimental and computational modelling of the flows in service reservoirs", PhD Thesis, Cranfield University.

Morvan, HP, 2005, "Automating CFD for non-experts", *J. Hydroinformatics*, 7, 1, 17-29.

Mühle, K, 1993, In: "*Coagulation and flocculation",* edited by Dobia, B, Marcel Dekker, New York, pp355-390.

Nauman, EB, 2004, Residence time distributions", In: "*Handbook of industrial mixing: science and practice*", edited by Paul, EL, Atiemo-Obeng, VA and Kresta, SM, pp 1-17.

Naude, I, Xuereb, C and Bertrand, J, 1998, Direct prediction of the flows induced by a propeller in an agitated vessel using an unstructured mesh, *Canadian Journal of Chemical Engineering,* 76: 631-640.

Ng, K, Borrett, NA and Yianneskis, M, 1999, "On the distribution of turbulence energy dissipation in stirred vessels", In: *IChemE Symposium Series No 146, Fluid Mixing 6*, Ed. Benkreira, H, pp 69-80.

No-Suk Park, Heekyung Park and Jong-Sub Kim, 2003, "Examining the effect of hydraulic turbulence in a rapid mixer on turbidity removal with CFD simulation and PIV analysis", *J Water Supply: Research and Technology-AQUA*, 52, 2, 95 - 108.

Nouri, JM, Whitelaw, JH and Yianneskis, M, 1987, "The scaling of the flow field with impeller size and rotational speeding a stirred reactor", *2nd International Conference on Laser Anemometry, Advances and Applications*, Strathclyde, Scotland, Sept. 21-23.

Oda, T, Yano, T, and Niboshi, Y, 2006, "Development and exploitation of a multipurpose CFD tool for optimisation of microbial reaction and sludge flow", *Water Science and Technology*, 53, 3, pp 101–110

Oldshue, JY, 1983, "*Fluid Mixing Technology*", McGraw-Hill, New York.

O'Melia, CR, 1972, "Coagulation and flocculation", In: *Physicochemical processes for water quality control*, Ed. WJ Weber Jr, Wiley Interscience, New York, pp 61-109.

O'Neil, S, 2001, "Hydraulic optimisation of service reservoirs to maintain water quality in distribution systems", EngD Thesis, Cranfield University.

Oshinowo, LM and Bakker, A, "CFD modelling of solids suspensions in stirred tanks", *Symposium on Computational Modelling of Metals and Materials, TMS Annual Meeting, February 17-21, Seattle.*

Oswald, L, 2006, *personal communication.*

Papadopoulos, G and Arik, EA, 2004, "Fundamental flow measurement", In: "*Handbook of industrial mixing: science and practice*", edited by Paul, EL, Atiemo-Obeng, VA and Kresta, SM, pp 202-256.

Parker, DS, Kaufman, WJ, and Jenkins, D (1972), "Floc Breakup in Turbulent Flocculation Processes". *Journal of the Sanitary Engineering Division: Proceedings of the American Society of Civil Engineers* SA 1 79-99.

Patterson, GK, Paul, EL, Kresta, SM and Etchells, AW, 2004, "Mixing and chemical reactions", In: "*Handbook of industrial mixing: science and practice*", edited by Paul, EL, Atiemo-Obeng, VA and Kresta, SM, pp 755-867.

Patterson, GK and Zipp, RP, 1999, "Turbulence modelling and mixing: modelling effects on chemical reactions", In: Amirtharajah *et al.*, 1999.

Paul, EL, Atiemo-Obeng, VA and Kresta, SM, 2004, "*Handbook of industrial mixing: science and practice*", Wiley-Interscience.

Piquet, J, 2001, "*Turbulent flows, models and physics*", Springer.

Polasek, P and Mutl, S, 1996, "*Design principles for coagulation and flocculation systems*", P Polasek and Associates, Marshalltown 2107, RSA.

Pollert, J and Stránsky, D, 2003, "Combination of computational techniques – evaluation of CSO efficiency for suspended solids separation, *Water Science and Technology*, 47, 4, 157 - 166.

Pope, S B, 2000, "Turbulent flow". Cambridge University Press.

Raffel, M, Willert, M and Kompenhans, J, 1998, "Particle image velocimetry: A practical guide", Springer-Verlag, Berlin.

Rahimi, M, Madacni, SS and Abbasi, K, 2005, "CFD modelling of permeate flux in cross-flow microfiltration membrane", *Journal of Membrane Science*, 255, 23-31.

Richardson, LF, 1922, cited in Moin and Kim, 1997.

Rodi, W, 1993, "*Turbulence models and their application in hydraulics*", IAHR, 3rd Edition.

Rogers, RH, 1978, "*Fluid Mechanics*" Routledge and Kegan Paul, London.

Rossini, M, Garcia Garrido, J, and Galluzzo, M, 1999, "Optimisation of the coagulation-flocculation treatment: influence of rapid mix parameters", *Water Research*, 33, 8, 1817-1826.

Salter, HE, Ta, CT, Ouki, SK and Williams, SC, 2000, "Three dimensional computational fluid dynamic modelling of a facultative lagoon", *Water Science and Technology*, 42, 10/11, 335 - 342.

Schmoluchowski, 1917, "Versuch einer mathematischen Theorie der Koagulation-skinetic Kolloider Losunger", *Zeit. Phys. Chemie*, 92, 129-168.

Shaw, CT, 1992, "*Using computational fluid dynamics*", Prentice Hall.

Shih, T-H, Liou, WW, Shabbir, A, Yang Z and Zhu, J, 1995, "A new k-ϵ eddy viscosity model for high Reynolds number turbulent flows", *Computers and Fluids*, 24, 3, 227-238.

Shilton, A, Glynn, D, and Phelps, P, 1999, "An inside look – the potential of CFD technology", *Water 21*, July-August, 37 - 38.

Shilton, A, Glynn, D, and Phelps, P, 2000, "Potential application of computational fluid dynamics to pond design", *Water Science and Technology*, 42, 10/11, 327 - 334.

Spicer, PT and Pratsinis, SE, 1996, "Shear-induced flocculation: The evolution of floc structure and the shape of the size distribution at steady state", Water Research, 30, 5, 1049-1056.

Spicer, PT, Pratsinis, SE, Raper, J, Amal, R, Bushell, G, and Meesters, G, 1998, Effect of Shear Schedule on Particle Size, Density and Structure During Flocculation in Stirred Tanks. *Powder Technology* 97 26-34.

Stanley, SJ and Smith, DW, 1995, "Measurement of turbulent flow in standard jar test apparatus", *J. Environmental Engineering*, December, 902 – 910.

Stovin, VR and Saul, AJ, 1996, "Efficiency prediction for storage chambers using computational fluid dynamics ", *Water Science and Technology*, 33, 9, 163-170.

Stovin, VR and Saul, AJ, 1998, "A computational fluid dynamics (CFD) particle tracking approach to efficiency prediction", *Water Science and Technology*, 37, 1, 285-293.

Stovin, VR, Saul, AJ, Drinkwater, A and Clifforde, I, 1999, "Field testing of CFD-based predictions of storage chamber gross solids separation efficiency", *Water Science and Technology*, 39, 9, 161 - 168.

Stovin, VR, Grimm, JP and Saul, AJ, 2002, "Fine sediment retention in storage chambers: an assessment of time-dependent effects", *Water Science and Technology*, 45, 7, 123 - 131.

Ta, CT, 1999, "Current CFD tool for water and waste water treatment processes", *ASME PVP99 396. Emerging Technologies in Fluids, Structures and Fluid/Structure Interaction*, Edited by Cheng, W.L. ASME, pp 79–85.

Ta, CT, Beckley, J and Eades, A, 2001, "A multiphase CFD model of DAF process", *Water Science and Technology*, 43, 8, 153-157.

Ta, CT and Brignal, WJ 1997, "Application of single phase computational fluid dynamics techniques to dissolved air flotation tank studies", In: *"Dissolved Air Flotation", International Conference*, London, April, CIWEM, 471 - 487.

Ta, CT and Brignal, WJ 1998, "Application of computational fluid dynamics technique to storage reservoir studies", *Water Science and Technology*, 37, 2, 219 - 226.

Ta CT and Hague J, 2004, "A two-phase computational fluid dynamics model for ozone tank design and troubleshooting in water treatment", *Ozone Science and Engineering,* 26, (4), pp 403-411.

Tang, P, Greenwood, J and Raper, JA, 2002, "A model to describe the settling behaviour of fractal objects", *Journal of Colloid and Interface Science* 247 210-219.

Thomas, DG, 1964, Turbulent Disruption of Flocs in Small Particle Size Suspensions, *J.AIChE*, 19, (4), 517-523.

Thomas, DN, Judd, SJ, and Fawcett, N, 1999, "Flocculation Modelling: A Review". *Water Research* 33 1579-1592.

Tomi, DT and Bagster, DF, 1978a, "Behaviour of aggregates in stirred vessels .1. Theoretical considerations on effects of agitation", *Transactions of the Institution of Chemical Engineers,* 56 (1): 1-7 1978

Tomi, DT and Bagster, DF, 1978b, "Behaviour of aggregates in stirred vessels .2. Experimental study of flocculation of Galena in a stirred tank", *Transactions of the Institution of Chemical Engineers,* 56 (1): 9-18.

Triton, DJ, 1988, "Physical fluid dynamics", Oxford, Oxford University Press.

Tung, KL, Chang, YL, Lai, JY, Chang, CH and Chuang, CJ, 2004, "A CFD study of the deep bed filtration mechanism for submicron/nano-particle suspension", *Water Science and Technology*, 50, 12,255-264.

Tyack, JN and Fenner, RA, 1999, "Computational fluid dynamics modelling of velocity profiles within a hydrodynamic separator", *Water Science and Technology*, 39, 9, 169 - 176.

UKWIR, 1997, "Using Computational Fluid dynamics to assess the impact of an anti-blockage device on the flow regime and solids retention efficiency of a stilling pond combined sewer overflow", UK Water Industry Research Ltd., Report Ref. No. 97/WW/08/3.

Valade, MT, Edzwald, JK, Tobiason, JE, Dalquhist, J, Hedberg, T and Amato, T, 1996, "Particle removal by flotation and filtration: pre-treatment effects", *J>AWWA*, 88 (12), 35-46.

Van der Walt, JJ, 2002, "The modelling of water treatment process tanks", Doctor Ingeneriae in Civil Engineering thesis, Rand Afrikaans University.

Vega GP, Pena MR, Ramirez C, and Mara, DD, 2003, "Application of CFD modelling to study the hydrodynamics of various anaerobic pond configurations", *Water Science and Technology* 48 (2), pp 163-171.

Versteeg, HK and Malalasekera, W, 1995, "*An introduction to computational fluid dynamics. The finite volume method*", Prentice Hall.

Wang, H and Falconer, R, 1998, "Simulating disinfection processes in chlorine contact tanks using various turbulence models and high-order accurate difference schemes", *Water Research*, 32 (5): 1529-1543

Westerweel, J, 1993, "*Digital particle image velocimetry – theory and application*", Delft University Press, Delft, The Netherlands.

Wilcox, D, 1998, *Turbulence modelling for CFD*, DCW Industries.

Wood, MG, Greenfield, PF, Howes, T, Johns, MR, and Keller, J, 1995, "Computational fluid dynamic modelling of wastewater ponds to improve design", *Water Science and Technology*, 11, 12, 111-118.

Wood, MG, Howes, T, Keller, J and Johns, MR, 1998, "Two dimensional computational fluid dynamic models for waste stabilisation ponds", *Water Research*, 32, 3, 958-963.

Wu, H and Patterson, GK, 1989, "Laser Doppler measurements of turbulent flow parameters in a stirred mixer", *Chem. Engrg. Sci.*, 44, 2207-2221.

Wu, CC, Wu, J.J, and Huang, R. Y. (2003) Floc Strength and Dewatering Efficiency of Alum Sludge. *Advances in Environmental Research* 7 617-621.

Yeung, AKC, and Pelton, R, 1996, Micromechanics: A New Approach to Studying the Strength and Breakup of Flocs. *Journal of Colloid and Interface Science* 184, 579-585.

Yeung, AKC, Gibbs, A, and Pelton, RP, 1997, Effect of Shear on the Strength of Polymer-Induced Flocs. *Journal of Colloid and Interface Science* 196 113-115.

Yeung, H, 2001, "Modelling of service reservoirs", *Journal of Hydroinformatics*, 03, 3, 165-172.

Yukselen, MA and Gregory, J, 2002, "Breakage and re-formation of alum flocs", *Environmental Engineering Science*, 19, 4, 229-236.

Yukselen, MA, and Gregory, J, 2004, "The Reversibility of Floc Breakage". *International Journal of Mineral Processing,* 73, 251-259.

Zhang, Z, Sisk, ML, Mashmoushy, H and Thomas, CR, 1999, "Characterisation of the breaking force of latex particle aggregates by micromanipulation", *Particle System Characterisation*, 16, 278-283.

Zhou, G and Kresta, SM, 1996, "Impact of geometry on the maximum turbulence energy dissipation rate for various impellers", *J.AIChE*, 42, 2476-2490.